Designing Chemical Reaction Networks for Self-Regulating Colloidal Assemblies and DNA Delivery Applications

Dissertation
zur Erlangung des Grades
„Doktor der Naturwissenschaften “
im Promotionsfach Chemie

am Fachbereich
Chemie, Pharmazie, Geographie und Geowissenschaften
der Johannes Gutenberg-Universität
in Mainz

Charu Sharma
geb. in Delhi, India

Mainz, October 2023

JOHANNES GUTENBERG
UNIVERSITÄT MAINZ

Reviewer 1: Prof. Dr. Andreas Walther
Reviewer 2: Prof. Dr. Pol Besenius
Date of Oral Examination:

Designing Chemical Reaction Networks for Self-Regulating Colloidal Assemblies and DNA Delivery Applications

Dissertation

Charu Sharma

The work presented in this thesis was carried out at the Institute of Macromolecular Chemistry, Albert-Ludwigs-University Freiburg from September 2019 to November 2020 and continued at Department of Chemistry, Johannes Gutenberg University of Mainz from December 2020 to October 2023 under the supervision of Prof. Andreas Walther.

Parts of this thesis have been published in the following scientific journals.

1. **Sharma, C.** & Walther, A. Self-Regulating Colloidal Co-Assemblies That Accelerate Their Own Destruction via Chemo-Structural Feedback. *Angew. Chem. Int. Ed*. 61, e202201573, doi: https://doi.org/10.1002/anie.202201573 (**2022**).
2. **Sharma, C.**, Maity, I. & Walther, A. pH-feedback systems to program autonomous self-assembly and material lifecycles. *Chem. Commun*. 59, 1125-1144, doi: http://doi:10.1039/D2CC06402B (**2023**).
3. **Sharma, C.**, Samanta, A., Schmidt, R. S. & Walther, A. DNA-Based Signaling Networks for Transient Colloidal Co-Assemblies. *J. Am. Chem. Soc*. 145, 17819-17830, doi: http://doi.org/10.1021/jacs.3c04807 (**2023**).
4. **Sharma, C.**, Sarkar, A. & Walther, A. Transient Co-Assemblies of Micron-Scale Colloids Regulated by ATP-Fueled Reaction Networks. *Chem. Sci.*, Accepted Manuscript, doi: https://doi.org/10.1039/D3SC04017H (**2023**).

Abstract

Biological self-assemblies for e.g., microtubules regulate in space and time via kinetically controlled reaction networks, feedback loops, and energy dissipation giving rise to non-equilibrium processes. Such structures provide an interesting approach for the development of artificial self-assembling molecular systems and materials functions. Early examples of synthetic out-of-equilibrium self-assemblies primarily include supramolecular systems that form transient gels, polymers, vesicles, and micelles. Colloids are rarely used as building blocks. However, they can give rise to functional materials with unique catalytic, photonic, magnetic, and electronic properties originating not only from the positional or dimensional order of the building blocks, but also from the type of material bulk (metallic, polymeric, semiconductor, inorganic). Employing biocompatible material for their fabrication can even pave the way into biomedical applications such as drug delivery and diagnostics. They can even serve as model systems to elucidate physical concepts underlying out-of-equilibrium biological self-assemblies.

The research of this thesis aims at developing new concepts for transient colloidal co-assemblies by either coupling or integrating micron-sized colloidal particles to chemical reaction networks (CRNs) of different origins. CRNs are composed of antagonistic activation and deactivation pathways decoupled by either chemical modulation, temporal modulation, or by energy dissipation strategy (reminiscent of biological self-assemblies). The activation pathway induces the formation of assembled structures that are subsequently degraded by the deactivation pathway giving the transient structures a limited lifetime. The kinetics of the antagonistic pathways are tunable and can be tuned to further modulate the lifetime and structural properties of the transient assemblies. Two major challenges addressed in this thesis to achieve successful transient assembly of colloids are: (i) time-dependency of interparticle potentials and (ii) matching the dynamics of micron-sized particles with kinetics of CRNs. Both conditions are indispensable to target transient structures without the system falling into kinetic traps.

Within the framework of this thesis, three main design strategies are established to program transient co-assemblies of micron-scale colloids.

In the first part of the thesis, a pair of pH-responsive, hetero-complementary colloids are integrated within a pH-feedback system (pH-FS) wherein an alkaline trigger facilitates transient assemblies and autonomous acid formation via an enzymatic cascade subsequent leads to disassembly. The system features advanced chemo-structural feedback where co-assemblies (structures) accelerate their own destruction (negative feedback).

To increase the programmability and modularity of transient assemblies, the second part of the thesis makes use of DNA-based networks such as toehold-mediated DNA strand displacement (TMDSD) reaction networks. A TMDSD reaction cascade directs two different colloids into transient co-assemblies. The colloids are functionalized with DNA and become an integral part of the network. The particles transduce two orthogonally different DNA trigger strands to transiently introduce a linker which brings two colloids together into co-assemblies. The system follows a complex trajectory passing through a transient state in the middle and ultimately reaching thermodynamic equilibrium. Although dynamic, the system operates under non-dissipative conditions as it resides in a new state (lowest energy state) and the original state cannot be acquired. The modularity of the design allows the installation of delay phases and accelerators by interconnecting modules to the upstream and downstream of the core network.

Moving away from the thermodynamically driven classic TMDSD reactions, the third part of the thesis deals with ATP-fueled enzymatic TMDSD reaction cascade which operates under dissipative conditions. The ATP-powered ligation and restriction of DNA components transiently generates a linker strand at the molecular level which temporally controls the downstream co-assembly of colloids. The resetting ability of the network restores the original state of the system and allows the system to be reused for subsequent cycles. Because

of their high robustness, ATP-fueled reaction networks are also installed in the extracellular medium of HeLa cells (cancer cells) to develop a DNA delivery system. The delivery mechanism proposed holds potential applications in gene therapy and gene silencing where therapeutic oligonucleotides such as small interfering RNA (siRNA) and micro RNA (miRNA) can be selectively delivered to target cells and tissues in response to ATP.

In a future perspective, strategies developed in this thesis for the fabrication of transient colloidal assemblies represent a step towards functional materials. The design principles can be extended to colloids of different origins, depending on the type of material or application they are targeted at. The modularity of CRNs. especially DNA-based networks, allows the insertion of additional feedback loops to achieve advance dynamic functionalities such as oscillations and bistability.

Kurzzusammenfassung

Biologische Selbst-assemblierungen, wie beispielsweise Mikrotubuli, regulieren im Raum und in der Zeit über kinetisch gesteuerte Reaktionsnetzwerke, Rückkopplungsschleifen und Energieabgabe, was zu nichtgleichgewichtigen Prozessen führt. Solche Strukturen bieten einen interessanten Ansatz für die Entwicklung künstlicher selbstassemblierender molekularer Systeme und Materialfunktionen. Frühe Beispiele für synthetische Nichtgleichgewichts-Selbst-assemblierungen umfassen hauptsächlich supramolekulare Systeme, die vorübergehende Gele, Polymere, Vesikel und Mizellen bilden. Kolloide werden selten als Bausteine verwendet. Sie können jedoch funktionale Materialien mit einzigartigen katalytischen, photonischen, magnetischen und elektronischen Eigenschaften hervorbringen, die nicht nur aus der räumlichen oder dimensionalen Anordnung der Bausteine resultieren, sondern auch aus dem Typ des Materialbulks (metallisch, polymer, halbleitend, anorganisch). Die Verwendung biokompatibler Materialien für ihre Herstellung kann sogar den Weg in biomedizinische Anwendungen wie Arzneimittelabgabe und Diagnostik ebnen. Sie können sogar als Modellsysteme dienen, um die physikalischen Konzepte hinter nichtgleichgewichtigen biologischen Selbst-assemblierungen zu klären.

Das Forschungsziel dieser Dissertation besteht darin, neue Konzepte für vorübergehende kolloidale Co-Selbst-assemblierungen zu entwickeln, indem mikroskopische kolloidale Partikel entweder an chemische Reaktionsnetzwerke (CRNs) unterschiedlicher Herkunft gekoppelt oder integriert werden. CRNs bestehen aus antagonistischen Aktivierungs- und Deaktivierungswegen, die entweder durch chemische Modulation, zeitliche Modulation oder durch eine Energieabgabestrategie (analog zu biologischen Selbst-assemblierungen) voneinander getrennt sind. Der Aktivierungsweg führt zur Bildung assemblierter Strukturen, die anschließend durch den Deaktivierungsweg abgebaut werden, wodurch den vorübergehenden Strukturen eine begrenzte Lebensdauer verliehen wird. Die Kinematik der antagonistischen Wege ist einstellbar und kann weiter moduliert werden, um die Lebensdauer und strukturellen Eigenschaften der vorübergehenden Assemblierungen zu beeinflussen. Zwei Hauptprobleme, die in dieser Dissertation angegangen werden, um eine erfolgreiche vorübergehende Assemblierung von Kolloiden zu erreichen, sind: (i) die zeitabhängigen Wechselwirkungspotenziale zwischen den Partikeln und (ii) die Anpassung der Dynamik der mikroskopischen Partikel an die Kinematik der CRNs. Beide Bedingungen sind unerlässlich, um vorübergehende Strukturen zu erreichen, ohne dass das System in kinetische Fallen gerät.

Im Rahmen dieser Dissertation werden drei Hauptkonstruktionsstrategien etabliert, um vorübergehende Co-Assemblierungen von mikroskopischen Kolloiden zu programmieren.

Im ersten Teil der Dissertation sind ein Paar pH-responsive, heterokomplementäre Kolloide in ein pH-Rückkopplungssystem (pH-FS) integriert, bei dem ein basischer Auslöser vorübergehende Assemblierungen und die autonome Bildung von Säure durch eine enzymatische Kaskade zur anschließenden Disassemblierung ermöglicht. Das System zeichnet sich durch eine fortgeschrittene Chemostruktur-Rückkopplung aus, bei der Co-Assemblierungen (Strukturen) ihre eigene Zerstörung beschleunigen (negative Rückkopplung).

Um die Programmierbarkeit und Modularität vorübergehender Assemblierungen zu erhöhen, nutzt der zweite Teil der Dissertation DNA-basierte Netzwerke wie das toehold-vermittelte DNA-Strangverdrängungsreaktionsnetzwerk (TMDSD). Eine TMDSD-Reaktionskaskade lenkt zwei verschiedene Kolloide in vorübergehende Co-Assemblierungen. Die Kolloide sind mit DNA funktionalisiert und werden ein integraler Bestandteil des Netzwerks. Die Partikel übertragen zwei orthogonal unterschiedliche DNA-Auslösestränge, um vorübergehend einen Verbindungsdraht einzuführen, der zwei Kolloide zu Co-Assemblierungen zusammenführt. Das System folgt einer komplexen Bahn, die durch einen vorübergehenden Zustand in der Mitte verläuft und letztendlich das thermodynamische Gleichgewicht erreicht. Obwohl dynamisch, arbeitet das System unter nicht-dissipativen Bedingungen, da es sich in einem neuen Zustand (niedrigster Energiezustand) befindet und der ursprüngliche Zustand nicht wiederhergestellt werden kann. Die

Modularität des Designs ermöglicht die Installation von Verzögerungsphasen und Beschleunigern, indem Module mit dem Kernnetzwerk nach oben und unten verbunden werden.

Im dritten Teil der Dissertation wird von den thermodynamisch getriebenen klassischen TMDSD-Reaktionen abgewichen und sich mit einer ATP-betriebenen enzymatischen TMDSD-Reaktionskaskade beschäftigt, die unter dissipativen Bedingungen arbeitet. Die ATP-betriebene Verknüpfung und Restriktion von DNA-Komponenten erzeugt vorübergehend einen Verbindungsdraht auf molekularer Ebene, der die nachfolgende Co-Assemblierung von Kolloiden zeitlich steuert. Die Rücksetzfähigkeit des Netzwerks stellt den ursprünglichen Zustand des Systems wieder her und ermöglicht die Wiederverwendung des Systems für nachfolgende Zyklen. Aufgrund ihrer hohen Robustheit werden ATP-betriebene Reaktionsnetzwerke auch im extrazellulären Medium von HeLa-Zellen (Krebszellen) installiert, um ein DNA-Liefersystem zu entwickeln. Der vorgeschlagene Liefersystemmechanismus hat Potenzialanwendungen in der Gentherapie und Gen-Silencing, bei denen therapeutische Oligonukleotide wie small interfering (siRNA) und micro RNA (miRNA) selektiv an Zielzellen und -gewebe in Reaktion auf ATP geliefert werden können.

In einer zukünftigen Perspektive repräsentieren die in dieser Dissertation entwickelten Strategien für die Herstellung vorübergehender kolloidaler Assemblierungen einen Schritt hin zu funktionalen Materialien. Die Gestaltungsprinzipien können auf Kolloide unterschiedlicher Herkunft ausgeweitet werden, abhängig von der Art des Materials oder der Anwendung, auf die sie abzielen. Die Modularität von CRNs, insbesondere DNA-basierten Netzwerken, ermöglicht die Einfügung zusätzlicher Rückkopplungsschleifen, um fortgeschrittene dynamische Funktionalitäten wie Oszillationen und Bistabilität zu erreichen.

Contents

Abbreviations

1-ethyl-3-(3-dimethylaminopropyl)carbodiimide
EDC 5
adenosine diphosphate
ADP 6
adenosine triphosphate
ATP 1
block copolymers
BCPs 50
chemical reaction networks
CRNs 42, 70
chemo-structural feedback
CSF 74
citric acid
CA 51, 71
complex coacervate core micelles
C3M 51
Confocal Fluorescence Laser Scanning Microscopy
CLSM 72
cryogenic transmission electron microscopy imaging
cryo-TEM 50
dimethylsulfate
DMS 4
dithiothreitol
DTT 9
DNA nanotubes
DNTs 21
DNA strand displacement
DSD 13
dodecylamine
DDA 51
dormant activator
DA 48
dormant deactivators
DD 43
double-stranded
dsDNA 19
dynamic light scattering
DLS 72
Dynamic Light Scattering
DLS 50
enzymatic cascade
EC 70
enzymatic cascades
EC 43
exonuclease III
Exo III 26
gene regulatory networks
GRNs 20
gluconic acid δ-lactone
δ-GL 44
glucose oxidase
GOX 12, 24, 71
Glucose Oxidase
GOX 47
glutathione
GSH 9
glycidyl methacrylate
GMA 72
Gold nanoparticles
Au-NPs 55
gold nanorods
AuNRs 56
guanosine diphosphate
(GDP) 1
guanosine triphosphate
(GTP) 1
horseradish peroxidase
HRP 24, 58
hydrogen peroxide
H2O2 9
invertase
INV 71
Invertase
INV 47
microgel
MG 70
microgels
MGs 57
microRNA
miRNA 28
N,*N*'-methylenebis(acrylamide)
MBA 72
N,N'-dibenzoyl-L-cystine
DBC 9
N,N-dimethylethylenediamine
DMEDA 73
N-benzoyl-L-cystine
BC 9
nicotinamide dinucleotide phosphate
NADPH 9
nucleotide triphosphates
NTPs 20
nucleotides
nt 12
oligonucleotides
ODNs 28
oxidant

1 Introduction

1.1 Autonomous Self-Assemblies and Materials Inspired by Biological Systems

Nature provides a great source of inspiration for building next-generation smart and intelligent materials via a bottom-up approach. They are designed to have unique properties allowing them to respond and adapt to environmental changes. Some examples include: (i) electroactive polymers draw inspiration from the way muscles and nerves in the human body respond to electrical signals, (ii) magnetic materials changing their properties in response to external magnetic field are inspired by migratory birds which have built-in magnetic sensors to navigate using the Earth's magnetic field, (iii) chromic materials which change their color in response to specific stimulus such as pH, temperature, and light; these materials take inspiration from various organisms that use adaptive coloration for camouflage, thermoregulation and communication purposes, (iv) miscellaneous materials such as adhesives inspired by gecko feet that can stick to surfaces without leaving residue, or materials inspired by spider silk known for its unique mechanical properties. An important point to note in all these examples is that they are equipped with responsive segments making them switch between different thermodynamic equilibrium states reversibly in dependence of external triggers such as pH, temperature, light, magnetic field, electric field, or ionic strength.

Such design has impacted the utilization of present-day responsive materials in sensing, photonics, electronics, drug delivery and for actuation. However, they are still far from being recognized as smart and intelligent. These terms are actually derived from living systems which have complex and functional out-of-equilibrium machinery regulating essential processes such as growth, movement, communication, and adaptation. On a cellular level, most of these life-distinguishing features are performed by cytoskeletal structures that exist dynamically in space and time under constant energy dissipation i.e., they require a constant supply of chemical fuel in order to sustain. Depending on the cellular function to be performed, cytoskeletal structures break down and reorganize, changing their life cycles and turnover. At the molecular level, such functions are orchestrated by series of reaction networks and feedback loops.

The cytoskeleton network is composed of three main structures: microtubule, actin, and intermediate filaments.[5] Microtubule consists of supramolecular self-assembly of heterodimer proteins (α/β-tubulin) bound to guanosine diphosphate (GDP) or guanosine triphosphate (GTP). Binding of GTP, a chemical fuel activates tubulin for getting added at the end of the microtubule (polymerization step), soon after its incorporation GTP-tubulin hydrolyzes to GDP-tubulin (energy dissipation step hinting towards a chemo-structural feedback). Once hydrolysis reaches the tips of microtubule and overcomes the growth by addition of GTP-tubulin, the microtubule begins to depolymerize rapidly. These dynamic instabilities assist in sorting chromosomes during cell division and serve as tracks for organelle transport. Actins following a similar mechanism form dynamic self-assemblies where adenosine triphosphate (ATP) bound actin monomers polymerize into filaments which are responsible for cell movement and mitotic stage of cell division.

1.2 Structure Formation Near Thermodynamic Equilibrium and Out-of-Equilibrium

Being able to transmit above-mentioned properties to present-day responsive assemblies and materials can pave the way towards smart and autonomous materials.[5] The first step towards this aim is to develop a responsive system which can be toggled back and forth between two thermodynamically stable states in response to two antagonistic triggers (stimulus/anti-stimulus). As an example, consider a system in its thermodynamically stable State A consisting of dissolved or disassembled building blocks (**Figure 1-1a**). The system remains infinitely stable in this state as long as switched to another thermodynamically stable State B

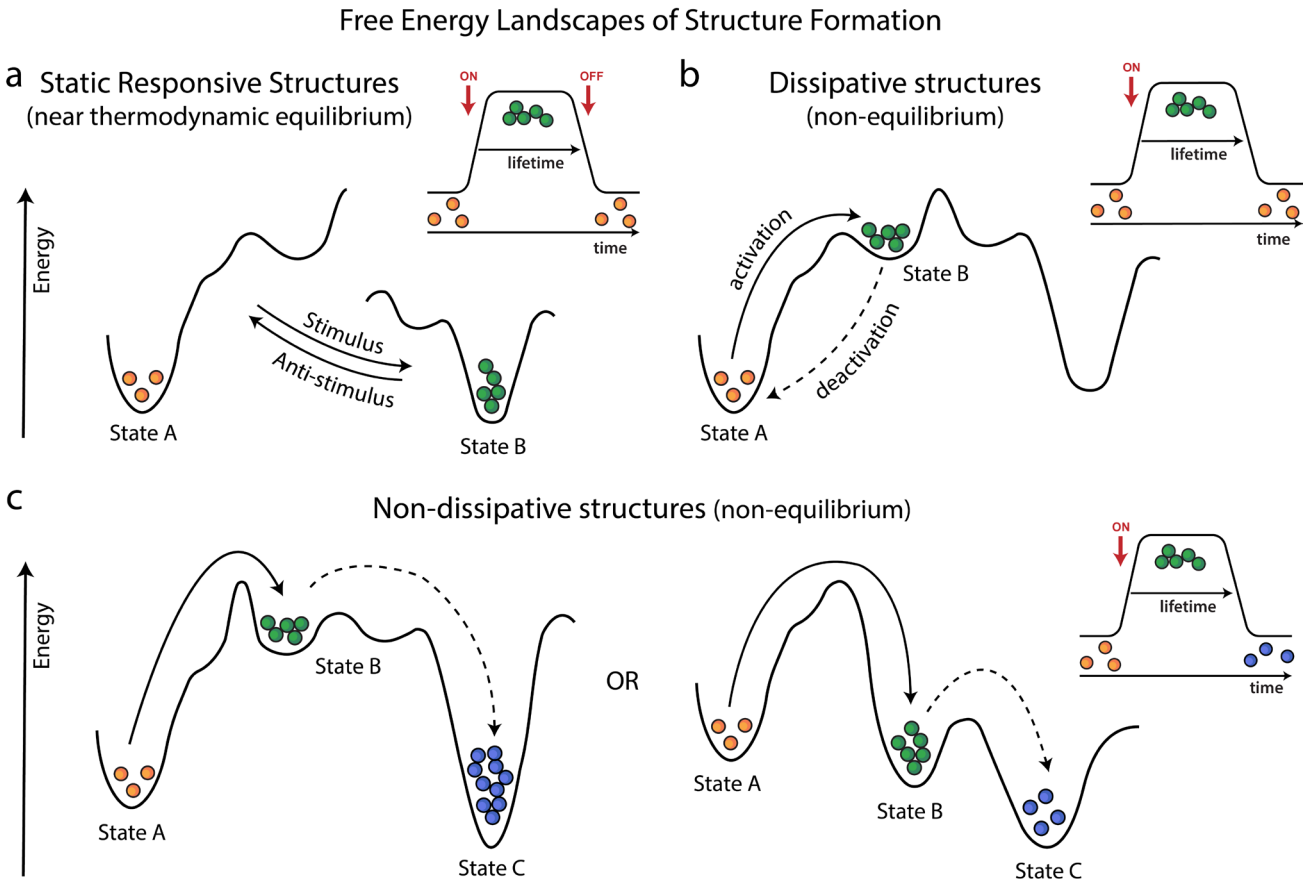

Figure 1-1. Three different cases of assembly formation. (a) Static structures reside in the minimum of the energy landscape and are stable as long as exposed to a fuel/stimulus which changes the energy landscape of the system whereupon structures switch to the new lowest energy state. This process must be reversible to obtain autonomous structures ((b), (c)). (b) Dissipative structures sustain in the dynamic steady state under constant supply of high energy fuel, the assembled structures are continuously activated and deactivated along chemically decoupled reaction pathways. (c) Assembly formation under non-dissipative condition occurs if the system instead of coming back to its initial State A enters into a thermodynamically more stable State C. The assembled structures either enter into a higher or lower energy state with respect to initial state.

in response to a stimulus (for e.g., pH, redox) activating self-assemblies. Applying a counter stimulus should bring the system back to its initial State A. These states are driven by enthalpy minimization and/or entropy maximization and reside in the global minimum of the energy landscape infinitely stable over time. Only the application of a stimulus/counter stimulus modulates the energy landscape and transitions the system to a new lowest energy state, hence termed as Static responsive structures near thermodynamic equilibrium.

In the above example, the pathways to switch from State A to State B and vice versa are exact opposite of each other. Achieving autonomous and transient behavior in these systems means going from State A → State B → State A just by introducing one trigger in the beginning eradicating the need of adding any extra trigger in the middle where State B is called a transient state associated with a limited lifetime. This cannot be simply done by mixing stimulus and anti-stimulus together as it will result in complete annihilation of the system. This will require breaking the reversibility and introducing asymmetry in the system. Imagine mixing base (stimulus) and acid (counter stimulus) together, this will merely result in salt formation. However, the problem can be solved if acid is produced autonomously (*in situ*) in the closed system without any manual intervention. The addition of a single trigger should elevate the system from State A to a thermodynamically labile, energy rich steady State B. This state now requires a constant supply of energy to persist and will otherwise return to its original state. For this, activation/deactivation pathways need to be decoupled either chemically, temporally or spatially or a combination of these categories.[6-8] The strategies developed so far can be divided into three broad categories as mentioned in **Info Box 1**.

Info Box 1. Strategies for decoupling activation/deactivation pathways.

(1) The first strategy exploits the chemical modulation by implementing reaction networks where activation and deactivation pathways are separated in time via formation of intermediate species meaning the deactivator generation is constrained by the activation pathway.
(2) The second strategy involves energy dissipation which is reminiscent of GTP fueled microtubules or ATP fueled actins. The availability of the energy influx is automatically anchored to the timeline of the dissipative assemblies that are stable as long as there is energy in the system (**Figure 1-1b**).
(3) The third strategy finally exploits temporal modulation where the rates of activation and deactivation pathways are controlled to achieve a steady state with programmed lifetime.

Strictly speaking, it is difficult to draw a fine line between the mentioned strategies and many times different aspects of these approaches are combined to develop a transient, non-equilibrium system. For example, even if the activation and deactivation pathways are chemically decoupled the former has to be faster than the latter for a transient signal to be observed. Moreover, in some cases the system instead of returning back to its original State A follows the trajectory, State A → State B → State C and returns to a new State C, hence regarded as non-equilibrium, non-dissipative system (**Figure 1-1c**). Within this category, State B can either reside in a thermodynamically higher (**Figure 1-1c, left**) or lower (**Figure 1-1c, right**) energy state with respect to State A.

These systems can be further classified based on the active component of the system. This component is responsible for harnessing the energy by fuel conversion and can either be the structural elements forming the self-assembly or the environment regulating them. Active environment offers a versatile approach that can be customized in accordance with the building block. Active components on the other hand require judicious tuning of the entire system to suit one particular type of building block. However, these are the systems where building blocks or their self-assembled structures can actively participate in the reaction kinetics showcasing emergent function such as chemo-structural feedback loop. The self-assembled structures can either accelerate their own destruction imposing a negative chemo-structural feedback or the small self-assembled clusters (nucleation centers) catalyze their own growth applying a positive chemo-structural feedback.[10]

1.3 Different Reaction Networks/Cycles for Transient Self-Assembling System

Based on the concepts defined so far, I will present examples of transient, self-assembling systems and categorize them based on the reaction network/cycle responsible for this behavior. These examples will be further classified according to the Strategy (1, 2, or 3) used to build the reaction cycle, and finally we will also identify the active component in the system (building block or environment).

1.3.1 Small Binding Molecules as High-Energy Fuels for Dissipative Self-Assembly

This category exploits Strategy 2 and Strategy 3. It constitutes a class of simple chemical fuels which activate the building block by either covalent or non-covalent modification towards dissipative self-assembly. The chemical reaction cycle comprises of activation and deactivation reaction. In the activation reaction, a building block is converted into product driven by the irreversible consumption of an energy source. This means, the reaction is driven by the consumption of a chemical fuel whereby the fuel is irreversibly burned, and the energy cannot be regained. In contrast, the deactivation reaction is spontaneous that returns the self-assembly into disassembled building blocks. The reaction cycle is conditioned by fast activation and slow deactivation. Although both reactions operate simultaneously, deactivation takes over once the fuel reaches suboptimal levels. As the reaction cycle operates by direct activation/deactivation of building blocks, they will be regarded as the active component of the system in all the examples which will be discussed in this section.

Dimethylating Agents For Dissipative Self-Assembly

Seminal work by van Esch and coworkers illustrated the first time use of methylating agent like methyl iodide as chemical fuel (**Figure 1-2a**).[11] For this, a bis-carboxylate gelator was selected as a building block and fueled by methyl iodide, the corresponding ester formed removes electrostatic repulsion and undergoes transient supramolecular polymerization to form fibrous networks. The subsequent hydrolysis of these esters (in both monomeric and polymeric state) dissipates energy and disassembles the polymers into initial carboxylates. The rate of methylation is critically designed to be faster than de-methylation/ester hydrolysis by tuning pH of the medium and concentrations of all chemical reagents. However, the dynamics of the system were too slow to be recognized as truly dissipative whereby material properties can be temporally modulated by fuel conversion kinetics. Therefore, methyliodide was replaced by a much stronger methylating agent dimethylsulfate (DMS) for further applications (**Figure 1-2b**).[12] The above systems are often compared to dissipative self-assembly of microtubules. However, there is a notable difference between the two systems. Upon its self-assembly into microtubules, GTP-tubulin complex undergoes some conformational changes,[13] which unlocks its ability to hydrolyze the fuel molecule. This makes GTP-tubulin inherently unstable both in

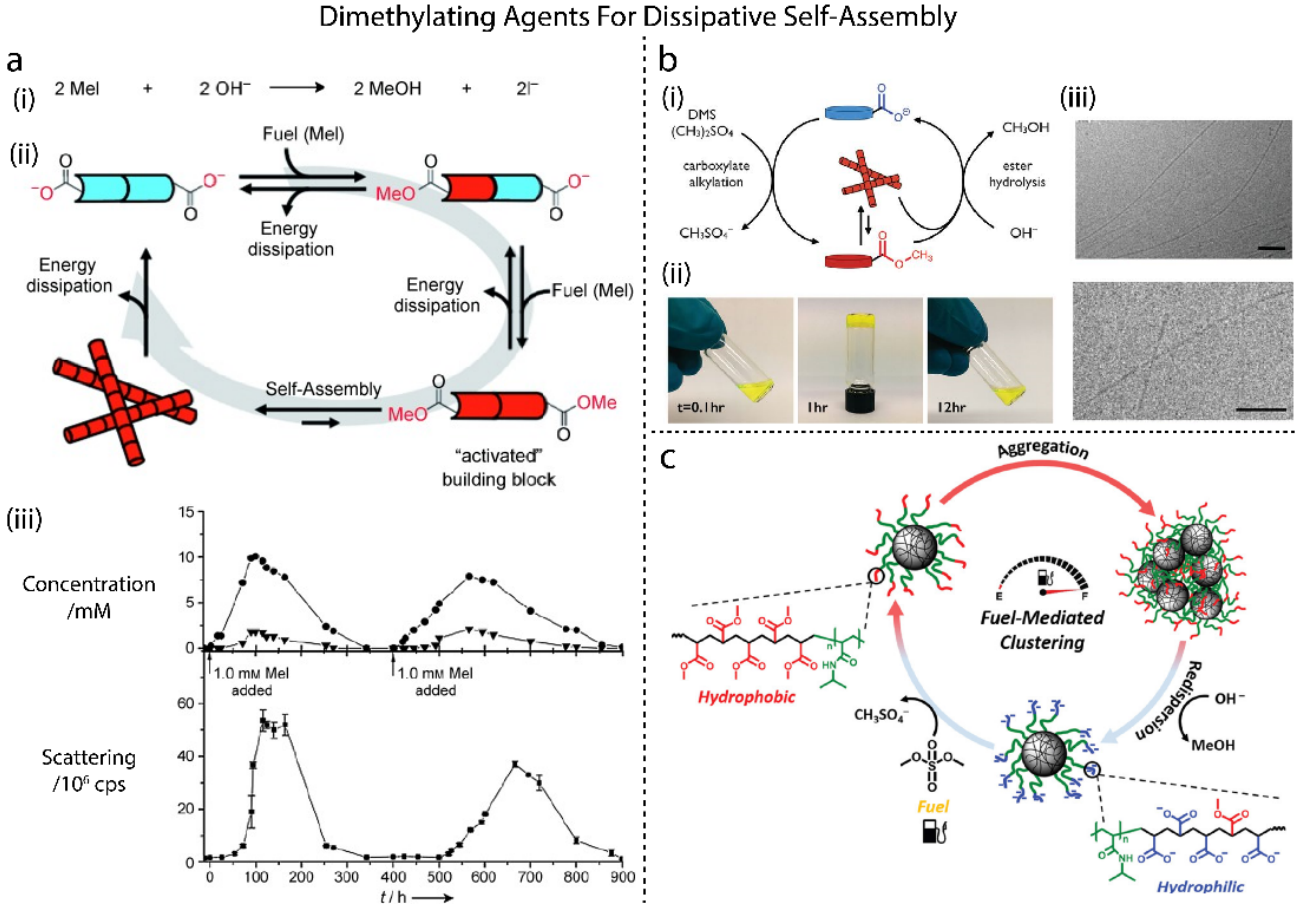

Figure 1-2. Schematics for the dissipative reaction cycle using methylating agents as fuel such as: (a) DMI, (i) The net reaction of one dissipative cycle. (ii) Dibenzoyl-(L)-cystine undergoes stepwise methylation with MeI to produce its diester analogue which can dissipate its energy through hydrolysis to form the building block again. The diester assembles into fibres, which will be in equilibrium between formation and hydrolysis of the diester until all the MeI has reacted. (iii) Concentrations of mono (solid circles) and dimethyl esters (solid triangles) as determined by HPLC-MS over time; (b) DMS, (i) Chemical reaction cycle for dissipative self-assembly of monocarboxylate building blocks. (ii) Real time images of the sample during reaction cycle. (iii) Cryogenic transmission electron microscopy (cryo-TEM) micrographs of a gel at 2 h; (c) DMS mediated clustering of colloidal particles. The high initial pH of the medium maintains colloidal stability due to deprotonated carboxylic groups in the p(MMA) segments (blue) of the grafted polymers. The addition of DMS removes electrostatic repulsion and increases the hydrophobicity of the polymer brush's outer corona (red). This triggers colloidal clustering. After fuel depletion, hydrolysis of formed ester groups dominates, reintroducing the negative charges. This leads to disintegration of formed clusters. Graphics adapted from ref. (11, 12, 14)

the monomeric and polymeric state. However, the activated building block in above proposed synthetic system is, on its own, a stable molecule, it is the externally introduced agent (OH^-) that renders it unstable. A similar strategy was extended to colloidal systems (**Figure 1-2c**).[14] The core-shell particles are dispersed in alkaline aqueous buffer where the shell is composed of pH-responsive polymethylmethacrylate (PMMA) outer segments and hydrophilic poly(N-isopropylacrylamide) (PNIPAM) inner segments which ensure steric stabilization. The PMMA segments undergo esterification when fueled with DMS. The hydrophobicity of the esters results in the transient clustering of the colloidal particles.[15-18]

EDC for Dissipative Self-Assembly

To increase the rates in the chemical reaction cycles, Boekhoven group (**Figure 1-3a**) and Hartley group (**Figure 1-3b**) independently developed a reaction cycle that is driven by the energy obtained by the hydrolysis of carbodiimides such as 1-ethyl-3-(3-dimethylaminopropyl)carbodiimide (EDC). The building block is a dicarboxylate that intramolecularly converts into its corresponding anhydride in the activation reaction. The anhydride reacts with water in a first-order reaction with a half-life of roughly 30 s at pH 6 and reproduces dicarboxylate (**Figure 1-3a**).

Due to the short half-life of anhydride, the reaction cycle is approximately 12 times faster than one observed with DMS. However, the authors reported that anhydrides follow 0^{th} order hydrolysis in the self-assembled state and hence exert negative feedback on themselves to slow down their own destruction. This allows self-assemblies to demonstrate a realistic lifetime. Moreover, under the employed conditions, the half-life of EDC is in the range of 14 h which reduces to roughly 14 min in the presence of the building block. This mandates the addition of an excessive amount of EDC to sustain the transient state. The reaction cycle was demonstrated on fluorenylmethyloxycarbonyl (Fmoc)-protected amino acids and peptides. The presence of anionic amino acids aspartic (D) or glutamic (E) acid on the C terminus of peptide yielded well-soluble building blocks. The addition of EDC converts the two carboxylates of the C-terminal aspartic (D) or glutamic (E) acid into their corresponding anhydride. The removal of two anions and formation of anhydride increases the hydrophobicity

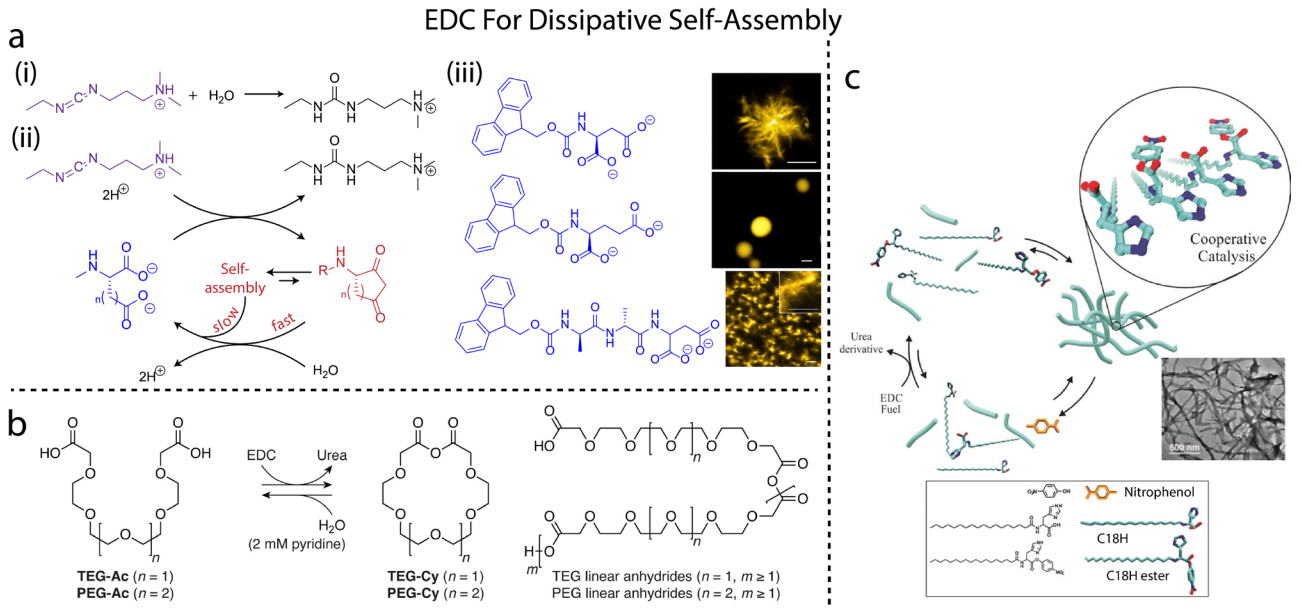

Figure 1-3. Chemical reaction cycles driven by the hydrolysis of carbodiimides. (a) Use of EDC hydrolysis for transient formation of anhydride from carboxylate-based building blocks. (iii) List of building blocks and representative micrographs of self-assembled supramolecular structures (top to bottom, spherulites, colloids and fibers). (b) Oligo(ethylene glycol) diacids undergo anhydride formation when treated with EDC, giving a mixture of cyclic and oligomeric linear anhydrides. The transient yields of cyclic and linear anhydrides depend on the alkali earth metal salts. (c) EDC fuels the coupling between nitrophenol and C18H amphiphile to form transient self-supporting gels. Graphics adapted from ref. (8, 15, 19)

of the building block and induces self-assembly. Depending on the design of the building block, it can be assembled into spherulites, colloids, micelles,[22] crystals, or hydrogel forming fibers.

Using EDC as the energy source, the group also developed a chemical reaction cycle based on N-hydroxysuccinimide (NHS).[23] Due to the increased stability of the NHS ester, the cycle lasts for roughly 15 h which is seven times longer compared to the anhydride based cycle. In a much recent report, they suggested formation of transient oxazolones over anhydrides and NHS ester as the reaction cycle is less prone to side reactions and provide better substate scope.[24] Das group also demonstrated the concept by using 4-nitrophenol to stabilize the transient active ester (**Figure 1-3c**).[25] It is evident from above example that the controlled formation of an unstable covalent bond is key to these systems and in a way they represent out-of-equilibrium analogues of the dynamic covalent chemistry.[26,27]

Biocatalyzed Hydrolysis of Aspartame for Dissipative Self-Assembly

Some reaction cycles require enzymes to carry out the hydrolysis of the chemical fuel. As an example, Ulijn and coworkers explored a different chemical reaction cycle that is driven by the energy obtained from the hydrolysis of the methyl ester of aspartame. In the activation reaction, the methylated C terminus of the peptide aspartame is reacted with the N terminus of phenylalanine amide (building block) to form a tripeptide product. The reaction is not spontaneous but carried out by enzyme chymotrypsin. Chymotrypsin also catalyzes the subsequent hydrolysis of tripeptide reproducing the initial building block. The one enzyme approach operates under biocompatible conditions suitable for biomedical applications.

ATP for Dissipative Self-Assembly

Herman and coworkers developed a reaction cycle driven by the energy obtained from hydrolyzing ATP to adenosine diphosphate (ADP).[29] Under the employed conditions, ATP has a half-life of more than hundred hours (**Figure 1-4a,b**).[30] Because of its frequent use in living systems, a broad range of ATP-driven cycles are available offering a great toolbox to choose reactions and enzymes. They used a combination of protein kinase A that phosphorylates the side chain of serine in the initial state driven by ATP hydrolysis to yield non-equilibrium product and a γ-protein phosphatase that simultaneously removes the phosphate group and reproduce the initial state. The phosphorylation/dephosphorylation cycle was implemented for transient change of supramolecular structure and chirality.

Non-covalent modification of building blocks by chemical fuels constitutes a special approach to access transient self-assemblies. This is reminiscent of the biological self-assemblies where GTP bind to tubulin and ATP to actin. The general strategy comprises of the two steps, activation by chemical fuel that non-covalently modifies the building block for self-assembly and the deactivation by an ATP decomposing enzyme that gradually brings the system to its initial state. In this context, Prins group have employed a charge neutralization strategy to transiently assemble small cationically charged building blocks (**Figure 1-4c**).[31] The building block has a positively charged polar head 1,4,7- triazacyclononane-zinc(II) which induces electrostatic repulsion and a dodecyl chain as a hydrophobic tail. The addition of a multivalent anionic molecule such as ATP neutralizes the positive charge resulting in formation of bilayer vesicles. The availability of phosphatase enzymes such as potato apyrase hydrolyzes ATP and breaks down the vesicles. Interestingly, the authors used the dissipative vesicles as transient nanoreactors for reactions that will not usually occur in water. These ampiphilic building blocks, when functionalized on gold nanoparticles can be used for transient signaling and catalytic functions.[32] Goerge and co-workers independently proposed a transient supramolecular polymerization of a chromophore functionalized with phosphate receptors like dipicolylethylenediamine-zinc complex (DPA-Zn) on binding with ATP in presence of potato apyrase (**Figure 1-4d**).[33] Using a similar approach,

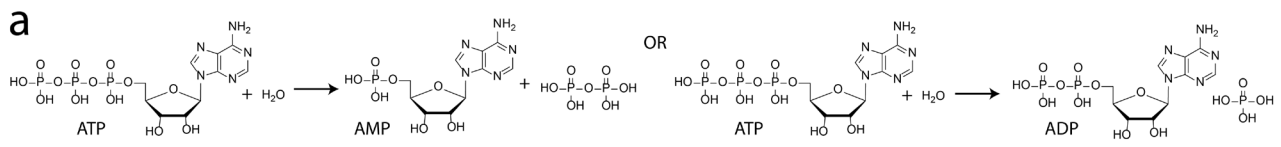

Covalent Modification of Building Blocks by ATP for Dissipative Self-Assembly

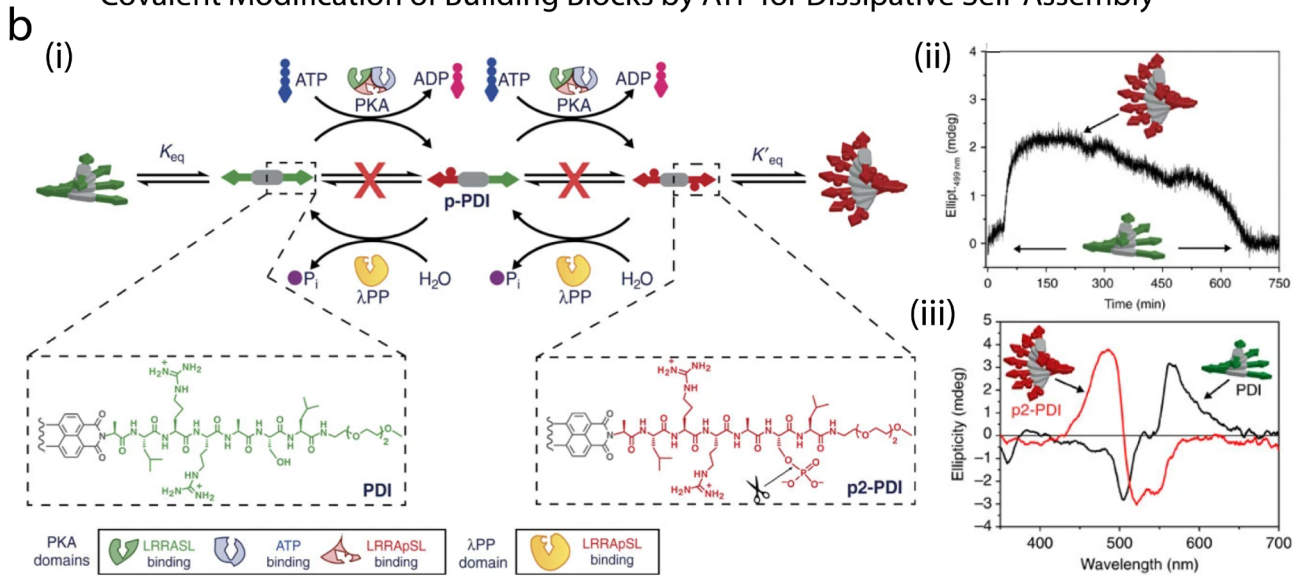

Non-Covalent Modification of Building Blocks by ATP for Dissipative Self-Assembly

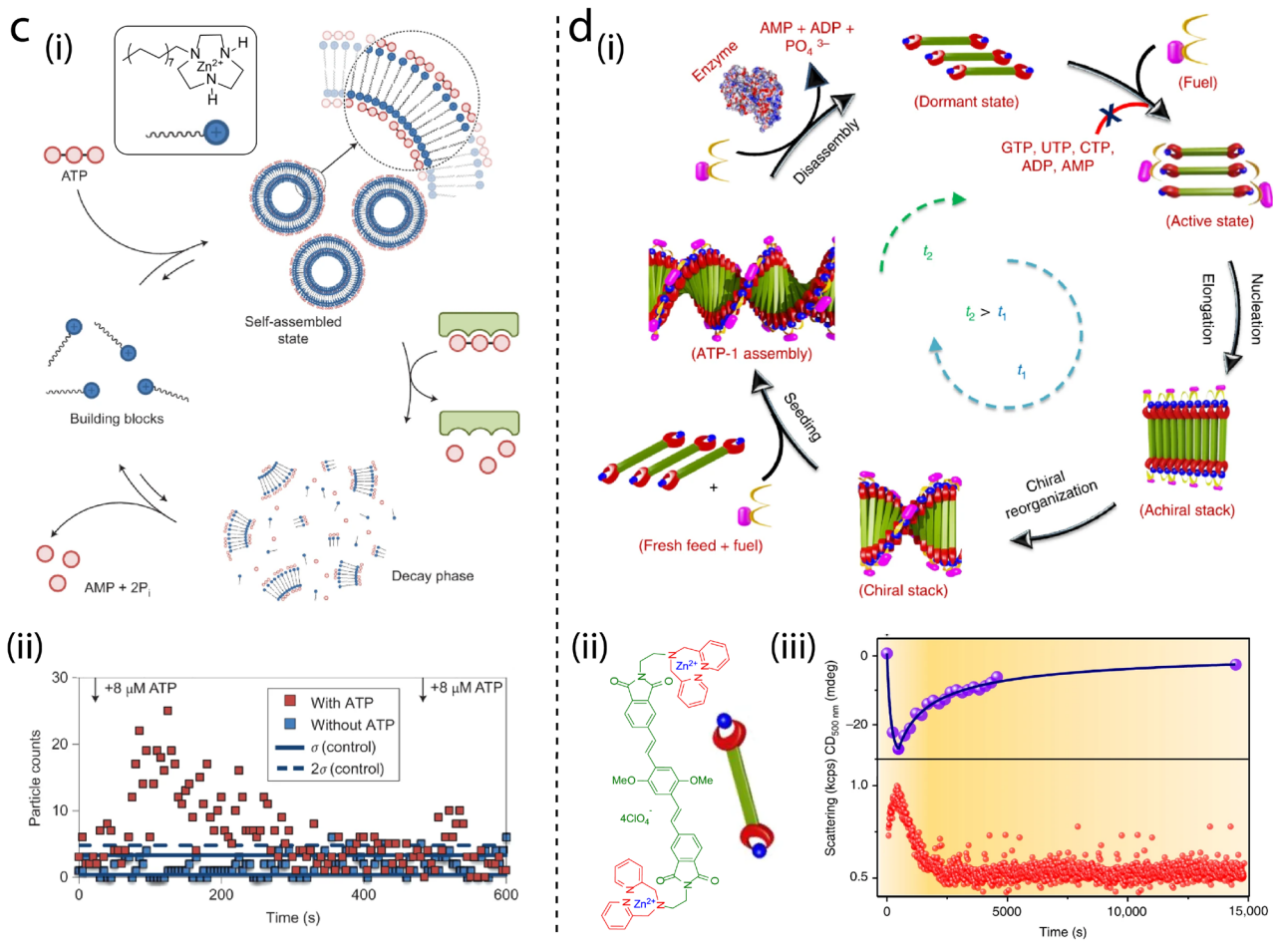

Figure 1-4. ATP hydrolysis for dissipative control over self-assembly. (a) Energy obtained from the ATP hydrolysis into AMP or ADP drives the chemical reaction cycle. (b) ATP as a fueling agent for covalent transient modification of building blocks. (i) Illustrations for the antagonistic phosphorylation/phosphorylation reaction network for transient chirality change of PDI based supramolecular polymers. Protein kinase A catalyzes the phosphorylation reaction and has three separate binding sites for ATP and two different configurations of peptide precursor, λ-protein phosphatase carries out phosphate hydrolysis and has only one binding site for ATP. (ii) Time-course CD measurements (monitored at 499 nm) right after batch addition of ATP. (iii) CD spectra of two different peptide configurations. (c), (d) ATP as a fueling agent for non-covalent transient modification of building blocks. (c) (i) Schematic representation of the dissipative self-assembly of vesicles. (ii) Time-dependent count of total number of fluorescent particles detected by CLSM in the presence and absence of ATP. (d) (i) Schematic representation of ATP-dependent nucleation-growth and seeded assembly of precursor with enzymatically modulated transient characteristics. t1 corresponds to the time required for the growth process and t2 is the time required for disassembly on enzymatic hydrolysis of ATP where t2 > t1, generating a transient assembly. (ii) Molecular structure of building block used in the study. (iii) CD and scattering measurements indicate temporal control over self-assembly. Graphics adapted from ref. (28, 29, 31)

Schanze and co-workers reported ATP-templated self-assembly of cationic porphyrins into chiral double superhelices and alkaline phosphatase-mediated disassembly.[34]

1.3.2 pH-Based Reaction Cycles for Dissipative Self-Assembly

pH as a stimulus/trigger is crucial in many chemical and biological processes. pH regulation is essential for maintaining internal environment of living organisms within a narrow and stable range. This pH homeostatis is critical for optimal operation of many cellular functions, DNA synthesis and enzymatic activities.[35] Disturbances and variations in pH can either be the cause or effect of disease and dysfunction within a biological system. Sensing and recognizing such anomalies are of prime importance in biomedical research. Tumor cell detection is one such example.[36] The acidic microenvironment of the affected cells compared to the healthy ones opens up possibilities for selective drug delivery. This has inspired the development of self-regulating drug release systems whereby a payload (usually a nanoparticle) charged with a drug of choice makes it release when triggered by low pH environment of the tumor.[37] The applications of pH-triggered autonomous soft materials has extended to microfluidic systems,[38,39] propulsion, drug-delivery applications,[30] and many more. The concepts behind the operation of these systems can be derived from the one or the combination of the Strategies (**Info Box 1**) suggested above.

(1) The first concept makes use of all three Strategies where our group temporally decoupled the antagonistic reaction pathways by making the activation reaction proceed faster than the deactivation pathway. This is achieved using a combination of fast activator and slow/dormant deactivator generating a transient signal. It is defined as pH-feedback systems (pH-FS) and will be discussed in greater detail in **Chapter 2**. Significant works by Taylor and Pojman,[41] Adams,[42] and van Hest[43-46] are also highlighted in greater detail in **Chapter 2**.

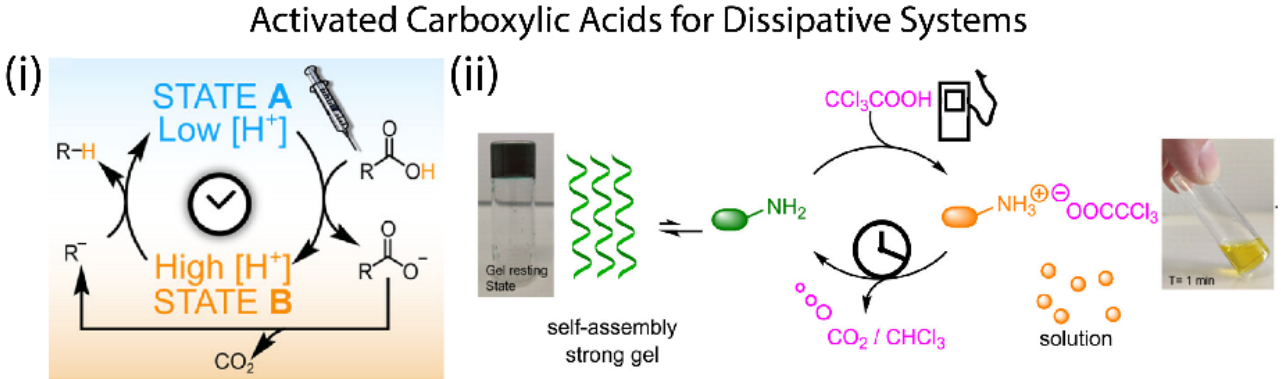

Figure 1-5. An activated carboxylic acid-driven dissipative system. (i) Schematic illustration of the reaction cycle. (ii) CCl_3COOH fueled gel-sol-gel transition of O-tert-butyl-l-tyrosine. Graphics adapted from ref. (45, 46)

(2) The other concept was proposed by the De Stefano group, it uses Strategy 1 and 2 by employing an activated carboxylic acid (RCO_2H) as the chemical fuel (**Figure 1-5**). The excess addition of RCO_2H lowers the initial basic pH of the solution. The carboxylate ion (RCO_2^-) formed is labile and loses CO_2 to be transformed into a strong carbanion (R^-) whose re-protonation causes pH to increase again. The only waste produced in the system is RH. However, the system only offers autonomous transition from high-low-high pH and the flip is not possible. Moreover, these systems require 20-30% organic co-solvents such as DMSO for their successful operation. The system was employed to control the host-guest interaction between α-cyclodextrin (α-CD) and p-aminobenzoic acid in a dissipative fashion.[48] Moving beyond the molecular scale, they showed the temporal operation of DNA-based nanodevices which undergo duplex-triplex transformation at low pH.[49] Together with our group, RCO_2H was combined with bilayer actuators (made of weak polyacid layer and polymer layer) to build soft-robotic devices capable of harpooning small object.[1,50] Although the reaction cycle is used for temporal programming of organogelators based materials for autonomous gel-sol-gel states, completely aqueous based self-assembling systems are still missing.

In both the systems described above, the fuel-driven chemical reaction cycle transiently changes the pH of the solution forming an active environment which indirectly induces transient self-assembly.

1.3.3 Redox Based Reaction Cycles for Transient Self-Assembly

Redox chemistry has been recently identified as an interesting tool to create transient, out of equilibrium systems. Redox reactions are ubiquitous in nature, the synchronous operation of redox couples: glutathione/oxidized glutathione (GSH/GSSG) and nicotinamide dinucleotide phosphate/oxidized nicotinamide dinucleotide phosphate (NADPH/NADP+) is crucial for the regulation of metabolites such as glucose and serve as a major redox buffer in cells. When a cell is exposed to oxidative stress or encounters a reactive oxygen species (ROX), GSH acts as an antioxidant while itself getting reduced to GSSG. NADPH is required to bring GSSG back to GSH allowing it to participate in further detoxification and defense mechanisms.

Taking inspiration from the above phenomenon, antagonistic oxidation-reduction reaction pathways are devised. The rates of these reactions can be controlled by the strength of respective oxidizing and reducing agents or by choosing naturally occurring redox enzymes. Care must be taken however to avoid or atleast minimize background reaction between oxidizing and reducing agents being used. As clear from above example, the most relevant example is disulfide chemistry as it is biologically important and offers a simple and general platform for the development of dynamic synthetic systems. Wojciechowski and coworkers employed a fast pH-triggered activation reaction for the transient gelation of a redox active supramolecular gelator, N,N'-dibenzoyl-L-cystine (DBC) and slow tris(2-carboxylethyl)phosphine (TCEP) induced reduction of DBC to N-benzoyl-L-cystine (BC), resulting in the dissolution of the hydrogel (Strategy 3, **Figure 1-6a**).[53] The protonation of the dicarboxylate moieties in the activation reaction conditions the reduction of the disulfide bond in activated building block during deactivation reaction. The system finally resides in State C and can only be refueled by providing a fresh batch of DBC given enough amount of TCEP is available. Ogden et al. combining Strategy 2 and Strategy 3 demonstrated a redox couple hydrogen peroxide (H_2O_2)/dithiothreitol (DTT) for dissipative gelation of cysteine thiol precursor (**Figure 1-6b**).[54] Fast oxidation by H_2O_2 dominates in the beginning and as it runs out, the competing reduction by DTT takes over. Since most of the redox reactions are pH sensitive, a cumulative reaction network combining redox and pH triggers was developed for transient coacervation between a polymer and a peptide.[55] Recently, a self-oscillating micellar system was proposed exploiting the disulfide bond-shuffling (**Figure 1-6c**).[56] The self-assembled structure catalyzes both the formation and breakdown of its building blocks inducing both positive feedback (autocatalytic formation) and

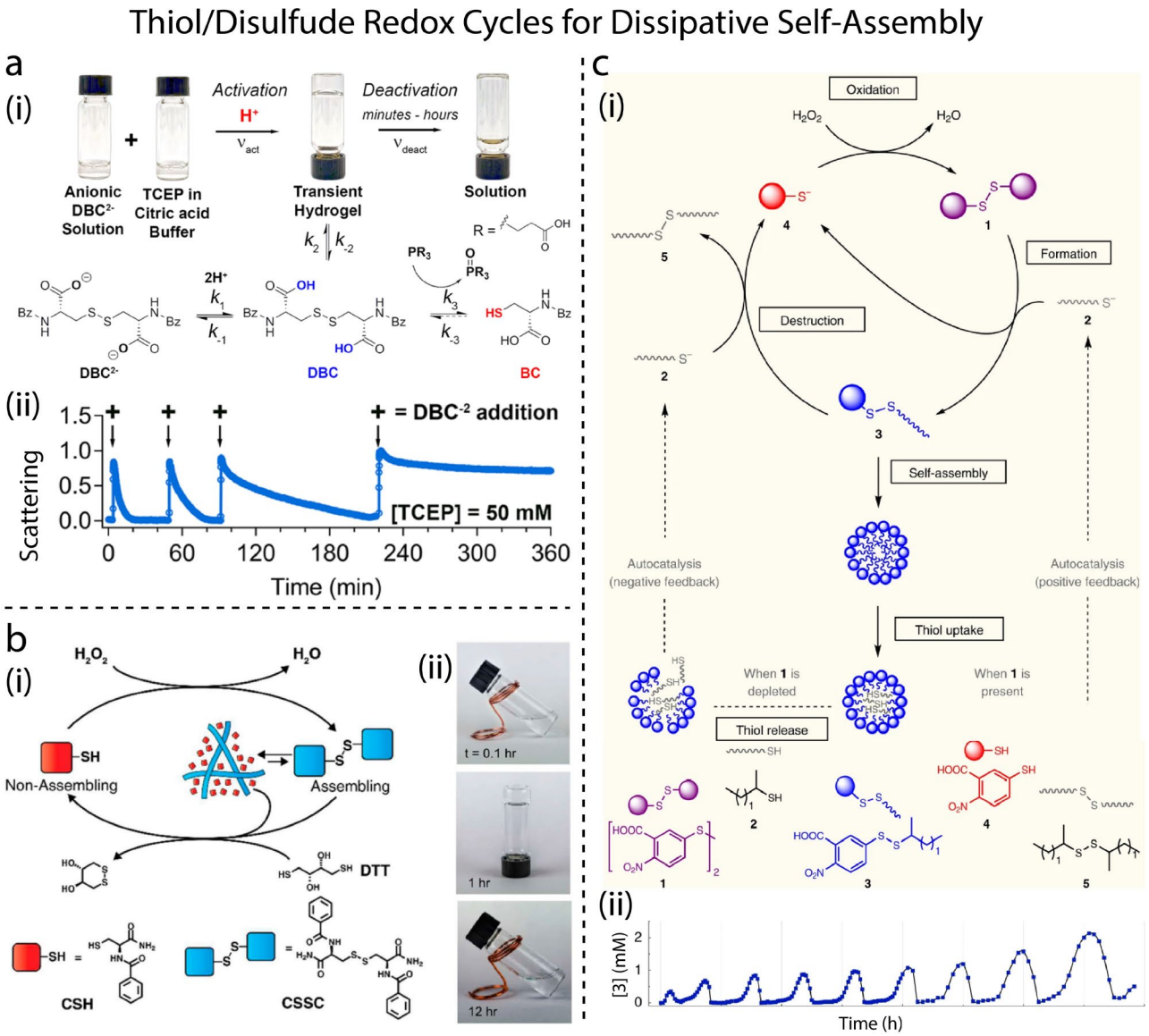

Figure 1-6. (a)Citric acid/TCEP based reaction cycle for the transient hydrogelation of DBC2-. (i) Schematics of the sol-gel-sol transition of the transient hydrogels. (ii) UV-vis scattering showing three transient hydrogel cycles in the presence of excess concentration of TCEP (here, 50 mM). (b) Antagonistic H2O2/DTT reaction cycle for dissipative self-assembly of CSH. (i) Conceptual schematics for the dissipative material using H2O2/DTT redox couple. (ii) Inverted vial test of the active material system. (c) Autonomously oscillating supramolecular system for self-replication function. (i) Reaction cycle illustrating the chemical steps and feedback processes involved in the oscillations: formation of 3, its self-assembly, thiol uptake, thiol release, destruction of self-assembly and finally oxidation. (ii) Concentration versus time plot of species, 3. Graphics adapted from ref. (9, 53, 55)

negative feedback (destruction cascade) in the network. Such advanced structural feedback is possible because the building block itself acts as the active component in the reaction cycle.

Apart from thiol/disulfide chemistry, other redox responsive building blocks such as naphthalene diimide has been used for temporal supramolecular polymerization.[57] A similar unit based on perylene diimide attained self-oscillating assemblies in a stirred semi-batch reactor (**Figure 1-7a**).[56,58] The nucleation-elongation-fragmentation process acts as a positive feedback mechanism, whereas the size-dependent reduction/disassembly of formed structures can be seen as a negative feedback. Such structural based feedback can be essential to obtain emergent properties such as oscillations. Viologens is another class of redox responsive moiety which is being actively used for dissipative supramolecular polymerization. Most of

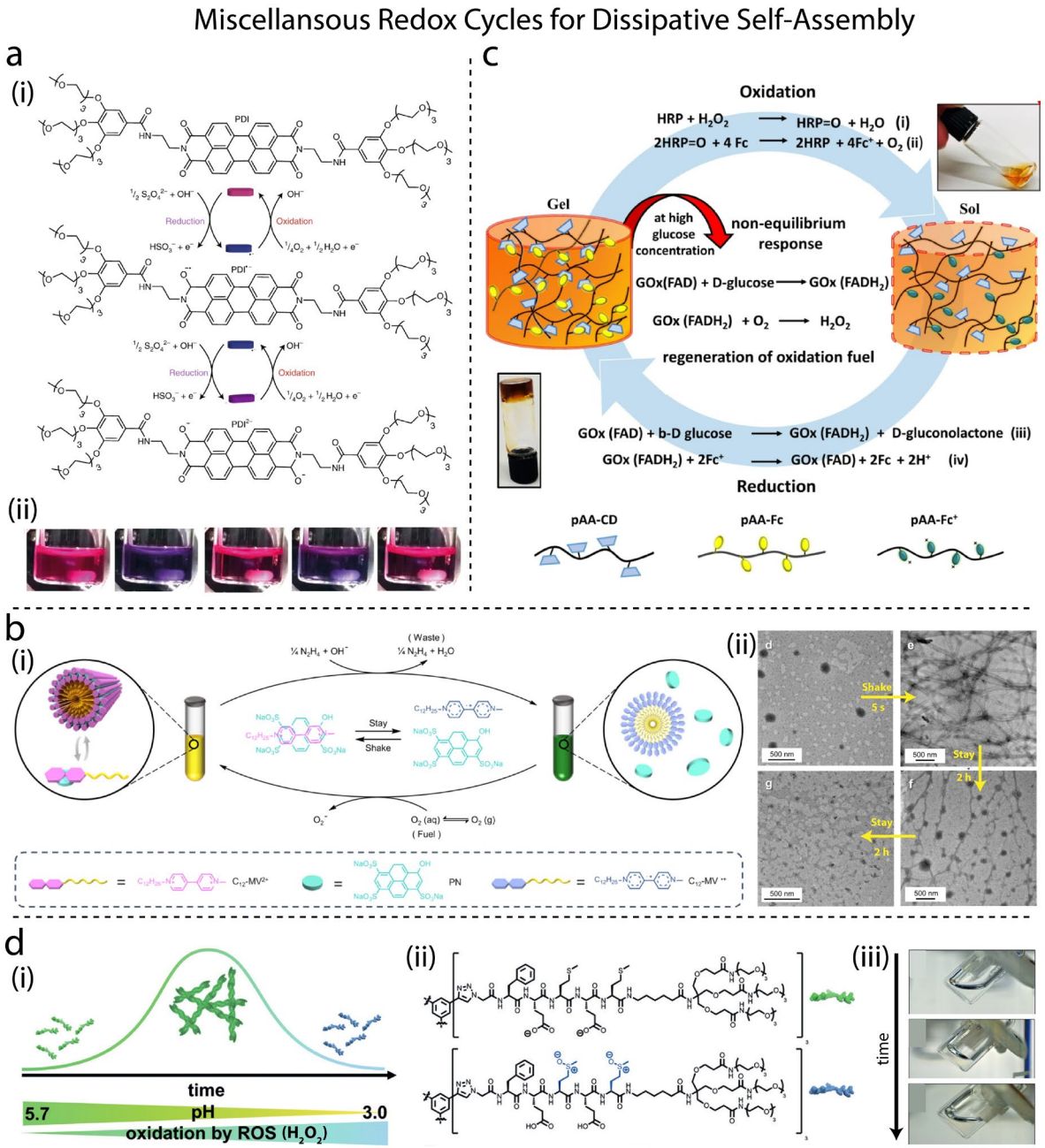

Figure 1-7. (a) Redox-fueled oscillating assembly and disassembly of PDI. (i) Chemical reactions explaining the system. PDI is reduced to PDI2- upon the addition of Na2S2O4. Spontaneous oxidation in air leads first to a radical anion PDI•- and then to the neutral PDI. (ii) Real time images of the system demonstrating two oscillating cycles. The disappearance of the red color indicates formation of PDI•- and PDI2- and a mostly disassembled state. Subsequent reappearance of red color indicates oxidation back to PDI which undergoes self-assembly again. (b) Shake induced transient supramolecular polymerization. (i) Schematic representation of dissipative supramolecular polymerization based on C12-MV2+ and PN triggered by shake. A little shake accelerates the diffusion of molecular oxygen into the solution oxidizing C12-MV•+ to C12-MV2+ followed by its co-assembly with pyranine into supramolecular polymers. Once the shaking is stopped, C12-MV2+ reduces back to C12-MV•+ in the presence of excess amount of N2H4.H2O which led to disassembly. (ii) TEM images of the system over time. (c) Redox responsive hydrogel for autonomous sol-gel-sol transition. A supramolecular hydrogel with polyacrylic backbone is crosslinked by non-covalent host-guest interactions between β-CD and ferrocene integrated within polymeric network. The gel formed is first oxidized by HRP/ H2O2 to form the initial disassembled state. The addition of GOX/glucose couple first reduces the ferrocene moieties forming a gel, H2O2 produced as a side product with the help of already present HRP reoxidizes the ferrocene units disassembling the gel. (d) Multi-stimuli responsive for transient thermogels. (ii) Schematic representation of the pH-driven supramolecular polymerization of β-sheet encoded peptide amphiphile and its oxidation-triggered disassembly. (ii) Molecular structures of peptide amphiphile and its oxidized form. (iii) Inversion vial tests showing transient hydrogelation. Graphics adapted from ref. (10, 59-61)

the systems discussed so far and also the ones which will be discussed later in this section consume all of their fuel within a single cycle, and repeated fuel addition for subsequent operation leads to the accumulation of

waste. This is the leading cause of amplitude damping and lifetime inflation of the transient state in some cases. To date, only the well-known Belousov-Zhabotinsky and a few related oscillators can show sustained oscillations in a closed system but there are no design rules that allow to extend a rational design as such in fuel driven closed systems. Very recently, Lang and coworkers demonstrated a shake triggered dissipative supramolecular polymerization from a gas-liquid two phase redox reaction system (**Figure 1-7b**).[60] A brief shaking diffuses the aerial oxygen into the liquid phase, instantly activating the self-assembly which subsequently disassembles in the presence of excess reducing agent. The only waste generated in the cycle is nitrogen gas which does not accumulate in the liquid phase and allows multiple cycles just induced by simple shaking of the reaction medium. An interesting report combines all three Strategies to achieve a transient gelation with host-guest (β-cyclodextrin-ferrocene) recognition (**Figure 1-7c**). The system uses glucose oxidase (GOX)/D-glucose for the reducing pathway, the intermediate in this reaction produces H_2O_2 which in the presence of horseradish peroxidase (HRP) forms the oxidizing couple acting in an antagonistic manner.[61] Spitzer and coworkers employed GOX/D-glucose couple to attain transient supramolecular polymerization of a multi-stimuli responsive peptide amphiphile. The action of GOX on D-glucose decrease the pH causing the transient self-assembly via pH-responsive segment, however, H_2O_2 produced as a side product oxidize the redox sensitive segment, thereby disassembling the structures forming new State C (**Figure 1-7d**).[62-64] The activation and deactivation pathways are both chemically and temporally decoupled to obtain a transient response. In all the systems discussed above, the active component was mainly the building block itself.

1.3.4 DNA-Based Reaction Networks for Transient Self-Assembly

DNA Nanotechnology can provide building blocks, but DNA-fueled processes are not that common, or they do not yet compete with the above mentioned processes. Here, DNA is either covalently or non-covalently decorated on the building block, where DNA complementarity can be exploited to mediate the assembly/disassembly behavior of the building blocks. Using DNA as a fuel (either produced *in situ* or provided manually) is one of the major conceptual developments in DNA nanotechnology. It is an information bearing fuel and can simultaneously act as a molecular address code that triggers only specific processes. Reaction networks are divided into two categories, depending on whether they are based on DNA alone or use specialized enzymes and machinery. The first category deals with the energetic considerations and the various improvements made in the reactions in chronological order. Interest shifts further to DNA-enzyme hybrid networks to discuss some of the requirements that these systems meet over DNA-only systems.

DNA-only (Non-Enzymatic) Reaction Networks

With thoroughly increasing understanding of DNA chemistry, including formation of phosphodiester bonds between adjacent nucleotides (nt), Watson–Crick base pairing and the double-helical structure, researchers found that the hybridization and strand displacement of DNA can be a controllable process for implementation as logic elements, neural computation, and reaction cascades. This process, also known as dynamic DNA nanotechnology, usually focuses on non-equilibrium dynamics rather than the equilibrium end states of the DNA strand hybridization (**Info Box 2**) process.

Info Box 2. Strand Hybridization Reaction. The left-hand side shows two complementary DNA oligomers A and A*. The right-hand side shows the duplex B formed by hybridization. Such systems are often modeled as two state systems where the DNA strands are either fully associated or fully dissociated. In this case, the forward reaction is second order, and its rate constant is denoted k_{hyb}. The reverse reaction in which the duplex B spontaneously dissociates, is first order, and its rate constant is denoted by k_{dis}. The equilibrium concentration of reactants and reaction products is determined by the equilibrium constant K given by:

$$K = \frac{k_{\mathrm{hyb}}}{k_{\mathrm{dis}}} = \frac{[B]}{[A][A^*]}$$

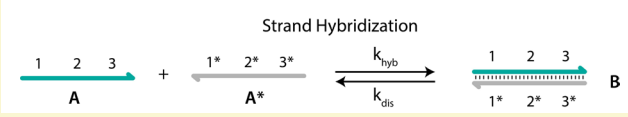

which is related to the standard Gibbs free energy change ΔG^{o} of the reaction via: $K\Gamma = e^{-\Delta G^{\mathrm{o}}/RT}$ where Γ has the numerical value of 1 with units that make the left-hand side of the equation

dimensionless. The free energy ΔG^{o} and other thermodynamic quantities can be adequately calculated for a duplex of any base sequence using a nearest neighbor model.[66] The rate constant k_{hyb} can vary by orders of magnitude and depends on temperature and buffer composition, but a value of 3×10^{6} M^{-1} s^{-1} is representative for oligomers with lengths of a few tens of nucleotides in commonly used hybridization buffers.[67] For the 10-mer oligo, k_{dis}.was measured to be at 1.1×10^{-2} at 30.5 °C in a 1 M NaCl/10 mM NaH_2PO_4 buffer.[66]

One of the first attempts to use DNA hybridization for parallel computing was reported in 1994.[67] In 1997, Ouyang et al. used DNA computation to solve the maximal clique problem, which further proved the high parallelism of DNA computing.[68] However, limitations such as (1) hybridization efficiency and (2) inverse relationship between library size and computational ability inhibited the promotion of DNA as a computing unit.[69] This finally led to the development of DNA strand displacement (DSD) reactions (**Info Box 3**).

Info Box 3. Spontaneous Strand Displacement Reactions. This illustrates a spontaneous DSD reaction in which one member of a duplex strand (substrate strand) trades partners (incumbent and invader strand). Although the base sequences of incumbent and invader strands are identical in this example, the DNA strands could carry labels allowing them to be distinguished. Access of invader to the complementary strand in substrate is blocked by the complementary partner (incumbent). As a consequence, the forward reaction is inhibited, as is the reverse reaction. However, the reaction rates will not be zero since incumbent strand can spontaneously dissociate and in this particular condition, the rates of forward and reverse reactions are equal. The reaction rates can be conditionally biased by interconnecting upstream/downstream reactions. In addition, breathing of the duplex strand or end fraying (state B) can make substrate available for binding with invader to initiate the exchange (state C). The branch migration follows a sawtooth pattern (state D) followed by the dissociation of incumbent strand (state E) and formation of final base pair (state F). Reynaldo et al. showed that spontaneous dissociation dominates near the melting temperature of the duplex while fraying-initiated three-way branch migration occurs at low temperatures.[67]

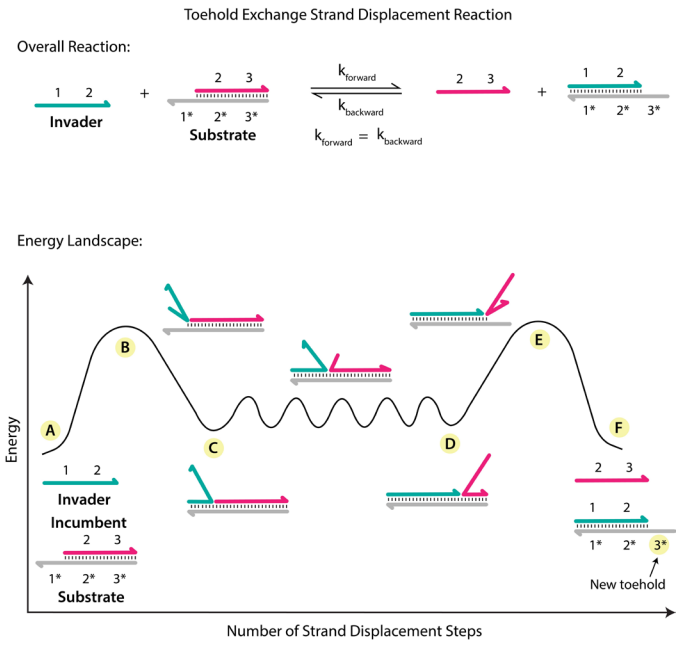

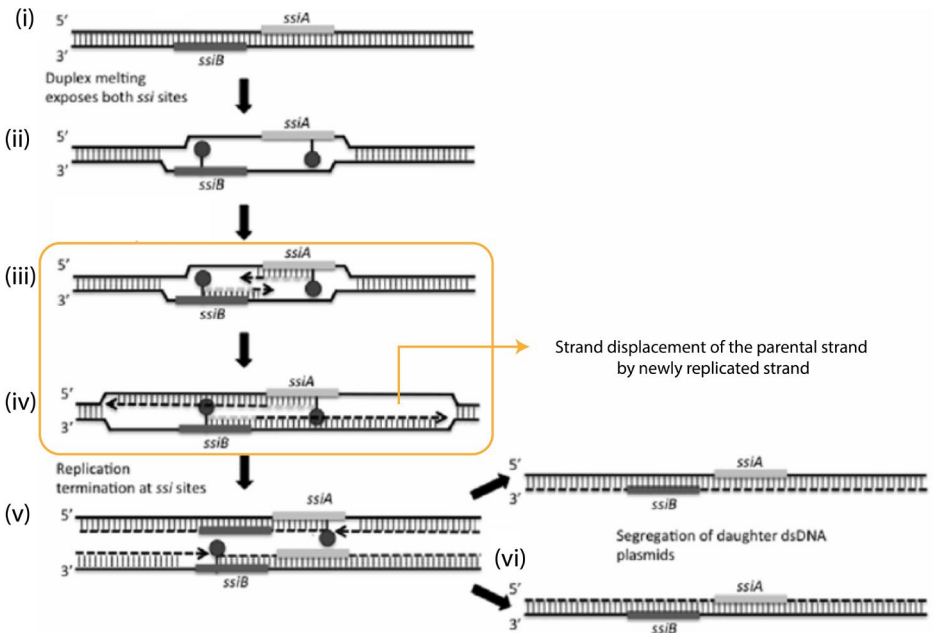

Figure 1-8. Model of plasmid replication by strand displacement. (i) Parental DNA duplex depicting two single stranded replication sites (light and dark grey boxes). (ii) The DNA duplex is melted through the binding of a special enzyme allowing the two sites to form hairpins (illustrated by ball and stick). (iii) DNA replication is initiated. (iv) The stepwise synthesis of replicated DNA strand is made possible by the simultaneous displacement of the parental strand. (v) Elongation is completed. (vi) The two daughter strands are ligated resulting in two DNA duplexes, each containing one parental strand and one daughter strand. Graphic adapted from ref. (69)

Displacement of one strand from a double-helical nucleic acid by concomitant replacement with an equivalent nucleotide sequence is a familiar and integral aspect of DNA or RNA replication and genetic recombination *in vivo* (**Figure 1-8**).[70] Displacement of strand is caused by branch migration, which can be regarded as a result of base-pair breathing.[71] Toeholds provide a means to increase the rate of spontaneous strand displacement by increasing the attempt frequency for three-way branch migration. These reactions (**Info Box 4**) are specifically regarded as toehold-mediated DNA strand displacement reactions (TMDSD).

Info Box 4. Toehold-Mediated Strand Displacement Reactions with Three-Way Branch Migration. Overall, the incumbent strand (having sequence "2 3"), is displaced from the substrate strand "1* 2* 3*" of the initial duplex by the invader strand (with sequence "1 2 3") to produce a final duplex. The toehold is the single-stranded extension "1*" on the starting duplex. It takes place in three main steps: (1) the binding of domain "1" of the invader strand to the toehold initiates the reaction. The system is moved from state A to B by formation of a first base pair within the toehold, each additional toehold that zips up defines a new state, with state C indicating the fully formed toehold. Overall, the process incurs a free energy penalty caused by the reduction of the translational and orientational degrees of freedom, as two different species have combined into one; (2) End fraying of incumbent strand then allows the invader strand to initiate a three-way branch migration process. This involves dissociation of a base of the incumbent strand from the substrate strand which enables the invader strand to bind with the substrate strand via one more base. This is the initial step of a random walk process in which the invader strand competes with the incumbent strand for binding with the substrate strand. The branch migration happens at a rate of 12–20 µs per base which is slower than the fraying of a single base pair.[72] During each step system pass through a single effective transition state of raised free energy, so each complete branch migration step is shown as a single tooth of the sawtooth pattern between states C and D. This process incurs a thermodynamic penalty which results from the partial disruption of the base stacking and reduction of conformational degrees of freedom as the two single-stranded extensions at the branch point are forced to bent away from each other.[67] (3) Finally, the incumbent strand will be completely displaced by the invader strand (state E) followed by the formation of the final base pair (state F). Due to the lack of a toehold with which the incumbent strand can bind the rate constant for the reverse reaction will be small compared to the forward reaction. The toehold thus drives the system from (A) to (F). At same concentrations of all oligomers, the ratio of the concentrations of the complexes Product and Invader is given by:

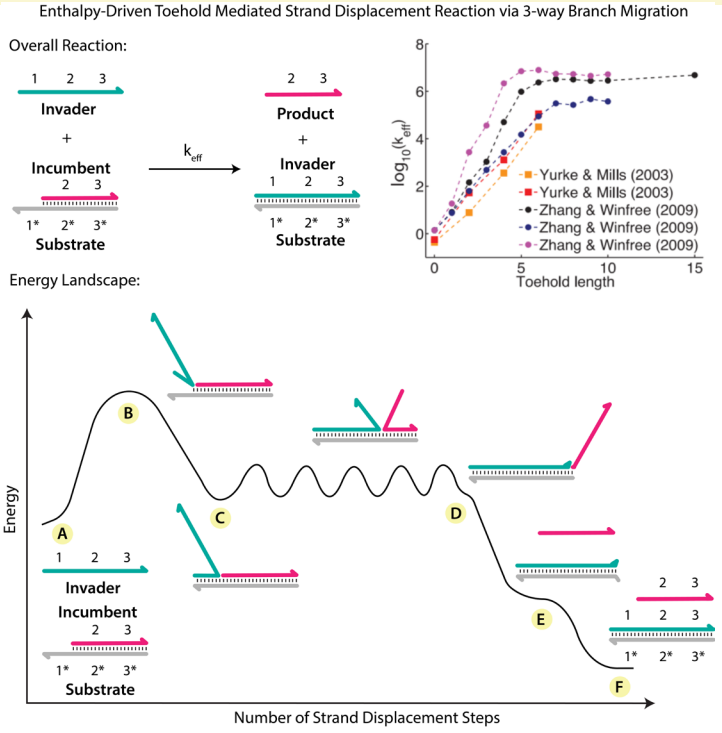

$$\frac{[\text{Product}]}{[\text{Invader}]} = \sqrt{\frac{k_f}{k_r}} = e^{-\Delta G^{\circ}/2\text{RT}}$$

where k_f and k_r are respectively the rate constants for the forward and reverse reactions. ΔG° is the free energy of hybridization of "1" with "1*". For longer toeholds, ΔG° becomes more negative and the equilibrium is pushed further in the forward direction.

Experimentally measured forward reaction rates as a function of toehold length are shown in Figure. Under low enough concentrations of starting species, the overall reaction can be modelled as an instantaneous second-order reaction.[72,73] For these conditions, the overall effective rate constant (k_{eff}) is given by hybridization rate constant for the toehold multiplied by the probability of displacement once the toehold is bound. For short toeholds, the probability that the invader strand will remain bound to the substrate's toehold long enough to displace the incumbent strand is lower because of the high dissociation rates and also because of the multiple returns

that branch point makes back towards the toehold. With sufficiently long toeholds, the dissociation rates are smaller and the probability that the random walk of the branch point moves towards the distal end of the substrate is higher. Hence, the forward reaction rates increase with increasing length of toeholds and saturate once they reach sufficient length.

A case of four-way branch migration arises when two double stranded complexes sharing a stem sequence interact with each either through one or two toeholds (**Info Box 5**). Although effective, the traditional TMDSD reaction suffers from some obvious weaknesses. For example, it is difficult to construct multilayered DNA circuits, because the competitor strand must be longer than the released strand. The largest circuit built with DSD cascades involved 12 initial DNA species out of which the logic gates were constructed with multi-stranded complexes.[55,72]

Such circuits follow more or less a well-defined trajectory with multiple transient states and finally approach thermodynamic equilibrium. The reaction rates within each layer can be tuned to increase/decrease the lifetime of a certain transient state (check **Chapter 4** for details). However, with increasing scale and number of layers, these circuits suffer from signal leakage and decayed performance. Introducing auxiliary gates such as amplification gate (signal amplification) and threshold gate (leakage removal) at intermediate or end steps within the cascades can improve the signal to noise ratio but does not provide a long-term solution.

Info Box 5. Toehold-Mediated Strand Displacement Reactions with Four-Way Branch Migration. Four-way branch migration is the process by which two double-stranded oligonucleotides that share the same stem sequence simultaneously exchange strands. The entire reaction pathway can be divided in seven key steps: state A where the two initial complexes (Substrate and Reporter are separated within a volume, the formation of the first base pair within the toehold marks the state B after which the Substrate and Complex are bound by all available toeholds (state C), in state D branch migration is initiated which continues until the two complexes are bound by the last base pair (state E), in state F, the two complexes are finally dissociated followed by the formation of the final base pair (state G). Here, the branch point consists of a mobile Holliday junction which enables the implementation of DNA actuators, molecular probes, directional motors, molecular robots.

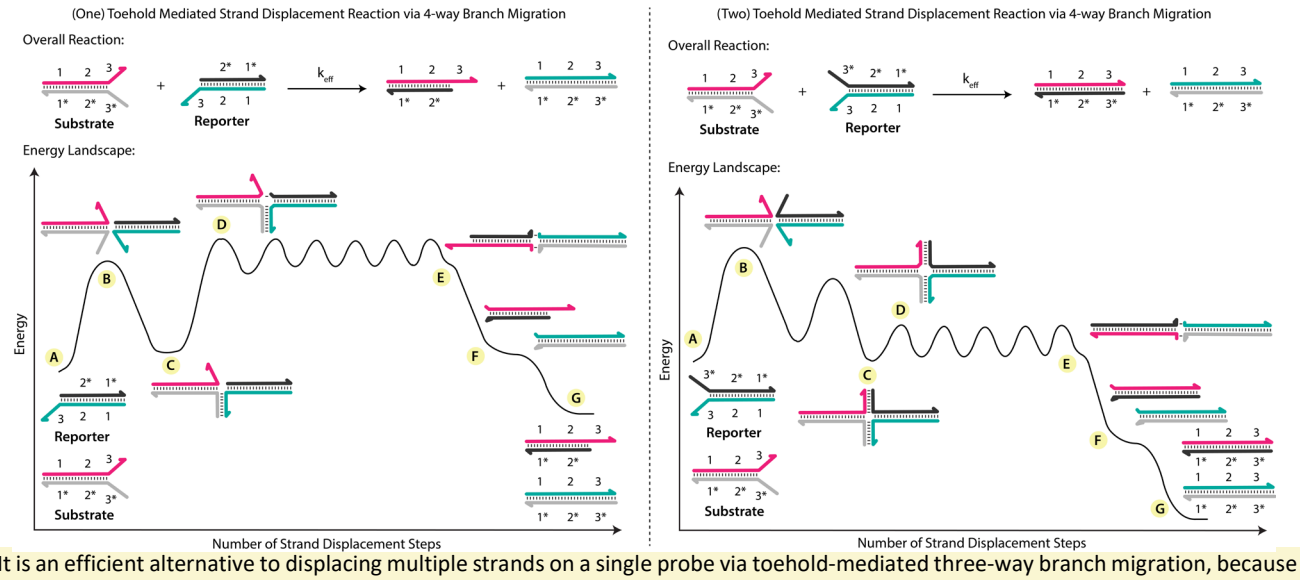

It is an efficient alternative to displacing multiple strands on a single probe via toehold-mediated three-way branch migration, because it reduces the number of complexes that must be added and thereby leaves all the waste products double-stranded or inert. The sequestering of DNA sequences in four-way branch migration systems also results in less cross-talk between single-stranded domains thereby making possible a slew of less noisy designs. The physical process of four-way branch migration enables the insertion or rearrangement of DNA molecules without requiring the complete disassociation of a single strand. The mechanism thus expands the space of what can be engineered with DNA. It occurs at a rate slower than the three-way branch migration and depends strongly on the valency of the salt cation of the buffer.[75]

Winfree et al. eliminated the problem by taking a different approach. They reported a strategy called toehold-exchange displacement reaction (**Info Box 6**).[55,76] The incoming strand hybridizes with the bottom strand of the duplex and displaces the top strand. Different from the traditional TMDSD reactions, the resulting double-

stranded DNA still has an active toehold that can be used to initiate the reverse displacement reaction. As such, toehold-exchange has two obvious advantages.

Info Box 6. Toehold-Exchange Strand Displacement Reactions. In TMDSD, the negative enthalpic change resulting from the hybridization of a toehold with its complement has been used to drive the reaction forward. Toehold exchange is similar to TMDSD reaction in that an invading strand binds by a toehold to initiate branch migration but differs from the latter in that the incumbent strand possesses a unique toehold that must spontaneously dissociate for the reaction to complete. Invader strand binds to substrate via invading toehold ("1", state B, C) and displaces incumbent's domain "2" by branch migration (continues from state C to D). The incumbent toehold ("3") then spontaneously dissociates after breaking the last base pair (state E), yielding free incumbent strand and a complex with a new toehold ("3*"). The end result of the toehold exchange reaction is that the originally active toehold "1*" is sequestered while the formerly sequestered toehold "3*" is activated. Thus, the active toehold is "exchanged" from "1*" to "3*". Please note that the toehold hybridization constants for both are assumed to be constant in the demonstrated example because of which forward and backward reactions are same.

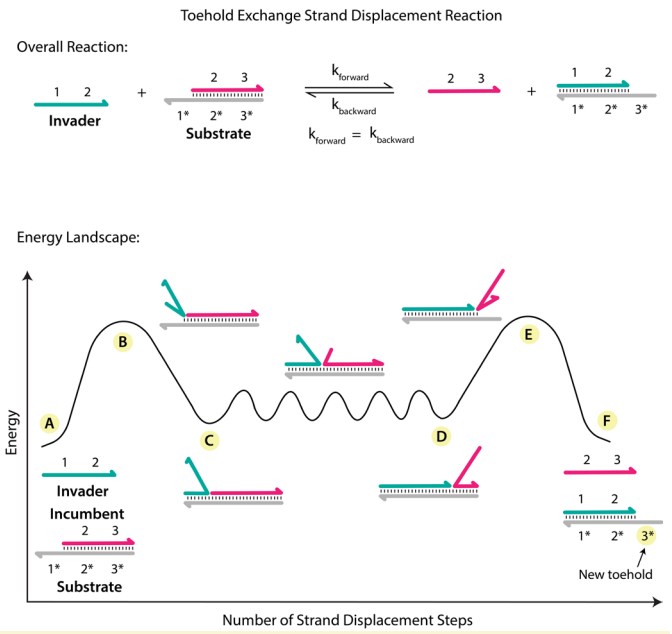

Functionally, toehold exchange offers two main advantages over TMDSD. First, the partially double-stranded product resulting from a toehold exchange reaction possesses a single-stranded domain (3*), allowing it to undergo further toehold-mediated reactions. Thus, in toehold exchange, two reactive reactants yield two reactive products, rather than yielding just one as in TMDSD. This preservation of the number of active molecules, in combination with the reaction's reversibility is helpful in larger reaction networks. Second, toehold exchange weakens the coupling between the kinetics of strand displacement and the thermodynamics of the reaction. For TMDSD reactions operating below their maximum rate, there is a strong coupling between the kinetics and the thermodynamics: to speed up the strand displacement reaction, the invading toehold must be made stronger thermodynamically, for example by increasing the toehold length. Consequently, faster strand displacement reactions are more thermodynamically favorable in the net reaction. In contrast, in toehold exchange, when both the invading and the incumbent toeholds (1* and 3*) are made stronger, the kinetics of both the forward and the reverse reactions are sped up, within the limits of sufficiently low concentration. Thus, a strand displacement reaction based on toehold exchange can be fast despite being only weakly thermodynamically favorable or even thermodynamically unfavorable.

First, the generated toehold after strand displacement allows the construction of downstream layers. In a way, forward or backward reactions can be biased by incorporating necessary upstream or downstream modules. Second, toehold exchange weakens the coupling between the kinetics of strand displacement and the thermodynamics of the reaction, so that a strand displacement reaction based on toehold exchange can be rapid despite being only weakly thermodynamically favorable or even thermodynamically unfavorable.

Based on this strategy, Winfree's group designed a catalytic DSD circuit which drives forward exclusively by the entropy gain of the entire system (**Info Box 7**).[68,78] Since then, the toehold-exchange displacement reaction has proved to be an effective strategy for artificial reaction network construction because of the tunable kinetics of the DNA reaction.

Info Box 7. Entropy-driven Toehold-mediated DNA Strand Displacement Reactions. Configurational entropy differences provide an alternative route to drive toehold exchange strand displacement reactions. In this case, an increase in the number of the products than the reactants drive the reaction in the forward direction due to consequent increase in configuration entropy. An example is shown in Figure where the increase in the number of species from two to three and not the additional base pairing, drive the reaction forward. The strength of this thermodynamic driving force can be estimated as follows: the system on the left can be regarded as the same as that on the right except that Signal and Output are colocalized within Substrate. Let this colocalization volume be denoted as V1. Now, when all oligomers are present at equal concentrations ρ, then the volume Output occupies when it is not forced to colocalize within Substrate is V2 = 1/ρ. The change in entropy going from the system on the left to that on the right is $\Delta S = k_B \, ln(V_2/V_1)$, corresponding to a free energy change of:

$$\Delta G_S = -T\Delta S = -k_B\, T\, ln(V_2/V_1)$$

A reasonable estimate of the colocalization volume V_1 is 1 Å^3. Considering concentration of all oligomers to be same as 100 nM, V_2 is 1.67 × 10^{10} Å^3. Taking T to be 300 K, $\Delta G_S = -0.6\, eV$. As the average free energy of hybridization is ≈0.073 eV per base pair,[80] the entropic driving force in this example is equivalent to the formation of eight base pairs, which actually is quite comparable to that inferred by the experiment. An advantage of employing configuration entropy as a driving force in DNA reaction networks is that it is insensitive to temperature, pH, and buffer composition. This has been successfully used to implement cascade networks and catalytic and autocatalytic networks.[81-83] Figure shows the overall reaction in which the substrate complex and the Invader strand react to form the waste product and release the oligomers Signal and Output. The reaction is entropically favored due to the increase in the number of components from two to three. Note that this reaction network employs a hidden toehold ("3*") that becomes exposed when Signal is released from intermediate. This toehold provides an attachment site for the Invader strand, which then drives the reaction to completion by toehold initiated strand invasion. The catalytic system of Figure 11 can interwined with other similar catalytic systems. In particular Signal and Output can serve as catalysts for other catalytic systems by virtue of the freedom available in choosing the base sequences for domains 1 and 2. Of particular note, the base sequence of Output can be chosen to be identical to that of the Catalyst. The resulting system is then autocatalytic, and the number of free catalyst strands is doubled with the completion of each catalytic cycle, resulting in exponential growth of catalyst concentration before substrate depletion.

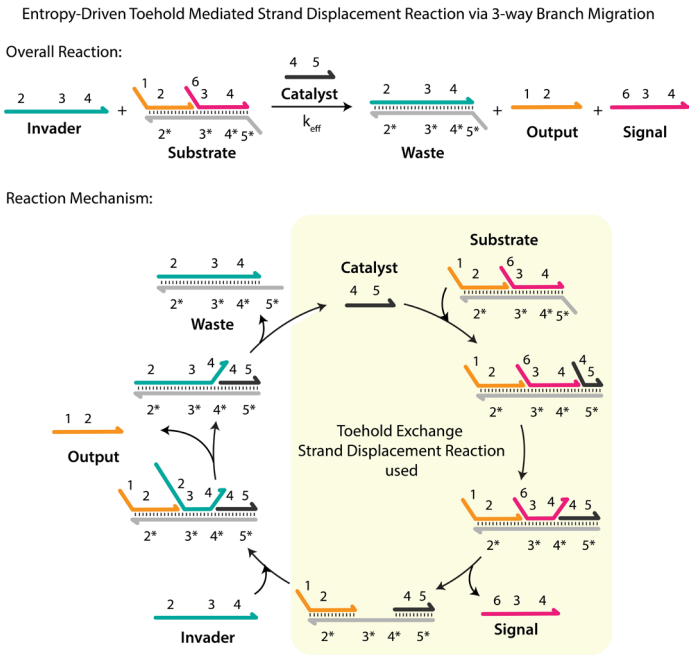

If Signal = Catalyst, the Catalytic cycle becomes Autocatalytic.

It has been demonstrated that the free energy released by the formation of 10 new base pairs is comparable with that released by the hydrolysis of ATP in standard conditions ($\Delta G°_{ATP}$ ≈ - 7.7 kcal/mol) and in cellular conditions ($\Delta G°_{ATP}$ ≈ - 14 kcal/mol). By contrast, the free energy released by the formation of a new base is $\Delta G°_{hybridization}$ ≈ - 1.4 kcal/mol/base pair. Thus, unpaired DNA can be used as a resource of free energy. Yurke et al. used single-stranded DNA as the fuel strand of a molecular machine.[85] Their DNA molecular machine, named molecular tweezers, can be controlled by an added fuel DNA strand and operates between the closed and open states of the tweezers. This work was the first systematic use of a toehold domain to design a DNA machine and proved that a DNA machine is sufficiently reliable to undergo a series of operations. Subsequent reports by Yan et al. showed that the force generated by formation of new base pairs is so strong that it can even change the orientation of DNA origami.[86] Seelig et al. reported the first logic gates totally constructed of DNA strands.[87]

Srinivas et al. experimentally developed an enzyme free DSD oscillator in a closed system (**Figure 1-9a**).[78] It is based on a "rock-paper-scissors" CRN which combines three autocatalytic reactions of sort A + B → 2A, where these three modules suppress each other. This is implemented by using a DNA gate that takes two different inputs and generates two identical outputs. The oscillations die after 3 cycles. The system relies entirely on thermodynamically controlled TMDSD reactions. The oscillations are a result of a highly sophisticated kinetic pathway that brings the system to the thermodynamic end state (Strategy 3). The new thermodynamic equilibrium is reached when all fuel species are converted into waste (that is, hybridized fuel) and, at that stage, cannot be reactivated. Joesaar et al. were the first to introduce DNA-only negative feedback circuit.[88] They demonstrated the circuit on two different populations of proteinosome-based protocells engaged in compartmentalized TMDSD reactions (**Figure 1-9b**). The activation of population 1 on addition of an Input strand results in the secretion of a signal strand and a concomitant increase in Cy5 fluorescence. The secreted signal can activate protocells of population 2, which then respond with an increase in Cy3 fluorescence and Fuel-amplified secretion of an orthogonal Inhibitor strand that can deactivate population 1. The results demonstrate that after the Input strand is added, population 1 is rapidly activated, followed by a more gradual activation of population 2 and the simultaneous deactivation of population 1. Our group extended the strategy for establishing communication behavior between two 3D DNA origami species (cylinders, shown in red and

DNA-based Oscillator using Thermodynamically driven DNA Cascades

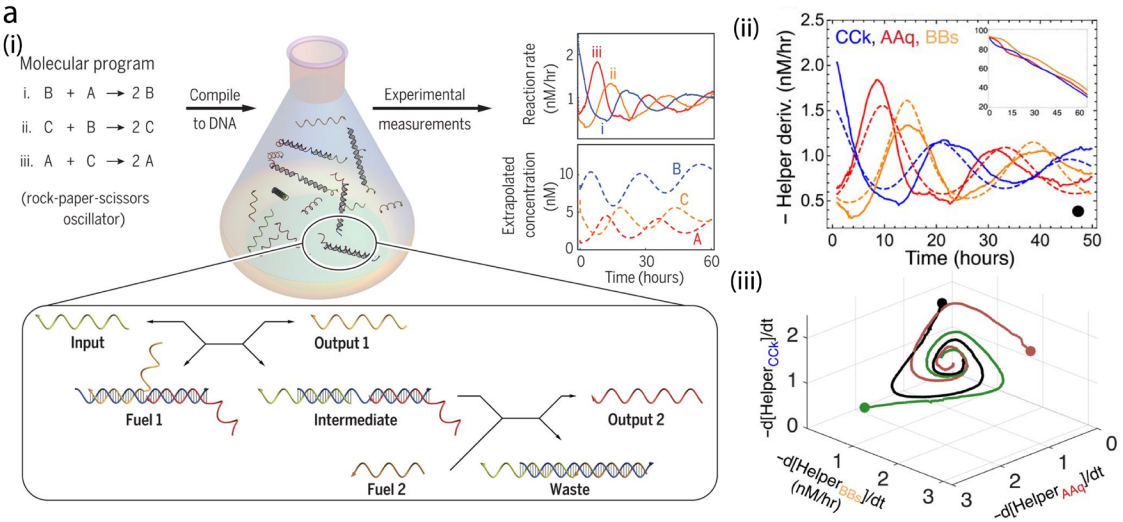

DNA-based Negative Feedback Circuit using Thermodynamically driven DNA Cascades

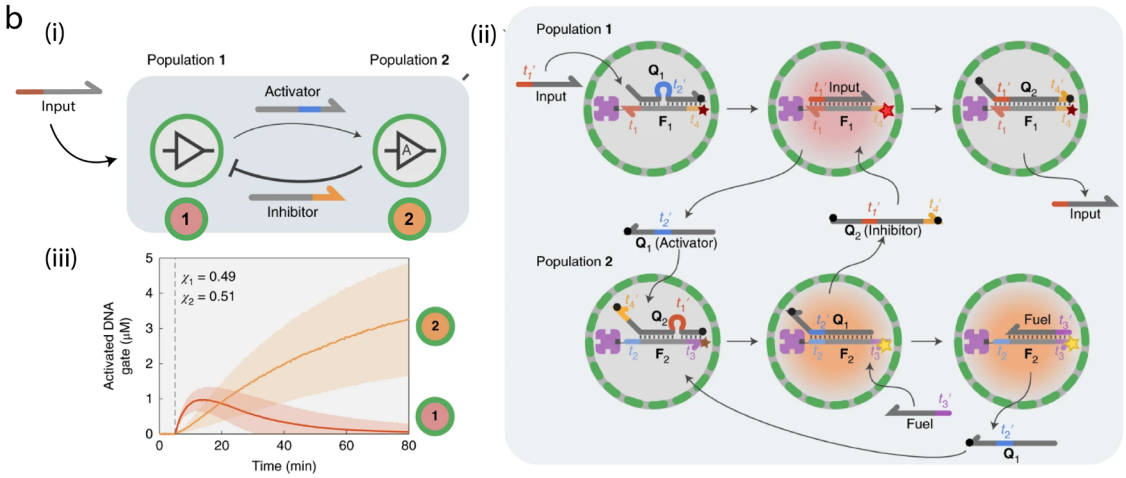

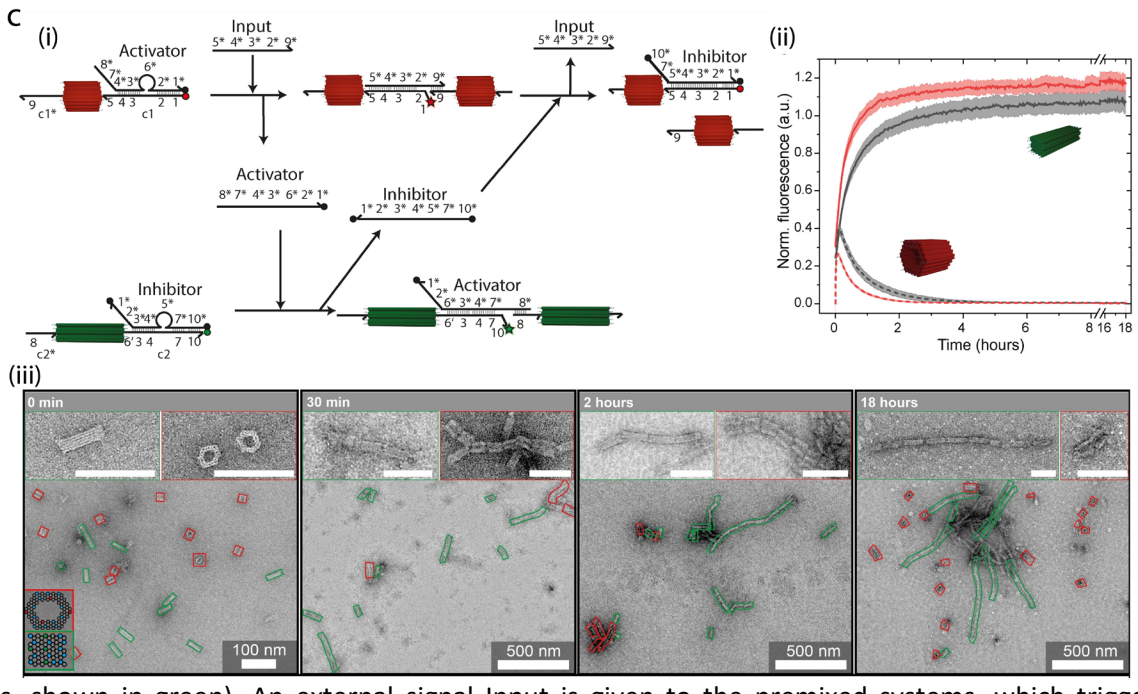

cuboids, shown in green). An external signal Input is given to the premixed systems, which triggers the

Figure 1-9. DNA-only dynamical system. (i) Schematics for the systematic design and implementation of rock-paper-scissors based DNA oscillator. Oscillations are observed from the reaction rates measures from three modules and in the extrapolated concentrations of oligonucleotides representing formal species. Inset shows a part of the strand displacement implementation where Input strand initiates a cascade that displaces two Output strands, in the process converting two Fuel molecules into Waste. (b), (c) DNA-only negative feedback circuits for: (b) protocellular communication. (i), (ii) Illustration of a negative feedback loop between two protocell populations engaged in compartmentalized TMDSD reactions. The circuit is triggered by Input strand which activates the Cy5-labelled DNA gate in population 1 thereby releasing a strand which acts as an activator for Cy3-labelled DNA gate in Population 2. The activation causes the release of Inhibitor which deactivates the DNA gate in Population 1 by switching off their fluorescence, however the Cy3 fluorescence sustains. (iii) Time-dependent fluorescence measurements for two proteinosome populations. The transient Cy5 fluorescence (red curve) is consistent with the negative feedback loop operating in Population 1. Cy3 fluorescence (orange curve) saturates due to fuel-mediated amplification; (c) self-sorting fibrillar self-assemblies. (i) Scheme of 3D DNA origami cylinders (red) polymerizing to nanotubes upon Input addition, thereby releasing activator which polymerizes 3D DNA origami (green) to fibrils. The Inhibitor released during activation depolymerizes the nanotubes back to cylinders. (ii) Time-resolved fluorescence of Cy5 (cylinder origami) and Cy3 (cuboid origami). (iii) Time dependent TEM images of origami polymerization for cylinders (red) and cuboids (green). Graphics adapted from ref. (85-87)

polymerization of the nanotubes by TMDSD at the expense of releasing an Activator strand for the polymerization of the cuboids (**Figure 1-9c**). This cuboid activation in turn releases an Inhibitor strand during the polymerization of the cylinders, which in a downstream reaction can depolymerize the initially formed nanotube filaments. Time dependent fluorescence and TEM measurements were performed to experimentally confirm the basic operation of the system at both molecular and structural level.

An apparent solution to sustain oscillations or reset DSD reactions discussed above will be to work in an open reactor-with constant supply of all DNA components. Since closed reactors are experimentally more practical, another idea would be to have a large amount of buffered inactivated components present in the solution which will be activated as soon as an activated component is consumed.[89-91] Other strategies rely on the presence of secondary reactions, logic circuits or non-isothermal conditions to reinstall the original state of the system. These strategy could also solve the fatigue after each refueling cycle observed in transient systems. Many reports have shown enzyme-dependent approach to reset TMDSD reactions which will be discussed in detail in the next section. Ricci and Siedel group together proposed a non-enzymatic strategy, based on disulfide-thiol redox reactions, to have a dissipative control over TMDSD reactions (**Figure 1-10**). They split a 25-nt DNA fuel into two parts (of different lengths) that were linked to each other through a disulfide bond. In the absence of any reducing agent the disulfide containing fuel strand could activate the strand displacement reaction and release the output. In contrast, a reducing agent (TCEP), by breaking the disulfide bond in single-stranded DNA (ssDNA) or double-stranded (dsDNA), can act as the fuel-consuming unit. The

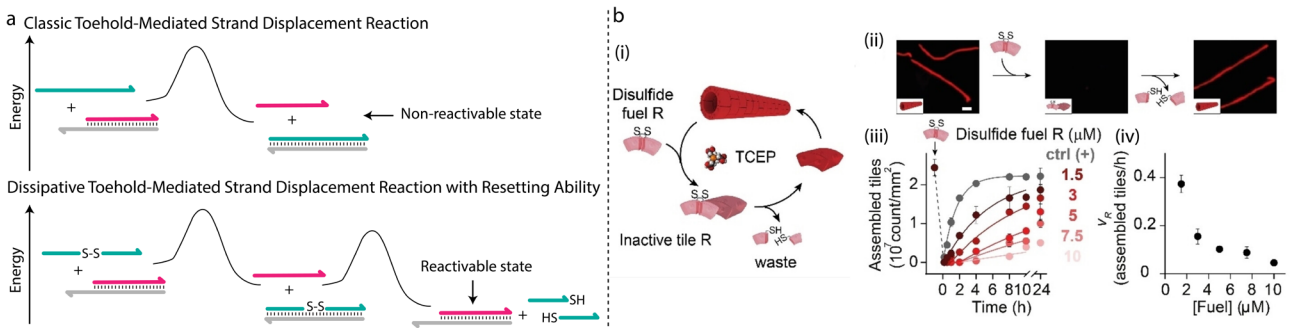

Figure 1-10. Dissipative control over TMDSD reaction. (a) Comparison of the simplified energy landscape diagram between a classic TMDSD (with non-reactivable final state) and dissipative TMDSD (with resetting ability). (b) Scheme of transient disassembly of DNTs driven by dissipative TMDSD using redox chemistry. (i) The disulfide fuel binds the fuel-binding domain including the disassembly of DNTs. A reducing agent (TCEP) acts as fuel reducing unit reducing the fuel in two halves that spontaneously de-hybridize from the DNA tile allowing the tiles to reassemble into DNTs. (ii) Fluorescence microscopy images showing a representative experiment of transient disassembly. (iii) Transient disassembly of red homo-polymers at different concentrations of red disulfide fuels. (iv) Re-assembly rates (assembled tiles/h, calculated by linear fitting of the initial part of the kinetic curves in panel (iii) at different concentrations of red disulfide fuels. Graphic adapted from ref. (91)

resulting fuel fragments should then spontaneously dissociate from the target, allowing for reloading of the output strand and the formation of the original duplex.

Another approach which can be useful in this regard is the incorporation of functional DNA such as DNAzymes[94] in the reaction networks. Also known as deoxyribosomes, DNAzymes are short oligonucleotides which demonstrate high catalytic activity towards specific substrates with the help of certain cofactors like metal ions and small molecules. Recently Wang et al. introduced the concept of constitutional dynamic networks to transiently control the catalytic activity of a Mg^{2+} ion dependent DNAzyme.[95] They built a three-layer transient catalytic cascade where one layer triggers the activation of subsequent layer. Such networks could solve the problems of scalability, reusability, leakage and open the field to systems with enhanced complexity.

DNA-based Enzymatic Reaction Networks

Thus far, the transient autonomous non-equilibrium behaviors of the presented DNA-only systems were mainly driven by the free energy of hybridization. This leads to energetic deadlocks of accumulated energy-minimized duplex states, which cannot be reactivated further. However, as evident from the catalytic reaction loops above, when striving for active and adaptive reversible dynamic behavior with autonomously repeating operation cycles we need to turn to continuously energy-dissipating non-equilibrium states. This requires first and foremost energy sources decoupled from the structures, preferentially with a high energy density and a free difusive, refuelable character, and secondly a functional energy sink in the system. In this respect, the free energy released from the hydrolysis of small molecules such as ATP/GTP or hydrolytic cleavage of a DNA/RNA strand is an interesting energy source to drive energetically uphill processes out-of-equilibrium while dissipating energy. Nature has evolved enzymes to perform unconceivable or atleast challenging tasks like these. For example, the completion time for each cycle in DSD oscillator presented in previous section is 20 h, employing enzymes for such tasks can decrease the cycle period by 7 times.[96] Hence, there are opportunities in fusing enzymes with DNA where the DNA components will provide the spatial organization, while the dynamics are driven by some biocatalyzed processes. The most common examples of these enzymes are polymerases, ligases, and nucleases. They accomplish the production and degradation of DNA fuels consuming nucleotide triphosphates (NTPs) and can therefore keep the system out-of-equilibrium as long as NTPS are supplied and waste products are removed. Within this first category, we will first begin with synthetic gene regulatory networks (GRNs) and their stripped-down minimalist versions. Next, we will discuss how the need for RNA removal from GRNs led to the development of the polymerase exonuclease nickase (PEN) toolbox and many other hybrid DNA enzyme reaction networks.

DNA-RNA-Enzyme systems

In cells, GRNs provide a general framework for the implementation of computing tasks at the molecular level (**Info Box 8**).[92] Such networks were later realized *in vitro* to construct bistable,[91] oscillatory circuits,[97,98] or simply a reactivable transient cycle. Extracting the essential dynamic features of GRN from the viewpoint of dynamical systems, Kim et al. proposed an *in vitro* analog of GRNs by applying a “genelet” architecture.

Info Box 8. Synthetic Transcriptional Network. This toolkit relies on two enzymes, bacteriophage T7 RNA polymerase for RNA production and RNaseH for RNA degradation. It simplifies GRNs by avoiding protein synthesis and instead using RNA to directly regulate its own transcription from short DNA gene analogs. These genelets are dsDNA complexes that have an incomplete promoter region. They require this missing ssDNA (activator) to initiate the transcription by T7 RNA polymerase to their RNA outputs. In turn, these RNA transcripts either sequester or release the labile DNA activators to other genelets, hence establishing a cross-regulation between different units. The presence of RNases provides an internal chemical sink that degrades. RNA bound to DNA is degraded by the enzyme RNase H. RNA units implement a necessary negative feedback in the system. A bistable or reactivable transient system can be realized by just using one genelet, and an oscillatory circuit with minimum of 2 genelets. Although the in vitro transcriptional oscillator operates 2 times faster than the DSD oscillator, the progressive loss of enzyme activity, as well as the accumulation of abortive transcripts and

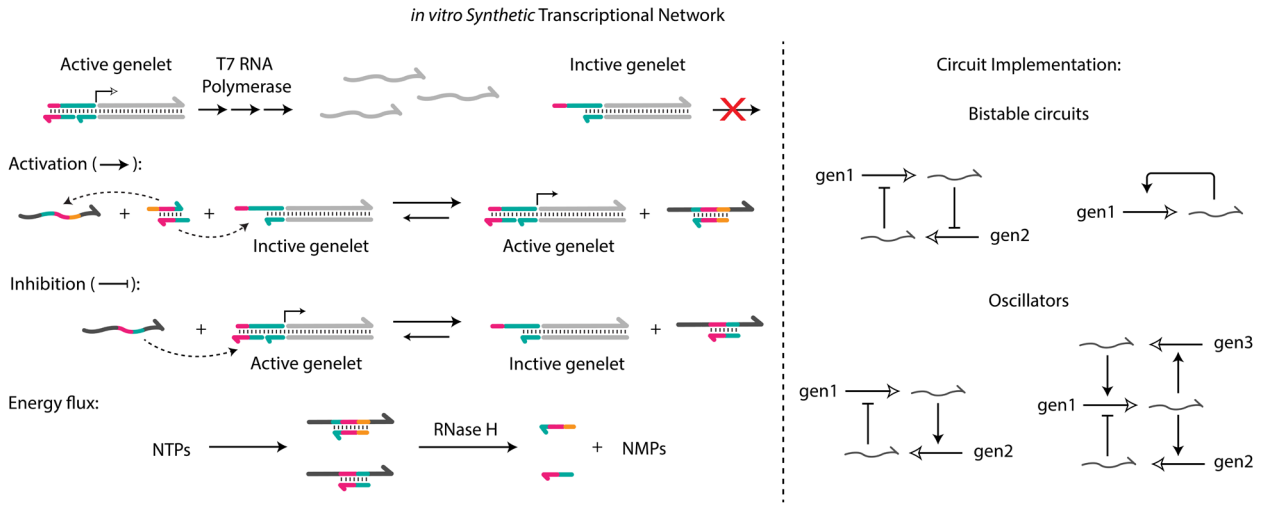

T7 RNA Polymerase catalyzes the formation of RNA from DNA in the 5′ to 3′ direction. RNase H catalyzes the cleavage of RNA in an RNA/DNA via a hydrolytic mechanism.

partially degraded RNA, cause oscillations to have fluctuating amplitude and frequency that cannot be sustained for more than 16-20 h (6 cycles).

Franco and coworkers used *in vitro* transcriptional network to first develop reversible self-assembling system and subsequently an oscillating system (**Figure 1-11a**).[102,103] First, they developed a simple switching system where activation and deactivation pathways are manually initiated. An RNA invader is transcribed (in the presence of T7 RNA polymerase) from a genelet in the presence of an Activator. Invader binds to the DNA nanotubes (DNTs) and disassembles them. RNase H simultaneously degrades the RNA invader. A complementary action of T7 RNA polymerase and RNase H breaks DNTs and reaches a disassembled steady state. A consequent addition of Inhibitor strand binds to the Activator and turns the gene off and thereby the production of RNA invader which further promotes the degradation of RNA invader by RNase H and allows the DNTs to assemble and grow again. The group then coupled a gene oscillator to DNTs; the oscillator is composed of two transcriptional switches, each switch contains a genelet, inhibitor and an activator. The RNA output of each switch 1 acts as activator for the other switch 2, however the RNA output of switch 2 inhibits switch 1 inducing negative feedback. The oscillator is further connected to an Insulator genelet that produces RNA invader. As described above, the invader regulates the oscillatory assembly/disassembly of the DNTs in presence of RNaseH.

Although use of these networks for self-assembly purposes is scare, but they show potential as minimal regulatory system in synthetic cells, as shown in studies conducted within droplet. Franco group[105] and Bausch group[106] independently used a stripped-down version of *in vitro* transcriptional network to develop a reactivable transient system by just using one genelet (**Figure 1-11b,c**). The activation reaction includes transcription to produce an RNA linker and its simultaneous degradation by RNase H. Faster transcription and slower RNA degradation satisfies conditions to realize transient system. The reaction cycle derives constant energy from RNA hydrolysis. Franco group adopted a one-pot approach and utilized the *in situ* synthesized RNA linker to transiently self-assemble DNTs (**Figure 1-11b**).

Bausch and coworkers however, externally added the NTP solution to trigger the reaction cycle and achieve transient co-assembly of DNA-coated colloidal particles (**Figure 1-11c**). If we strip out even the transcription machinery from the above system, then RNA can be directly introduced as an external trigger to drive a certain transient function. Ricci group exploited the strategy to achieve dissipative control over TMDSD reaction (**Figure 1-11d**).[107,108] The high energy RNA invader strand displaces a certain strand of DNA duplex to produce a transient DNA-RNA complex. Simultaneous degradation by RNase H return DNA duplex. Due to the resetting ability of the system, it can be reactivated for up to 10 cycles.

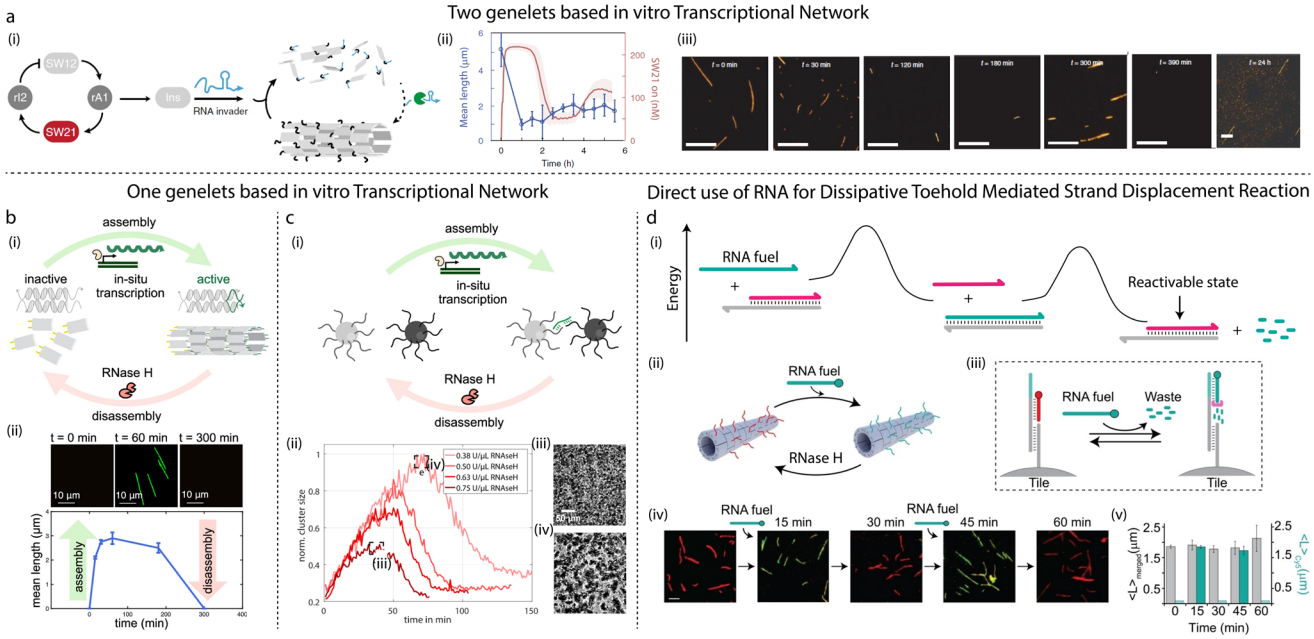

Figure 1-11. Transient assembly formation using synthetic in vitro transcriptional reaction network. (a) DNTs assembly directed by two-genelet synthetic molecular oscillator. (i) Scheme showing two genelet switches SW12 and SW12. The output of switch SW12 is RNA activator rA1, which turns on switch SW21; in turn SW21 produces an RNA inhibitor (rI2) that turns off switch SW12. The oscillator is coupled to an insulator genelet (Ins), which produces RNA invader. The invader disassembles the DNTs, and simultaneous degradation of RNA invader bound to DNTs by RNase H refurnishes the DNTs. (ii) Fluorimetry experiments report the fraction of active SW21 (in red) and nanotube mean length (in blue). (iii) Representative fluorescence microscopy images at different time points. (b) Dissipative control over assembly and disassembly of hybrid DNA/RNA NTs. (i) Schematics showing transient activation of inactive DNA tile towards self-assembly. The structure formation is induced by complementary RNA-linker strands which link the two DNA tiles together. The production of the RNA-linker is realized using a T7 RNA Polymerase under use of free dsDNA templates and NTPs in solution. A subsequent disintegration of the so formed DNTs is achieved by RNaseH, which degrades the RNA-linkers once bound to DNA. (c) Transient colloidal structure formation using antagonistic RNA generation and degradation network. (i) 1 µm sized polystyrene colloids are functionalized with two sorts of ssDNA docking strands. (ii) The lifetime and size of the colloidal clusters is controlled by varying the RNase H concentrations. (iii), (iv) Bright field images of the maximal cluster size for the shortest and the longest pulse, respectively. (d) Enzymatically driven dissipative toehold-mediated DNA/RNA hybrid strand displacement. (i) Simplified energy landscape diagram for the system showing resetting ability. (ii) Schematics showing the transient labeling of DNTs when adding an RNA fuel strand in presence of RNase H. (iii) Initially each DNA tile carries a target strand hybridized to a Quasar-570 fluorophore-conjugated DNA output strand (red). Addition of a Cy5 conjugated RNA fuel strand displaces the output strand resulting in a different labeling of the DNTs. In the presence of RNase H the re-labeling is transient and reversible due to fuel degradation and output rebinding. (iv) ex situ Fluorescence microscopy images of the sample solution taken at different times intervals. (v) Average length (<L>, µM) of the structures obtained from the analysis of the merged channel (left, <L>merged, grey) and the Cy5 channel (right, <L>Cy5, green) showing that the structures remained intact during relabeling and imaging. Graphics adapted from ref. (98, 99, 101, 104)

DNA-Enzyme systems

In the previous section, the antagonistic RNA generation and degradation reaction cycle was utilized for various transient functions. The advantage of using RNA fuel within mixed RNA/DNA assemblies is the easy control over the selectivity of fuel consumption by RNases while maintaining DNA strands as structural elements within the assemblies. However, RNA is expensive and chemically less stable than DNA due to the presence of an extra hydroxyl group that renders this biomacromolecule more susceptible to hydrolysis under a wide variety of conditions. This fact not only limits the use of environments where such RNA fuel-based assemblies can be applied, as in biological media, but might also cause undesired fuel consumption. As an alternative, only DNA-based enzymatic reaction networks are designed and developed such as PEN DNA toolbox (**Info Box 9**).

Info Box 9. PEN toolbox.

The PEN dynamic network assembly toolbox architecture simplified GRNs further by eliminating RNA altogether. Due to this, the oscillator developed from PEN toolbox can run for 30 cycles. Montagne at al. developed the toolbox by using pseudo-genes (ssDNA

templates) that directly regulate each other by emitting small signal molecules. These DNA signals either activate or inhibit DNA templates. DNA polymerase extends single-stranded domains of active templates; the extended domain is recognized and cleaved by nickases, causing the 'replicated' short strand to be released. These short, replicated strands can be used to activate or inhibit other templates, thereby building circuits. Dissipation is introduced by the nickase and by the exonuclease, which respectively release and degrade ssDNA fueling the dynamics; in the absence of these enzymes, the system would reach thermodynamic equilibrium. Because of simpler architecture, it can be used to build bistable circuits, amplifiers, oscillators and memory switches.[110]

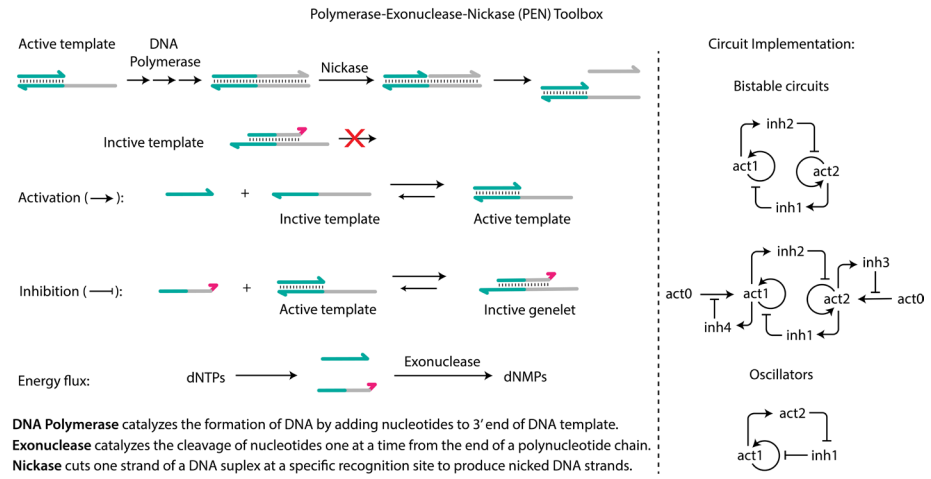

Gines et al. integrated the DNA coated particles within the PEN toolbox to create autonomous functions such as bistability, communication and cooperative mechanisms in symbiotic clusters.[111] Dehne et al. customized the toolbox to construct an oscillating network to produce DNA linkers which bring two DNA-coated colloids together into co-assemblies (**Figure 1-12**).[112]

Danielsen group[113] and Xie group[114] independently introduced a minimal dissipative network using a nickase enzyme as fuel-consuming unit (**Figure 1-13a**). Fuel binds to a target DNA to create a restriction site that is recognized by a strand-specific endonuclease that cleaves the fuel into two pieces leaving the target DNA intact. The target DNA is hence recycled for fresh fuel and the process of hybridization, cleavage, and dissociation repeats. The nicking-assisted recycling strategy was later implemented to design catalytic operating dissipative TMDSD circuits (**Figure 1-13a**).[115] Here, the initial system consists of a DNA gate (F:S) and catalyst I. The Nickase enzyme performs a site specific nicking digestion at the F strand in F:S complex creating a final complex as F1:F2:S. Now, catalyst is able to displace F1 from F1:F2:S exposing a toehold in the middle

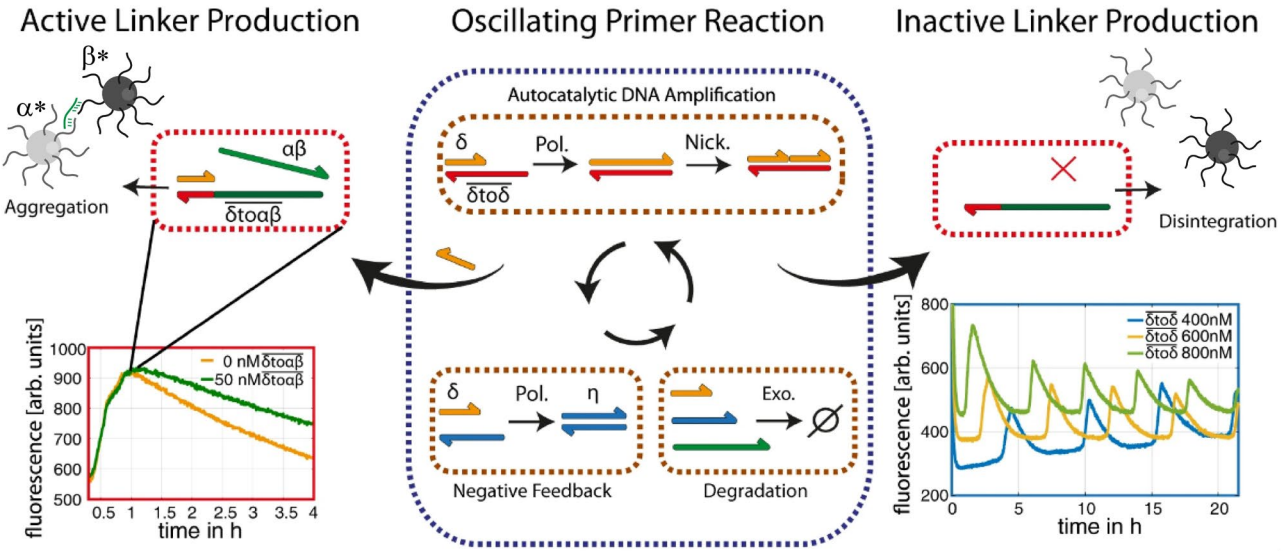

Figure 1-12. Scheme for the oscillating colloidal aggregation using DNA reaction networks based on PEN toolbox. The underlying reaction network (blue dotted box) and the coupled linker reaction (red dotted boxes). The oscillation of the DNA amplification (blue box) can be controlled in terms of frequency and can activate the linker production during the DNA concentration peaks (red box). Here, one cycle of the oscillation is shown with (green) and without (orange) additional linker production. Oscillating linker concentration thereby synchronizes colloidal aggregation. Graphic adapted from ref. (109)

of the duplex complex. This metastable structure allows for one full-length F strand to simultaneously displace both of the I and F2 strands, thus leading to the recycling of the DNA catalyst I and the regeneration of F:S.

Willner group rounded the story by exploring nicking assisted recycling strategy for dissipative TMDSD (**Figure 1-13b**).[116] Parallel and cascadic operation of two dissipative networks was shown using the nicking assisted dissipative TMDSD. The system was recently utilized to transiently co-assemble two DNA strands where each DNA strand carries one enzyme partner of the enzymatic cascade for e.g., glucose oxidase (GOX) and horseradish peroxidase (HRP).[117] The co-assembled complex enhances the biocatalytic cascade operation by four-fold due to the effective communication between the two enzymes enabled by close proximity. A transient aggregation of AuNPs and semiconductor quantum dots (QDs) was also shown using the above

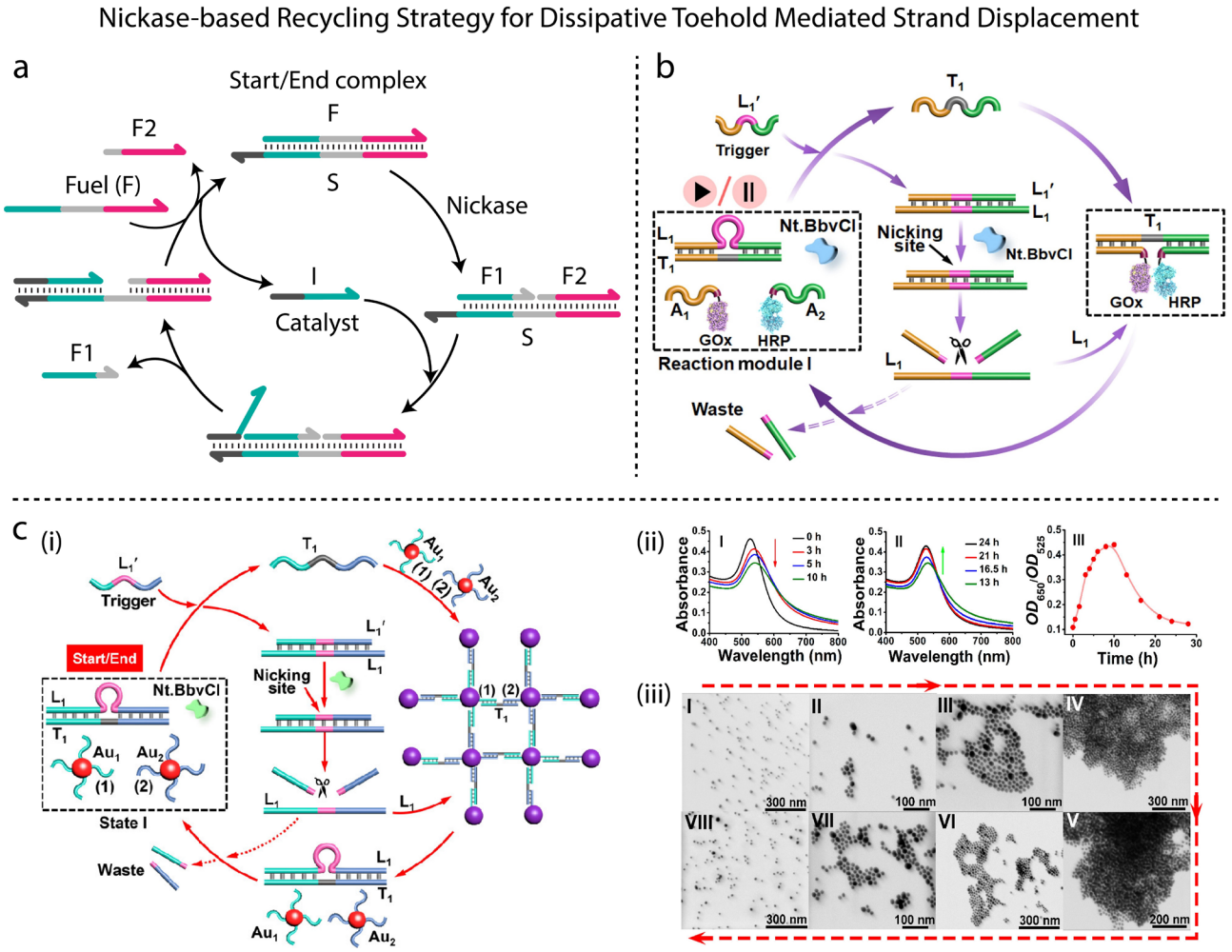

Figure 1-13. Nickase-based resetting mechanism for dissipative TMDSD. (a) Schematics for the nicking-assisted catalytic DNA circuit. In the presence of Nickase enzyme, the starting complex F:S produces an active gate complex F1:F2:S which triggers the displacement of F1 by catalyst I. The resulting transient complex I:F2:S allows to simultaneously displace both I and F2 refurnishing starting duplex F:S. (b) Transient operation of the GOX/HRP biocatalytic cascade. The system initially consists of a DNA duplex L1:T1, where T1 includes complementary sequence domains to the ssDNA functionalized on two different AuNPs and the nicking enzyme Nt.BbvCl. Treatment of the system in this state with the fuel strand L1' displaces T1 from duplex L1:T1 to yield energetically stabilized L1:L1'. The released T1 co-assembles two different ssDNA where each strand carries one enzyme partner of the enzymatic cascade. The resulting complex enhances the biocatalytic cascade. Meanwhile, the nicking enzyme specifically cleaves L1' in duplex L1:L1' generating two waste fragments and refurnishing L1 which is now available to rebind with T1, disassembling the supramolecular complex thereby decreasing the efficiency of the biocatalytic cascade. (c) Fuel-triggered transient aggregation and disaggregation of AuNPs. (i) Schematics showing the underlying reaction network. (ii) Panel I and II demonstrate the time-dependent absorbance spectra of the fuel-triggered aggregation and nicking enzyme-generated disaggregation of the AuNPs. Panel III shows the transient interparticle coupled plasmon absorbance of the AuNPs (followed by the OD650/OD525 ratio). (iii) Time-dependent TEM images following the transient co-assembly process. Graphics adapted from ref. (113, 115)

reaction cycle (**Figure 1-13c**). This is exemplified here with the transient dissipative co-assembly between two AuNPs.[118]

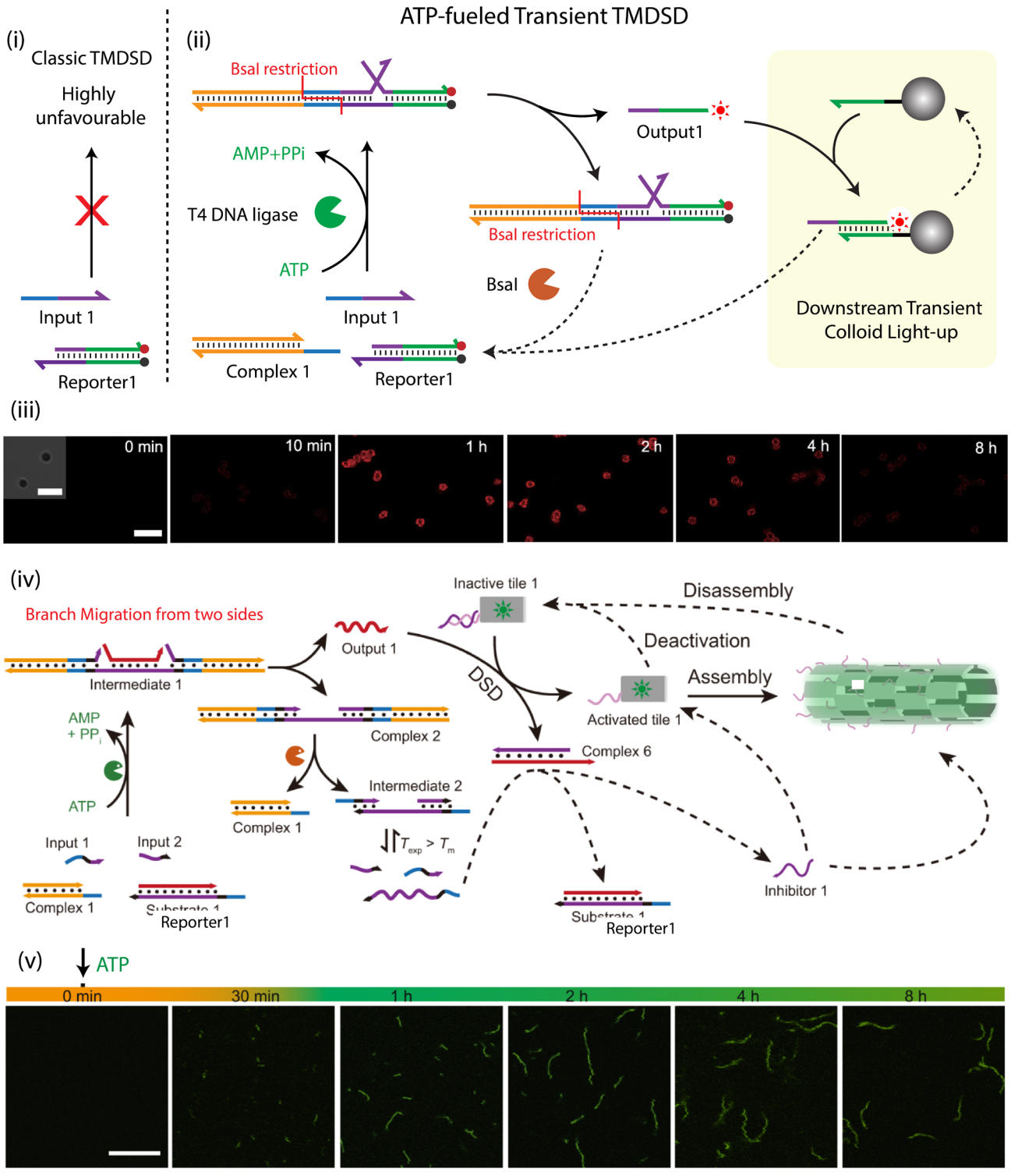

Figure 1-14. ATP-fueled transient TMDSD and its use for transient functions. (i) Schematics for a classic TMDSD between Reporter1 and Input1 which is unfavorable due to uncompetitive toehold length. (ii) The ATP-fueled ligation biases strand displacement reactions by increasing the toehold length and increasing the local concentration by covalent fixation, while the concurrent endonuclease restriction eliminates this bias, allowing to reset the system. The in situ generated Output1 is used for transient fluorescent labeling of colloidal particles. (iii) Time-dependent CLSM images for the colloids for transient colloid functionalization via transient DSD. (iv) Schematics for the dual inversion strategy in ATP-fueled transient DNT self-assembling system. (v) Time-dependent CLSM images for ATP-fueled transient DNT self-assembly. Graphics adapted from ref. (117, 118)

Hermann group employed a DNA consuming enzyme, exonuclease III (Exo III) instead.[119] ExoIII specifically degrades dsDNA with 3'-blunt ends or 3'-overhangs that are shorter than four bases. High energy DNA fuel serves as a linker for two co-assembling AuNPs, ExoIII subsequently digests the linker strand rendering the DNA on the AuNPs intact. The system returns to its disassembled state and is ready for another batch of fuel addition. In most of the DNA-based or DNA/RNA hybrid systems discussed so far, the linker strand responsible for bridging two building blocks together into assemblies is either added as a fuel or generated *in situ* transiently. After pre-programmed time, this fuel is degraded to waste forming nucleotide monomers. Although the system recycles the initial components but resembles a rather energetically downhill process opposed to what is found in nature where the chemical fuel is processed and all the building block components including the linker remain intact.

Towards this, our lab developed dissipative conditions in DSD systems by introducing an antagonistic network composed of ATP-powered ligation/restriction (**Figure 1-14**).[120] The invading strand Input1 cannot displace Output from Reporter because of uncompetitive length of toehold, hence unfavorable conditions. Addition of ATP, however, powers the ligation by T4 ligase between Complex1, Input1 and Reporter which increases the length of toehold and its local concentration due to covalent fixation. Consequently, strand migration happens and Output1 is expelled from Reporter1. Complex1 changes to Complex2. Simultaneously, BsaI endonuclease is able to cleave the newly formed Complex2 to regenerate Complex1 and a dsDNA Intermediate1, which dissociates into two ssDNA due to its low T_m and thereby reproduces Input1 as well as Reporter1 by rehybridization with Output1. The transiently released Output1 is available for downstream functions such as fluorescent labeling of colloids. To generalize the strategy and expel even longer Output1 strands, a dual inversion strategy was further proposed.[121] After some modifications in the design, two equivalents of Complex1 can ligate with 1 Reporter complex in the presence of Input1 and an additional Input2. The chain migration from two sides releases Output1 with stronger thermodynamic push. Output1 subsequently displaces an Inhibitor strand from a DNA tile exposing the complementary domains between the tiles and triggering transient self-assembly. Once ATP reaches subcritical level, restriction takes over and Output1 is reassociated within Reporter resetting the whole system. The transient Output1 generation is used for the downstream regulation of DNTs. Output1 released from the upstream ATP-fueled network displaces the blocker strand from Inactive DNA tile rendering it active for self-assembling into DNTs. As soon as ATP diminishes, Output1 more favorably rebinds within Reporter1 complex, allowing the blocker strand to inactive DNA tile again and disassembling the formed structures. Although the design has been generalized for transient and autonomous 4D self-sorting hierarchical systems,[122] coacervates,[123] and catalysis,[124-126] but complex functions such as bistability, oscillations cannot be achieved in the present form. An ATP recycling/producing system can impose a missing positive feedback loop which might be helpful to achieve advanced non-linear functions such as bistability and oscillations.

1.4 Non-Linear Reaction Networks for Drug Delivery Applications

The applications of out-of-equilibrium reaction networks, especially DNA (both enzymatic and non-enzymatic) circuits are not limited to programming self-assemblies and materials but are also extending for present and future drug delivery applications in living cells. The non-linearity and biocompatibility of these circuits can transform drug delivery by enabling kinetic control over drug release, thereby improving the efficacy and safety of the therapeutics.

For example, minimalistic RNase/Nicking enzyme based reaction networks are utilized to design a synthetic ligand-binding DNA nanodevice that can transiently load and release molecular cargo (**Figure 1-15a,b**). The DNA-nanodevice is a clamp-like structure that recognizes a specific DNA cargo through the formation of a triplex DNA structure (involving both Watson Crick pairing and Hoogsteen interactions, **Figure 1-15a**).[128] Addition of an RNA fuel induces a conformational change in the triplex resulting in its unfolding and a

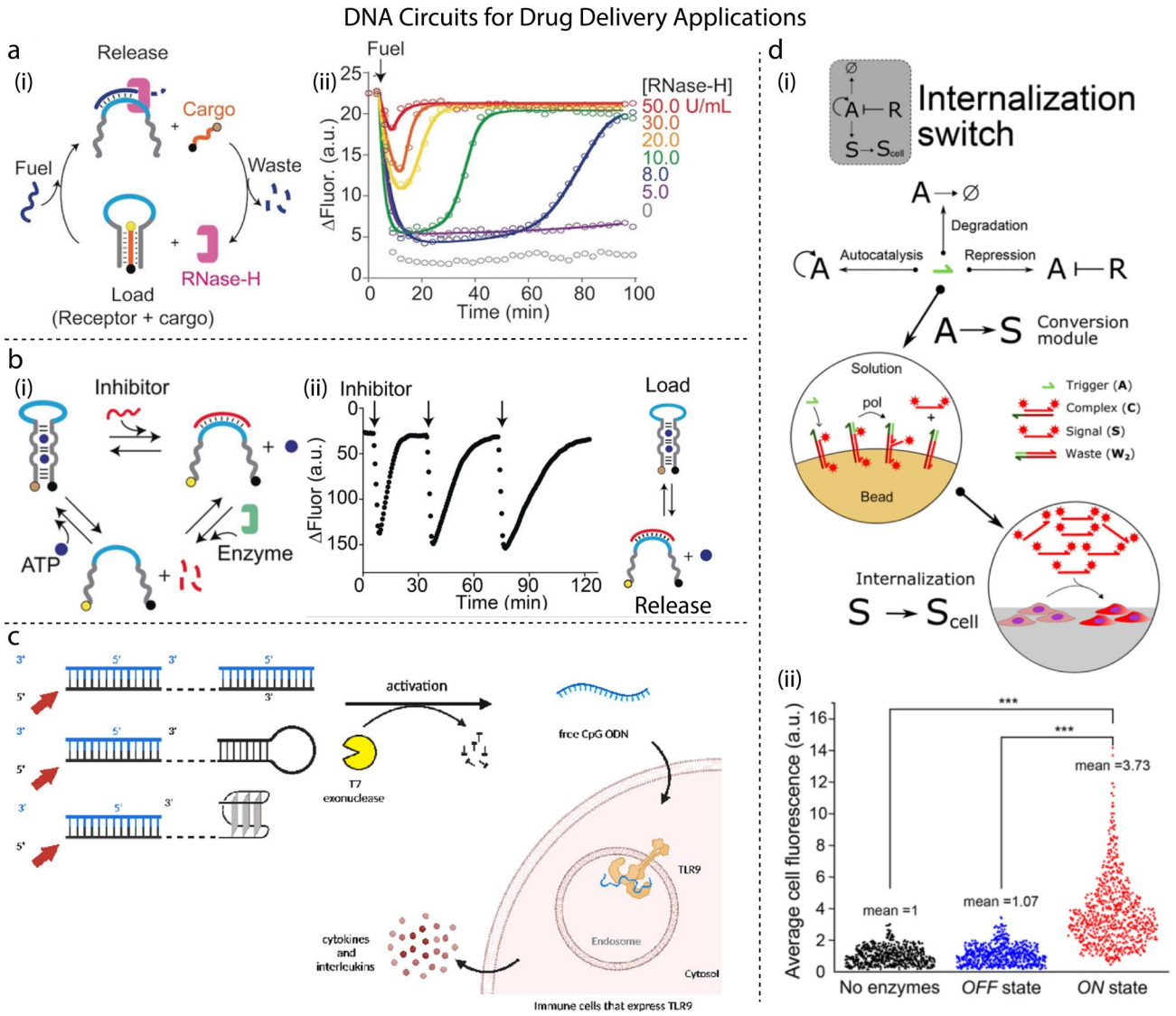

Figure 1-15. DNA circuits for present and future drug delivery applications. (a) A dissipative DNA nanodevice for transient release of cargo DNA. (i) A clamp like DNA device recognizes specific DNA sequence through the formation of triplex structure. An RNA fuel strand binds to the loop of clamp device inducing the release of cargo DNA. RNase H is used as a fuel consuming unit and hydrolyzes the RNA in the RNA/DNA duplex. (ii) Time-dependent fluorescence traces showing the transient release of the cargo after addition of fuel strand at different concentrations of RNase H. (b) Cocaine/aptamer load complex as the functional carrying device. (i) A split ATP-binding aptamer is used as a dissipative receptor. A DNA inhibitor allosterically triggers the release of ATP. In the presence of Nicking enzyme, the Inhibitor is selectively hydrolyzed resulting in the re-capture of ATP by receptor. (ii) Kinetic fluorescence traces showing the transient release of ATP for three consecutive cycles. (c) The blue strand shows the CpG ODN which is blocked from cell internalization by hybridization with complementary DNA in three different configurations (linear, hairpin or G-quadruplex). Selective hydrolysis of this complementary strand activates the release of free CpG ODN which thereby stimulates the intracellular TLR9 receptor. (d) Out-of-equilibrium extracellular medium that controls the internalization of fluorescently labeled DNA in living cells. (i) Schematics describing the internalization switch installed in the culture medium. Grey box shows the network topology composed of bistable switch and conversion module. Freely produced A from bistable switch triggers the release of signal strand, S from conversion module fixed on hydrogel bead. (ii) Mean fluorescence intensity per cell in the dynamic medium in the absence of enzymes (black dots), in the OFF state (blue dots), and in the ON state (red dots). Graphics adapted from ref. (125, 126, 127, 129)

consequent release of DNA cargo. The presence of RNase H in the system simultaneously hydrolyzes the RNA in DNA/RNA duplex. This allows for the DNA cargo to rebind within the nanodevice with kinetics depending on the respective enzyme and fuel concentration. The sequence-specific binding properties between aptamers and low-molecular-weight ligands, such as ATP or cocaine were used to develop transient DNA carrier-based load release and uptake devices.[129]

A cocaine aptamer/cocaine load complex was also used as the functional carrying device (**Figure 1-15b**). Subjecting the system to the fuel strand, in the presence of the nicking enzyme Nt.BsmAI leads to the formation of a stable duplex between the fuel strand and the aptamer sequence resulting in the release of the cocaine load, and the formation of an expanded nucleic acid structure, where the fluorophore is non-quenched. The nicking of the fuel strand by Nt.BsmAI leads to fragmented waste products that uncage the aptamer sequence that refolds, in the presence of cocaine, to the original aptamer-cocaine complex.

Most of the similar strategies that make use of such DNA nanodevices are mainly focused on delivering small molecules and cargos where DNA merely acts as information processing unit. Herrmann and coworkers designed DNA circuits for delivering therapeutic nucleotides sequences that are actually part of the DNA circuit as drug themselves (**Figure 1-15c**).[127] These therapeutic nucleic acids belong to a special class of oligonucleotides (ODNs) that are designed and used for the treatment of various diseases including genetic disorders.[128] Some of the examples include antisense ODNs, small interfering RNA (siRNA), and microRNA (miRNA).

The group designed a DNA-enzyme hybrid circuit for the delivery of pharmacologically active CpG ODNs (short ssDNA synthetic molecules that contain a cyosine triphosphate deoxynucleotide followed by a guanine triphosphate deoxynucleotide) that stimulate the immune system through recognition by the toll-like receptor 9 (TLR9) protein. The entire circuit is installed in the culture-media of the cells where the CpG ODN is initially blocked from getting internalized in cells by hybridization with complementary DNA sequence. T7 exonuclease catalyzes the removal of complementary blocking DNA thereby activating the release of ODN in cells. The rate of release and resulting immunostimulation activity can be controlled by the enzyme and blocker concentration. Although strategy offers a good starting point for the direct integration of DNA circuits in delivery mechanisms, the circuit drives the system towards thermodynamic equilibrium rather than operating out-of-equilibrium.

Torres and coworkers engineered the cell culture media of HeLa cells to install out-of-equilibrium reaction networks using PEN toolbox (**Figure 1-15d**).[130] They created an internalization module by coupling a bistable switch to a conversion module (A→S), which releases a fluorescently labeled ssDNA signal strand, S later to be internalized in cells. The bistable switch targets two antagonistic steady states: ON and OFF state in the absence and presence of a repressor strand, R respectively. The ON state maintains a high steady-state concentration of A for downstream processes, however in the OFF state combined degradation of A by R and exonuclease overcomes autocatalysis making it unavailable for further processes. The conversion module relies on the reaction A + C → S + W_2, where C is a partially dsDNA complex, whose shorter strand is S, and the longer strand is functionalized on hydrogel bead. This fixation avoids any uncontrolled internalization of S or C into cells. S is passively internalized by cells and the timing of which can be pre-programmed by tuning the reaction kinetics of out-of-equilibrium medium. Such strategies can further be extended by coupling other reaction networks with DNA controlled delivery of anti-sense ODNs,[131] siRNA,[132] miRNA,[133] or DNA-peptide conjugates,[133] for instance to control cell physiology and providing aid in gene therapy and gene silencing. The applications of such systems are discussed briefly in **Chapter 6**.

1.5 Coupling Colloidal Particles to Reaction Networks

Colloidal building blocks that undergo transient co-assembly are usually bigger analogues than their supramolecular and biological counterparts. For reaction networks to regulate transient assembly of colloids, a detailed understanding and precise modulation of forces that govern interparticle potentials is necessary. The effective potential (U) acting between colloidal particles is determined by the sum of attractive and repulsive (surface) forces of varying strengths and ranges. The most widely used theories to predict U between a pair of colloidal particles as a function of separating distance is Derjaguin, Landau, Verwey, Overbeek (DLVO)

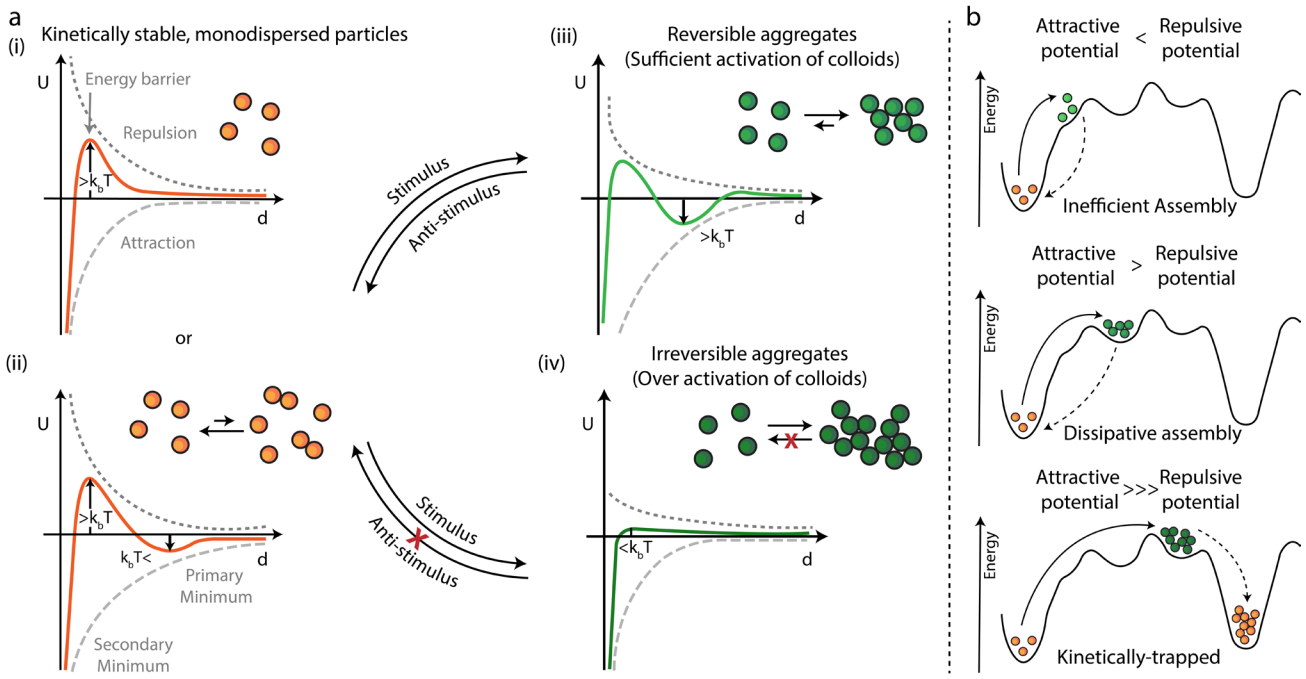

Figure 1-16. (a) Schematic representation of the total interparticle potentials (U) acting between (i), (ii) the particles prior to trigger addition (orange curves) and (iii), (iv) the trigger induced activated state (green curves). The net potentials are sum of repulsive (dark grey, dotted) and attractive (grey, dashed) contributions. For stable dispersions, the repulsive contributions generate a potential energy barrier, preventing the colloids from accessing the primary potential energy minimum. Prior to trigger addition, the interparticle potential energy barrier, highly dominating repulsive contributions at moderate interparticle distances maintain colloidal stability. (iii) In the activated state, the diminished repulsive contributions and deepening or formation of sufficiently deep potential well favors the colloidal aggregation. (iv) If the building blocks are over activated such that they become too attractive, primary minimum is accessed resulting in irreversible aggregates. (b) Respective energy landscapes for three possible cases after stimulus introduction-(i) if repulsive potential exceeds attractive potential, particles will form inefficient assemblies, (ii) if attractive potential is sufficiently higher than repulsive potential, particles will successfully form out-of-equilibrium assemblies, (iii) however, if attractive potential exceeds the optimal value, particles will fall into kinetic traps.

theory. The original DLVO theory determines colloidal stability based on contributions from van der Waals and electrostatic interactions only, However, the integration of additional contributions is proposed in later extensions (xDLVO) for precise estimation of surface characteristics. **Figure 1-16** schematically represents the superimposition of attractive and repulsive forces in the form of energy-distance curve. While the attractive forces favor aggregation of particles, the repulsive forces promote disaggregation and maintain stable dispersions.

The attractive contributions (Figure, grey dashed curve) to interparticle potentials are sourced by van der Waals forces. These forces are a combination of London Dispersion forces (instantaneously induced dipoles) and Debye forces (permanent dipoles) which originate from fluctuating polarizability between colloidal particles and the surrounding medium. They are (a) distance-dependent, strongly attractive at comparatively shorter interparticle distances and (b) size-dependent, the force strength increases with the size of the colloidal particle due to larger surface area and higher electron count.

To balance the attractive contributions and prevent unwanted irreversible aggregation, repulsive forces (Figure, grey dotted curve) are required to create an energy barrier that restricts the minimal interparticle distance. The repulsive forces include electrostatic, steric and/or electrosteric forces as a combination of both mechanisms.[133] Steric stabilization is achieved by adsorption or covalent grafting of macromolecules on the surface of the colloidal particles. The total contribution of steric forces is derived from both ligand-ligand and ligand-solvent interactions whereby the magnitude of each of these forces is determined by the chemical nature of both ligand and surrounding medium/solvent. When two particles come in close contact with each

other, the outer segment of the ligands on their surface overlap and interdigitate leading to the exclusion of the solvent molecules within the ligand interaction region which thereby causes the increase of the total osmotic pressure and consequently the increase of repulsions between the colloidal particles. start to deform and/or overlap. This clearly implies the dependence of solvent properties, ligand properties, coverage density and ordering degree on osmotic contribution. Close contact of colloidal particles also lead to the deformation and compression of ligand molecules providing an elastic contribution to the steric forces.[133]

For electrostatic stabilization, particles carry a net surface charge due to dissociation of acidic/basic surface tethered groups, isomorphic substitution, or covalent functionalization of ionic species. The charge neutrality is satisfied by the electrochemical double layer in which the concentration of the counter ions is higher than that found in the surrounding medium/bulk solution. When two similarly charged colloidal particles approach each other, a repulsive osmotic force is generated due to the partial overlap between the electrochemical double layers of the particles which pushes them apart and maintains overall colloidal stability. The Debye length which describes the thickness of the electrochemical double layer is a function of ionic strength and dielectric constant of the medium.[133] An increase in ionic strength further extends the ionic cloud but at the expense of compactness of the double layer which results in a decrease of the electrostatic repulsions. For specific cases, in addition to forces mentioned above, other contributions for e.g., hydrophobic,[134] depletion,[134] and Casimir forces[1] might also need to be taken in account when calculating interparticle potentials.

The effective potential curve shows a primary energy minimum at very short interparticle distances, a potential energy barrier at intermediate distances (**Figure 1-16a**, (i)), there's also a possibility of a shallow secondary minimum at relatively greater interparticle distances (**Figure 1-16a**, (ii)). The deep potential well of the primary minimum occurs at short interparticle distances due to the short-range nature and inverse power law dependence on the distance of the attractive van der Waals interactions. In an ideal case, repulsive forces must dominate attractive ones prior to the fuel addition. The well-defined maximum in the potential energy curve satisfies this condition by providing a barrier between primary and secondary energy minimum. Brownian diffusion provides the source of kinetic energy for the particles to collide which is related to the system's thermal energy (k_bT). If this energy with which particles collide is more than the maximum energy barrier, then particles experience inelastic collision and form irreversible aggregates. On the contrary, if the barrier is high due to sufficient repulsive interactions, less particles will be prone to irreversible aggregation. Even though the particles reach thermodynamic equilibrium when they are in close contact and sitting in the deep primary minimum, the maximum energy of the barrier decides the final state of the particles. Within this scenario, when the secondary minimum is absent or it is shallow enough for the thermal energy to drive the particles out of secondary minimum, particles overall remain dispersed in the solution and acquire kinetic stability.

Starting from a stable particle dispersion (not-aggregated), in which long-range repulsive particle interactions exceed attractive short-range potentials, the aggregation process can be initiated by an external stimulus that leads to an increase of the depth of the secondary potential well (**Figure 1-16a**, (iii)). In this way, colloidal assemblies are stable enough and cannot be broken by thermal fluctuations. However, it should be kept in mind that stimuli do not act only on the secondary minimum, but also on the primary one and on the potential energy barrier. Accessing the primary potential energy minimum in the activated state must be avoided to prevent irreversible loss of colloidal stability (**Figure 1-16a**, (iv)). Limiting the attractive contributions allows the particles to reconfigure and find their optimum position during assembly and also spontaneous disintegration of the colloidal clusters after fuel depletion or action of antagonistic stimulus. For example, particles stabilized by electrostatic repulsion can be aggregated in the secondary minimum by increasing salt concentration (i.e., increasing the ionic strength) and disassembled upon salt dilution. However, the increase

of ionic strength also decreases the potential energy barrier, thus also favoring irreversible aggregation. For the above reasons, good control of the physical and chemical properties of the system such as particles, medium, thermal fluctuations are important to achieve reproducible and reversible assemblies of the particles. Now, it's already challenging to fine-tune the interaction potentials for equilibrium self-assembling system, introducing a time function further increases the complexity of the building block design.

1.6 Aim of This Thesis

The unique properties of the biological self-assemblies have sparked a quest of finding both an appropriate building block and a compatible reaction cycle to emulate life-like behavior at the conceptual level. Early examples of synthetic out-of-equilibrium self-assemblies primarily include supramolecular systems that form transient gels, polymers, vesicles, and micelles. Colloids are rarely used as building blocks. However, they can give rise to functional materials with unique catalytic, photonic, magnetic, and electronic properties originating not only from the positional or dimensional order of the building blocks, but also from the type of material bulk (metallic, polymeric, semiconductor, inorganic). Employing biocompatible material for their fabrication can even pave the way into biomedical applications such as drug delivery and diagnostics. They can even serve as model systems to elucidate physical concepts underlying out-of-equilibrium biological self-assemblies.

Two main challenges that are needed to be overcome to achieve successful transient assembly of colloids are:

(1) Time dependence of interparticle potentials. Already for the equilibrium self-assembly (static systems), fine tuning the interparticle potentials of colloids in terms of strength and range is a challenging task. Introducing time dependence as an additional criterion further increases the complexity of the chemical system.
(2) With increasing dimensions of the colloids: (i) the dynamics of the particles get slower; therefore, the kinetics of the activation and deactivation pathways have to be matched to these slower dynamics. If the activation pathway is quite slower than the deactivation pathway, the particles will not get enough time to activate and find and interact with each other via diffusive processes, on the other hand if deactivation pathway is very slow, the particles can undergo overactivation and fall into unnecessary kinetic traps; (ii) van der Waals forces are significantly stronger because the force scales with size and requires stronger repulsive forces to prevent irreversible aggregation and flocculation. Because of these reasons, the transient colloidal systems reported till date rely on small nanoparticle sized colloids, while studies on larger micrometer sized colloids are still sparse.

Now, it is important to realize that in the case of transient colloidal systems where active environment controls the transient structure formation, the reaction cycle partially contribute towards the overall system dynamics. Hence a simple tuning of the reaction environment can modulate lifetime and intensity of the transient assemblies. On the contrary, when building blocks themselves are the active components, the kinetics of both reaction cycle and building blocks are strongly correlated and sensitive to the type of building block used.

The aim of this thesis is to overcome some of the abovementioned challenges and present different design principles for achieving transient colloidal assemblies of micron-sized particles. I have shown systems where both building block and environment are active, as both approaches entail different challenges and hence different solutions. Some of the experimental challenges addressed in this thesis include successful functionalization of responsive groups (enzymes, DNA, etc.,.) on the particles, their density optimization to target only transient structures and avoid kinetically trapped structures and increasing colloidal stability against any minute changes in ionic strength and pH during the reaction cycle. The next section provides a detailed overview of the all the projects and overall organization of the thesis by chapters.

1.7 Thesis Outline

Motivated by the biological self-assemblies, **Chapter 1** highlights the concepts developed to introduce such autonomous behavior in artificial self-assembling and material systems. Necessary theoretical background and strategies in terms of energy landscapes for the structure formation are provided. It mainly requires developing a reversible and responsive self-assembling system and then coupling or integrating the classical system to temporally modulating CRN. Different examples based on modulating stimulus are classified: pH, redox, small hydrolyzing molecules involving both covalent/non-covalent modification of building blocks, DNA, DNA-enzyme hybrid systems.

Chapter 2 lays a conceptual foundation for **Chapter 3** by discussing different generations of pH-FS based on the coupling of acid and base producing steps in a CRN, principles of coupling such systems to self-assemblies with programmable lifetimes and highlight emerging concepts for the design of autonomous materials. The second chapter uses concepts of pH-FS (**Chapter 3**) to develop a transient colloidal system whereupon we introduce a rational design approach for chemo-structural feedback (**Figure 1-17a**). Although established and studied in biological self-assemblies, complex phenomena such as chemo-structural feedback where self-assembly itself participates in the CRN is challenging to achieve in artificial systems. We achieve this by immobilizing enzymes of a deactivating acid-producing enzymatic cascade on pH-switchable microgels that can form co-assemblies at high pH. The co-assembled state thereby brings the two enzyme partners close enough for enhanced acid generation. The amplified deactivator production (acid) leads to an almost two-fold reduction in the lifetime of the transiently formed pH-state. The system in principle utilizes all three Strategies to build transient co-assemblies. The enzymatic formation of deactivator from dormant deactivator relies on activation pathway as high pH changes the initial reference point of the enzymes where slow acid production autocatalytically pushes them eventually into their optimum range to perform the deactivation (Strategy 1).

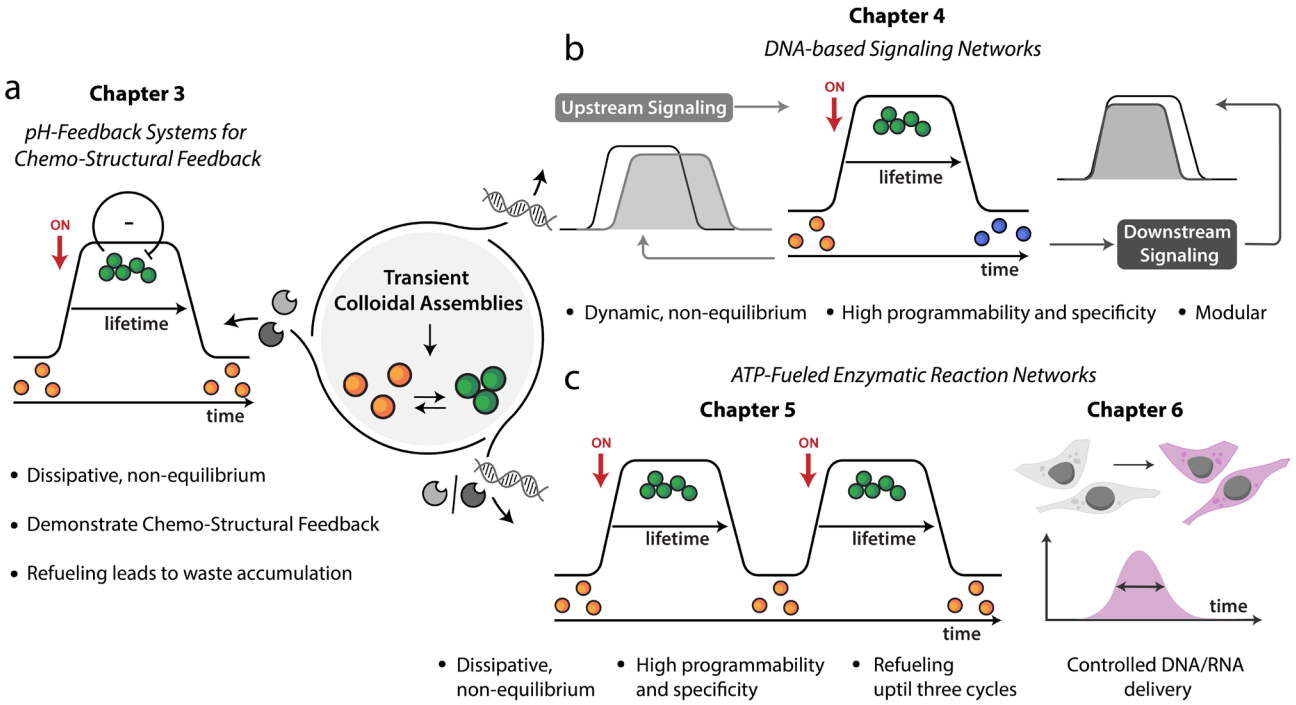

Figure 1-17. Graphical abstract of this thesis. (a) Chemo-structural feedback in pH-driven transient co-assemblies of microgels. Addition of alkaline buffer triggers transient co-assembly of two pH-responsive MGs, whereby each microgel carries one enzyme partner of the acid producing enzymatic cascade. (b) Autonomous control of microgel co-assemblies via DNA-based reaction networks. Integration with downstream signaling module results in faster inhibition of co-assemblies and an upstream module results in the modulation of onset time, delay, and increased lifetime. (c) ATP-fueled transient co-assemblies of microgels regulated by upstream antagonistic ATP-fueled ligation and restriction based enzymatic reaction network. Such non-linear networks are also installed in the culture media of HeLa cells to temporally control delivery of DNA via microgels.

The transient co-assemblies sustain as long as high pH is maintained in the system (Strategy 2) and start to degrade as soon as the deactivation reaction takes over. There is an inherent requirement of deactivation pathway to be slower than activation to (i) match the slow dynamics of the micron-scale particles and (ii) to attain a pH high enough for forming co-assemblies.

In the next chapter (**Chapter 4**), we shifted towards DNA-based reaction networks and exploited the programmability, predictability, and specificity of DNA. A TMDSD reaction cascade directs two different microgels into transient co-assemblies (**Figure 1-17b**). The microgels are functionalized with DNA and become integral part of the network. The particles transduce two orthogonally different DNA trigger strands to introduce a linker which brings two microgels together into co-assemblies. The activation pathway further forms an intermediate species which initiates the deactivation reaction (chemically decoupled using Strategy 1). The system thereby follows a complex trajectory passing through a transient state in the middle and ultimately reaching thermodynamic equilibrium. Although dynamic, the system operates under non-dissipative conditions as it resides in a new state (lowest energy state) and the original state cannot be acquired. The co-assemblies are only realized when inhibition is slower than activation (Strategy 3). The modularity of the design allows the installation of delay phases and accelerators by interconnecting modules to the upstream and downstream of the core network.

Moving away from the thermodynamically driven classic TMDSD reactions, we switched to ATP-fueled enzymatic TMDSD reaction cascade in **Chapter 5** which operates under dissipative conditions (**Figure 1-17c**, left panel). The ATP-powered ligation and restriction of DNA components transiently generates a linker strand at the molecular level which temporally controls the downstream co-assembly of microgels. The linker strand is recovered as soon as ATP is consumed (Strategy 2) disassembling the formed structures. The chemically and temporally decoupled, faster ligation and slower restriction assures transience in the system (Strategy 1 and 3). The resettling ability of the network restores the original state of the system and allows the system to be reused for subsequent cycles.

As an application, we installed the ATP-driven enzymatic reaction networks in the cell-culture media of HeLa cells for temporally controlled delivery of DNA (**Chapter 6**). The system operates at three different layers, the first layer controls the transient release of an Output strand from ATP-fueled enzymatic network (**Figure 1-17c**, right panel). Output invades the second layer and displace a Signal strand docked on microgel particle. This immobilization prevents unnecessary internalization of Signal by cells. Only upon ATP introduction, Signal is available to be uptaken by cells, the carefully chosen fluorophore labeling allows temporal tracking of DNA within cells. After ATP consumption, no Signal is available to be internalized as the system resettles to its original state. Such controlled delivery mechanisms can be proposed for specific organelle targeting for gene silencing and gene therapy applications. **Chapter 7** finally concludes with a synopsis summarizing the main results of the thesis along with the concluding remarks giving a perspective on the future advancements of the research.

1.8 References

1 Stuart, M. A. C. *et al.* Emerging applications of stimuli-responsive polymer materials. *Nat. Mater.* **9**, 101-113, doi:10.1038/nmat2614 (2010).

2 Yang, M. *et al.* Photoresponsive Actuators Built from Carbon-Based Soft Materials. *Adv. Opt. Mater.* **7**, 1900069, doi:https://doi.org/10.1002/adom.201900069 (2019).

3 Jeong, U. & Yin, Y. Smart and Responsive Micro- and Nanostructured Materials. *Adv. Funct. Mater.* **30**, 1907059, doi:https://doi.org/10.1002/adfm.201907059 (2020).

4 Hohmann, T. & Dehghani, F. The Cytoskeleton—A Complex Interacting Meshwork. *Cells* **8**, 362 (2019).

5 Merindol, R. & Walther, A. Materials learning from life: concepts for active, adaptive and autonomous molecular systems. *Chem. Soc. Rev.* **46**, 5588-5619, doi:10.1039/C6CS00738D (2017).

6 Heinen, L. & Walther, A. Celebrating Soft Matter's 10th Anniversary: Approaches to program the time domain of self-assemblies. *Soft Matter* **11**, 7857-7866, doi:10.1039/C5SM01660F (2015).

7 Sharma, C. & Walther, A. Self-Regulating Colloidal Co-Assemblies That Accelerate Their Own Destruction via Chemo-Structural Feedback. *Angew. Chem. Int. Ed.* **61**, e202201573, doi:https://doi.org/10.1002/anie.202201573 (2022).

8 Bal, S., Das, K., Ahmed, S. & Das, D. Chemically Fueled Dissipative Self-Assembly that Exploits Cooperative Catalysis. *Angew. Chem. Int. Ed.* **58**, 244-247, doi:https://doi.org/10.1002/anie.201811749 (2019).

9 Howlett, M. G., Engwerda, A. H. J., Scanes, R. J. H. & Fletcher, S. P. An autonomously oscillating supramolecular self-replicator. *Nat. Chem.* **14**, 805-810, doi:10.1038/s41557-022-00949-6 (2022).

10 Leira-Iglesias, J., Tassoni, A., Adachi, T., Stich, M. & Hermans, T. M. Oscillations, travelling fronts and patterns in a supramolecular system. *Nat. Nanotechnol.* **13**, 1021-1027, doi:10.1038/s41565-018-0270-4 (2018).

11 Boekhoven, J. *et al.* Dissipative Self-Assembly of a Molecular Gelator by Using a Chemical Fuel. *Angew. Chem. Int. Ed.* **49**, 4825-4828, doi:https://doi.org/10.1002/anie.201001511 (2010).

12 Boekhoven, J., Hendriksen, W. E., Koper, G. J., Eelkema, R. & van Esch, J. H. Transient assembly of active materials fueled by a chemical reaction. *Science* **349**, 1075-1079, doi:10.1126/science.aac6103 (2015).

13 Caplow, M., Ruhlen, R. L. & Shanks, J. The free energy for hydrolysis of a microtubule-bound nucleotide triphosphate is near zero: all of the free energy for hydrolysis is stored in the microtubule lattice. *J. Cell Biol.* **127**, 779-788, doi:10.1083/jcb.127.3.779 (1994).

14 van Ravensteijn, B. G. P., Hendriksen, W. E., Eelkema, R., van Esch, J. H. & Kegel, W. K. Fuel-Mediated Transient Clustering of Colloidal Building Blocks. *J. Am. Chem. Soc.* **139**, 9763-9766, doi:10.1021/jacs.7b03263 (2017).

15 Tena-Solsona, M. *et al.* Non-equilibrium dissipative supramolecular materials with a tunable lifetime. *Nat. Commun.* **8**, 15895, doi:10.1038/ncomms15895 (2017).

16 Tena-Solsona, M., Wanzke, C., Riess, B., Bausch, A. R. & Boekhoven, J. Self-selection of dissipative assemblies driven by primitive chemical reaction networks. *Nat. Commun.* **9**, 2044, doi:10.1038/s41467-018-04488-y (2018).

17 Rieß, B. *et al.* Dissipative assemblies that inhibit their deactivation. *Soft Matter* **14**, 4852-4859, doi:10.1039/C8SM00822A (2018).

18 Grötsch, R. K. *et al.* Pathway Dependence in the Fuel-Driven Dissipative Self-Assembly of Nanoparticles. *J. Am. Chem. Soc.* **141**, 9872-9878, doi:10.1021/jacs.9b02004 (2019).

19 Kariyawasam, L. S. & Hartley, C. S. Dissipative Assembly of Aqueous Carboxylic Acid Anhydrides Fueled by Carbodiimides. *J. Am. Chem. Soc.* **139**, 11949-11955, doi:10.1021/jacs.7b06099 (2017).

20 Kariyawasam, L. S., Kron, J. C., Jiang, R., Sommer, A. J. & Hartley, C. S. Structure–Property Effects in the Generation of Transient Aqueous Benzoic Acid Anhydrides by Carbodiimide Fuels. *J. Org. Chem.* **85**, 682-690, doi:10.1021/acs.joc.9b02746 (2020).

21 Würbser, M. A. *et al.* Chemically Fueled Block Copolymer Self-Assembly into Transient Nanoreactors**. *ChemSystemsChem* **3**, e2100015, doi:https://doi.org/10.1002/syst.202100015 (2021).

22 Grötsch, R. K. *et al.* Dissipative Self-Assembly of Photoluminescent Silicon Nanocrystals. *Angew. Chem. Int. Ed.* **57**, 14608-14612, doi:https://doi.org/10.1002/anie.201807937 (2018).

23 Chen, X. *et al.* A Carbodiimide-Fueled Reaction Cycle That Forms Transient 5(4H)-Oxazolones. *J. Am. Chem. Soc.* **145**, 6880-6887, doi:10.1021/jacs.3c00273 (2023).

24 Rowan, S. J., Cantrill, S. J., Cousins, G. R. L., Sanders, J. K. M. & Stoddart, J. F. Dynamic Covalent Chemistry. *Angew. Chem. Int. Ed.* **41**, 898-952, doi:https://doi.org/10.1002/1521-3773(20020315)41:6<898::AID-ANIE898>3.0.CO;2-E (2002).

25 Debnath, S., Roy, S. & Ulijn, R. V. Peptide Nanofibers with Dynamic Instability through Non-equilibrium Biocatalytic Assembly. *J. Am. Chem. Soc.* **135**, 16789-16792, doi:10.1021/ja4086353 (2013).

26 Pappas, C. G., Sasselli, I. R. & Ulijn, R. V. Biocatalytic Pathway Selection in Transient Tripeptide Nanostructures. *Angew. Chem. Int. Ed.* **54**, 8119-8123, doi:https://doi.org/10.1002/anie.201500867 (2015).

27 Sorrenti, A., Leira-Iglesias, J., Sato, A. & Hermans, T. M. Non-equilibrium steady states in supramolecular polymerization. *Nat. Commun.* **8**, 15899, doi:10.1038/ncomms15899 (2017).

28 Williams, N. H. Magnesium Ion Catalyzed ATP Hydrolysis. *J. Am. Chem. Soc.* **122**, 12023-12024, doi:10.1021/ja0013374 (2000).

29 Maiti, S., Fortunati, I., Ferrante, C., Scrimin, P. & Prins, L. J. Dissipative self-assembly of vesicular nanoreactors. *Nat. Chem.* **8**, 725-731, doi:10.1038/nchem.2511 (2016).

30 Pezzato, C. & Prins, L. J. Transient signal generation in a self-assembled nanosystem fueled by ATP. *Nat. Commun.* **6**, 7790, doi:10.1038/ncomms8790 (2015).

31 Mishra, A. *et al.* Biomimetic temporal self-assembly via fuel-driven controlled supramolecular polymerization. *Nat. Commun.* **9**, 1295, doi:10.1038/s41467-018-03542-z (2018).

32 Li, Z., Zeman, C. J. I. V., Valandro, S. R., Bantang, J. P. O. & Schanze, K. S. Adenosine Triphosphate Templated Self-Assembly of Cationic Porphyrin into Chiral Double Superhelices and Enzyme-Mediated Disassembly. *J. Am. Chem. Soc.* **141**, 12610-12618, doi:10.1021/jacs.9b04133 (2019).

33 Lardner, A. The effects of extracellular pH on immune function. *J. Leukoc. Biol.* **69**, 522-530 (2001).

34 Tannock, I. F. & Rotin, D. Acid pH in tumors and its potential for therapeutic exploitation. *Cancer Res.* **49**, 4373-4384 (1989).

35 Siegel, R. A. Stimuli sensitive polymers and self regulated drug delivery systems: a very partial review. *J. Control. Release.* **190**, 337-351, doi:10.1016/j.jconrel.2014.06.035 (2014).

36 Heuser, T., Steppert, A. K., Lopez, C. M., Zhu, B. & Walther, A. Generic concept to program the time domain of self-assemblies with a self-regulation mechanism. *Nano Lett.* **15**, 2213-2219, doi:10.1021/nl5039506 (2015).

37 Heuser, T., Merindol, R., Loescher, S., Klaus, A. & Walther, A. Photonic Devices Out of Equilibrium: Transient Memory, Signal Propagation, and Sensing. *Adv. Mater.* **29**, 1606842, doi:https://doi.org/10.1002/adma.201606842 (2017).

38 Fusi, G., Del Giudice, D., Skarsetz, O., Di Stefano, S. & Walther, A. Autonomous Soft Robots Empowered by Chemical Reaction Networks. *Adv. Mater.* **35**, 2209870, doi:https://doi.org/10.1002/adma.202209870 (2023).

39 Zheng, J., Qi, R., Dai, C., Li, G. & Sang, M. Enzyme Catalysis Biomotor Engineering of Neutrophils for Nanodrug Delivery and Cell-Based Thrombolytic Therapy. *ACS Nano* **16**, 2330-2344, doi:10.1021/acsnano.1c08538 (2022).

40 Jee, E., Bánsági Jr., T., Taylor, A. F. & Pojman, J. A. Temporal Control of Gelation and Polymerization Fronts Driven by an Autocatalytic Enzyme Reaction. *Angew. Chem. Int. Ed.* **55**, 2127-2131, doi:https://doi.org/10.1002/anie.201510604 (2016).

41 Panja, S. & Adams, D. J. Urea-Urease Reaction in Controlling Properties of Supramolecular Hydrogels: Pros and Cons. *Chem. Eur. J.* **27**, 8928-8939, doi:https://doi.org/10.1002/chem.202100490 (2021).

42 Che, H., Cao, S. & van Hest, J. C. M. Feedback-Induced Temporal Control of "Breathing" Polymersomes To Create Self-Adaptive Nanoreactors. *J. Am. Chem. Soc.* **140**, 5356-5359, doi:10.1021/jacs.8b02387 (2018).

43 Berrocal, J. A., Biagini, C., Mandolini, L. & Di Stefano, S. Coupling of the Decarboxylation of 2-Cyano-2-phenylpropanoic Acid to Large-Amplitude Motions: A Convenient Fuel for an Acid–Base-Operated Molecular Switch. *Angew. Chem. Int. Ed.* **55**, 6997-7001, doi:https://doi.org/10.1002/anie.201602594 (2016).

44 Biagini, C. & Di Stefano, S. Abiotic Chemical Fuels for the Operation of Molecular Machines. *Angew. Chem. Int. Ed.* **59**, 8344-8354, doi:https://doi.org/10.1002/anie.201912659 (2020).

45 Del Giudice, D. & Di Stefano, S. Dissipative Systems Driven by the Decarboxylation of Activated Carboxylic Acids. *Acc. Chem. Res.* **56**, 889-899, doi:10.1021/acs.accounts.3c00047 (2023).

46 Olivieri, E., Gasch, B., Quintard, G., Naubron, J.-V. & Quintard, A. Dissipative Acid-Fueled Reprogrammable Supramolecular Materials. *ACS Appl. Mater. Interfaces* **14**, 24720-24728, doi:10.1021/acsami.2c01608 (2022).

47 Del Giudice, D. *et al.* Time-programmable pH: decarboxylation of nitroacetic acid allows the time-controlled rising of pH to a definite value. *Chem. Sci.* **12**, 7460-7466, doi:10.1039/D1SC01196K (2021).

48 Mariottini, D., Del Giudice, D., Ercolani, G., Di Stefano, S. & Ricci, F. Dissipative operation of pH-responsive DNA-based nanodevices. *Chem. Sci.* **12**, 11735-11739, doi:10.1039/D1SC03435A (2021).

49 Jones, D. P. Redox theory of aging. *Redox Biol.* **5**, 71-79, doi:https://doi.org/10.1016/j.redox.2015.03.004 (2015).

50 Meister, A. Selective Modification of Glutathione Metabolism. *Science* **220**, 472-477, doi:doi:10.1126/science.6836290 (1983).

51 Liu, B. *et al.* Out-of-Equilibrium Self-Replication Allows Selection for Dynamic Kinetic Stability in a System of Competing Replicators. *Angew. Chem. Int. Ed.* **61**, e202117605, doi:https://doi.org/10.1002/anie.202117605 (2022).

52 Pappas, C. G. *et al.* Emergence of low-symmetry foldamers from single monomers. *Nat. Chem.* **12**, 1180-1186, doi:10.1038/s41557-020-00565-2 (2020).

53 Wojciechowski, J. P., Martin, A. D. & Thordarson, P. Kinetically Controlled Lifetimes in Redox-Responsive Transient Supramolecular Hydrogels. *J. Am. Chem. Soc.* **140**, 2869-2874, doi:10.1021/jacs.7b12198 (2018).

54 Ogden, W. A. & Guan, Z. Redox Chemical-Fueled Dissipative Self-Assembly of Active Materials. *ChemSystemsChem* **2**, e1900030, doi:https://doi.org/10.1002/syst.201900030 (2020).

55 Chowdhuri, S. *et al.* Cumulative Effect of pH and Redox Triggers on Highly Adaptive Transient Coacervates. *Chem. Eur. J.* **29**, e202203820, doi:https://doi.org/10.1002/chem.202203820 (2023).

56 Jalani, K., Das, A. D., Sasmal, R., Agasti, S. S. & George, S. J. Transient dormant monomer states for supramolecular polymers with low dispersity. *Nat. Commun.* **11**, 3967, doi:10.1038/s41467-020-17799-w (2020).

57 Jalani, K., Dhiman, S., Jain, A. & George, S. J. Temporal switching of an amphiphilic self-assembly by a chemical fuel-driven conformational response. *Chem. Sci.* **8**, 6030-6036, doi:10.1039/C7SC01730H (2017).

58 Dhiman, S., Jalani, K. & George, S. J. Redox-Mediated, Transient Supramolecular Charge-Transfer Gel and Ink. *ACS Appl. Mater. Interfaces* **12**, 5259-5264, doi:10.1021/acsami.9b17481 (2020).

59 Lang, X. *et al.* Mechanosensitive non-equilibrium supramolecular polymerization in closed chemical systems. *Nat. Commun.* **14**, 3084, doi:10.1038/s41467-023-38948-x (2023).

60 Jain, M. & Ravoo, B. J. Fuel-Driven and Enzyme-Regulated Redox-Responsive Supramolecular Hydrogels. *Angew. Chem. Int. Ed.* **60**, 21062-21068, doi:https://doi.org/10.1002/anie.202107917 (2021).

61 Spitzer, D., Rodrigues, L. L., Straßburger, D., Mezger, M. & Besenius, P. Tuneable Transient Thermogels Mediated by a pH- and Redox-Regulated Supramolecular Polymerization. *Angew. Chem. Int. Ed.* **56**, 15461-15465, doi:https://doi.org/10.1002/anie.201708857 (2017).

62 Yurke, B., Turberfield, A. J., Mills, A. P., Jr., Simmel, F. C. & Neumann, J. L. A DNA-fuelled molecular machine made of DNA. *Nature* **406**, 605-608, doi:10.1038/35020524 (2000).

63 SantaLucia, J. A unified view of polymer, dumbbell, and oligonucleotide DNA nearest-neighbor thermodynamics. *Proc. Natl. Sci. U.S.A.* **95**, 1460-1465, doi:doi:10.1073/pnas.95.4.1460 (1998).

64 Okumura, S. *et al.* Nonlinear decision-making with enzymatic neural networks. *Nature* **610**, 496-501, doi:10.1038/s41586-022-05218-7 (2022).

65 Morrison, L. E. & Stols, L. M. Sensitive fluorescence-based thermodynamic and kinetic measurements of DNA hybridization in solution. *Biochem.* **32**, 3095-3104, doi:10.1021/bi00063a022 (1993).

66 Adleman, L. M. Molecular Computation of Solutions to Combinatorial Problems. *Science* **266**, 1021-1024, doi:doi:10.1126/science.7973651 (1994).

67 Ouyang, Q., Kaplan, P. D., Liu, S. & Libchaber, A. DNA Solution of the Maximal Clique Problem. *Science* **278**, 446-449, doi:10.1126/science.278.5337.446 (1997).
68 Fu, T. *et al.* DNA-Based Dynamic Reaction Networks. *Trends Biochem. Sci.* **43**, 547-560, doi:10.1016/j.tibs.2018.04.010 (2018).
69 Lilly, J. & Camps, M. Mechanisms of Theta Plasmid Replication. *Microbiol. Spectr.* **3**, 10.1128/microbiolspec.plas-0029-2014, doi:doi:10.1128/microbiolspec.plas-0029-2014 (2015).
70 Cubero, E., Sherer, E. C., Luque, F. J., Orozco, M. & Laughton, C. A. Observation of Spontaneous Base Pair Breathing Events in the Molecular Dynamics Simulation of a Difluorotoluene-Containing DNA Oligonucleotide. *J. Am. Chem. Soc.* **121**, 8653-8654, doi:10.1021/ja991067t (1999).
71 Reynaldo, L. P., Vologodskii, A. V., Neri, B. P. & Lyamichev, V. I. The kinetics of oligonucleotide replacements. *J. Mol. Biol.* **297**, 511-520, doi:10.1006/jmbi.2000.3573 (2000).
72 Green, C. & Tibbetts, C. Reassociation rate limited displacement of DNA strands by branch migration. *Nucleic Acids Res.* **9**, 1905-1918, doi:10.1093/nar/9.8.1905 (1981).
73 Srinivas, N. *et al.* On the biophysics and kinetics of toehold-mediated DNA strand displacement. *Nucleic Acids Res.* **41**, 10641-10658, doi:10.1093/nar/gkt801 (2013).
74 Zhang, D. Y. & Winfree, E. Control of DNA Strand Displacement Kinetics Using Toehold Exchange. *J. Am. Chem. Soc.* **131**, 17303-17314, doi:10.1021/ja906987s (2009).
75 Seelig, G., Soloveichik, D., Zhang, D. Y. & Winfree, E. Enzyme-Free Nucleic Acid Logic Circuits. *Science* **314**, 1585-1588, doi:doi:10.1126/science.1132493 (2006).
76 Zhang, D. Y. & Seelig, G. Dynamic DNA nanotechnology using strand-displacement reactions. *Nat. Chem.* **3**, 103-113, doi:10.1038/nchem.957 (2011).
77 Venkataraman, S., Dirks, R. M., Rothemund, P. W. K., Winfree, E. & Pierce, N. A. An autonomous polymerization motor powered by DNA hybridization. *Nat. Nanotechnol.* **2**, 490-494, doi:10.1038/nnano.2007.225 (2007).
78 Panyutin, I. G. & Hsieh, P. The kinetics of spontaneous DNA branch migration. *Proc. Natl. Sci. U.S.A.* **91**, 2021-2025, doi:doi:10.1073/pnas.91.6.2021 (1994).
79 Zhang, D. Y., Turberfield, A. J., Yurke, B. & Winfree, E. Engineering entropy-driven reactions and networks catalyzed by DNA. *Science* **318**, 1121-1125, doi:10.1126/science.1148532 (2007).
80 Qian, L., Winfree, E. & Bruck, J. Neural network computation with DNA strand displacement cascades. *Nature* **475**, 368-372, doi:10.1038/nature10262 (2011).
81 Qian, L. & Winfree, E. Scaling Up Digital Circuit Computation with DNA Strand Displacement Cascades. *Science* **332**, 1196-1201, doi:doi:10.1126/science.1200520 (2011).
82 Alberty, R. A. & Goldberg, R. N. Standard thermodynamic formation properties for the adenosine 5'-triphosphate series. *Biochem.* **31**, 10610-10615, doi:10.1021/bi00158a025 (1992).
83 Zhao, B. *et al.* Visualizing Intercellular Tensile Forces by DNA-Based Membrane Molecular Probes. *J. Am. Chem. Soc.* **139**, 18182-18185, doi:10.1021/jacs.7b11176 (2017).
84 Yan, H., Zhang, X., Shen, Z. & Seeman, N. C. A robust DNA mechanical device controlled by hybridization topology. *Nature* **415**, 62-65, doi:10.1038/415062a (2002).
85 Srinivas, N., Parkin, J., Seelig, G., Winfree, E. & Soloveichik, D. Enzyme-free nucleic acid dynamical systems. *Science* **358**, eaal2052, doi:doi:10.1126/science.aal2052 (2017).
86 Joesaar, A. *et al.* DNA-based communication in populations of synthetic protocells. *Nat. Nanotechnol.* **14**, 369-378, doi:10.1038/s41565-019-0399-9 (2019).
87 Scalise, D., Dutta, N. & Schulman, R. DNA Strand Buffers. *J. Am. Chem. Soc.* **140**, 12069-12076, doi:10.1021/jacs.8b05373 (2018).
88 Garg, S. *et al.* Renewable Time-Responsive DNA Circuits. *Small* **14**, 1801470, doi:https://doi.org/10.1002/smll.201801470 (2018).
89 DelRosso, N. V., Hews, S., Spector, L. & Derr, N. D. A Molecular Circuit Regenerator to Implement Iterative Strand Displacement Operations. *Angew. Chem. Int. Ed.* **56**, 4443-4446, doi:https://doi.org/10.1002/anie.201610890 (2017).
90 Hahn, J. & Shih, W. M. Thermal cycling of DNA devices via associative strand displacement. *Nucleic Acids Res.* **47**, 10968-10975, doi:10.1093/nar/gkz844 (2019).

91 Gentile, S., Del Grosso, E., Prins, L. J. & Ricci, F. Autonomous and Programmable Reorganization of DNA-Based Polymers Using Redox Chemistry**. *Chem. Eur. J.* **29**, e202300394, doi:https://doi.org/10.1002/chem.202300394 (2023).

92 Grosso+, E. D. & , P. I., Serena Gentile, Leonard J. Prins, Ralf Seidel,* and Francesco Ricci. Dissipative Control over the Toehold-Mediated DNA Strand Displacement Reaction. *Angew. Chem. Int. Ed.*, doi:e202201929 (2022).

93 Zhang, X.-B., Kong, R.-M. & Lu, Y. Metal Ion Sensors Based on DNAzymes and Related DNA Molecules. *Annu. Rev. Anal. Chem.* **4**, 105-128, doi:10.1146/annurev.anchem.111808.073617 (2011).

94 Wang, J., Li, Z. & Willner, I. Cascaded dissipative DNAzyme-driven layered networks guide transient replication of coded-strands as gene models. *Nat. Commun.* **13**, 4414, doi:10.1038/s41467-022-32148-9 (2022).

95 Tyson, J. J., Chen, K. C. & Novak, B. Sniffers, buzzers, toggles and blinkers: dynamics of regulatory and signaling pathways in the cell. *Curr. Opin. Cell Biol.* **15**, 221-231, doi:https://doi.org/10.1016/S0955-0674(03)00017-6 (2003).

96 Schaffter, S. W. & Schulman, R. Building in vitro transcriptional regulatory networks by successively integrating multiple functional circuit modules. *Nat. Chem.* **11**, 829-838, doi:10.1038/s41557-019-0292-z (2019).

97 Kim, J., White, K. S. & Winfree, E. Construction of an in vitro bistable circuit from synthetic transcriptional switches. *Mol. Syst. Biol.* **2**, 68, doi:10.1038/msb4100099 (2006).

98 Dehne, H., Reitenbach, A. & Bausch, A. R. Transient self-organisation of DNA coated colloids directed by enzymatic reactions. *Sci. Rep.* **9**, 7350, doi:10.1038/s41598-019-43720-7 (2019).

99 Agarwal, S. & Franco, E. Enzyme-Driven Assembly and Disassembly of Hybrid DNA–RNA Nanotubes. *J. Am. Chem. Soc.* **141**, 7831-7841, doi:10.1021/jacs.9b01550 (2019).

100 Kim, J. & Winfree, E. Synthetic in vitro transcriptional oscillators. *Mol. Syst. Biol.* **7**, 465, doi:https://doi.org/10.1038/msb.2010.119 (2011).

101 Green, L. N. *et al.* Autonomous dynamic control of DNA nanostructure self-assembly. *Nat. Chem.* **11**, 510-520, doi:10.1038/s41557-019-0251-8 (2019).

102 Weitz, M. *et al.* Diversity in the dynamical behaviour of a compartmentalized programmable biochemical oscillator. *Nat. Chem.* **6**, 295-302, doi:10.1038/nchem.1869 (2014).

103 Dupin, A. & Simmel, F. C. Signalling and differentiation in emulsion-based multi-compartmentalized in vitro gene circuits. *Nat. Chem.* **11**, 32-39, doi:10.1038/s41557-018-0174-9 (2019).

104 Del Grosso, E. *et al.* Dissipative Control over the Toehold-Mediated DNA Strand Displacement Reaction. *Angew. Chem. Int. Ed.* **61**, e202201929, doi:https://doi.org/10.1002/anie.202201929 (2022).

105 Montagne, K., Plasson, R., Sakai, Y., Fujii, T. & Rondelez, Y. Programming an in vitro DNA oscillator using a molecular networking strategy. *Mol. Syst. Biol.* **7**, 466, doi:https://doi.org/10.1038/msb.2010.120 (2011).

106 Baccouche, A., Montagne, K., Padirac, A., Fujii, T. & Rondelez, Y. Dynamic DNA-toolbox reaction circuits: A walkthrough. *Methods* **67**, 234-249, doi:https://doi.org/10.1016/j.ymeth.2014.01.015 (2014).

107 Padirac, A., Fujii, T. & Rondelez, Y. Bottom-up construction of in vitro switchable memories. *Proc. Natl. Sci. U.S.A.* **109**, E3212-E3220, doi:doi:10.1073/pnas.1212069109 (2012).

108 Gines, G. *et al.* Microscopic agents programmed by DNA circuits. *Nat. Nanotechnol.* **12**, 351-359, doi:10.1038/nnano.2016.299 (2017).

109 Dehne, H., Reitenbach, A. & Bausch, A. R. Reversible and spatiotemporal control of colloidal structure formation. *Nat. Commun.* **12**, 6811, doi:10.1038/s41467-021-27016-x (2021).

110 Kiesling, T. *et al.* Sequence specific detection of DNA using nicking endonuclease signal amplification (NESA). *Nucleic Acids Res.* **35**, e117-e117, doi:10.1093/nar/gkm654 (2007).

111 Li, J. J., Chu, Y., Lee, B. Y.-H. & Xie, X. S. Enzymatic signal amplification of molecular beacons for sensitive DNA detection. *Nucleic Acids Res.* **36**, e36-e36, doi:10.1093/nar/gkn033 (2008).

112 Zhang, C. *et al.* Nicking-Assisted Reactant Recycle To Implement Entropy-Driven DNA Circuit. *J. Am. Chem. Soc.* **141**, 17189-17197, doi:10.1021/jacs.9b07521 (2019).

113 Zhou, Z., Ouyang, Y., Wang, J. & Willner, I. Dissipative Gated and Cascaded DNA Networks. *J. Am. Chem. Soc.* **143**, 5071-5079, doi:10.1021/jacs.1c00486 (2021).

114 Ouyang, Y., Zhang, P. & Willner, I. Dissipative biocatalytic cascades and gated transient biocatalytic cascades driven by nucleic acid networks. *Sci. Adv.* **8**, eabn3534, doi:doi:10.1126/sciadv.abn3534 (2022).

115 Ouyang, Y., Zhang, P., Manis-Levy, H., Paltiel, Y. & Willner, I. Transient Dissipative Optical Properties of Aggregated Au Nanoparticles, CdSe/ZnS Quantum Dots, and Supramolecular Nucleic Acid-Stabilized Ag Nanoclusters. *J. Am. Chem. Soc.* **143**, 17622-17632, doi:10.1021/jacs.1c07895 (2021).

116 Luo, M. *et al.* Four-Dimensional Deoxyribonucleic Acid–Gold Nanoparticle Assemblies. *Angew. Chem. Int. Ed.* **59**, 17250-17255, doi:https://doi.org/10.1002/anie.202007616 (2020).

117 Deng, J. & Walther, A. Fuel-Driven Transient DNA Strand Displacement Circuitry with Self-Resetting Function. *J. Am. Chem. Soc.* **142**, 21102-21109, doi:10.1021/jacs.0c09681 (2020).

118 Deng, J. & Walther, A. Autonomous DNA nanostructures instructed by hierarchically concatenated chemical reaction networks. *Nat. Commun.* **12**, 5132, doi:10.1038/s41467-021-25450-5 (2021).

119 Deng, J. & Walther, A. ATP-powered molecular recognition to engineer transient multivalency and self-sorting 4D hierarchical systems. *Nat. Commun.* **11**, 3658, doi:10.1038/s41467-020-17479-9 (2020).

120 Deng, J. & Walther, A. Programmable ATP-Fueled DNA Coacervates by Transient Liquid-Liquid Phase Separation. *Chem* **6**, 3329-3343, doi:https://doi.org/10.1016/j.chempr.2020.09.022 (2020).

121 Deng, J., Liu, W., Sun, M. & Walther, A. Dissipative Organization of DNA Oligomers for Transient Catalytic Function. *Angew. Chem. Int. Ed.*, e202113477, doi:10.1002/anie.202113477 (2022).

122 Luo, S. *et al.* ATP production from electricity with a new-to-nature electrobiological module. *Joule* **7**, 1745-1758, doi:https://doi.org/10.1016/j.joule.2023.07.012 (2023).

123 Liu, H., Arbing, M. A. & Bowie, J. U. Expanding the use of ethanol as a feedstock for cell-free synthetic biochemistry by implementing acetyl-CoA and ATP generating pathways. *Sci. Rep.* **12**, 7700, doi:10.1038/s41598-022-11653-3 (2022).

124 Pols, T. *et al.* A synthetic metabolic network for physicochemical homeostasis. *Nat. Commun.* **10**, 4239, doi:10.1038/s41467-019-12287-2 (2019).

125 Del Grosso, E., Amodio, A., Ragazzon, G., Prins, L. J. & Ricci, F. Dissipative Synthetic DNA-Based Receptors for the Transient Loading and Release of Molecular Cargo. *Angew. Chem. Int. Ed.* **57**, 10489-10493, doi:https://doi.org/10.1002/anie.201801318 (2018).

126 Del Grosso, E., Ragazzon, G., Prins, L. J. & Ricci, F. Fuel-Responsive Allosteric DNA-Based Aptamers for the Transient Release of ATP and Cocaine. *Angew. Chem. Int. Ed.* **58**, 5582-5586, doi:https://doi.org/10.1002/anie.201812885 (2019).

127 Ishaqat, A., Zhang, X., Liu, Q., Zheng, L. & Herrmann, A. Programming DNA Circuits for Controlled Immunostimulation through CpG Oligodeoxynucleotide Delivery. *J. Am. Chem. Soc.* **145**, 12465-12474, doi:10.1021/jacs.2c09359 (2023).

128 Kulkarni, J. A. *et al.* The current landscape of nucleic acid therapeutics. *Nat. Nanotechnol.* **16**, 630-643, doi:10.1038/s41565-021-00898-0 (2021).

129 Van Der Hofstadt, M., Galas, J. C. & Estevez-Torres, A. Spatiotemporal Patterning of Living Cells with Extracellular DNA Programs. *ACS Nano* **15**, 1741-1752, doi:10.1021/acsnano.0c09422 (2021).

130 Ämmälä, C. *et al.* Targeted delivery of antisense oligonucleotides to pancreatic β-cells. *Sci. Adv.* **4**, eaat3386, doi:doi:10.1126/sciadv.aat3386 (2018).

131 Ren, K. *et al.* A DNA dual lock-and-key strategy for cell-subtype-specific siRNA delivery. *Nat. Commun.* **7**, 13580, doi:10.1038/ncomms13580 (2016).

132 Lee, S. W. L. *et al.* MicroRNA delivery through nanoparticles. *J. Control. Release.* **313**, 80-95, doi:https://doi.org/10.1016/j.jconrel.2019.10.007 (2019).

133 Tarvirdipour, S., Skowicki, M., Schoenenberger, C. A. & Palivan, C. G. Peptide-Assisted Nucleic Acid Delivery Systems on the Rise. *Int. J. Mol. Sci.* **22**, doi:10.3390/ijms22169092 (2021).

134 Theodoor, J. & Overbeek, G. Strong and weak points in the interpretation of colloid stability. *Adv. Colloid Interface Sci.* **16**, 17-30, doi:https://doi.org/10.1016/0001-8686(82)85003-3 (1982).

135 Zhulina, E. B., Borisov, O. V. & Priamitsyn, V. A. Theory of steric stabilization of colloid dispersions by grafted polymers. *J. Colloid interface Sci.* **137**, 495-511, doi:https://doi.org/10.1016/0021-9797(90)90423-L (1990).

136 Dickinson, E. Basic principles of colloid science: By D. H. Everett, Royal Society of Chemistry, London, 1988. Paperback, pp. xv + 243, price £9.95, $ 19.50. ISBN 0-85186-443-0. *J. Chem. Technol. Biotechnol.* **45**, 328-329, doi:https://doi.org/10.1002/jctb.280450412 (1989).

137 Marshall, C. E. "Theory of the stability of lyophobic colloids. The interaction of particles having an electric double layer." E. J. W. Verwey and J. T. G. Overbeek, with the collaboration of K. van Ness. Elsevier, New York-Amsterdam, 1948, 216 pp., $4.50. *J. Polym. Sci.* **4**, 413-414, doi:https://doi.org/10.1002/pol.1949.120040321 (1949).

138 Israelachvili, J. & Pashley, R. The hydrophobic interaction is long range, decaying exponentially with distance. *Nature* **300**, 341-342, doi:10.1038/300341a0 (1982).

139 Ye, X. *et al.* Depletion interactions in colloid-polymer mixtures. *Phys. Rev. E* **54**, 6500-6510, doi:10.1103/PhysRevE.54.6500 (1996).

140 Bonn, D. *et al.* Direct Observation of Colloidal Aggregation by Critical Casimir Forces. *Phys. Rev. Lett.* **103**, 156101, doi:10.1103/PhysRevLett.103.156101 (2009).

2 pH-Feedback Systems to Program Autonomous Self-Assembly and Material Lifecycles

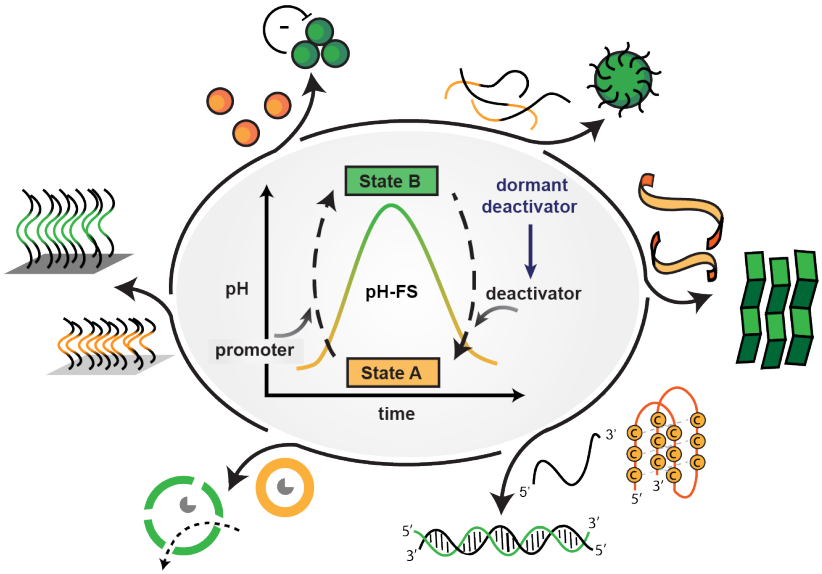

Preliminary note: *This chapter is based on the feature article published in Chem. Commun. 59, 1125-1144, doi:10.1039/D2CC06402B (2023) by* ***C. Sharma****, I. Maity, and A. Walther. Minor changes have been made concerning formatting style.*

Author contributions: C.S., I.M, and A.W conceptualized the review, C.S. and I.M wrote the first draft, C.S and A.W edited and finalized the article.

I acknowledge the efforts and creativity of previous team members working on this topic.

Abstract: pH-responsive systems have gained importance for the development of smart materials and for biomedical applications because they can switch between different states by simple acid/base triggers. However, such equilibrium systems lack the autonomous behaviour that is so ubiquitous in living systems that self-regulate out of equilibrium. As a contribution to the emerging field of autonomous chemical systems, we have developed pH feedback systems (pH-FS) based on the coupling of acid- and base-producing steps in chemical reaction networks. The resulting autonomous nonlinear pH curves can be coupled with a varietyof pH-sensitive building blocks to program the life cycles of the associated transient state at the level of self-assemblies and material systems. In this article, we discuss the different generations of such pH feedback systems, the principles of their coupling to self-assemblies with lifecycles and highlight emerging concepts for the design of autonomous functional materials. The specificity, robustness, and flexible operation of such pH-FS can also be used to realize chemical-structural and chemical-mechanical feedback that extend the behavior of such materials systems towards complex and functional life-like systems.

2.1 Introduction

Stimuli-responsiveness has been a key principle for the engineering of advanced functional soft matter and so-called smart materials.[1] It is based on the principle that a chemically or physically switchable moiety in a chemical structure leads to a change in the organization of a self-assembly (SA) or in the physical properties and functionality of a material. pH effects, or more generally acid/base reactions, have been among the key triggers, as they are easy to apply and straightforward to understand using simple principles of pK_a and pK_b values. In addition, they are important for practical applications, for example in biomedicine, where it is known that the microenvironment of tumours is more acidic, which opens up possibilities for selective delivery.[2] In smart materials applications, pH effects have been widely developed from switchable rheology modifiers to optical display applications.[3-7]

On a fundamental level, such responsive systems are typically engineered for a minimum of fatigue and to realize many switching cycles in a very robust manner. In such a switching cycle, the forward trigger, e.g., addition of acid, leads to a protonation that is followed by a SA or material property switch from State A to State B. State B will be infinitely stable until the counter-trigger (base) is given, that leads to a reversion to State A (**Figure 2-1a,b**). Often many switching cycles can be performed that are at some point challenged by the accumulation of salt from the constant neutralization. It is important to realize that such systems do typically not show any kind of more complex autonomous behavior.

In contrast, in nature, we can identify systems of formidable complexity that can perform functions in an autonomous and signal-adaptive fashion.[8] These functions are ultimately fuelled by chemical energy and regulated through feedback-controlled chemical reaction networks (CRNs).[9-11] Examples are – on a more global level – the circadian clock regulating our day/night cycles that adapt to long distance travel (jet lag) or the dissipative SA of microtubules.[12] In abstracted terms, the former is a chemical oscillator, and the latter is a chemically fuelled system. Both can only run if there is fuel in the system and high-energy non-equilibrium states are temporarily populated.

The step we took to realize pH feedback systems (pH- FS) for the design of autonomous chemical systems was to identify the conditions required to overcome the limitations of classical static responsive systems by considering the essential boundary conditions of energy-fuelled SA in microtubules (**Figure 2-1c,d**). The microtubule state can only be temporally populated if the rate of activation is larger than the rate of deactivation. Ultimately, to make a system transient, deactivation must eventually prevail. This can be accomplished by (a) allowing the deactivation reaction to gain importance over time, or (b) coupling the activation reaction with a chemical reaction that results in an unstable product under environmental conditions. The former systems are based on so-called active environments (as is the case for pH-FS), while

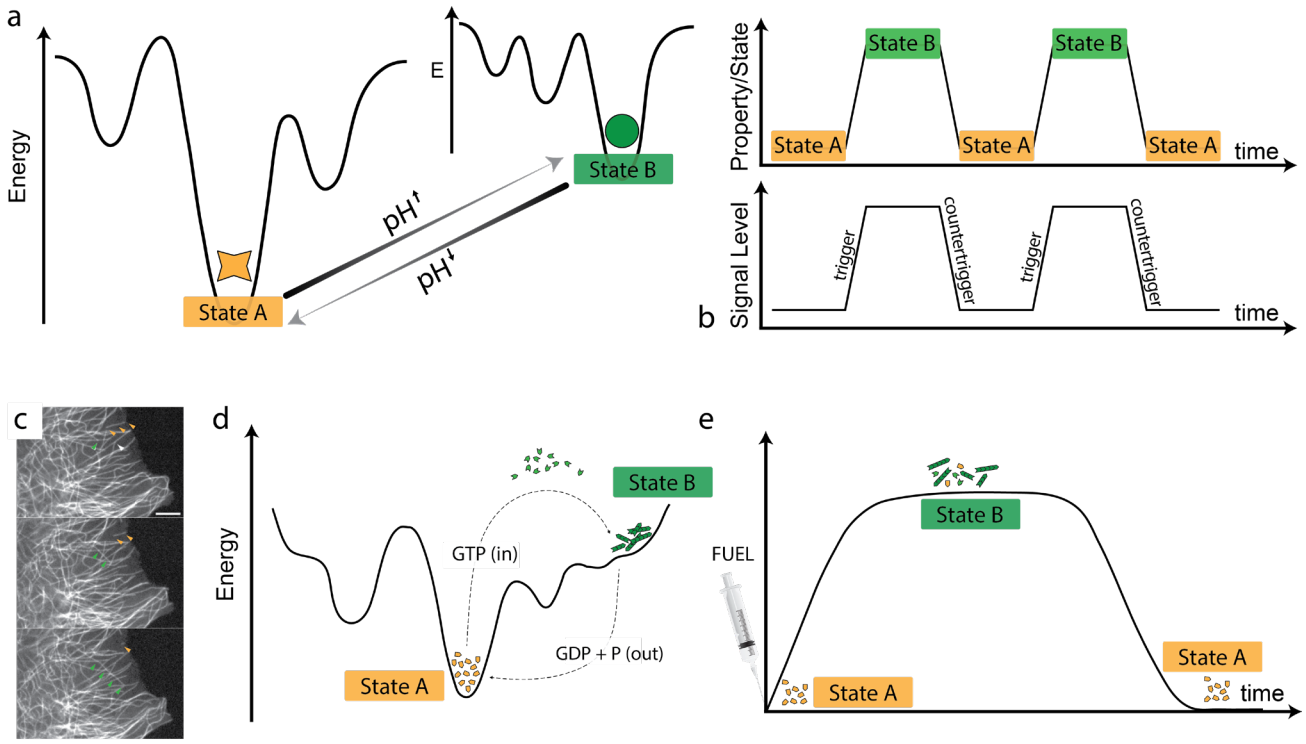

Figure 2-1. Comparison between responsive equilibrium systems and dissipative non-equilibrium self-assemblies with fuel-dependent lifetimes. (a) A classic responsive system switches between state A and state B by modulation of the energy landscapes upon application of a trigger (in this case pH). (b) Multiple switching cycles can be performed featuring little to no fatigue. (c-d) Microtubules as chemically fueled energy-dissipative systems where the assembled state B is maintained by constant influx and dissipation of chemical energy (guanosine triphosphate, GTP). (e) Lifetimes can be controlled by the amount of chemical fuel.

the latter are chemically fuelled active structures.[13-16] In both cases an autonomous system with limited lifetimes is formed, where hidden chemical energy sources are used over time. Concepts of CRNs apply in both cases.

We have been developing pH-FSs based on these kinetic boundary conditions by first introducing the concept of dormant deactivators (DD; e.g., esters) that only release active deactivators (e.g., acids) over time to make transient basic pH-feedback loops when combined with basic buffers as activators and when starting from an acidic pH value. We extended these strategies to (i) the combination with more complex pH-regulatory effects using pH-modulating enzymes with pH-dependent activity curves, (ii) the combination of antagonistic enzymes, and (iii) enzymatic cascades (EC). These additional modules lead to new behaviour, higher levels of non-linearities in the chemistry of the CRN, and thereby also to an increased non-equilibrium behaviour on a CRN system level. The kinetics can be additionally tuned by compartmentalization of acid- and base-producing enzymes. The key step towards using the resulting non-linear pH-curves of the pH-FS for materials and SA lifecycle programming is the fact that pH-switchable systems[2-7,17,18] are highly developed and can be coupled as a system load into the pH-FS. We could demonstrate this for a vast range of building blocks for SAs and couple it to relevant effects for autonomous materials design.[19-27]

In this feature article, we will highlight some history of pH-feedback-driven chemistry and oscillations, discuss the basic ideas of programming pH-FSs, and discuss what kind of SAs and material effects could be realized thus far. At selected points, we also highlight systems of other groups. We will finish with a succinct outlook on possible future applications of such systems.

2.2 History of oscillatory reaction networks and pH-feedback reactions

Half a century ago, far-from-equilibrium phenomena in synthetic systems were rare, poorly understood, and underappreciated. This changed slowly after the introduction of the Belousov–Zhabotinsky reaction[28], which displayed oscillating behaviour and spatiotemporal pattern formation in a feedback-controlled CRN. After 1980, the field of far-from-equilibrium thermodynamics progressively expanded in both experiment and theory with the aim of proper understanding of such feedback-assisted non-linear chemical phenomena, but most of the progress was made for inorganic CRNs. Till to date, more than 200 variants of chemical oscillators have been reported, and they cover all fields from classical inorganic redox oscillators to small molecule organic ones to proteins and DNA.[29-32]

pH oscillators are an interesting subgroup that has attracted much attention because of their ability to exhibit nonlinear temporal and spatial phenomena. The first pH-oscillator was discovered by Epstein and co-workers while studying a non-halogen chemical oscillator system (sulfide ion-H_2O_2) which displayed bistability and oscillated between acidic and basic pH.[33] Since this serendipitous discovery, the number of pH-oscillators has grown rapidly. All the known pH-oscillators are found to contain two antagonistic key reactions pathways involving H^+: one reaction autocatalytically produces H^+ providing the positive-feedback while the other consumes H^+ in a slow process providing the negative feedback with a sufficient delay time. The pH-oscillators in inorganic CRNs can be categorised into two main groups: one-substrate systems and two-substrate systems (**Figure 2-2**).

One-substrate pH-oscillators[33-38] comprise an oxidant (Ox) and a single reductant (Red), which follow two pathways (i.e., partial oxidation and total oxidation) depending on the initial pH and stoichiometry of the components (**Figure 2-2a,c**). Partial oxidation is an inhibitory step where Ox and Red react with each other consuming the H^+ in the system and producing a stable intermediate (Int; **Figure 2-2a**, left blue panel). The consumption of H^+ rises the pH of the system. Upon increase in pH, the partial oxidation slows down gradually and then at some point stops essentially. Additionally, the high pH environment allows the system to proceed through an alternative route, in which the preformed Int and Red undergoes total oxidation upon reacting with Ox (**Figure 2-2a**, right red panel). In this step, the autocatalytic production of H^+ effectively increases the concentration of H^+ and reverts the system to its original low pH value. Thus, this pH cycle is repeated with time in a flow reactor.

On the contrary, two-substrate systems[39-44] contain an Ox and two other substrates (**Figure 2-2b,d**). Among the two substrates, one is a Red and the other could be either a Red, or other H^+-consuming components like conjugate acid–base pairs or organic species. In this mechanism, the 1st step leads to an autocatalytic production of H^+ which occurs through the total oxidation of substrate 1 (S_1, always a Red) by Ox (**Figure 2-2b**, right red panel). Thereafter, the resulting acidic environment initiates the 2nd oxidation or neutralisation pathway in which H^+ produced in the 1st step is consumed largely by the reaction between Ox and substrate 2 (S_2) (**Figure 2-2b**, left blue panel). Thereby, the system periodically reaches the high and low pH states in a flow reactor. Furthermore, some arguments exist on some special cases whether they are true pH-driven oscillators or not (**Figure 2-2e**). Although H^+-producing and consuming steps are seen, no autocatalysis pathway has been identified so far.[45-48]

Towards higher complexity in inorganic networks, multi-feedback pH-oscillation systems, oscillation amplification, oscillation elimination,[49] beat phenomenon,[50] and synchronization[51] were achieved successfully in recent years. Subsequently, moving towards organic CRNs, Taylor and co-workers introduced the first experimental example of an organic-based pH-oscillator utilizing the base-catalysed dehydration of methylene glycol as a source of positive feedback (OH^- autocatalysis) coupled with the base-catalysed hydrolysis of gluconic acid δ-lactone (δ-GL) for negative feedback (H^+ production). In this design, the pH oscillated between pH 7 and 10.[48]

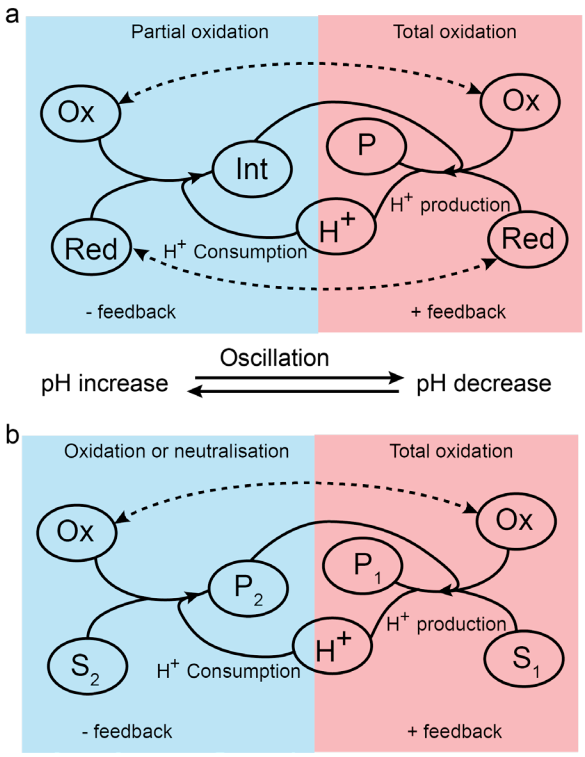

c One-substrate pH-oscillator

Entry	Oxidant	Reductant	pH range	Ref
1.	H_2O_2	S^{2-}	6.0-8.0	33
2.	IO_4^-	NH_2OH	4.0-6.0	34
3.	BrO_2^-	I^-	6.0-8.2	35
4.	BrO_3^-	SO_3^{2-} (Mn^{2+})	3.5-7.2	36
5.	H_2O_2	$S_2O_4^{2-}$	3.5-9.5	37
6.	H_2O_2	$S_2O_3^{2-}$ (Cu^{2+})	4.9-8.5	38

d Two-substrate pH-oscillator

Entry	Oxidant	Reductant	2nd Substrate	pH range	Ref
1.	IO_3^-	SO_3^{2-}	$Fe(CN)_6^{4-}$	3.0-7.3	39
2.	IO_3^-	SO_3^{2-}	$S_2O_3^{2-}$	5.0-7.0	40
3.	BrO_3^-	SO_3^{2-}	$Fe(CN)_6^{4-}$	2.7-6.2	41
4.	BrO_2^-	$S_2O_3^{2-}$	C_6H_6OH	4.5-7.5	42
5.	BrO_2^-	NH_2OH	C_6H_6OH	4.5-7.5	43
6.	H_2O_2	SO_3^{2-}	Na_2CO_3	5.0-7.0	44

e Special pH-oscillator

Entry	Composition	pH range	Ref
1.	H_2O_2, $Fe(CN)_6^{4-}$	5.0-7.0	45
2.	ClO_2^-, SO_3^{2-}	5.9-7.9	46
3.	$S_2O_4^{2-}$,H_2O	4.9-6.3	47
4.	HCHO, SO_3^{2-},Gluconolactone	7.2-10	48

Ox : Oxidant; Red : Reductant; Int : Intermediate; P : Product
S_1 : Reductant (Substrate 1); S_2 : Substrate 2

Figure 2-2. Examples of pH-oscillators. CRN topology and feedbacks process in (a) a one-substrate pH-oscillatory system and (b) a two-substrate pH-oscillatory system. A few examples for (c) one-substrate pH-oscillators, (d) two-substrate pH-oscillators and (e) special pH-oscillators.

Oscillatory behaviour is ubiquitous in living systems and is largely associated with enzyme-catalysed reactions.[52] Thus, designing enzymatic pH-feedback mechanisms and oscillators is attractive because they can mimic living systems and are helpful in conceptual understanding of complex dynamic networks in cellular systems such as glycolytic oscillations, circadian rhythms, and others. For instance, enzymes were coupled with inorganic pH-oscillators with the aim for modification of the existing chemical pH-oscillator by influencing one inherent feedback module of the inorganic systems.[53] Moreover, a flip flop circuit with a bistable pH-modulating system was designed with switching between pH 6.8 and 9.6 using a logic gate with biochemical CRNs.[54] This system was based on the reaction between glucose and the enzyme glucose dehydrogenase producing H^+, which was coupled with a H^+-consumption pathway involving an antagonistic reaction between acetaldehyde and alcohol dehydrogenase to increase the pH of the system.

Ester/ lactone	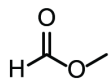	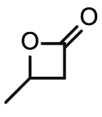	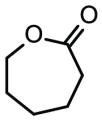	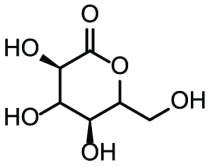	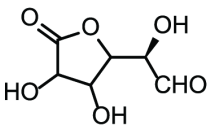
	Methyl formate (MF)	β-Butyrolactone (β-BL)	ε-Caprolactone (ε-CL)	D-(+)-Gluconic acid δ-lactone (δ-GL)	D-(+)-Glucoronic acid γ-lactone (γ-GL)
p*K*a:	3.77	4.11	4.88	3.70	3.77
solubility$_{H_2O}$:	> 300 g/L	>15.3 g/L	fully immiscible	>500 g/L	>948 g/L

Table 2-1. List of dormant deactivators (DDs) that slowly form acids together with their solubility in water and the pK_a values of their corresponding acids.

However, to date the urease/urea couple is probably the most widely studied pH-modulating system with inherent feedback. The inherent feedback is caused by the bell-shaped activity curve of the enzymatic activity as a function of pH. Urease, like many other enzymes, has maximum activity at pH 7, and significantly less activity at high and low pH.[26] This means that, starting from low pH, the formation of NH_3 and CO_2 by the conversion of the fuel/substrate (urea) leads to autocatalytic self-acceleration. Once the maximum at ca. pH 7 is crossed, continued production of base leads to a shift outside of the activity window and thus to negative feedback concerning the rate of fuel conversion. This nonlinear pH-dependent activity is central to achieve non-linear kinetic phenomena needed for bistability and oscillations. For instance, Taylor, Pojman and co-workers demonstrated pH wave fronts, bifurcation, bistability and oscillations.[55-58] Urease has also been an enzyme of choice to design pH-FSs for temporal programming of autonomous lifecycles that we are going to discuss in this article.

2.3 Basics of programming pH-feedback lifecycles

In principle, programming the lifetime of SAs or materials using active environments requires a delicate temporal balance between two antagonistic triggers (activation v_1, deactivation v_2) to generate a temporally non-linear response. The addition of a positive stimulus drives the system from State A to a transient State B, and subsequently, a negative stimulus is needed to bring the system back to its original State A. Notably, the deactivation process must be delayed, and the time lag until deactivation becomes effective will determine the lifetime of the transient state (State B). Achieving this time delay in an autonomous fashion requires the activation and deactivation processes to be completely decoupled - either temporally, spatially, or chemically - or coupled into appropriate feedback-controlled CRNs.

The key problem when aiming for an autonomous regulation of the lifetimes of pH-switchable SAs is the fact that the two primary antagonistic triggers, H^+ and OH^-, cannot be added simultaneously as direct triggers as they would simply annihilate each other. This would not lead to an active environment with a programmable time signature. To address this problem, we have invented and developed several generic pH- FS approaches that can be coupled to virtually all pH-triggered SAs and materials that function in the respective pH regimes(**Figure 2-3**). Those pH-FSs have been advanced across different generations. Generation 1 aimed for an almost complete kinetic decoupling between a quickly acting activator and a slowly acting DD. Generation 2 introduced a pH-modulating enzyme with a pH-dependent activity curve to include distinct feedback. Generation 3 expanded the concept to two antagonistic pH-modulating enzymes that could allow for flip-flop programming of pH-profiles and allowed to install lag times. Finally, generation 4 refers to spatially immobilized enzymes (e.g., in gel layers), whereby additional diffusion obstacles are implemented to tune the kinetics of the pH-profile of a supernatant solution orthogonal to the CRN.

Generation 1: In the first generation, we aimed for an almost complete decoupling of the activation and deactivation pathways by introducing a DD (**Figure 2-3a**). As the name suggests, the DD only decays slowly (v^*) to liberate the active deactivator. Such DD compounds can for example be esters or lactones that slowly hydrolyse in water to give acids (**Table 2-1**) or urea which undergoes enzymatic catalysis to produce ammonia. This means that the stringent kinetic boundary conditions to achieve transient states are simplified to $v_1 > v^*$. Simultaneous addition of both activator (e.g., an alkaline buffer) and DD (e.g., an ester) leads to an alkaline pH-flip. Even though the strategy aimed for a complete kinetic decoupling of the activation and deactivation pathways, it is important to bear in mind that the decay rate/hydrolysis of the DD (v^*) is pH-dependent. It is high at high pH, low at intermediate pH and autocatalytically accelerated at low pH. Hence there is a simple background CRN, but we later will discuss more important coupling effects.

To demonstrate the concept, we targeted a transient alkaline pH-FS by simultaneous injection of a basic activator and the acid-generating DDs.[22] In principle, either a base or an alkaline buffer can be used, but experimentally it is highly preferable to choose a buffer substance, because this leads to a pH jump to a defined

pH value, which itself sets the starting kinetics for the hydrolysis of the DD. Additionally, it is possible to extend the lifetime of the plateau quite easily by increasing the buffer capacity without changing the pH value. This leads to a much higher programmability of the system as compared to using different concentrations of a base. The temporal signature of the pH-profile can be programmed further using different DDs, that is lactones or ester, which are differently activated towards hydrolysis, and which have different pK_a values of the liberated acid (**Table 2-1**). By changing the concentration of both components (activator vs. DD) and changing to different DDs, the resulting transient lifetimes can be tuned from minutes to days. The magnitude of the pH jump is mainly a function of the used buffer and the starting pH.

Generation 2: Following up on the first report, we developed a more advanced feedback-controlled pH-FSs in the acidic regime.[23] Therein the generation of the active deactivator (now a base) was realized using the enzyme urease that converts urea to NH_3 and CO_2 (**Figure 2-3b**). In combination with an acidic promoter (again a buffer) transient acidic pH-feedback loops could be realized. In stark contrast to the previous design, urease is associated with a more defined CRN topology and with a kinetic advantage.[57] First of all, by changing from a "self-decaying" DD to a catalytically converted DD, it is clear that the time signature of the overall process depends on the concentration of the enzyme. This catalytic control represents a practical advantage for programming the temporal signature as the time stamp can be designed independently of the fuel concentration (urea; as long as there is enough for the pH change). Moreover, urease has a bell-shaped activity profile with close-to-zero activity in alkaline and acidic pH. This means that systems can be designed at high (and low) pH, where the enzyme can hardly process the fuel, i.e., fully dormant system. However, starting from high pH, injection of the acidic promoter to a pH of ca. 3.5 (which is used to trigger an acid/base responsive system later on), the non-linear pH dependence activates the urease from a nearly inactive alkaline state (pH > 9) to an active acidic state (pH = 3.5). This not only activates a coupled SA, but also activates the urease to produce base. Due to the self-acceleration (positive feedback on the left side of the pH curve) the pH-feedback proceeds sharply across the neutral pH regime, whereupon the urease leaves its activity window and forms an $(NH_4)_2CO_3$ buffer at high pH. Thereby the acidic promoter not only activates the SA, but also activates its internal urease/urea kill switch.

Moving forward in this direction, we installed an acid-producing EC regulating a transient alkaline pH state. [24] As a proof of concept, two ECs, namely (a) Invertase (INV)/Glucose Oxidase (GOX) and (b) β-Galactosidase (β-GAL)/Glucose Oxidase (GOX) were chosen (**Figure 2-3c**). INV catalyses the hydrolysis of sucrose to glucose and fructose, whereafter GOX catalyses glucose to δ-GL, which spontaneously breaks down to gluconic acid, the final acid of the EC. Similarly, the β-GAL/GOX EC catalyses the tandem conversion of lactose to gluconic acid with glucose as an intermediate. Interestingly, all three enzymes show bell-shaped activity curves and inherent pH-feedback on their activity. This means the deactivation step experiences self-acceleration (positive feedback) arising from the EC's metabolic chains, which lead to a fast pH decay starting from an alkaline pH regime. In contrast to the single-enzyme pH-FS above, the pH-dependent lifecycles of the ECs are regulated concerning their K_m (Michaelis-Menten constant) of the downstream GOX. In the case of the INV/GOX EC, the wide pH-dependent activity maximum of INV pushes the glucose concentration above the K_m of GOX. In contrast, the β-GAL/GOX EC leaves the glucose concentration below the K_m of GOX at low concentrations of β-GAL, whereas when fed with enough β-GAL and lactose, the intermediate glucose concentration is pushed above the K_m of GOX. To summarize, individual enzyme concentrations and tuning respective turnover numbers affect the performance of the EC and the pH-FS as a whole. This provides an extra layer of complexity and control.

Generation 3: Till now, we described the regulation of transient pH states in both the acidic and basic regimes and introduced catalytic control mechanisms with feedback operation. Both generations 1 and 2 however make use of a rapid activator (acidic or alkaline buffer). We hypothesized that higher flexibility and better

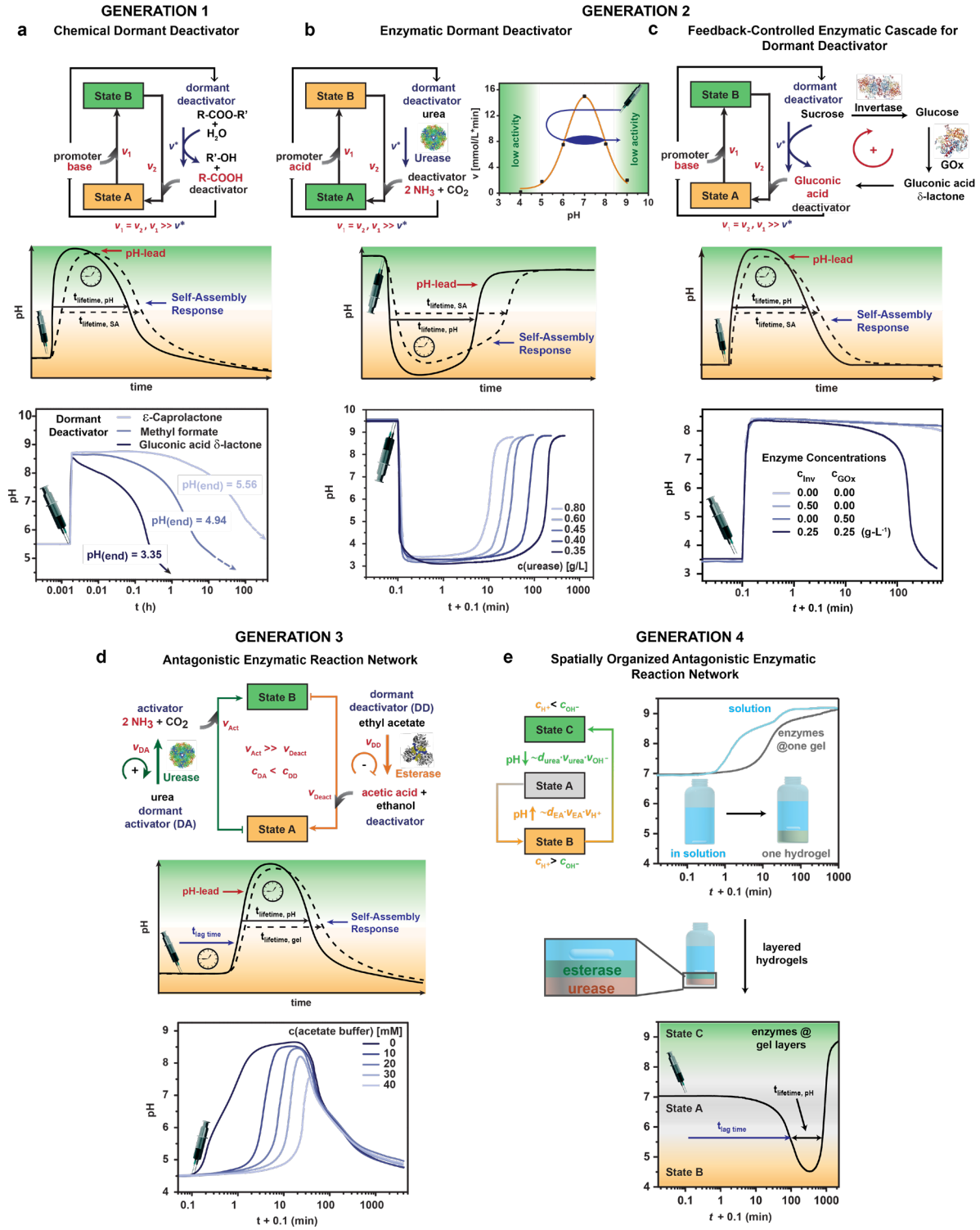

Figure 2-3. Different generations of pH-FS. (a) Generation 1 pH-FS featuring kinetic decoupling by combining a fast activator and a chemical DD. (b) Generation 2 pH-FS employ a pH-modulating enzyme or EC for the conversion of DDs into active deactivators. (d) Generation 3 pH-FS is composed of two antagonistic feedback-controlled enzymatic reactions. For instance, urease catalyses the conversion of urea (DA) into base while esterase transforms ethyl acetate (DD) into active acid. Lag times can be programmed using a buffer substance at the start pH. (e) Generation 4 highlights compartmentalization of two antagonistic enzymatic reactions to add additional diffusion processes for substrates and pH effectors to further control the lifecycles.

system control features would be in reach if we were to combine the concept of the dormant/slow deactivator together with a dormant activator (DA; **Figure 2-3d**).[19] To this end, we combined an acid-producing enzyme (e.g. esterase) together with a base-producing enzyme (e.g. urease). In principle, we envisaged that by

changing the ratios of both enzymes, it should be possible to either obtain a transient alkaline or a transient acidic pH-FS at the same fuel concentrations (ester vs. urea) because each reaction speed can be selectively accelerated. In fact, due to the mismatch of the pH-dependent activity profiles of both enzymes, it was however only possible to reliably program transient alkaline pH-FSs. Such a system was for instance obtained by setting up a system containing both enzymes at an initial pH of 4.5 in sodium acetate/acetic acid buffer (NaOAc/AcOH), followed by simultaneous addition of urea (DA) and alkyl acetic acid esters (DD). At this low pH, both enzymes remain almost inactive, but, because of the higher turnover rate of urease, ammonia begins to produce. The base generation self-accelerates (positive feedback) and leads to a steep pH jump. Meanwhile, esterase enters its activity range, and both enzymes operate. The overall pH continues to increase (higher urease activity) until it reaches pH 9, which marks the formation of the $(NH_4)_2CO_3$ buffer. The esterase reaction becomes dominant once the DA (urea) is sufficiently consumed. The esterase, being highly active in the alkaline state, initiates the return to the acidic state by excess formation of acetic acid. The pH decay is comparatively slower than the pH increase because of the lower activity of the esterase. The rate further decreases once the pH reaches a value of 6.5 as the esterase moves out of its activity window owing to its self-deactivating acid production (negative feedback). Finally, the system reaches a pH of ca. 4.8 in the NaOAc/AcOH buffer region.

However, one of the most important system advantages of using a DA with DD is that adding a buffer at the starting pH allows for a lag time as both effectors (acid or base) are produced slowly. Thus, the buffer capacity first needs to be overcome before the pH increase sets in. This allows to program a lag time before the transient pH-profile starts to emerge. This critically extends the concept of transient lifetimes to full lifecycles including control over the lag time.

Generation 4: It is clear from the above discussion that enzyme concentrations are decisive to program the lifetimes of transient pH states. However, limitations remain. For instance, the combination esterase-urease cannot be used to reliably program transient acidic pH-FSs, as the urease is more powerful and because there is a mismatch of the pH-dependent activity profiles. Hence, we raised the question, how can we control such lifetimes and even the associated lag times at constant enzyme concentrations? To this end, we introduced spatial control by compartmentalizing two antagonistic enzymes (urease and esterase) within separate gel layers, and even adding a dummy gel layer as additional diffusion obstacle between them (**Figure 2-3e**).[25] This multilayer strategy introduced temporal effects based on diffusion of fuel and pH effector, that are of critical relevance to the system behaviour. Indeed, three main effects were observed: (i) It is now possible to program acidic pH-profiles when the esterase is the top gel layer and hence reacts first with the ester fuel, (ii) varying the height of the individual enzyme layers (hence the diffusion pathways of fuel and products) allows to pre-design the magnitude of the pH dive, the lifetimes and the lag times of the pH-profiles, which is qualitatively similar to changing the enzyme and substrate concentrations, and, (iii) finally, embedding a dummy gel layer between two active gel layers offers orthogonal ways to program the lifecycles and to chemically separate enzymatic reactions and potentially interference between them.

2.4 Programming self-assemblies and materials with lifecycles

This section will describe some important examples for coupling pH-FSs to SAs to encode a self-regulatory mechanism on a system level. To satisfy the coupling conditions for transient SAs, a pH-switchable SA needs to be in state A and couple with a transition within the pH jump or pH dive to reach state B in a transient fashion. These coupled systems act like a load on the pristine pH-FS. The concentration and pK_a value associated with the SA contribute a buffer capacity and introduce a delay in the response. We will discuss different systems by first classifying them among different building blocks (e.g., block copolymers, peptides, nanoparticles, DNA and microparticles), while later discussing selected material aspects. Certainly, there are

no strict boundaries between the different subtopics as for instance peptide fibrils are building blocks for hydrogels and DNA can be used to assemble nanoparticles.

2.4.1 Block copolymers

The concept for temporal programming of SAs was first demonstrated for block copolymers (BCPs; **Figure 2-4**).[22] These BCPs were composed of a pH-switchable poly(diethylaminoethyl methacrylate) (PDEAEMA) block with a p*K*a ≈ 7.2 and different non-charged and permanently hydrophilic blocks. Based on the weight fractions of PDEAEMA, such BCPs can self-assemble into spherical micelles or vesicles (Figure 2-4a). Temporal programming was achieved by combining these BCPs with the generation 1 pH-FS using simultaneous co-injection of the promoter, Tris-buffer (pH = 8.8), and δ-GL as DD to a BCP solution at a starting pH ≈ 5.0. Detailed investigations for the system forming transient micelles revealed distinct differences between the pure pH-FS and the BCP-coupled pH-FS system (**Figure 2-4b-d**). First, the pH jump is reduced in the presence of the BCP, because OH^- ions of the promoter are scavenged by the DEAEMA-H^+ units. Second, a brief plateau during the pH decay is visible, which corresponds to the pK_a of DEAEMA and its buffering capacity. Simultaneous monitoring of the light scattering intensity ($I_{90°}$) allowed to trace the transient formation of the micelles by displaying a plateau-like profile (**Figure 2-4b**). This scattering curve lags somewhat behind the pH evolution due to kinetic retardations in the physical transformation involved (i.e., disassembly). Size distributions of the aggregates by Dynamic Light Scattering (DLS, **Figure 2-4c**) and cryogenic transmission electron microscopy imaging (cryo-TEM, **Figure 2-4f**)) corroborated the formation of transient micelles. Repeated transient SAs upon re-injection of the pH-FS were also possible.

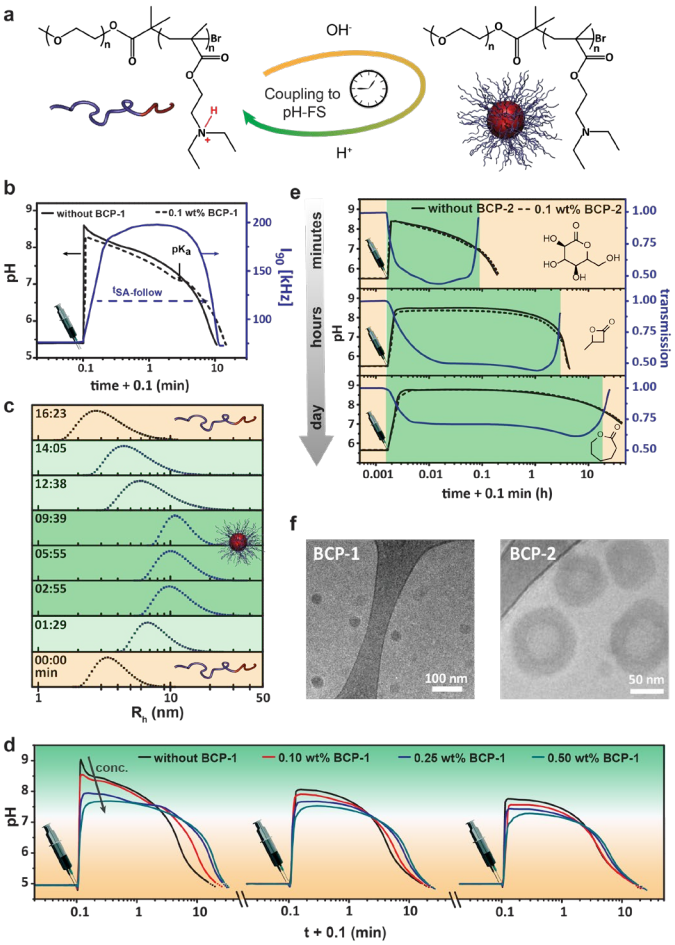

Figure 2-4. Temporal programming of self-regulating BCP SAs using generation 1 pH-FS. (a) Unimer-micelle-unimer transition of BCP-1 as a response to the pH-FS, tracked by (b) pH measurements and scattering intensity at 90° ($I_{90°}$) and (c) hydrodynamic radius distributions. (d) Repeated pH jumps for different concentrations of BCP-1. (e) Effect of chemical structure of the DD on the lifetimes of transient vesicles formed from BCP-2. (f) Cryo-TEM images of micellar (BCP-1) and vesicular (BCP-2) morphologies. Adapted and reprinted with permission from ref. 22 Copyright 2015 American Chemical Society.

As expected from above discussion, a decrease in the pH jump is observed with increasing the BCP concentration. This also led to longer lifetimes due to (i) slower ester hydrolysis at lower pH jumps and (ii) increasing the buffering capacity due to the DEAEMA units during the autonomous pH decrease (**Figure 2-4d**). Repeated injections of the pH-FS are also possible for different concentrations of the BCPs (**Figure 2-4d**). A

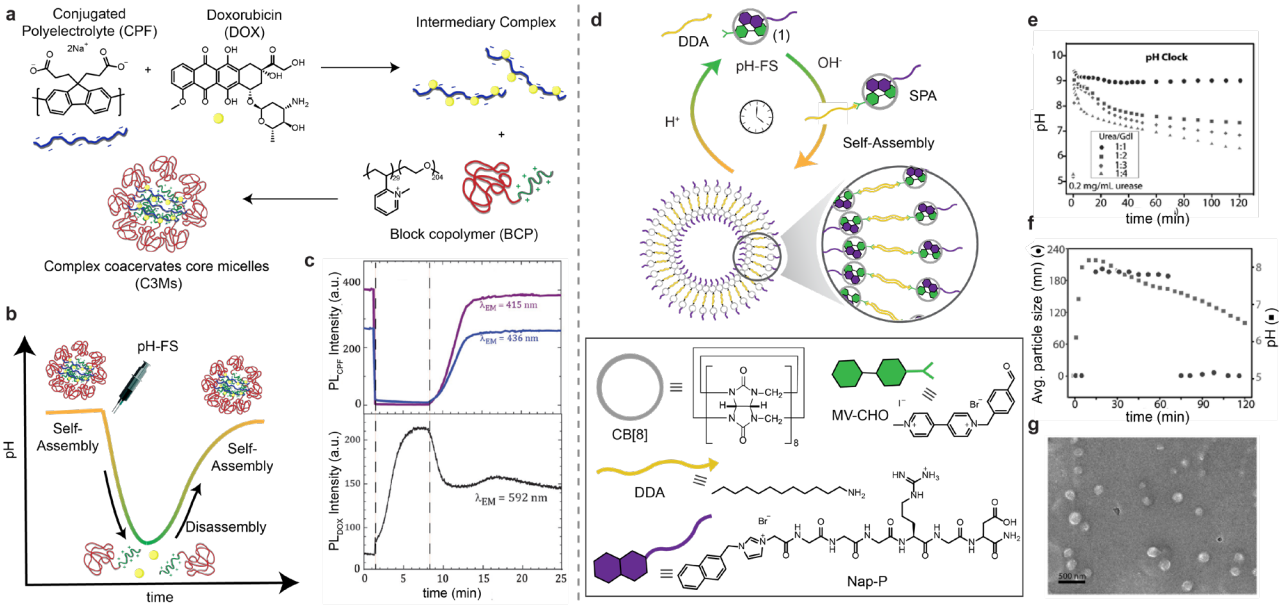

Figure 2-5. Temporal programming of transient SAs of other polymer systems. (a-c) Transient SA of C3Ms by coupling with a pH-FS producing a transient acidic state.[9] (c) Fluorimetric monitoring of transient states. (d-g) Transient SA of a CB[8]-assisted supramolecular peptide amphiphile and its vesicles followed by (e) pH measurements at four different urea/δ-GL, (f) DLS and (g) SEM. Adapted and reprinted with permission from ref. 61 Copyright 2018 John Wiley & Sons. Reproduced under terms of the CC-BY license, ref. 62 Copyright 2019, published by Royal Society of Chemistry.

change of the DD to less activated DDs (i.e., from δ-GL to β-butyrolactone (β-BL) and ε-caprolactone could then stretch out the lifetimes to hours or days, as shown for the vesicle-forming block copolymer (**Figure 2-4e**).

Related pH-FSs were subsequently used to program other SAs from the BCP and polymer amphiphile fields.[59,60] For instance, Voets and co-workers showed the transient disassembly of complex coacervate core micelles (C3M).[61] These C3Ms were formed by electrostatic co-assembly of a weak, anionic polyelectrolyte (CPF) and a cationic BCP at high pH and underwent disassembly at low pH (**Figure 2-5a**). Their temporal disassembly was obtained by combination with a transient acidic pH-FS using sodium citrate (Na_3C)/citric acid (CA) buffer as a rapid promoter and the urease/urea switch as deactivation process, starting from an initial pH of 9.2 (**Figure 2-5b**). Due to the presence of a specific fluorescence sensor and a p-conjugated anionic polyelectrolyte, the overall process could be followed by *in situ* fluorescence spectroscopy (**Figure 2-5c**).

Similarly, transient formation of a supramolecular peptide amphiphile (SPA) and their subsequent vesicular assembly could be triggered by simultaneous addition of urea (DA), and δ-GL (DD) to an aqueous solution of urease containing all the building blocks (**Figure 2-5d**).[62] The construction of the SPA was assisted by a pH-responsive imine bond formation between dodecylamine (DDA) and a ternary complex (1) of cucurbit[8]uril (CB[8]) with viologen (MV-CHO) and a naphthalene functionalized peptide (Nap-P).

2.4.2 Peptide systems and the transition to hydrogels

One may raise the question to what extent more delicate SAs such as pH-switchable fibril-forming peptides, supramolecular systems or even DNA may be programmable using such pH-FSs that contain a diversity of additional components. To this end, we first turned to an oligopeptide which contains primary amines (**Figure 2-6a**).[22] The oligopeptide chosen undergoes a isotropic-nematic transition (fluids or gels depending upon the concentration of peptide) upon base-induced nano-fibrillization by switching its conformation from coils to β-sheets at a pH ≈ 7.6 (**Figure 2-6b,d**). The oligopeptide was coupled to a pH-FS with a transient alkaline pH state

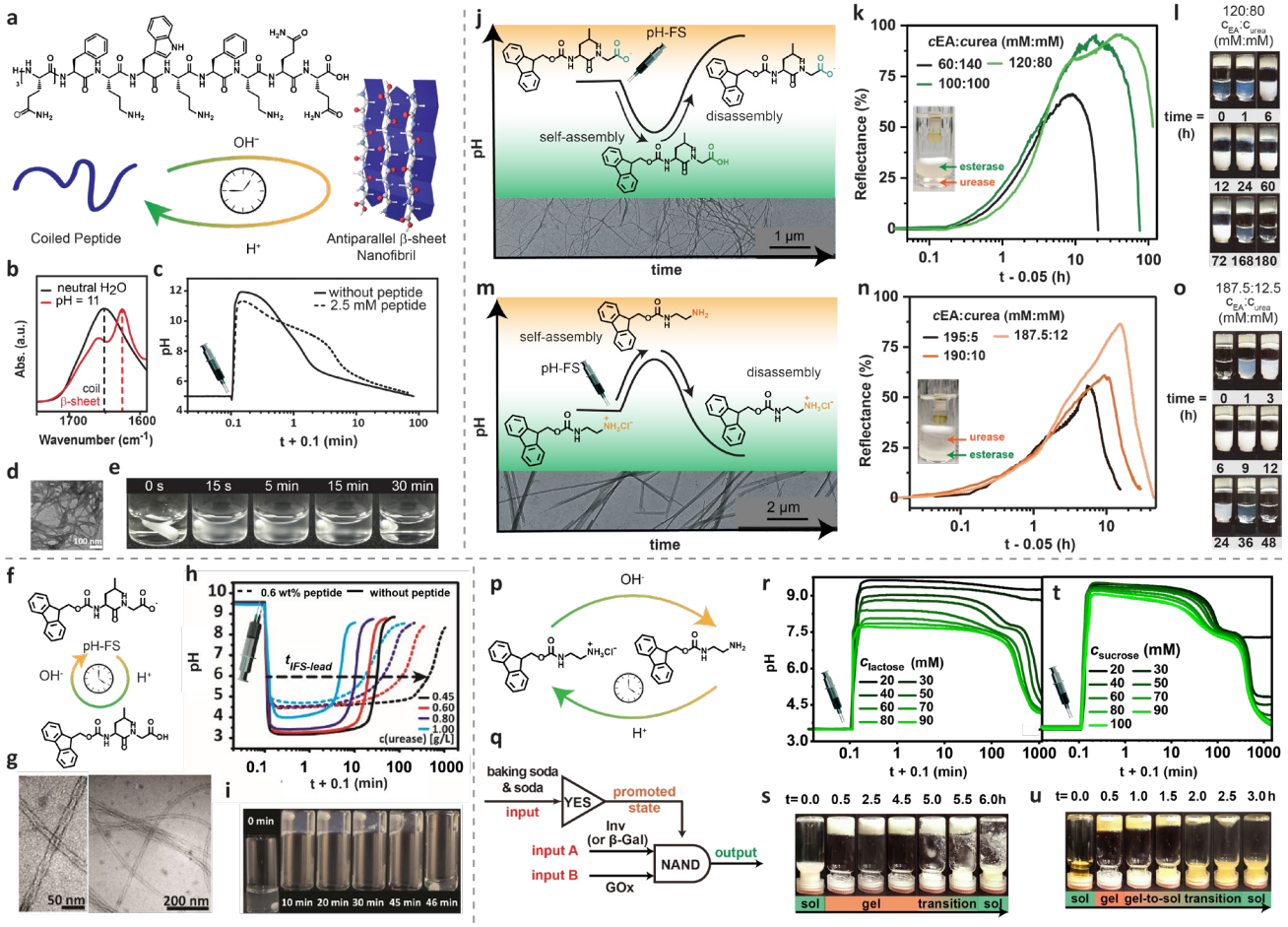

Figure 2-6. Transient SAs of peptides into nanofibrillar structures and hydrogels. (a-d) Transient SA of an oligopeptide with coil-to-β-sheet-to-coil transitions traced by (b) FTIR spectroscopy, (c) pH measurements, (d) TEM of the transient SA, and (e) macroscopic turbidity from snapshot series. (f-i) Transient hydrogelation of Fmoc-L-G-OH by coupling with a generation 2 pH-FS followed by (g) cryo-TEM of the transient fibrils. (h) Transient Fmoc-L-G-OH hydrogels programmed to different lifetimes by different concentrations of urease. (i) Snapshot series of a transient peptide hydrogel at 0.8 g/L urease. (j-o) Coupling of Fmoc-L-G-OH to transient acidic pH-flips (inserted TEM image depicts transient nanofibrils) and of Fmoc-ethylenediamine hydrochloride to transient alkaline pH-flips (inserted TEM image depicts transient SA) programmed by a generation 4 pH-FS with layered compartmentalization of urease and esterase. (k, n) Reflectance measurements of the supernatant solution inside view and (l, o) respective snapshot series of (k, l) Fmoc-G-L-OH and (n, o) Fmoc-ethylenediamine hydrochloride at different fuel ratios (EA = ethyl acetate, and urea). (p-u) Programming the lifetime of Fmoc-ethylenediamine hydrochloride using food-grade reagents. (r-u) pH-lifecycles fueled by baking soda, soda, milk, and β-GAL/GOX or INV/GOX networks at different fuel concentrations and the corresponding snapshots at (s) 60 mM concentration of lactose and at (u) 100 mM sucrose, respectively. Adapted and reprinted with permission from ref. 22 Copyright 2015 American Chemical Society, ref. 23 Copyright 2015 John Wiley & Sons. Reproduced under terms of the CC-BY license, ref. 25 Copyright 2021, published by John Wiley & Sons, ref. 24 Copyright 2021, published by John Wiley & Sons.

employing NaOH as a fast activator and β-BL as DD, and indeed showed successful transient fibrillization. Similar to above, the presence of the peptide at 2.5 mM acted as a load on the pH-FS that manifested in a smaller pH jump and a longer lifetime of the integrated system (**Figure 2-6c,e**).

Although these oligopeptide nanofibrils were successfully programmed into an autonomous system, their concentration was insufficient to allow for full gelation. In the search also for a more economical solution, we picked a simplified dipeptide, Fmoc-L-G-OH (Fmoc = fluorenylmethoxycarbonyl, L = leucine , G = glycine; **Figure 2-6f**), that self-assembles into well-defined twisted ribbon-type nanofibrils and hydrogels at low pH upon removal of electrostatic repulsion at the carboxylate groups (**Figure 2-6g**).[23] We combined this dipeptide gelator with a generation 2 pH-FS using a urease/urea switch for deactivation and Na_3C/CA buffer as activator. Due to the operation above the critical gelation concentration, we could successfully achieve the first transient gels with programmable lifetimes. The lifetimes could be tuned from 20 min to 11 h simply by decreasing the

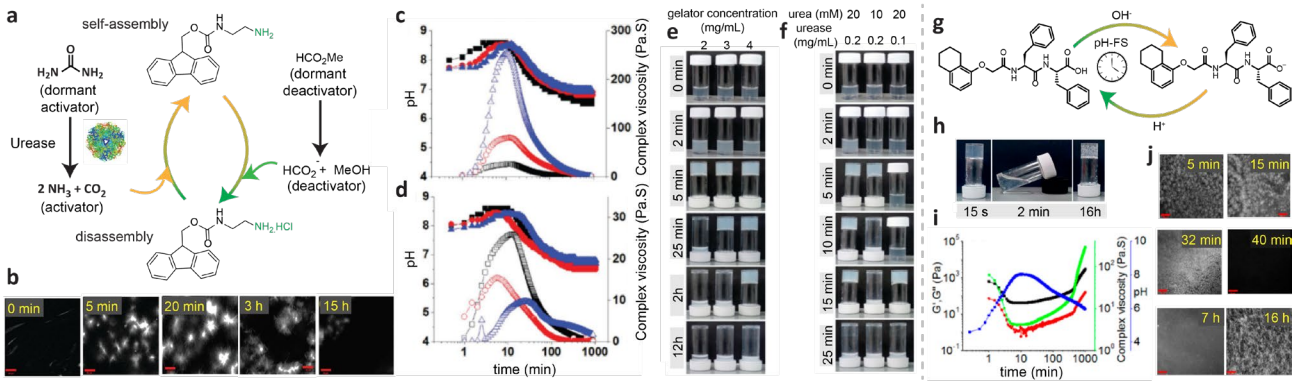

Figure 2-7. Further examples of transient hydrogels. (a-f) Transient hydrogelation of Fmoc-ethylenediamine hydrochloride as confirmed with (b) time-dependent Confocal Laser Scanning Microscopy (CLSM) images showing transient transformation of spherulitic structures into interlinked fibers. (c) Influence of gelator concentration on the lifetime of the transient gels traced by pH (closed symbols), complex viscosity (open symbol), and (e) series of snapshots. (d) Influence of urease/urea concentration on the lifetimes of transient gels traced by pH (closed symbols), complex viscosity (open symbol), and (f) series of snapshots. (g-j) Transient gel-sol-gel transitions of 1ThNapFF traced by (h) photographs, (i) rheology and (j) imaging. Reproduced under terms of the CC-BY license, ref. 64 Copyright 2019, published by John Wiley & Sons, ref. 65 Copyright 2020, published by American Chemical Society.

urease concentration, hence, by slowing down the fuel conversion (**Figure 2-6h,i**). Analogously, transient supramolecular hydrogels were also developed from Cbz-F (Cbz = benzyloxycarbonyl, F = phenylalanine). Rapid pH decrease induced fibrillation and gelation, which was reverted by a subsequent generation of ammonia from urea.[63]

Building on this understanding, we further applied the Generation 4 pH-FS with layered hydrogels to spatially separate esterase and urease to program peptide fibres and gels in the supernatant solution. Indeed, it was found that the Fmoc-L-G-OH can be programmed with lifetimes of more than 70 h by compartmentalizing a bottom layer of urease with a top layer of esterase (**Figure 2-6j**) as traced by transient increase in opaqueness of the self-assembling system and vial inversion tests (**Figure 2-6k,l**).[25] By switching the arrangements of individual gel layers, transient alkaline pH-flips were achieved, and the resulting pH-FS can be coupled to a different peptide-like structure (Fmoc-ethylenediamine hydrochloride) that undergoes base-induced fibrillization (**Figure 2-6m-o**).

A further step towards even more biocompatible systems could be made by employing an EC reaction producing acid on the deactivating side while the promoter consisted of an alkaline buffer. The EC consisted either of β-GAL/GOX or INV/GOX, which are able to convert sucrose or lactose, respectively, into glucose and then gluconic acid (**Figure 2-6p,q**).[24] We could demonstrate that transient alkaline pH-flips could not only be programmed using reagent-grade chemicals, but also be induced by combining soda and baking soda with milk or sugar beet syrup (**Figure 2-6r-u**). Even such multicomponent systems were robust enough to allow for the transient formation of hydrogels with programmable lifetimes based on Fmoc-ethylenediamine hydrochloride.

Building on the basic principles of such pH-FS, Adams and co-workers demonstrated an approach where the urease/urea reaction (fast activation process) was combined with the methyl formate hydrolysis (slow deactivation process; **Figure 2-7a-f**).[64] The resulting transient alkaline pH state was combined with pH-switchable Fmoc-ethylenediamine hydrochloride to form transient gels with tunable lifetimes.[64,65] Interestingly, by decreasing the urease/urea concentration, the appearance of the gels could be delayed (initial lag time ≈ 15 minutes) keeping other conditions constant (**Figure 2-7d,f**). Working on the same pH-FS, the group demonstrated also a complementary gel-sol-gel transition using the dipeptide gelator 1ThNap-F-F (1ThNap = Tetrahydronaphthalen-1-yloxy, F = Phenylalanine; **Figure 2-7g**).[66]

2.4.3 DNA

DNA is classically used to program SAs and materials using the sequence-specific duplex formation which furnishes temperature-dependent behaviour regarding the dissociation according to the melting temperature. However, there are also specific DNA sequences that are switchable using pH, most notably the so-called i-motif DNA and the triplex-forming species.

We focused on programming the i-motif DNA using pH-FSs (**Figure 2-8a**).[20] The i-motif DNA is a cytosine-rich sequence that folds intramolecularly at acidic pH due to partial protonation of the cytosine nucleobases forming parallel duplexes stabilized via hemiprotonated cytosine$^+$-H-cytosine base pairs (e.g., pH 5). However, the i-motif DNA is available for duplex hybridization with a complementary strand i* at high pH (e.g., pH 8). To monitor the basic behaviour, the i-motif strand was tagged with Cy3 at the 5' end and a black hole quencher at the 3' end so as to monitor the folding using time-dependent fluorescence spectroscopy. Indeed, the i-motif strand folds into a tetraplex at lower pH 5 (fluorescence is quenched) and reversibly hybridizes to its complementary strand under alkaline conditions (fluorescence appears; **Figure 2-8b**). When injected with a pH-FS, Tris buffer (pH = 8.8) as promoter and β-BL as DD, the system showed lifetimes in the range of 2 to 6 h by either increasing the Tris concentration or decreasing the β-BL concentration as monitored by *in situ* pH and fluorescence measurements (**Figure 2-8c,d**).

A higher-level integration of this i-motif system was achieved by combining it with a generation 3 pH-FS, where the activation and deactivation processes are regulated by two antagonistic enzymes (urease and esterase). To this end we focused on the realization of a hydrogel lifecycle system, for which the complementary strand i* was copolymerized into long polyacrylamide chains (PAm; **Figure 2-8e**). In presence of a short double-stranded DNA crosslinker containing the i-motif DNA at both sides, such systems can undergo reversible acid/base-switchable sol/gel transitions. Since the system gels in alkaline conditions, we optimized the respective urease/esterase pH-FS to furnish a transient alkaline state.

Therefore, an initial system contained the i*-appended PAm, the i-motif DNA crosslinker and different concentrations of urease and esterase in NaOAc/AcOH buffer (10 mM) at pH 4.5. The system was subsequently

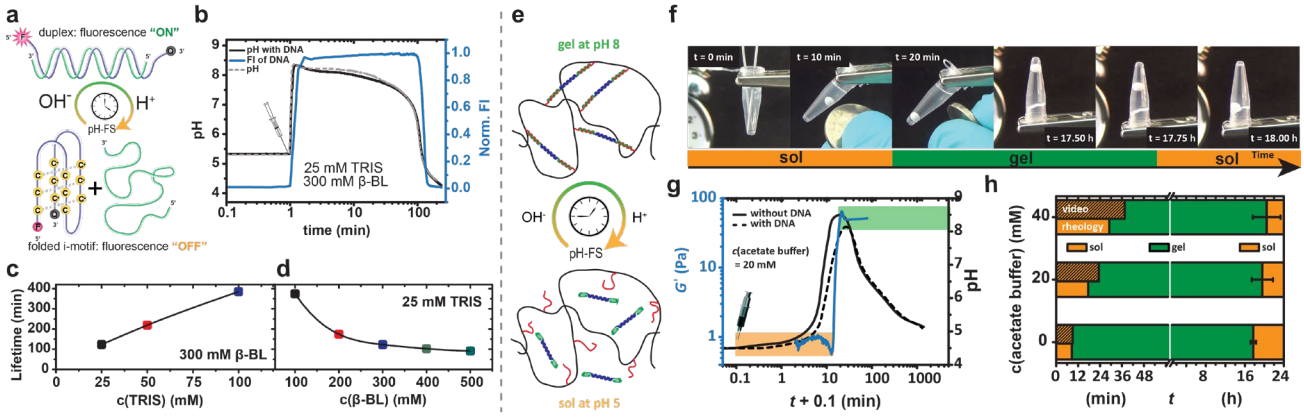

Figure 2-8. Transient hybridization of DNA systems. (a-d) Schematic illustration of the i-motif switch programmed with a generation 1 pH-FS as traced by (b) time-resolved fluorescence output (blue curve) and pH measurements. Pristine pH-FS (dashed curve) and in the i-motif integrated pH-FS (black curve) are shown. (c,d) Temporal programming of transient dsDNA formation by variation of activator (Tris) and DD (β-BL) concentration. (e-h) Transient DNA hydrogels based on pH-sensitive i-motif switch crosslinkers using a generation 3 pH-FS (urease-esterase). (f) Snapshot series of the DNA polymer solution undergoing gelation after a lag time of 20 minutes and returning back to the sol state after a lifetime of 18 hours. (g) Rheological determination of *G'* (blue curve) along with pH measurements of the pristine pH-FS (black curve) and in the presence of DNA hydrogel components (dashed curve). (h) Programmable lag times of the sol-gel-sol plots as a function of the NaOAc/AcOH buffer concentration used to set the starting pH. Reproduced under terms of the CC-BY license, ref. 20 Copyright 2017, published by Royal Society of Chemistry, ref. 19 Copyright 2017, published by American Chemical Society.

initiated by the simultaneous addition of both fuels (60 mM urea and 240 mM ethyl acetate). Indeed, the systems showed robust programmability of the transient hydrogels (**Figure 2-8f,g**). Most importantly, it could be shown that lag times before gelation occurred could be elongated from 9 min for an unbuffered system to 30 min for 40 mM NaOAc/AcOH buffer, while the overall transient lifetime of the gel remained rather unaffected (**Figure 2-8h**).

2.4.4 Nanoparticles

Gold nanoparticles (Au-NPs) and their reversible SAs have been extensively studied under various external stimuli e.g., pH, light and can also be mediated by small molecules and biomacromolecules. These plasmonic nanostructures possess localized surface plasmon resonance (SPR) due to the collective oscillation of conduction electrons upon interaction with light. Since these optical properties are highly dependent on the shape, size and spatial arrangement of the plasmonic structures, this phenomenon is primarily utilized to characterize the assembly/disassembly of Au-NPs. There is a prominent shift in SPR (red to blue upon assembly or vice-versa) which can be easily quantified by UV-Vis. The applicability of pH-FSs can also be generalized to Au-NPs to temporally program their transient assembly for advanced applications in optical sensors.[67,68] In the first example,[22] phenol-ligand functionalized Au-NPs (R ≈ 3.9 nm) were selected, which undergo declustering at high pH owing to deprotonation of the phenolic group (pK_a ≈ 8.3). A particularly alkaline buffer (3-(cyclohexylamino)-1-propanesulfonic acid, pH = 11) was used to trigger the disassembly of the clusters formed under initial conditions. The co-injected DD (methyl formate) reacidified the system slowly, which re-assembled the Au-NPs due to gradual protonation of the phenolate groups. The system could be easily tracked by *in situ* absorption measurements in addition to conventional pH measurements to confirm the programmability of the lifetimes.

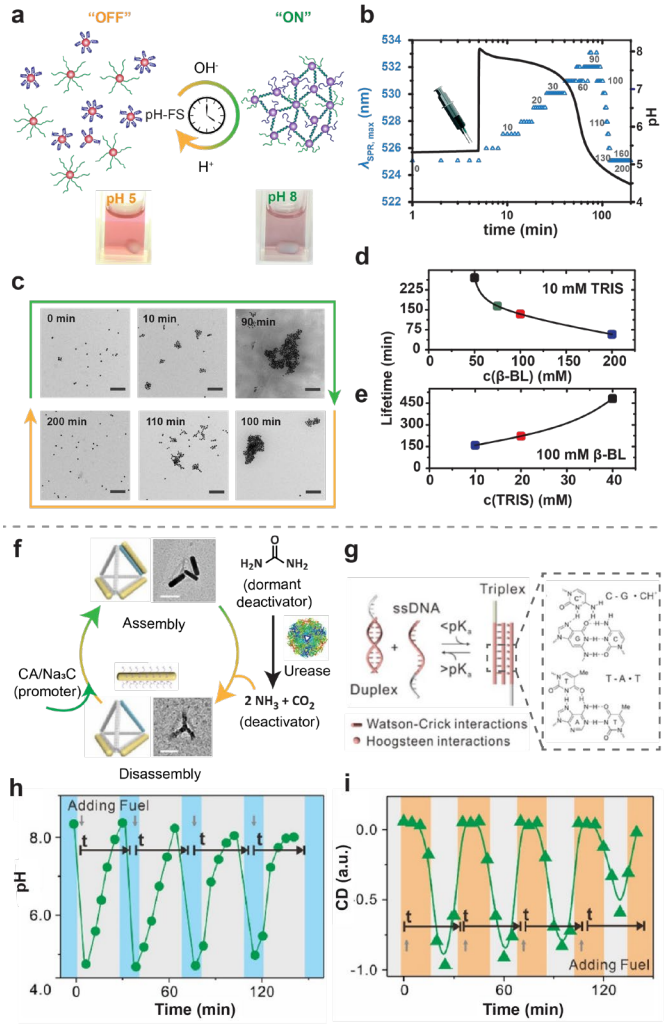

Figure 2-9. Transient assemblies of Au-NPs. (a) Transient co-assemblies of DNA-Au-NP networks where one Au-NP carries the i-motif, and the other Au-NP carries the complementary strand using a generation 1 pH-FS (Tris-β-BL). (b) Time-resolved UV-visible trace of the maximum position of the plasmon band (blue triangles) along with the pH curve (black line). (c) TEM images of aliquots at defined time-intervals. (d,e) Lifetime variation of Au-NP aggregates at different concentration of activator/DD. (f-i) Transient SA of chiral plasmonic metamolecules controlled by transient acidic pH-FS mediated triplex formation and the readout by CD spectroscopy. Reproduced under terms of the CC-BY license, ref. 20 Copyright 2017, published by Royal Society of Chemistry. Adapted and reprinted with permission from ref. 69 Copyright 2019 American Chemical Society.

The developed transient i-motif hybridization system (**Figure 2-8**) was further combined with Au-NPs (R ≈ 10 nm), where one half population of Au-NPs was functionalized with the i-motif strand and the other half with the complementary strand (**Figure 2-9a**).[20] Transient co-assemblies of these DNA-functionalized Au-NPs were achieved by injection of a generation 1 pH-FS (Tris, promoter and β-BL, DD; **Figure 2-9b-e**), whereupon time-regulated aggregates emerged that could be

programmed from 1 h to 8 h by either increasing the concentration of Tris or decreasing the concentration of the DD. Strikingly, the magnitude of the shift in the SPR band increased with extended lifetimes owing to larger aggregate sizes.

Moving in the same line, Fan and co-workers demonstrated the transient SA of chiral plasmonic DNA metamolecules (**Figure 2-9f**).[69] Therein, the cytosine-rich single-stranded DNA on gold nanorods (AuNRs) got protonated upon a pH decrease which then assembled them onto tetrahedron-shaped DNA origami (composed of 6 sides) through a pH-sensitive DNA triplex (**Figure 2-9g**). The transience of this SA could be controlled upon coupling with a pH-FS having a transient acidic state (Na_3C/CA buffer as promoter; and urease/urea switch as DD; **Figure 2-9h**). Intentionally, when only 3 AuNRs were allowed to bind on a tetrahedron origami, three structural isomers were obtained, out of which two were chiral and mirror images of each other. This allowed the monitoring of the SAs via *in situ* circular dichroism measurements which demonstrated a transient dip in the signal upon addition of the pH-FS when chiral plasmonic metamolecules only in the R-state were targeted (**Figure 2-9i**). Notably, transient SAs were only observed under low urease concentrations, which caused a delay in pH decay and hence allowed SAs to be formed before they dissolved upon subsequent generation of base.

2.4.5 Microparticles

The most challenging task while dealing with colloidal assembly and disassembly, especially on a micro(scale), is maintaining their overall stability in solution. This is achieved by balancing electrostatic and steric repulsion with van der Waals attraction. Since pH-FSs can accumulate significant quantities of salt, the stability/SA balance might be influenced unfavourably for SA transitions to occur. We recently introduced a transient colloidal co-assembly system featuring a chemo-structural feedback, where the formed co-assemblies

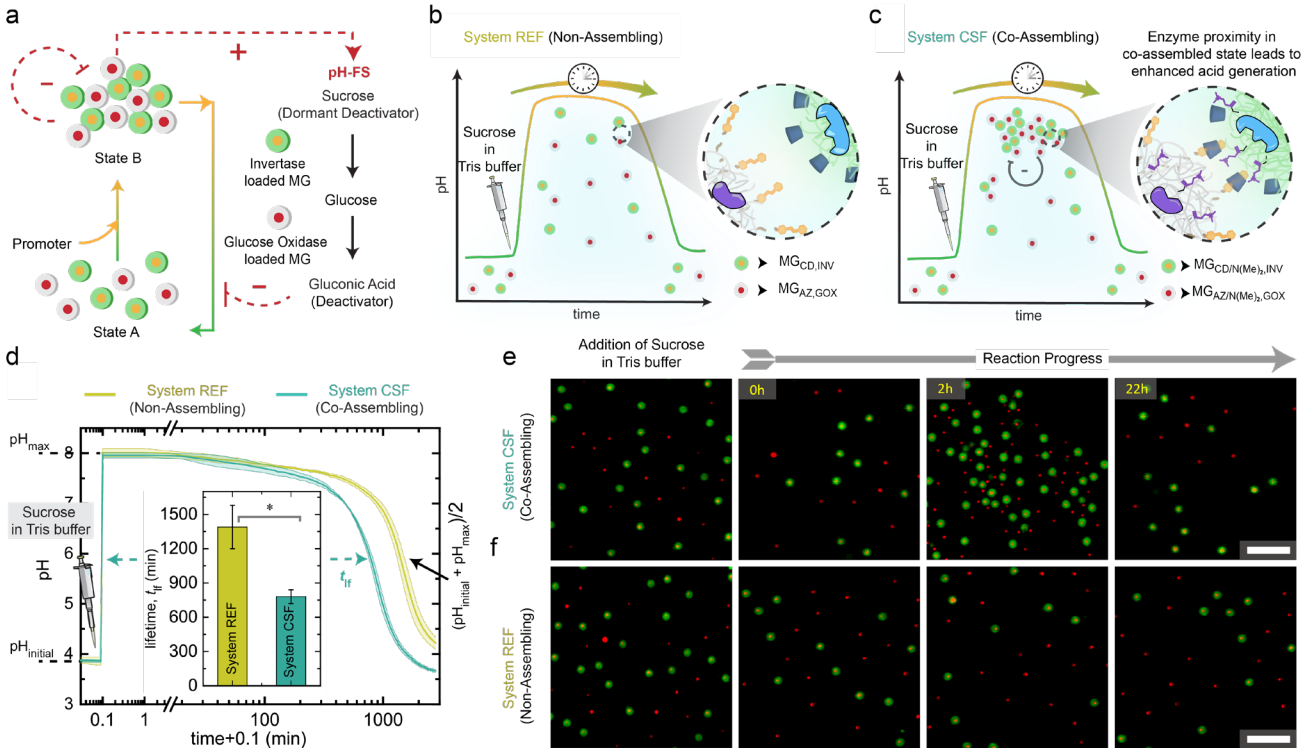

Figure 2-10. Transient co-assembling microgels (MGs) featuring chemo-structural feedback. (a) System design of chemo-structural feedback in transient co-assemblies of MGs. (b,c) Schematic representation of a non-assembling system (System REF, b) composed of a 1:1 mixture of $MG_{CD,INV}$ and $MG_{AZ,GOX}$ and a co-assembling system (System CSF, c) composed of a 1:1 mixture of $MG_{CD/N(Me)2,INV}$ and $MG_{AZ/N(Me)2,GOX}$. (d) pH-profiles and lifetimes of both systems. (e,f) *ex situ* CLSM images of System REF (f) and System CSF (e). Assembly in the CSF system accelerates the pH-FS via chemo-structural feedback. Reproduced under terms of the CC-BY license, ref. 27 Copyright 2022, published by John Wiley & Sons.

accelerate their own destruction (**Figure 2-10a**).[27] We achieved this by synthesizing core-shell microgels (MGs) that feature hetero-complementary units (α-cyclodextrin = CD, and azobenzene = AZ) on two individual MGs for providing basic information for co-assembly vs homo-assembly. Additionally, when pH-dependent weak cationic groups (-$N(Me)_2$) were additionally present, the co-assembly could in fact be triggered at high pH due to removal of electrostatic repulsion.

These MG systems were next coupled to a generation 2 pH-FS by immobilizing enzymes of the deactivating acid-producing EC (INV and GOX) on each of the MGs. To better understand the effect of chemo-structural feedback we built two systems: (i) A reference system incapable of co-assembly (System REF, **Figure 2-10b**) composed of $MG_{CD,INV}$ and $MG_{AZ,GOX}$ and (ii) system capable of co-assembly (System CSF, **Figure 2-10c**)) composed of $MG_{CD/N(Me)_2,INV}$ and $MG_{AZ/N(Me)_2,GOX}$. When coupled to a pH-FS, only the CSF system co-assembled. Most importantly, the tight co-assembly in the CSF system brought INV and GOX into close proximity, which enhanced the EC and provided a quicker pH-feedback (**Figure 2-10d,e**). The transient timescale of the pH-FS was almost cut in half compared to the non-assembling but otherwise identical REF system. This shows the operation of a chemo-structural feedback and hence an intimate kinetic coupling of the SA with the pH-FS. The study thereby offers advancements towards self-regulating dynamic materials and introduces new strategies for programming chemo-structural feedback into synthetic systems.

2.5 Compartmentalized system

Compartmentalization is pivotal to life to sequester elements and organize catalytic processes, as well as regulate exchange of energy and matter. The principle is now being applied to the development of biomimetic systems by mimicking biochemical CRNs in cell-like microcompartments. In the context of pH-FS it is important to understand how compartmentalization of different effectors, such as pH-modulating enzymes, or the type of the compartment, e.g., a pH-responsive element, cross-regulate processes beyond plain solutions.

For instance, Taylor and co-workers reported experimental and modelling approach to realize pH-oscillations in giant liposomes.[70] By theoretical modelling, a sufficient and necessary condition was established to achieve pH-oscillation from the urease/urea network, which was suggested as the transport rate of acid (k_H) being larger than the transport rate of urea (k_S). As such condition is unattainable in a homogeneous batch reaction, they encapsulated urease and a pH probe, pyranine (8-hydroxy-1,3,6-pyrenetrisulfonate) in POPC (1-palmitoyl-2-oleoyl-sn-glycero-3-phosphatidylcholine) liposome and dispersed them into a urea-containing acid sink. The POPC liposome compartment exhibited different membrane permeabilities (P_m) for H^+ (10^{-3} cm/s) and urea (10^{-6} cm/s), which led the system to oscillate. The diffusion disparity depended on the properties and size of the lipid boundary. Further, the various diffusion rates of urea, H^+, NH_3, and NH_4^+ were modeled to display the change in oscillation (sustained vs. damped) and other dynamical behaviours, such as low and high pH steady states, autocatalysis, clock regimes, etc.

Later, the urease/urea system was also immobilized in hydrogel beads to program bistability and pH clock times.[71,72] The urease was immobilized in alginate gel bead, into which urea and H_2SO_4 diffused from the enzyme-free surrounding solution. The pH response varied as a function of total enzyme activity and the concentration of substrate at the boundary. The urease loaded beads were in an unreacted, low pH state (pH = 4) with a low substrate concentration, which turned into a reacted, high pH state (pH = 10) with an increase in substrate concentration. In the bistable regime, both states (low and high) co-existed for the same parameters. The span of bistability was theoretically estimated to be in the range of 6-10 mM of urea concentration. However, experimentally, bistability existed with urea concentrations of 3-5 mM. The relative

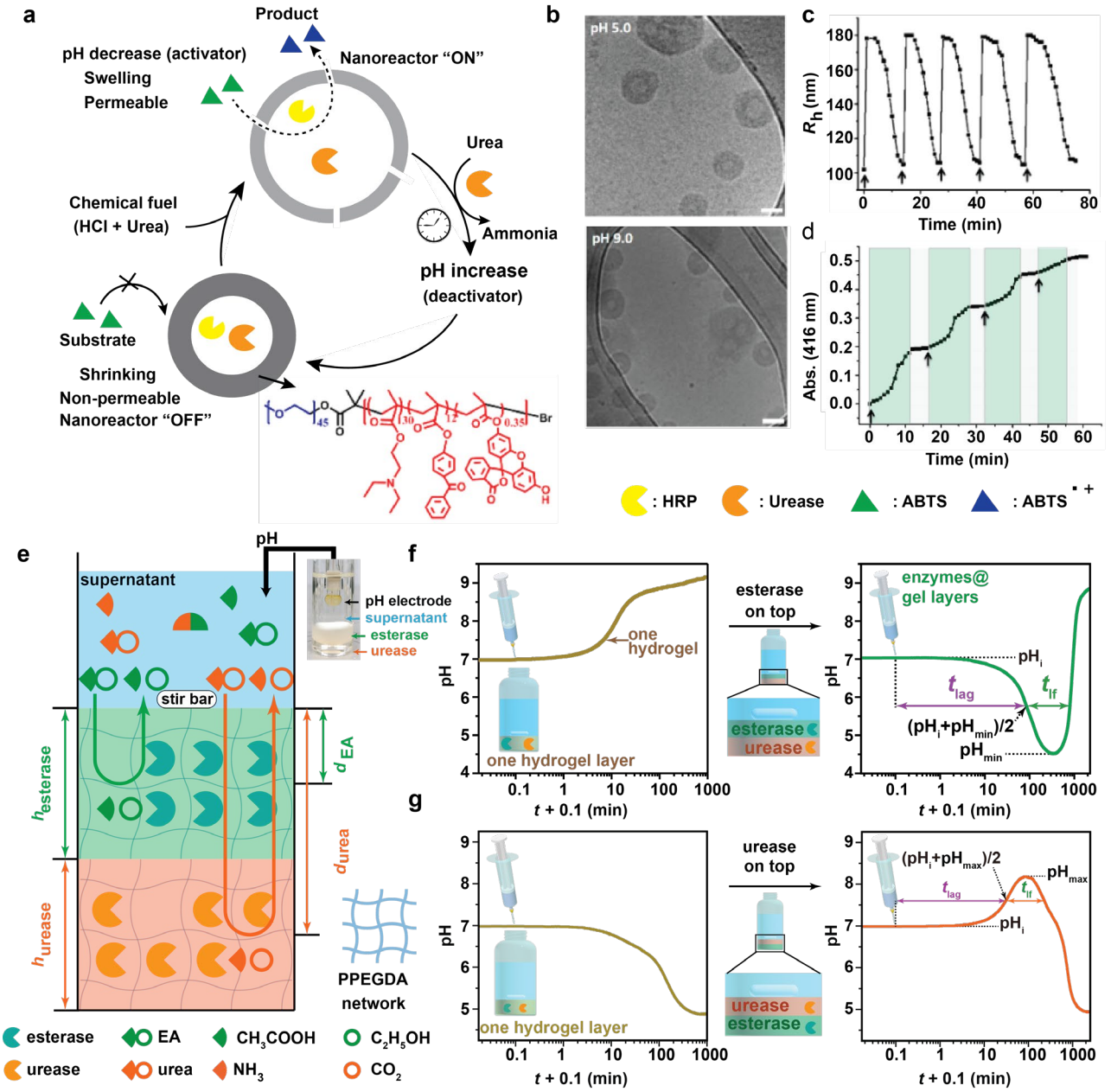

Figure 2-11. Compartmentalized reaction networks for self-regulation of catalysis and emergence of pH-flip responses. (a-d) Strategy to achieve the temporal control over the polymersome nanoreactors with an acidic pH-FS. (b) Cryo-TEM images of polymersomes at pH 5.0 (top) and pH 9.0 (bottom). Scale bars are 100 nm. (c) Reversible size changes and "ON−OFF" catalysis modulation during repeated fuelling with a pH-FS (e-g) 4th generation pH-FS with layered hydrogel (PPEGDA) compartmentalization of antagonistic enzymatic reactions. (f-g) Layered compartmentalization of urease and esterase allow to convert a pH increase or decrease when both enzymes are in a single hydrogel layer into a transient acidic pH-FS or alkaline pH-FS, respectively. Reproduced under terms of the CC-BY license, ref. 73 Copyright 2018, published by American Chemical Society, ref. 25 Copyright 2021, published by John Wiley & Sons.

activity of the urease-loaded beads was articulated by the pH-clock time, which ran nonlinearly with urea concentration and progressively decreased with increased urea concentration.

Towards compartments that take important roles in the pH-FS, van Hest and co-workers designed a pH-sensitive polymersome with encapsulated horseradish peroxidase (HRP) and urease which demonstrated self-regulated, temporal control of "breathing" of polymersomes and catalytic activity (**Figure 2-11a-d**).[73] The polymersomes based on PDEAEMA were rather impermeable at high pH, preventing the uptake of the substrate ABTS (2,2'-azino-bis(3-ethylbenzothiazoline-6-sulfonic acid)) for the HRP (OFF state). However, the addition of HCl and urea decreased the pH sharply and protonation of PDEAEMA rendered the polymersome permeable for ABTS, bringing the polymersomes in the "ON" state

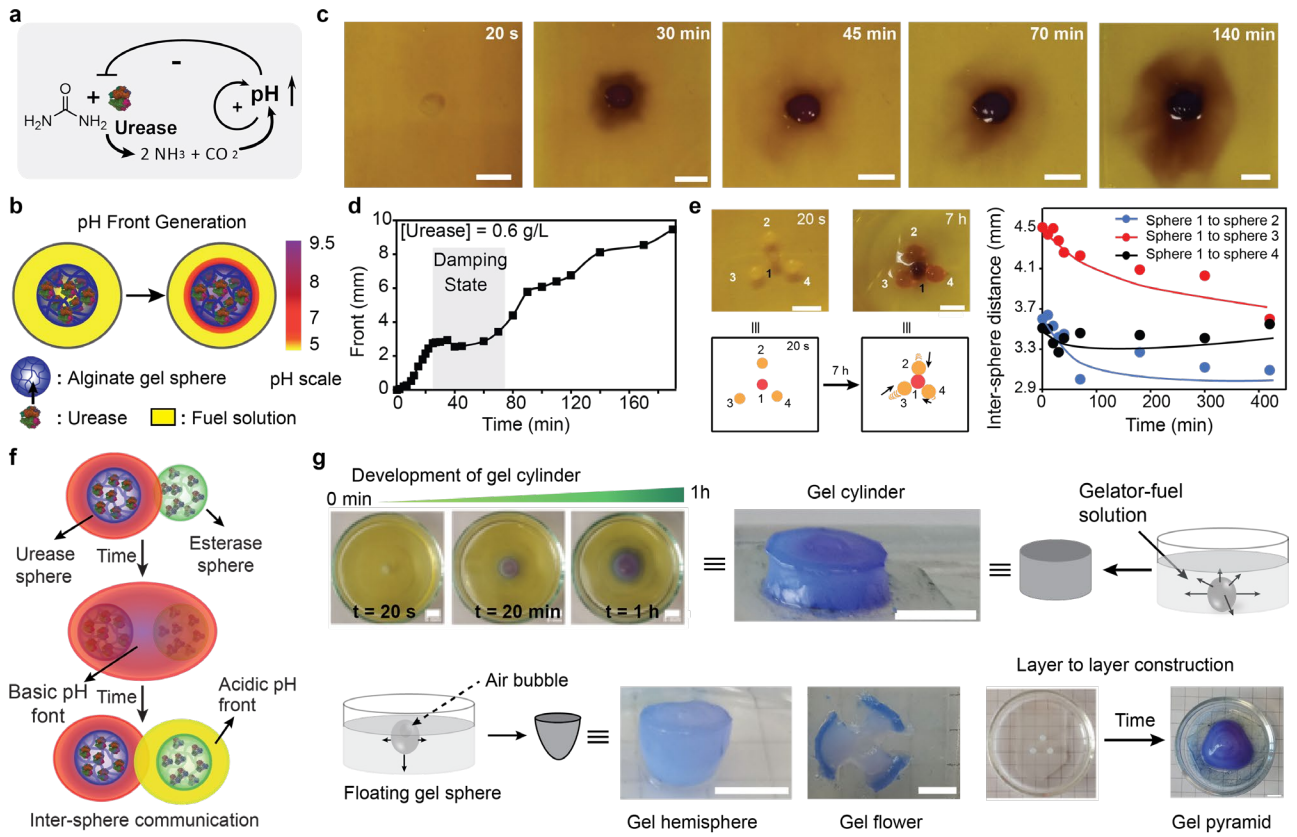

Figure 2-12. pH fronts, communication and material synthesis from beads with compartmentalized pH-modulating enzymes. (a) Urea-urease network topology with inherent + and – feedback. (b) Scheme of a pH front emerging from a urease-loaded alginate sphere when placing into a fuel solution at acidic pH. (c-d) Photographs and quantification of the basic pH front emerging from compartmentalized urea-urease reaction network, highlighting the non-linear damping phenomenon (0.6 g L^{-1} urease). (e) Inter-sphere attraction of a central and surrounding spheres containing urease (2.4 g L^{-1}) and esterase (10 g L^{-1}) respectively. Plot of center-to-center distance vs. time revealing inter-sphere attraction (right). Fuel solution: 100 mM urea, 10 mM Na_3C/CA (pH 3.5), and 1.0 M EA. (f) Schematic development of pH signals in systems containing beads with urease and esterase in different beads. (g) Hydrogel structures with various geometric shapes (cylinder, hemisphere, flower) were grown from a non-injectable hydrogel without the help of 3D printing or molds. Scale bars: 5 mm. Reproduced under terms of the CC-BY license, ref. 26 Copyright 2021, published by John Wiley & Sons.

(**Figure 2-11a-b**). Over time, the pH gradually increased by conversion of urea and thereby reverted the polymersomes back to the initial collapsed state. As a result, the HRP catalysis changed to the "OFF" state again. Periodic additions of the pH-FS allowed transient pulses of HRP catalysis (**Figure 2-11c-d**). This approach is a different dimension of chemo-structural feedback, where the coupled "load" (i.e., the pH-responsive membrane) provides additional function to the chemical reactions operating in the system, albeit not on the urease/urea one but on a secondary catalytic process.

Driven in parts by practical considerations of how to reach even better programmability of enzymatic pH-FS, we established layered hydrogel compartments to house different pH-modulating enzymes (Generation 4 pH-FS). This was motivated by the fact that sets of antagonistic pH-modulating enzymes (urease/urea-esterase/ester) have such a mismatch in their pH-dependent activity that even large changes in the ratios of enzymes or fuels only allow to program a transient alkaline state, while a transient acidic state remain difficult to reach.[19] To address this unfavourable mismatch of activity in solution, we added additional diffusion delays to the fuels and resultant pH-effectors by embedding the enzymes into layered hydrogels based on PPEGDA (poly(poly(ethylene glycol) diacrylate); **Figure 2-11e**).[25] Such systems contained typically two or three gel layers. The top and bottom gel layers housed the enzymes, whereas a dummy layer could be added in-between to further tune the diffusion time scale. After injection of the fuels into the supernatant phase, ethyl acetate

(for esterase) and urea (for urease) diffused into the hydrogel layers, where they were converted into respective acidic (acetic acid, AcOH) and basic (NH_3) products. Thereafter, diffusion of such pH-effectors into the supernatant from the respective gel layers allowed to control the pH-profiles. As clear proof of principle, this layered compartmentalization allowed to completely change systems that either provided a pure pH increase or a pure pH decrease into systems that show a transient acidic pH-flip or a transient alkaline pH-flip, respectively. Further, a precise control over the spatial arrangement (layer height) and activity (enzyme and fuel concentration) allowed to program the depth of the pH lifecycle (pH_{min}), lag time (t_{lag}, defined as the time that the pH-profile needs to decrease to half of initial pH (pH_i) and pH_{min}), and lifetime (t_{lf}) of the respective pH-profile. Moreover, since enzymes are now completely separated from the supernatant pH-flip system, this system is preferred for *in situ* analytical techniques, such as scattering or spectroscopy, where signatures of enzymes might harm the signal quality.

Towards more complex communication, we recently established how compartmentalized urease/urea or more complex urease/urea-esterase/ester CRNs can send self-regulating pH fronts from enzyme-containing beads and between enzyme-containing beads (**Figure 2-12a-d**).[26] To emit a pH front, the enzyme urease or a set of enzymes (urease/esterase) were immobilized in alginate beads and then immersed into a fuel solution containing urea or urea/ethyl acetate in Na_3C/CA at pH 3.5 (**Figure 2-12b**). The pH front propagation was followed by a pH tracer dye, and showed non-linearities, such as damping and acceleration originating from the feedback-controlled reaction networks (+ and – feedbacks; **Figure 2-12c-d**). When encapsulating antagonistic enzymes (urea and esterase) separately into different hydrogel spheres communication, pattern formation and attraction by chemotaxis occurred (**Figure 2-12f**). Importantly, we also showed how these defined pH fronts and pH landscapes can be utilized in developing hydrogel structures with various geometric shapes by coupling a pH-switchable supramolecular gelator (**Figure 2-12g**). Various 2D and 2.5D gel structures (gel cylinder, hemisphere, flower, and others) as well as multi-layered geometric hydrogel shapes (gel pyramid) were grown *in situ* from a specific hydrogelator that typically fails to print using conventional 3D printing. Therefore, this approach paves the way to exploit pH-modulating CRNs for materials design.[26]

2.6 Functional aspects of autonomous materials systems

The above sections summarize the development and application of pH-FS to program autonomous SAs of varied building blocks from the nano- to the micron-scale. Additionally, we have touched upon possibilities for applications in the context of for instance making transient hydrogels. However, the question remains for what kind of applications such transient gels may be suitable. Moreover, what functions and applications beyond a transient gel can be realized by implementing such an autonomous self-regulation behaviour?

In the context of time-programmed hydrogels, we demonstrated early on that they can be useful for temporally programmed release based on a pre-encoded clock, as for instance useful for burst release applications (**Figure 2-13c**).[23] Additionally, we demonstrated that injectable solutions of pre-gels and pH-FS can be set up in double barrel syringe, and that such mixtures can for instance be delivered into microfluidic circuits to undergo temporal gelation locally to reroute the flow patterns into different directions for a pre-programmed amount of time (**Figure 2-13a,b**). Such temporal blocking could be interesting for surgical interventions or also fundamental aspects of controlling fluid flow in technical systems.

Towards applications within hydrogels, the Wang group reported improved healing by controlling the dynamics of acyl hydrazone bonds (**Figure 2-13d**).[74] A kinetically stable gel was initially harmed, followed by addition of an acidic pH-FS pair (HCl, urease/urea) at the damaged site (**Figure 2-13e**). As a result, the dynamized bonds in an acidic pH region allowed recovery of the damage, and the gradual increase of the pH ultimately led to kinetically stable gels with completely recovered gel properties. Different healing efficiencies could be realized depending on the pH-FS (**Figure 2-13f**).

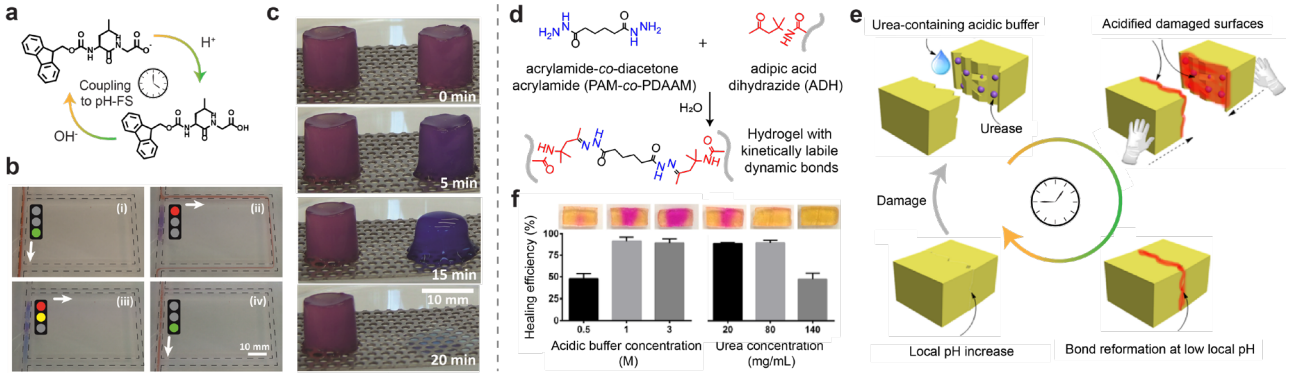

Figure 2-13. Applications of time-programmed hydrogels. (a,b) Fluid guidance in microfluidic systems based on time-programmed Fmoc-L-G-OH hydrogel systems. (c) Self-erasing hydrogels for burst release applications depicted with the help of series of snapshots of micromolded cylinders without pH-FS (on the left) and with pH-FS (on the right). (d-f) Accelerated healing via dynamization of acyl hydrazone-containing bonds inside hydrogels using a generation 1 pH-FS with an acidic transient state. (f) Healing process of hydrogels (containing pH-indicator, neutral red) and healing efficiency calculated from the compressive stress versus compressive strain curves for different concentrations of activator and urea. Adapted and reprinted with permission from ref. 23 Copyright 2015 John Wiley & Sons, ref. 74 Copyright 2020 American Chemical Society.

Towards application of such hydrogels on a higher system level, we and Di Stefano group recently demonstrated the autonomous operation of soft robotic systems (**Figure 2-14**).[75] To this end, we used the very simple one component pH-flips based on self-decarboxylating acids.[76-82] Such activated acids, e.g. tribromoacetic acid, lead to a quick drop in pH, that is followed by decarboxylation and re-capture of the proton and a subsequent return to the original pH (**Figure 2-14a**). We combined those one-component acidic pH-FS first with bilayer actuators composed of a layer of a weak polyacid and a neutral polymer. Owing to the spatially confined collapse of the polyacid layer, the devices showed bending, and, due to the self-decarboxylation, autonomous return to the original position (**Figure 2-14b,c**). This contrasts classical sequential operation of soft robotic devices. It could be shown that a critical fuel amount is needed to induce bending and that the lifetime of the bent state could be programmed by the concentration of the fuel amount. We further demonstrated "fire-and-forget" operation of such devices for the interlocking of interface or for harpooning objects, where spatial obstacles would typically prevent the application of a counter trigger, thus representing clear advantages of autonomously programmed devices (**Figure 2-14d,e**). Furthermore, advanced chemo-mechanical feedback could be achieved by integrating urea-urease patches that accelerated the pH-FS and the operation of the soft-robotics devices.

Regarding optical effects, already above we shortly discussed about transient assembly or disassembly of Au-NPs which can lead to aggregation-dependent plasmonic coupling and color changes. Here, we briefly discuss more sophisticated effects in soft photonic materials.[21]

To this end, we used polystyrene-*b*-poly(2-vinyl pyridine) (PS-b-P2VP) diblock copolymers, that form lamellar mesophase in bulk and which can undergo selective hydrophobic/hydrophilic switching of the P2VP layer (**Figure 2-15a**). At high pH, the film remains dry and transparent, whereas at pH < pK_a of P2VP (≈3.2 in photonic film), protonation of the P2VP leads to swelling of its layer, which induces a photonic bandgap in the visible regime. The system was integrated with an alkaline pH-FS (Na_3C/CA-urease/urea) and monitoring of the reflected light indeed showed the transient appearance of a macroscopic reflective color in the range of 560 nm, which disappeared after a programmable lifetime (**Figure 2-15b,c**). The approach was further used to build patterned self-regulating photonic displays for the very first time. The device was made by covering a BCP photonic mirror with a PDMS mask featuring three letters (**Figure 2-15d**). When exposed to pH-FS solutions with different urease concentrations, a characteristic reflective state could be encoded with different lifetimes (**Figure 2-15c**). The approach was further used to build a reaction/diffusion signal conduction pathway by exploiting the autocatalytic self-acceleration of OH^-

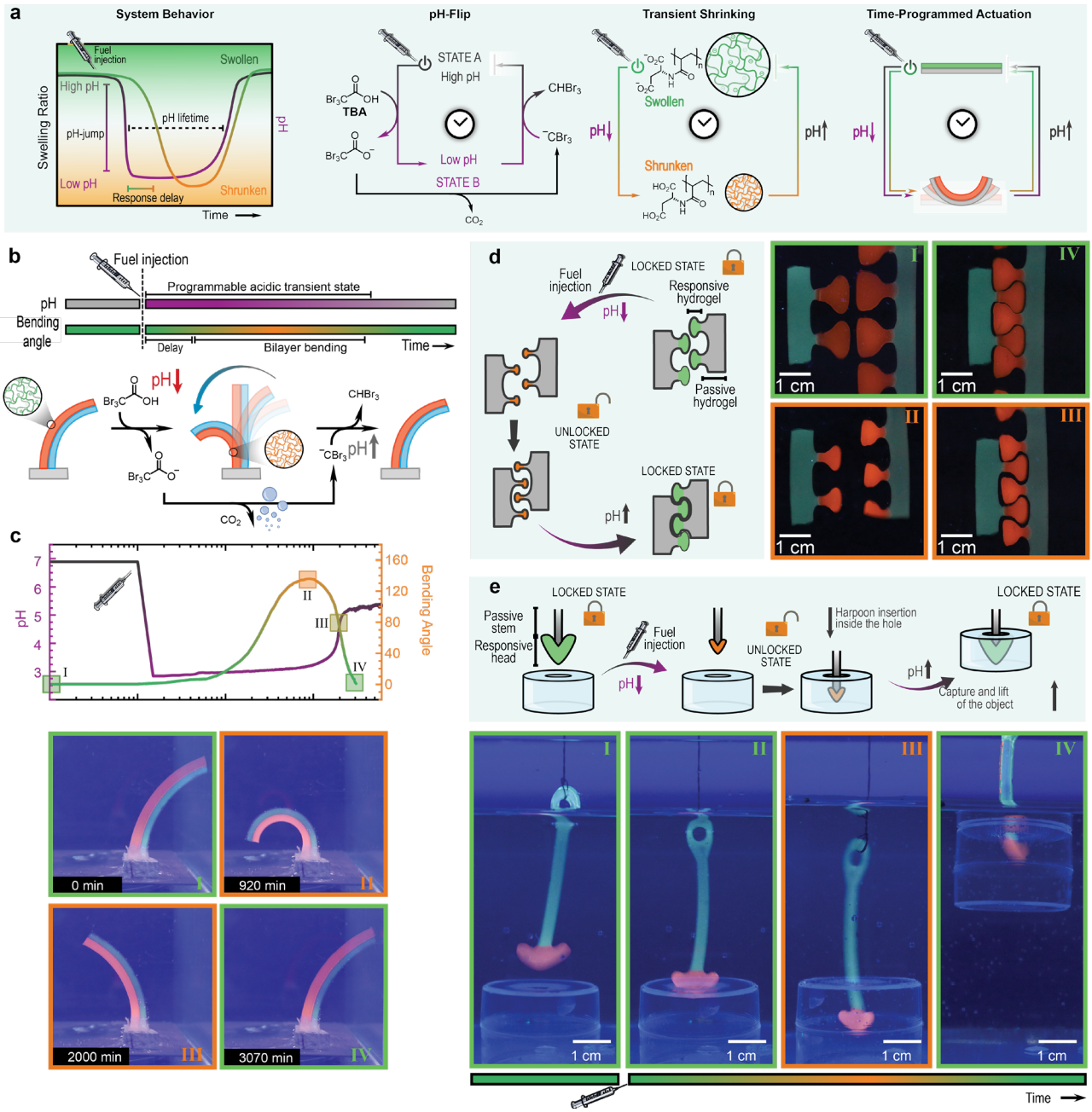

Figure 2-14. Autonomous soft robotics programmed by coupling one-component acidic pH-flips to pH-responsive hydrogel actuators. (a) System design to achieve soft robots by coupling TBA-based pH-flips to pH-responsive bilayer hydrogels. (b-c) Schematic representation for the effect of self-decarboxylating TBA, the associated pH response and the bending angle of the bilayer actuator. (d-e) Autonomous "fire-and-forget devices" as shown for the interlocking of interfaces and for harpooning devices, able to grab objects with small orifices. Reproduced under terms of the CC-BY license, ref. 77 Copyright 2022, published by John-Wiley & Sons.

generation when starting from the acidic flank of a urease/urea system (**Figure 2-15e,f**). First, a metastable state with negligible enzymatic activity was maintained in a PDMS channel using optimized amounts of urease/urea solution in Na_3C/CA (pH = 3.1). The subsequent addition of a small amount of base on one end of the channel locally activated the urease which thereby generated a self-sustaining pH-wave (positive feedback). The snapshot series of the photonic channels (**Figure 2-15g**) and the respective kymograph (**Figure 2-15h**) confirm a stable front propagation with a constant speed, that was tunable by changing the concentration of the urease. However, the kymograph taken under identical conditions but using bromocresol purple as the pH-indicator depicts slower speed of the chemical font due to undesirable chemical interference

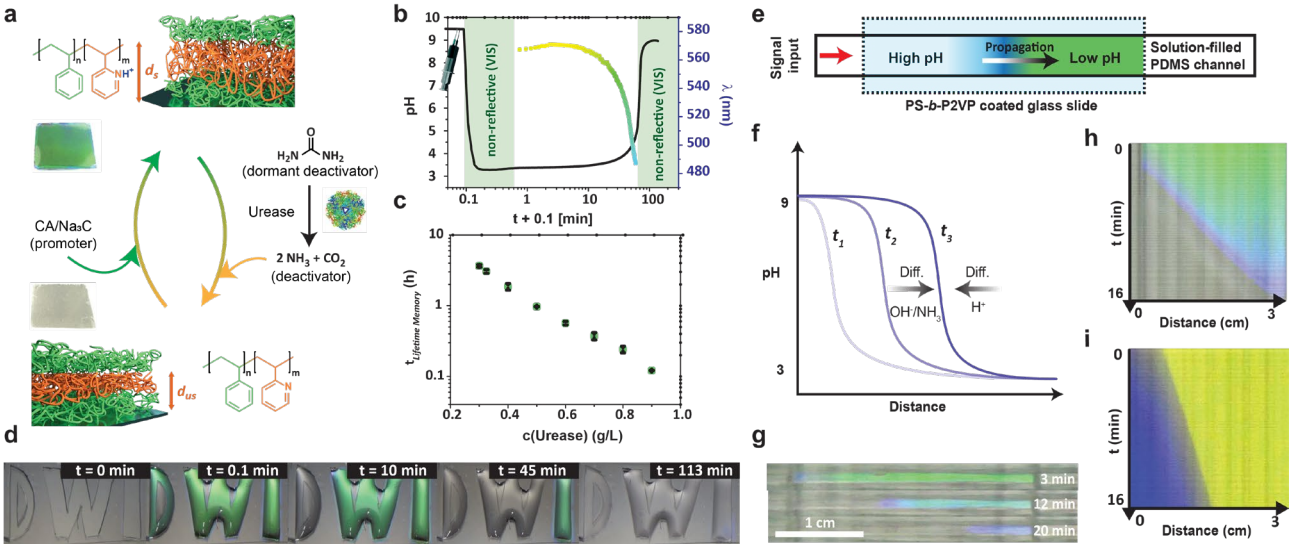

Figure 2-15. Autonomous photonic devices demonstrating transient memory, sensing and signal propagation. (a) Schematic illustration for the control over the lifetime of transient optical reflections from BCP photonic gels upon integration with a generation 2 pH-FS (Na_3C/CA-urease/urea). (b) Transient optical reflection of a BCP photonic film together with pH of the supernatant. (c) Variation in the lifetime of the optical response of the photonic film for different urease concentrations and corresponding snapshot series (d) for selected urease concentrations. (e) Schematic representation of a PDMS channel device made with a photonic mirror showing a top view of the propagating pH wave and (f) the corresponding pH-profiles in the channel at different times ($t_1<t_2<t_3$). (g) Photographs of the propagating pH wave at different times. (h,i) Corresponding kymographs for the BCP photonic display (h) and for bromocresol purple (i) with front position on the horizontal axis and time on the vertical axis. Adapted and reprinted with permission from ref. 21 Copyright 2017 John Wiley & Sons.

(**Figure 2-15i**). This study was a first demonstration how advanced autonomous behaviors like transient memory, displays and photonic information patterning and signal transfer can be achieved, which is otherwise very challenging to obtain in classical responsive photonic systems.

In the interest of a more complete coverage of applications, we point to the transient gels with front propagation established by Taylor, Pojman and co-workers,[83] as well as the removal of memories in "learning material" by Ikkala and co-workers,[84] as well as the transient regulation of catalysis by Ward and co-workers,[85] and the transient operation of molecular switches and machines by Di Stefano and co-workers.[76,77,79,81] These studies clearly show the flexibility with which pH-FS can be applied for augmenting the behavior of classical materials towards autonomous, active and adaptive systems.

2.7 Conclusions and Outlook

In summary, this feature article aimed to give a comprehensive overview of pH-FS from their basic design principles to the applications of the concept for developing self-assembling systems with programmable lifecycles and advanced self-regulating materials with autonomous functions. The classification into the different generations of pH-FSs reflects the developments towards better control over the lifecycles, including, most notably, enhanced chemical feedback, the introduction of biocatalytic control mechanisms, and the addition of the spatial domain to achieve higher degrees of self-regulation and also overcome some limiting factors of the operation in plain solution. Common to the design of all these autonomous pH-FS systems is the presence of a fuel – a source of latent chemical energy – that is able to provide a programmable evolution of the chemical potential of the environment. Depending on the particular type of pH-FS, acidic and basic transient states can be programmed with great ease, ranging from minutes to days. Additional lag times before the transient pH state can be encoded for specific types of these networks. These developments were not only driven by our group, but, most notably, we have highlighted the most significant works by Pojman, Taylor, Adams, van Hest and di Stefano, as well as others.

The overall concept has proven extremely robust with respect to programming the lifecycles of SAs from diverse chemical origins – from the domain of polymers, colloids, up to peptides, DNA and molecular machines. In all cases, the coupled SA acts as a load on the pH-FS and influences the development of the coupled chemical system. The overall versatility of such "active environments" sets these principles apart from the design of dissipative systems with active building blocks, which typically require judicious tuning of the CRN to suit one particular type of building block. The simplicity of this pH-FS approach has helped to push towards first-time applications, most notably, the first time-programmed hydrogels, the first transient information storage in photonics, or unique autonomously operating soft robotic devices. The facile principles, easy monitoring and wide tuneability has also enabled other researchers to use these pH-FS concepts in different materials systems settings to develop new autonomously acting functionalities.

Despite the relative maturity of some aspects of pH-FSs and their coupled SA or material systems, many challenges remain. It would for instance, be highly desirable to have a unified kinetic description of the pH-regulating components and their CRNs in a public database or even in a software to further democratize the use of such systems. Additionally, their full potential with respect to coupled systems and advanced self-regulatory mechanisms has not yet been completely realized. Despite the fact that the first chemo-structural and chemo-mechanical feedbacks on top of the pristine pH-FSs have been realized, reaching the true potential of feedback beyond the level of chemistry would enable higher degrees of adaptive behavior, potentially resulting in signal-adaptive behavior, pH-oscillations (which are still difficult to obtain for pH in closed systems), and autonomous control mechanisms in general. In an application world, it will also be decisive to move beyond the present-day proof-of-concept devices and understand how such systems might find their use in real-world technologies. Additionally, the application scenarios need to be broadened towards a broader spectrum of functionalities to fully understand the potential of such autonomous material systems driven by a CRN. In a wider perspective, the combination of such simple CRN-empowered embodied intelligence will however be a key to the development of life-like material systems. These developments are driven by a range of science disciplines and are globally at the very beginning. Thus, exciting developments can be foreseen.

2.8 References

1 Stuart, M. A. *et al.* Emerging applications of stimuli-responsive polymer materials. *Nat. Mater.* **9**, 101-113, doi:10.1038/nmat2614 (2010).

2 Bohn, T. *et al.* Tumor immunoevasion via acidosis-dependent induction of regulatory tumor-associated macrophages. *Nat. Immunol.* **19**, 1319-1329, doi:10.1038/s41590-018-0226-8 (2018).

3 Lee, Y.-J. & Braun, P. V. Tunable Inverse Opal Hydrogel pH Sensors. *Adv. Mater.* **15**, 563-566, doi:https://doi.org/10.1002/adma.200304588 (2003).

4 Zarzar, L. D., Kim, P. & Aizenberg, J. Bio-inspired Design of Submerged Hydrogel-Actuated Polymer Microstructures Operating in Response to pH. *Adv. Mater.* **23**, 1442-1446, doi:https://doi.org/10.1002/adma.201004231 (2011).

5 Aggeli, A. *et al.* pH as a Trigger of Peptide β-Sheet Self-Assembly and Reversible Switching between Nematic and Isotropic Phases. *J. Am. Chem. Soc.* **125**, 9619-9628, doi:10.1021/ja021047i (2003).

6 Cheng, E. *et al.* A pH-Triggered, Fast-Responding DNA Hydrogel. *Angew. Chem. Int. Ed.* **48**, 7660-7663, doi:https://doi.org/10.1002/anie.200902538 (2009).

7 Go, D. *et al.* Programmable Phase Transitions in a Photonic Microgel System: Linking Soft Interactions to a Temporal pH Gradient. *Langmuir* **33**, 2011-2016, doi:10.1021/acs.langmuir.6b04433 (2017).

8 Walther, A. Viewpoint: From Responsive to Adaptive and Interactive Materials and Materials Systems: A Roadmap. *Adv. Mater.* **32**, 1905111, doi:https://doi.org/10.1002/adma.201905111 (2020).

9 Inniss, Mara C. & Silver, Pamela A. Building Synthetic Memory. *Curr. Biol.* **23**, R812-R816, doi:https://doi.org/10.1016/j.cub.2013.06.047 (2013).

10 Wong, A. S. Y. & Huck, W. T. S. Grip on complexity in chemical reaction networks. *Beilstein J. Org. Chem.* **13**, 1486-1497, doi:10.3762/bjoc.13.147 (2017).
11 Barabási, A.-L. & Oltvai, Z. N. Network biology: understanding the cell's functional organization. *Nat. Rev. Genet.* **5**, 101-113, doi:10.1038/nrg1272 (2004).
12 Merindol, R. & Walther, A. Materials learning from life: concepts for active, adaptive and autonomous molecular systems. *Chem. Soc. Rev.* **46**, 5588-5619, doi:10.1039/c6cs00738d (2017).
13 Deng, J. & Walther, A. ATP-Responsive and ATP-Fueled Self-Assembling Systems and Materials. *Adv. Mater.* **32**, e2002629, doi:10.1002/adma.202002629 (2020).
14 Sharko, A., Livitz, D., De Piccoli, S., Bishop, K. J. M. & Hermans, T. M. Insights into Chemically Fueled Supramolecular Polymers. *Chem. Rev.* **122**, 11759-11777, doi:10.1021/acs.chemrev.1c00958 (2022).
15 Schwarz, P. S., Tena-Solsona, M., Dai, K. & Boekhoven, J. Carbodiimide-fueled catalytic reaction cycles to regulate supramolecular processes. *Chem. Commun.* **58**, 1284-1297, doi:10.1039/d1cc06428b (2022).
16 Amano, S., Borsley, S., Leigh, D. A. & Sun, Z. Chemical engines: driving systems away from equilibrium through catalyst reaction cycles. *Nat. Nanotechnol.* **16**, 1057-1067, doi:10.1038/s41565-021-00975-4 (2021).
17 Han, K., Go, D., Hoenders, D., Kuehne, A. J. C. & Walther, A. Switchable Supracolloidal Coassembly of Microgels Mediated by Host/Guest Interactions. *ACS Macro Lett.* **6**, 310-314, doi:10.1021/acsmacrolett.7b00053 (2017).
18 Han, K. *et al.* Social Self-Sorting of Colloidal Families in Co-Assembling Microgel Systems. *Angew. Chem. Int. Ed.* **56**, 2176-2182, doi:10.1002/anie.201612196 (2017).
19 Heinen, L., Heuser, T., Steinschulte, A. & Walther, A. Antagonistic Enzymes in a Biocatalytic pH Feedback System Program Autonomous DNA Hydrogel Life Cycles. *Nano Lett.* **17**, 4989-4995, doi:10.1021/acs.nanolett.7b02165 (2017).
20 Heinen, L. & Walther, A. Temporal control of i-motif switch lifetimes for autonomous operation of transient DNA nanostructures. *Chem. Sci.* **8**, 4100-4107, doi:10.1039/c7sc00646b (2017).
21 Heuser, T., Merindol, R., Loescher, S., Klaus, A. & Walther, A. Photonic Devices Out of Equilibrium: Transient Memory, Signal Propagation, and Sensing. *Adv. Mater.* **29**, doi:10.1002/adma.201606842 (2017).
22 Heuser, T., Steppert, A. K., Lopez, C. M., Zhu, B. & Walther, A. Generic concept to program the time domain of self-assemblies with a self-regulation mechanism. *Nano Lett.* **15**, 2213-2219, doi:10.1021/nl5039506 (2015).
23 Heuser, T., Weyandt, E. & Walther, A. Biocatalytic Feedback-Driven Temporal Programming of Self-Regulating Peptide Hydrogels. *Angew. Chem. Int. Ed.* **54**, 13258-13262, doi:10.1002/anie.201505013 (2015).
24 Fan, X. & Walther, A. pH Feedback Lifecycles Programmed by Enzymatic Logic Gates Using Common Foods as Fuels. *Angew. Chem. Int. Ed.* **60**, 11398-11405, doi:https://doi.org/10.1002/anie.202017003 (2021).
25 Fan, X. & Walther, A. Autonomous Transient pH Flips Shaped by Layered Compartmentalization of Antagonistic Enzymatic Reactions. *Angew. Chem. Int. Ed.* **60**, 3619-3624, doi:https://doi.org/10.1002/anie.202009542 (2021).
26 Maity, I., Sharma, C., Lossada, F. & Walther, A. Feedback and Communication in Active Hydrogel Spheres with pH Fronts: Facile Approaches to Grow Soft Hydrogel Structures. *Angew. Chem. Int. Ed.* **60**, 22537-22546, doi:https://doi.org/10.1002/anie.202109735 (2021).
27 Sharma, C. & Walther, A. Self-Regulating Colloidal Co-Assemblies That Accelerate Their Own Destruction via Chemo-Structural Feedback. *Angew. Chem. Int. Ed.* , e202201573, doi:10.1002/anie.202201573 (2022).
28 Zhabotinskii, A. M. [PERIODIC COURSE OF THE OXIDATION OF MALONIC ACID IN A SOLUTION (STUDIES ON THE KINETICS OF BEOLUSOV'S REACTION)]. *Biofizika* **9**, 306-311 (1964).
29 Maity, I. *et al.* A chemically fueled non-enzymatic bistable network. *Nat. Commun.* **10**, 4636, doi:10.1038/s41467-019-12645-0 (2019).

30 van Roekel, H. W. H. *et al.* Programmable chemical reaction networks: emulating regulatory functions in living cells using a bottom-up approach. *Chem. Soc. Rev.* **44**, 7465-7483, doi:10.1039/C5CS00361J (2015).

31 Ashkenasy, G., Hermans, T. M., Otto, S. & Taylor, A. F. Systems chemistry. *Chem. Soc. Rev.* **46**, 2543-2554, doi:10.1039/C7CS00117G (2017).

32 Wagner, N., Hochberg, D., Peacock-Lopez, E., Maity, I. & Ashkenasy, G. Open Prebiotic Environments Drive Emergent Phenomena and Complex Behavior. *Life* **9**, 45 (2019).

33 Orban, M. & Epstein, I. R. Systematic design of chemical oscillators. 26. A new halogen-free chemical oscillator: the reaction between sulfide ion and hydrogen peroxide in a CSTR. *J. Am. Chem. Soc.* **107**, 2302-2305, doi:10.1021/ja00294a016 (1985).

34 Rabai, G. & Epstein, I. R. Oxidation of hydroxylamine by periodate in a continuous-flow stirred tank reactor: a new pH oscillator. *J. Phys. Chem.* **93**, 7556-7559, doi:10.1021/j100359a009 (1989).

35 Orban, M. & Epstein, I. R. A new type of oxyhalogen oscillator: the bromite-iodide reaction in a continuous flow reactor. *J. Am. Chem. Soc.* **114**, 1252-1256, doi:10.1021/ja00030a021 (1992).

36 Okazaki, N., Rábai, G. & Hanazaki, I. Discovery of Novel Bromate−Sulfite pH Oscillators with Mn2+ or MnO4- as a Negative-Feedback Species. *J. Phys. Chem. A.* **103**, 10915-10920, doi:10.1021/jp992626l (1999).

37 Kovács, K. M. & Rábai, G. Large Amplitude pH Oscillations in the Hydrogen Peroxide−Dithionite Reaction in a Flow Reactor. *J. Phys. Chem. A.* **105**, 9183-9187, doi:10.1021/jp012007o (2001).

38 Orban, M. & Epstein, I. R. Systematic design of chemical oscillators. 39. Chemical oscillators in group VIA: the copper(II)-catalyzed reaction between hydrogen peroxide and thiosulfate ion. *J. Am. Chem. Soc.* **109**, 101-106, doi:10.1021/ja00235a017 (1987).

39 Edblom, E. C., Orban, M. & Epstein, I. R. A new iodate oscillator: the Landolt reaction with ferrocyanide in a CSTR. *J. Am. Chem. Soc.* **108**, 2826-2830, doi:10.1021/ja00271a007 (1986).

40 Rabai, G. & Beck, M. T. Exotic kinetic phenomena and their chemical explanation in the iodate-sulfite-thiosulfate system. *J. Phys. Chem.* **92**, 2804-2807, doi:10.1021/j100321a021 (1988).

41 Rábai, G., Kaminaga, A. & Hanazaki, I. Mechanism of the Oscillatory Bromate Oxidation of Sulfite and Ferrocyanide in a CSTR. *J. Phys. Chem.* **100**, 16441-16442, doi:10.1021/jp960670k (1996).

42 Orban, M. & Epstein, I. R. A New Bromite Oscillator. Large-Amplitude pH Oscillations in the Bromite-Thiosulfate-Phenol Flow System. *J. Phys. Chem.* **99**, 2358-2362, doi:10.1021/j100008a018 (1995).

43 Orban, M. & Epstein, I. R. Simple and Complex pH Oscillations and Bistability in the Phenol-Perturbed Bromite-Hydroxylamine Reaction. *J. Phys. Chem.* **98**, 2930-2935, doi:10.1021/j100062a032 (1994).

44 Frerichs, G. A. & Thompson, R. C. A pH-Regulated Chemical Oscillator: The Homogeneous System of Hydrogen Peroxide−Sulfite−Carbonate−Sulfuric Acid in a CSTR. *J. Phys. Chem. A.* **102**, 8142-8149, doi:10.1021/jp983070p (1998).

45 Rabai, G., Kustin, K. & Epstein, I. R. Systematic design of chemical oscillators. 57. Light-sensitive oscillations in the hydrogen peroxide oxidation of ferrocyanide. *J. Am. Chem. Soc.* **111**, 8271-8273, doi:10.1021/ja00203a035 (1989).

46 Frerichs, G. A., Mlnarik, T. M., Grun, R. J. & Thompson, R. C. A New pH Oscillator: The Chlorite−Sulfite−Sulfuric Acid System in a CSTR. *J. Phys. Chem. A.* **105**, 829-837, doi:10.1021/jp003363u (2001).

47 Kovács, K. M. & Rábai, G. Mechanism of the oscillatory decomposition of the dithionite ion in a flow reactor. *Chem. Commun.*, 790-791, doi:10.1039/B200981A (2002).

48 Kovacs, K., McIlwaine, R. E., Scott, S. K. & Taylor, A. F. An Organic-Based pH Oscillator. *J. Phys. Chem. A.* **111**, 549-551, doi:10.1021/jp068534v (2007).

49 Niu, H. *et al.* Oscillation alternation in pH oscillator with additional feedback species. *Chem. Phys. Lett.* **757**, 137885, doi:https://doi.org/10.1016/j.cplett.2020.137885 (2020).

50 Lawson, H. S. *et al.* Design of non-autonomous pH oscillators and the existence of chemical beat phenomenon in a neutralization reaction. *Sci. Rep.* **11**, 11011, doi:10.1038/s41598-021-90301-8 (2021).

51 Pešek, O., Schreiberová, L. & Schreiber, I. Dynamical regimes of a pH-oscillator operated in two mass-coupled flow-through reactors. *Phys. Chem. Chem. Phys.* **13**, 9849-9856, doi:10.1039/C1CP20125E (2011).

52 Boiteux, A., Goldbeter, A. & Hess, B. Control of oscillating glycolysis of yeast by stochastic, periodic, and steady source of substrate: a model and experimental study. *Proc. Natl. Acad. Sci. U.S.A.* **72**, 3829-3833, doi:10.1073/pnas.72.10.3829 (1975).

53 Hauser, M. J. B., Fricke, N., Storb, U. & Müller, S. C. Periodic and Bursting pH Oscillations in an Enzyme Model Reaction. *Z. Phys. Chem.* **216**, 375, doi:10.1524/zpch.2002.216.3.375 (2002).

54 Deng, Y., Miyake, T., Keene, S., Josberger, E. E. & Rolandi, M. Proton mediated control of biochemical reactions with bioelectronic pH modulation. *Sci. Rep.* **6**, 24080, doi:10.1038/srep24080 (2016).

55 Bánsági, T. & Taylor, A. F. Modelling Bacteria-Inspired Dynamics with Networks of Interacting Chemicals. *Life* **9**, 63 (2019).

56 Wrobel, Magdalena M. *et al.* pH Wave-Front Propagation in the Urea-Urease Reaction. *Biophys. J.* **103**, 610-615, doi:https://doi.org/10.1016/j.bpj.2012.06.020 (2012).

57 Hu, G., Pojman, J. A., Scott, S. K., Wrobel, M. M. & Taylor, A. F. Base-Catalyzed Feedback in the Urea−Urease Reaction. *J. Phys. Chem. B.* **114**, 14059-14063, doi:10.1021/jp106532d (2010).

58 Bánsági, T. & Taylor, A. F. Role of Differential Transport in an Oscillatory Enzyme Reaction. *J. Phys. Chem. B.* **118**, 6092-6097, doi:10.1021/jp5019795 (2014).

59 Paramonov, S. E., Jun, H.-W. & Hartgerink, J. D. Self-Assembly of Peptide−Amphiphile Nanofibers: The Roles of Hydrogen Bonding and Amphiphilic Packing. *J. Am. Chem. Soc.* **128**, 7291-7298, doi:10.1021/ja060573x (2006).

60 Duan, X. *et al.* Smart pH-Sensitive and Temporal-Controlled Polymeric Micelles for Effective Combination Therapy of Doxorubicin and Disulfiram. *ACS Nano* **7**, 5858-5869, doi:10.1021/nn4010796 (2013).

61 Cingil, H. E., Meertens, N. C. H. & Voets, I. K. Temporally Programmed Disassembly and Reassembly of C3Ms. *Small* **14**, e1802089, doi:10.1002/smll.201802089 (2018).

62 Dowari, P., Das, S., Pramanik, B. & Das, D. pH clock instructed transient supramolecular peptide amphiphile and its vesicular assembly. *Chem. Commun.* **55**, 14119-14122, doi:10.1039/c9cc06934h (2019).

63 Mondal, S., Podder, D., Nandi, S. K., Roy Chowdhury, S. & Haldar, D. Acid-responsive fibrillation and urease-assisted defibrillation of phenylalanine: a transient supramolecular hydrogel. *Soft Matter* **16**, 10115-10121, doi:10.1039/D0SM00774A (2020).

64 Panja, S., Patterson, C. & Adams, D. J. Temporally-Programmed Transient Supramolecular Gels. *Macromol. Rapid Commun.* **40**, e1900251, doi:10.1002/marc.201900251 (2019).

65 Panja, S. & Adams, D. J. Maintaining homogeneity during a sol–gel transition by an autocatalytic enzyme reaction. *Chem. Commun.* **55**, 47-50, doi:10.1039/C8CC08501C (2019).

66 Panja, S., Fuentes-Caparros, A. M., Cross, E. R., Cavalcanti, L. & Adams, D. J. Annealing Supramolecular Gels by a Reaction Relay. *Chem. Mater.* **32**, 5264-5271, doi:10.1021/acs.chemmater.0c01483 (2020).

67 Grzelczak, M., Vermant, J., Furst, E. M. & Liz-Marzan, L. M. Directed self-assembly of nanoparticles. *ACS Nano* **4**, 3591-3605, doi:10.1021/nn100869j (2010).

68 Glotzer, S. C. & Solomon, M. J. Anisotropy of building blocks and their assembly into complex structures. *Nat. Mater.* **6**, 557-562, doi:10.1038/nmat1949 (2007).

69 Man, T. *et al.* Chiral Metamolecules with Active Plasmonic Transition. *ACS Nano* **13**, 4826-4833, doi:10.1021/acsnano.9b01942 (2019).

70 Miele, Y., Bánsági, T., Taylor, A. F. & Rossi, F. in *Advances in Bionanomaterials: Selected Papers from the 2nd Workshop in Bionanomaterials, BIONAM 2016, October 4-7, 2016, Salerno, Italy* (eds Stefano Piotto *et al.*) 63-74 (Springer International Publishing, 2018).

71 Bubanja, I. N., Bánsági, T. & Taylor, A. F. Kinetics of the urea–urease clock reaction with urease immobilized in hydrogel beads. *React. Kinet. Mech. Catal.* **123**, 177-185, doi:10.1007/s11144-017-1296-6 (2018).

72 Muzika, F., Bánsági, T., Schreiber, I., Schreiberová, L. & Taylor, A. F. A bistable switch in pH in urease-loaded alginate beads. *Chem. Commun.* **50**, 11107-11109, doi:10.1039/C4CC03936J (2014).

73 Che, H., Cao, S. & van Hest, J. C. M. Feedback-Induced Temporal Control of "Breathing" Polymersomes To Create Self-Adaptive Nanoreactors. *J. Am. Chem. Soc.* **140**, 5356-5359, doi:10.1021/jacs.8b02387 (2018).

74 Zhong, Y., Li, P., Hao, J. & Wang, X. Bioinspired Self-Healing of Kinetically Inert Hydrogels Mediated by Chemical Nutrient Supply. *ACS Appl. Mater. Interfaces* **12**, 6471-6478, doi:10.1021/acsami.9b20445 (2020).

75 Fusi, G., Giudice, D. D., Skarsetz, O., Stefano, S. D. & Walther, A. Autonomous Soft Robots Empowered by Chemical Reaction Networks. *Adv. Mater.* **n/a**, 2209870, doi:https://doi.org/10.1002/adma.202209870.

76 Berrocal, J. A., Biagini, C., Mandolini, L. & Di Stefano, S. Coupling of the Decarboxylation of 2-Cyano-2-phenylpropanoic Acid to Large-Amplitude Motions: A Convenient Fuel for an Acid-Base-Operated Molecular Switch. *Angew. Chem. Int. Ed.* **55**, 6997-7001, doi:10.1002/anie.201602594 (2016).

77 Del Giudice, D. *et al.* Time Programmable Locking/Unlocking of the Calix[4]arene Scaffold by Means of Chemical Fuels. *Chem. Eur. J.* **26**, 14954-14962, doi:10.1002/chem.202002574 (2020).

78 Ghosh, A., Paul, I., Adlung, M., Wickleder, C. & Schmittel, M. Oscillating Emission of [2]Rotaxane Driven by Chemical Fuel. *Org. Lett.* **20**, 1046-1049, doi:10.1021/acs.orglett.7b03996 (2018).

79 Mariottini, D., Del Giudice, D., Ercolani, G., Di Stefano, S. & Ricci, F. Dissipative operation of pH-responsive DNA-based nanodevices. *Chem. Sci.* **12**, 11735-11739, doi:10.1039/d1sc03435a (2021).

80 Ghosh, A., Paul, I. & Schmittel, M. Time-Dependent Pulses of Lithium Ions in Cascaded Signaling and Out-of-Equilibrium (Supra)molecular Logic. *J. Am. Chem. Soc.* **141**, 18954-18957, doi:10.1021/jacs.9b10763 (2019).

81 Del Giudice, D. *et al.* Time-programmable pH: decarboxylation of nitroacetic acid allows the time-controlled rising of pH to a definite value. *Chem. Sci.* **12**, 7460-7466, doi:10.1039/d1sc01196k (2021).

82 Ghosh, A., Paul, I. & Schmittel, M. Multitasking with Chemical Fuel: Dissipative Formation of a Pseudorotaxane Rotor from Five Distinct Components. *J. Am. Chem. Soc.* **143**, 5319-5323, doi:10.1021/jacs.1c01948 (2021).

83 Jee, E., Bansagi, T., Jr., Taylor, A. F. & Pojman, J. A. Temporal Control of Gelation and Polymerization Fronts Driven by an Autocatalytic Enzyme Reaction. *Angew. Chem. Int. Ed.* **55**, 2127-2131, doi:10.1002/anie.201510604 (2016).

84 Liu, X. *et al.* Magnetic field–driven particle assembly and jamming for bistable memory and response plasticity. *Sci. Adv.* **8**, eadc9394, doi:doi:10.1126/sciadv.adc9394 (2022).

85 Okamoto, Y. & Ward, T. R. Cross-Regulation of an Artificial Metalloenzyme. *Angew. Chem. Int. Ed.* **56**, 10156-10160, doi:10.1002/anie.201702181 (2017).

3 Self-Regulating Colloidal Co-Assemblies that Accelerate their Own Destruction via Chemo-Structural Feedback

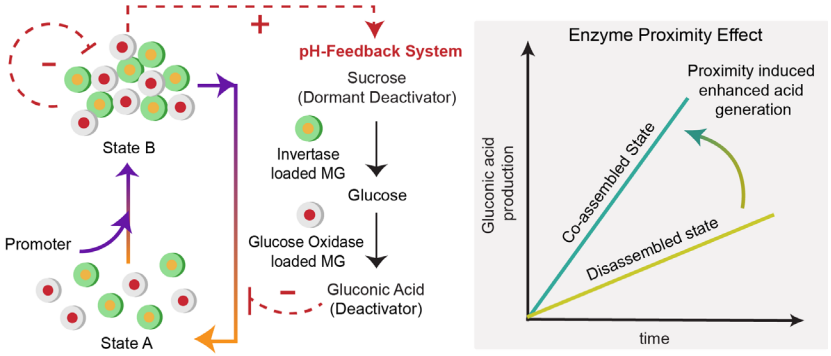

Preliminary note: *This chapter is based on the journal article published in Angew. Chem. Int. Ed. 61, e202201573, doi:10.1002/anie.202201573 (2022) by* ***C. Sharma*** *and A. Walther. Minor changes have been made concerning formatting style.*

Author contributions: C.S. and A.W. conceptualized the project. C.S. conceived, designed, and performed the experiments, and analyzed the data. A.W. conceived and supervised the project. C.S. and A.W. discussed and analyzed the results. C.S. wrote the first draft, C.S and A.W edited and finalized the article.

I thank Dr. S. Ludwanowski for sharing expertise in microgel synthesis, Dr. I Maity and Dr. A. Samanta for discussions.

Abstract: Biological self-assemblies self- and cross-regulate each other via chemical reaction networks (CRNs) and feedback. Although artificial transient self-assemblies have been realized via activation/deactivation CRNs, the transient structures themselves do mostly not engage in the CRN. We introduce a rational design approach for chemo-structural feedback, and present a transient colloidal co-assembly system, where the formed co-assemblies accelerate their destruction autonomously. We achieve this by immobilizing enzymes of a deactivating acid-producing enzymatic cascade on pH-switchable microgels that can form co-assemblies at high pH. Since the enzyme partners are immobilized on individual microgels, the co-assembled state brings them close enough for enhanced acid generation. The amplified deactivator production (acid) leads to an almost two-fold reduction in the lifetime of the transiently formed pH-state. Our study thus introduces versatile mechanisms for chemo-structural feedback.

3.1 Introduction

Biological systems have the capability to assemble relatively simple building blocks into ordered yet dynamic structures that self-regulate and cross-regulate each other autonomously via complex networks of chemical reactions, feedback loops, and/or energy dissipation. This gives rise to emergent properties like signal-processing, motion, and adaptation. In contrast, in synthetic systems, there have been significant advances in hierarchical self-assemblies (SAs) and in making those switchable by sequential application of external "on"/"off" triggers (e.g., pH). However, such systems do typically not feature higher levels of autonomous behavior or self-regulation. Autonomous dynamics and self-regulatory control require the antagonistic pathways of reversible SAs to be pre-organized using appropriately designed kinetics in networks of antagonistic (activating/deactivating) reactions. This generates a time-lapse between activation and deactivation necessary for controlling the time-domain of SAs. Most successful approaches to realize SAs with programmable lifecycles involve either so-called dissipative environments to which a SA is coupled, that is for instance pH-feedback curves or enzymatic ATP-degradation in ATP-co-assembling systems, or so-called dissipative structures, whereby a building block is temporally activated for SA using a chemical fuel. However, in most of these approaches towards temporally programmed, non-equilibrium systems, the intermediately formed SA does not distinctly participate in the deactivation pathways. This is, in fact, unlike biological structures, e.g., microtubules, that feature a catalytic pocket for GTP hydrolysis that activates for GTP hydrolysis when the assembly is formed.[12-15] Such a mechanism - a chemo-structural feedback process – would extend beyond principles of pure chemical feedback and allow for new types of self-regulatory behavior and cooperativity. Only a handful of examples exist – most notably from the peptide and nanofiber SA field – in which dissipative structures engage in the reaction network to catalyze downstream processes. However, rational design of building blocks in such systems remains a challenging task.

To address the challenge of designed chemo-structural feedback, we introduce a concept for temporally self-regulating co-assembling microgel (MG) systems, whereby the assembly of the MGs accelerates its own disassembly. The concept makes use of a pre-organized pH-feedback system (pH-FS), wherein an alkaline trigger leads to assembly, while the counter-trigger is provided by an acid-producing enzymatic cascade (EC). Critically, the two components of the EC are immobilized on individual MGs such that the transient MG co-assembly brings them close enough to enhance the production of the acidic deactivator. The system thereby features an amplified deactivator generation, demonstrating advanced chemo-structural feedback; namely, co-assemblies promote their own destruction.

3.2 Results and Discussion

3.2.1 System design chemo-structural feedback in pH-driven transient co-assemblies in MGs

In more detail, the key concept relies on coupling elements of a deactivating, acid-producing EC (invertase (INV)/glucose oxidase (GOX)) to pH-switchable, co-assembling MGs (**Figure 3-1a**). We chose MGs because they are well dispersible, can be surface-functionalized with interacting groups, and most importantly, can harbor functional molecules (i.e., enzymes) in their interior to allow implementing features of an embodied intelligence for autonomous operation. The MGs need to be equipped with adhesive hetero-complementary supramolecular units (α-cyclodextrin = CD, and azobenzene = AZ) to allow for ordered co-assembly, as well as with weak cationic groups (-N(Me)$_2$) to allow for assembly at high pH and repulsive behavior at low pH. Additionally, each MG partner needs to be equipped with one enzyme of the EC (**Figure 3-1d**). In a final system, starting from a ground State A, where both MGs ($MG_{CD/N(Me)_2,INV}$ and $MG_{AZ/N(Me)_2,GOX}$) are well dispersed in citric acid (CA)/sodium citrate buffer (Na_3C), a solution of an alkaline promoter (tris buffer) containing sucrose as chemical fuel (dormant deactivator) is added. The tris buffer lifts the system to State B thereby activating the MG co-assembly (**Figure 3-1b**). Concurrently, $MG_{CD/N(Me)_2,INV}$ catalyzes the hydrolysis of sucrose to the

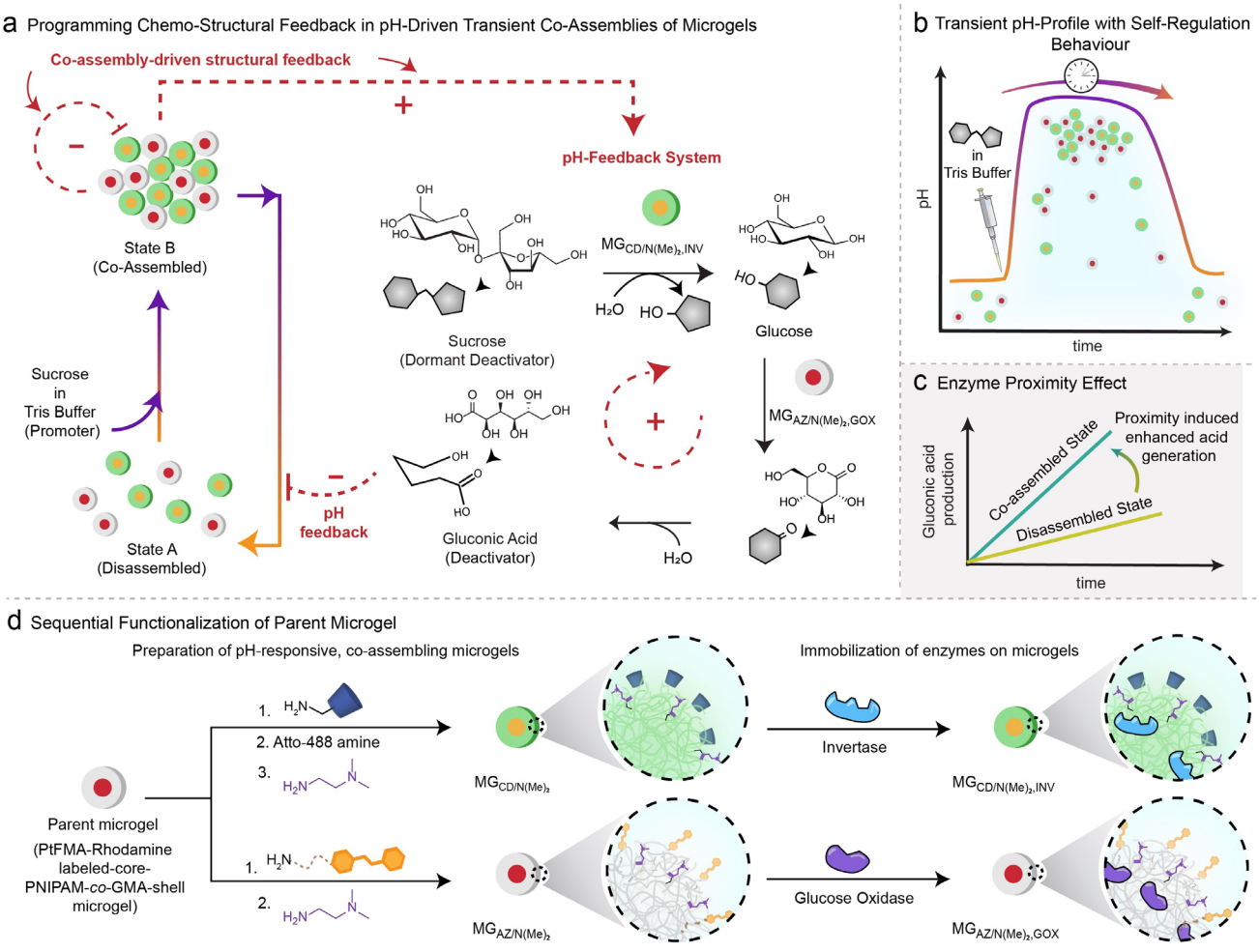

Figure 3-1. System design for rational design of chemo-structural feedback in pH-driven transient co-assemblies of MGs. (a) Addition of promoter (tris buffer) triggers the transient co-assembly of two pH-responsive MGs, (b) whereby each MG carries one enzyme partner of the acid-producing EC (Invertase/Glucose Oxidase; INV/GOX). The EC converts sucrose (dormant deactivator) to gluconic acid which drives the system back to the disassembled state (State A) hence providing negative feedback to the co-assembled state (State B). (c) Enzyme proximity in State B provides a chemo-structural feedback, leading to strongly amplified acid generation and faster disassembly. (d) Sequential functionalization of parent MGs generate two pH-responsive and co-assembling MGs ($MG_{CD/N(Me)_2}$ and $MG_{AZ/N(Me)_2}$) followed by successive enzyme immobilization ($MG_{CD/N(Me)_2,INV}$ and $MG_{AZ/N(Me)_2,GOX}$).

intermediates glucose and fructose. As a result of the co-assembly, the glucose only has a short diffusive pathway to the GOX on $MG_{AZ/N(Me)_2,GOX}$ to yield gluconic acid δ-lactone and finally gluconic acid (**Figure 3-1b,c**; **Figure 3-5**). The latter serves as a deactivator and induces disassembly. We employed MGs with core-shell architecture.

3.2.2 Synthesis and characterization of two co-assembling MGs

The MGs are composed of a water-insoluble poly(2,2,2-trifluoroethyl methacrylate) (PtFMA) core that is refractive index-matched with water and labeled with Rhodamine B for Confocal Fluorescence Laser Scanning Microscopy (CLSM). These cores are surrounded by a water-soluble hydrogel shell composed of *N*-isopropylacrylamide (NIPAM, 90 wt%), *N*,*N*'-methylenebis(acrylamide) (MBA, 1 wt%), and glycidyl methacrylate (GMA, 9 wt%) (**Figure 3-2a**, SI 3.4.3.1 and 3.4.3.2). The MGs have a z-average radius, $\langle R_h \rangle_z$, of 649 nm with a core of $\langle R_h \rangle_z$ = 198 nm as measured by dynamic light scattering (DLS) at pH 7 (**Figure 3-6**). The initiator (2,2'-azobis(2-methylpropionamidine) dihydrochloride) used for the synthesis imparts a minimal positive charge (zeta (ζ)-potential value = + 1.2 mV) to the MGs, that is constant across the entire pH range (**Figure 3-2b**).

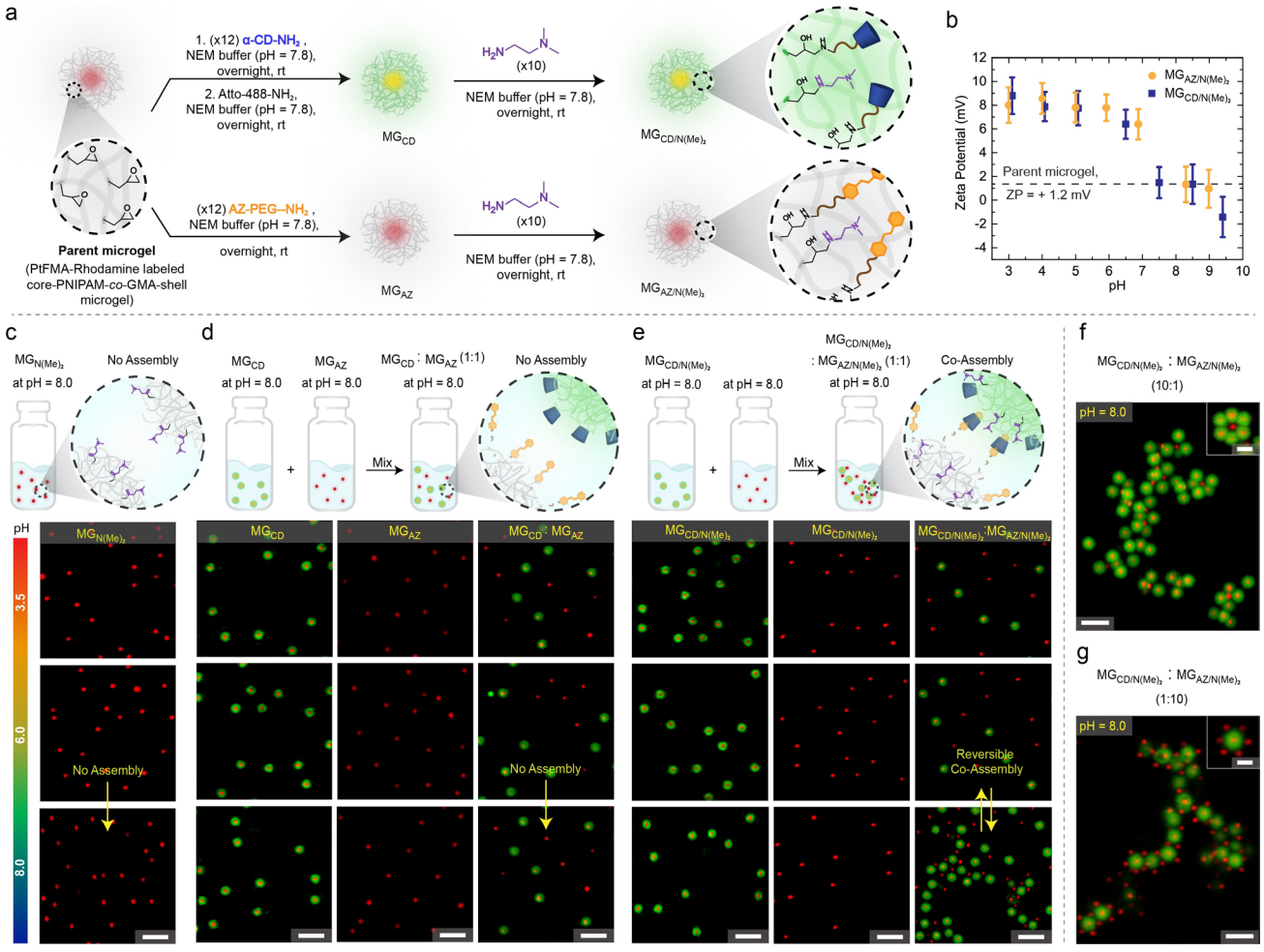

Figure 3-2. Synthesis and characterization of two co-assembling MGs. (a) Synthesis scheme for $MG_{CD/N(Me)_2}$ and $MG_{AZ/N(Me)_2}$ (SI 3.4.3.4). Rhodamine B labels (red channel) are present in the core, while only the shells of CD-containing MGs are labelled with Atto-488 (green channel) to differentiate them from $MG_{AZ/N(Me)_2}$. (b) pH-dependent zeta potential of $MG_{AZ/N(Me)_2}$ and $MG_{CD/N(Me)_2}$. Error bars represents the standard deviation from three independent measurements. (c,d) pH-dependent CLSM images of $MG_{N(Me)_2}$, MG_{CD}, MG_{AZ} and 1:1 mixture of MG_{CD} and MG_{AZ}. (e) pH-dependent CLSM images of $MG_{CD/N(Me)_2}$, $MG_{AZ/N(Me)_2}$ and 1:1 mixture of $MG_{CD/N(Me)_2}$ and $MG_{AZ/N(Me)_2}$. Co-assemblies only occur for the desired $MG_{AZ/N(Me)_2}$/$MG_{CD/N(Me)_2}$ mixture at pH 8.0 and disassemble reversibly at acidic pH. Scale bars (c-e), 3 µm. (f,g) Hierarchical structures for non-stoichiometric mixtures of $MG_{CD/N(Me)_2}$ and $MG_{AZ/N(Me)_2}$. Scale bars (f,g), 3 µm; scale bars in insets, 1 µm. The final concentration of MGs in all suspensions is 0.0064 wt%.

To integrate the MG system to a pH-FS in an alkaline regime (**Figure 3-1a**), the prospective building blocks must be capable of forming reversible SAs at alkaline pH (pH 8-9). Additionally, a hetero-particle aggregation with controlled co-assembly is beneficial to assure spatial proximity of the enzymes of the EC in the co-assembled state. To meet these requirements, we co-functionalized the MGs with pH-responsive *N,N*-dimethylethylenediamine (DMEDA, pK_a ≈ 10.2) and the CD/AZ pairs. CD and AZ are immobilized separately on two batches. This leads to $MG_{AZ/N(Me)2}$ and $MG_{CD/N(Me)2}$ (**Figure 3-2a;** synthetic details in SI 3.4.3.4, **Figure 3-7**). Additionally, we synthesized control MGs, bearing only the DMEDA groups ($MG_{N(Me)2}$) or only the CD and AZ groups (MG_{CD} and MG_{AZ}) using the same reaction protocols to maintain a close to identical functionalization, respectively.[24]

pH-dependent ζ-potential measurements of the amine-modified MGs ($MG_{AZ/N(Me)2}$ and $MG_{CD/N(Me)2}$, $MG_{N(Me)2}$) show a continuously increasing electrostatic repulsion when reducing the pH from 9 to 3 due to increased protonation of the $N(Me)_2$ groups (**Figure 3-2b**, **Figure 3-8**). This contrasts the constant ζ-potential for the parent MGs (flat line in **Figure 3-2**). For accurate treatment of ζ-potential measurements, that are not hard sphere colloids, we refer to literature by Saunders and group.[25] The successful functionalization is further corroborated by DLS, which, for instance, shows a size increment of ~70 nm in the case of MG_{AZ} to $MG_{AZ/N(Me)2}$ functionalization due to increased repulsion between the protonated $N(Me)_2$ groups (**Figure 3-6**).

To probe for the selective co-assembly at alkaline pH, we visualized the dispersions of the controls and of the relevant mixtures via CLSM at pH 3.5, 6.0 and 8.0 (**Figure 3-2c,d**). For better visualization, the MGs bearing CDs were labeled with a green-emitting dye (Atto-488, SI 3.4.3.4), while only the cores are visible in red for the other MGs. Gratifyingly, only mixtures of $MG_{AZ/N(Me)2}$ and $MG_{CD/N(Me)2}$ assemble at high pH, and they do so reversibly (**Figure 3-2e**, **Figure 3-10**). The control, $MG_{N(Me)2}$, does not assemble at high pH (**Figure 3-2c**). This underscores that the low ζ-potential and the slightly hydrophobic stickiness of the deprotonated $N(Me)_2$ groups alone are insufficient for assembly at high pH, but that the attractive interactions provided by the CD/AZ pair are important for the co-assembly. Similarly, the mixture of MG_{AZ} and MG_{CD} without $N(Me)_2$ does also not assemble at high pH, which we associate to the lack of some beneficial hydrophobicity effect of the deprotonated $N(Me)_2$ groups in the co-functionalized MG system (**Figure 3-2d**). Hence both components are important to jointly promote co-assembly at high pH.

Non-stochiometric ratios of $MG_{CD/N(Me)2}$ and $MG_{AZ/N(Me)2}$ lead to core-satellite structures, which underscores that co-assemblies are primarily based on hetero-complementary recognition units, assisted by some hydrophobic effects from $N(Me)_2$ (**Figure 3-2f,g**). Overall, these building blocks and their behavior are the first steps towards chemo-structural feedback.

3.2.3 Enzyme immobilization on MGs and their characterization

To integrate these pH-switchable building blocks with a self-regulating feature brought about by the EC, the MG offsprings bearing the supramolecular units need to be functionalized with the individual enzymes.

To this end, CD-functionalized MGs (MG_{CD} and $MG_{CD/N(Me)2}$) were coupled with INV (**Figure 3-3a**, SI 3.4.3.5) and AZ-modified MGs (MG_{AZ} and $MG_{AZ/N(Me)2}$) with GOX (**Figure 3-3b**, SI 3.4.3.5). Since immobilization can change enzyme activities,[26] we characterized the respective activities using fluorometric activity assays (details on the activity assays are in SI 3.4.3.6,**Figure 3-9**; **Figure 3-3c, d**). Both assays probe for the oxidation of a substrate that is generated by the H_2O_2 side product of the GOX-mediated oxidation of glucose. This means that free GOX has to be present in the activity assay for INV-modified MGs to complete the EC. Overall, the activity of immobilized INV on MGs ($MG_{CD,INV,}$ and $MG_{CD/N(Me)2,INV}$) is higher than that of immobilized GOX ($MG_{AZ,GOX,}$ and

$MG_{AZ/N(Me)_2,GOX}$) (**Figure 3-3c,d**). Importantly, for all enzyme-modified MGs, the assays clearly show a substantial catalytic activity required in later stages.

Towards the final system integration, we performed minimalistic pH assays, aiming at the formation of a transient alkaline pH-FS (**Figure 3-3e,f**, SI 3.4.3.7). To this end, we injected a mixture of respective fuel (sucrose for INV, glucose for GOX) and tris buffer (20 mM, pH 8.8; promoter) into suspensions containing one of the enzyme-loaded MGs. In the case of the INV systems, GOX is additionally provided in the solution. The starting point is a CA/Na_3CA buffer (1.5 mM, pH = 3.5).

In all cases, we find the desired autonomous pH-curves in alkaline regime, which clearly demonstrates the successful operation of the enzymes on the MGs for each individual enzyme-modified MG.

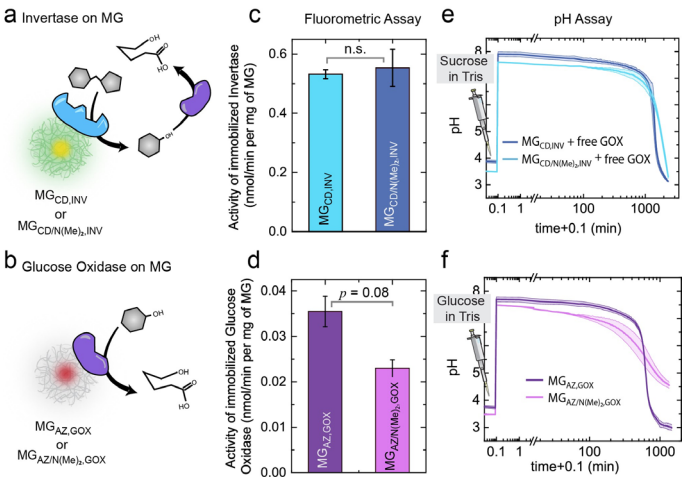

Figure 3-3. Enzyme immobilization on MGs and their characterization. (a,b) Scheme for the catalytic activity. (c,d) Quantified activity of covalently immobilized enzymes by fluorometric assay. (SI 3.4.3.6). Error bars represent the standard deviation from two independent measurements. p value indicated above. n.s. not statistically significant. (e,f) Simplified transient pH-curves using only one enzyme-functionalized MG and either sucrose or glucose as fuel, respectively. Free GOX needs to be added in (e) to complete the EC (SI 3.4.3.7). The shaded areas represent the standard deviation from two independent measurements. Conditions: (e) 200 mM sucrose, 1.5 mM CA/NA_3C (pH 3.5), 20 mM Tris buffer (pH 8.8), 0.14 g/L GOX (here, we used minimum amount of GOX which is required to complete the EC and furnish transient alkaline pH-FS) and concentration of $MG_{CD,INV}$/$MG_{CD/N(Me)_2,INV}$ in the system is 0.0032 wt%.; (f) 200 mM glucose, 1.5 mM CA/NA_3C buffer (pH 3.5), 20 mM tris buffer (pH 8.8) and concentration of $MG_{AZ,GOX}$/$MG_{AZ/N(Me)_2,GOX}$ in the system is 0.0032 wt%.

3.2.4 Chemo-structural feedback in transient co-assemblies of MGs

For the final system integration towards co-assembling systems with chemo-structural feedback (CSF), we define two systems: (i) System REF: A reference system incapable of co-assembly using a 1:1 mixture of $MG_{CD,INV,}$ and $MG_{AZ,GOX}$ (**Figure 3-4a**). (ii) System CSF: Capable of co-assembly, which is composed of a 1:1 mixture of $MG_{CD/N(Me)_2,INV}$ and $MG_{AZ/N(Me)_2,GOX}$ (**Figure 3-4b**). Due to the elemental composition of the MGs, it is not possible to determine the exact quantity of enzyme. This is why we study the system also with enzyme-loaded, but non-assembling MGs (due to lack of supramolecular interactions → System REF). The suspensions for both systems were prepared by mixing the respective MGs in CA/Na_3CA buffer (pH 3.5, 1.5 mM). The addition of sucrose with the promoter tris buffer (pH 8.8, 20 mM) increases the pH rapidly to ca. pH ≈ 8.0 in both systems (**Figure 3-4c**). However, a striking difference in the pH profiles of REF and CSF can be observed. The pH almost remains constant (or slowly decreases) until 20 minutes due to the low activity of enzymes (**Figure 3-5**), after which CSF takes off and demonstrates a decrease in pH. Moreover, REF is clearly associated with a delayed response which ultimately results in a lifetime ($t_{lf,REF}$ ≈ 1390 min) ~1.8 times longer than CSF ($t_{lf,CSF}$ ≈ 780 min).

The lifetime (t_{lf}) is defined as the time that the pH profile takes to decrease to half of initial pH and maximum pH. The delay in REF continues until the recorded end point, where the final pH for CSF (pH_{final} ≈ 3.7) is substantially lower than that for REF (pH_{final} ≈ 4.2). This effect is even more significant because the activity assays in **Figure 3-3d** showed a higher activity of $MG_{AZ,GOX}$ that is used for REF. Concurrently, *ex-situ* CLSM images of REF and CSF confirm that REF remains disassembled over the entire time-period, whereas CSF yields transient co-assembled structures that dissolve autonomously (**Figure 3-4d,e**). Collectively, these results

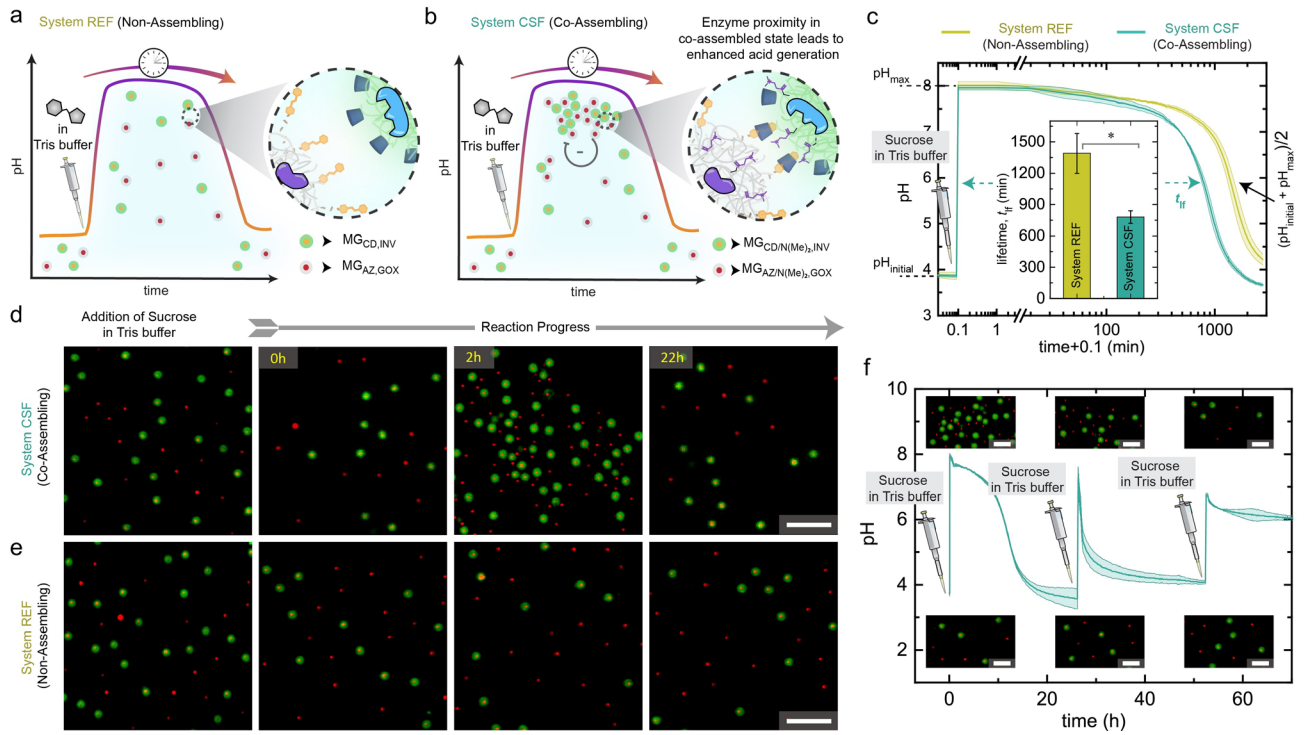

Figure 3-4. Chemo-structural feedback in transient co-assemblies of MGs. (a,b) Schematic representation of two experiments. (a) System REF is composed of 1:1 mixture of two non-assembling microgels $MG_{CD,INV}$ and $MG_{AZ,GOX}$. (b) System CSF is composed of 1:1 mixture of two co-assembling microgels $MG_{CD/N(Me)_2,INV}$ and $MG_{AZ/N(Me)_2,GOX}$. (c) pH profiles and lifetimes of both systems. Error bars represent the standard deviation from two independent measurements.* indicate that $p < 0.05$. (d,e) ex-situ CLSM of System REF (e) and System CSF (d) during the transient state. (f) Re-addition of sucrose in tris to 1:1 mixture of System CSF leads to dampened response. Conditions: 200 mM sucrose, 1.5 mM CA/NA_3C buffer (pH 3.5), 20 mM tris buffer (pH 8.8), and total concentration of MGs in System REF and System CSF is 0.0064 wt%. All shaded areas represent the standard deviation from two independent measurements. Scale bars (d, e), 5 µm; (f), 3 µm.

conclusively show that the presence of co-assemblies in CSF brings the two enzyme partners close enough to enable enhanced operation of the EC.[27] The consequence is amplified acid generation and the emergence of chemo-structural feedback wherein co-assemblies accelerate their own destruction.

In the interest of a more complete description of such transient systems, we also tested for reactivation using the same fueling solution. Re-addition of sucrose in tris buffer to System CSF leads to successive damping in pH response (**Figure 3-4f**). In a second run, the pH rises to only 7.3 because more equivalents of tris are required for neutralization of previously formed gluconic acid. The resulting pH is neither high enough to trigger co-assemblies nor to access a prolonged plateau. The third injection shows lower pH feedback to acidic regime, which can stem from waste accumulation.[27]

3.3 Conclusion

In summary, we introduced a first rational design approach to reach transient colloidal co-assemblies which accelerate their own destruction by chemo-structural feedback. The approach uses co-assembly of enzyme-loaded MGs to force proximity effects for enhancing an acid-producing EC that accelerates disassembly. Such concepts could be generalized to other chemistries, in particular redox systems or systems with specific chemical response. Looking out to the future, truly self-regulating systems, in which self-assembling structures take a prominent role in the reaction network by programming their own destruction, are still in their infancy with limited examples. We believe that the concept proposed in this study allows advancement of transient systems towards autonomously dynamic materials with higher regulatory capacity.

3.4 Experimental

3.4.1 Materials

All chemicals and reagents are purchased from Sigma Aldrich or Merck and used without further purification unless otherwise stated:

2,2,2-trifluoroethyl methacrylate (ABCR GMBH, 99 %), N-isopropylacrylamide (97 %), 2,2'-azobis(2-methylpropionamidine) dihydrochloride (ABCR GMBH, 96 %), divinylbenzene (80 %), acryloxyethyl thiocarbamoyl Rhodamine B (POLYSCIENCES, INC.), Silica60 (0.04 - 0.063 mm, MACHEREY-NAGEL GMBH CO. KG), N,N'-methylenebis(acrylamide) 99%), Glycidyl methacrylate (>97%), Boc-TOTA (IRIS BIOTECH GMBH), Al_2O_3 90 neutral (CARL ROTH GMBH), EDC (ABCR GMBH, 98 %), trifluoroacetic acid (ABCR GMBH, 99 %) and $NaHCO_3$ (CARL ROTH GMBH, >99.5 %), $CDCl_3$ (Euriso-top, 99.80 %), dichloromethane (VWR INTERNATIONAL, >99 %), ethyl acetate (VWR INTERNATIONAL, >99 %), MeOH (FISHER CHEMICALS, 99.8 %), cyclohexane (VWR INTERNATIONAL, >99 %), 3A-Amino-3A-deoxy- (2A *S* , 3A *S*) -α-cyclodextrin (TCI, >90.0%), Atto 488 amine (ATTO-TEC GMBH), Azobenzene-4-sulfonyl chloride (TCI, ≥ 98%), Triethylamine (≥99.5%), citric acid monohydrate (CA, BioXtra, ≥99.5%), trisodium citrate dihydrate (Na_3C, BioXtra, ≥99.0%), sodium dihydrogen phosphate (BioXtra, ≥99.0%), disodium hydrogen phosphate (BioXtra, ≥99.0%), tris(hydroxymethyl)aminomethane (Tris, BioXtra, ≥99.9%), hydrochloride acid (36.5-38.0%, bioreagent), *N, N*-dimethylethylenediamine (95%), invertase from baker's yeast (S. cerevisiae) (Inv, grade VII, ≥300 units/mg solid), glucose oxidase from Aspergillus niger (GOX, Type VII, lyophilized powder, ≥100,000 units/g solid), sucrose (≥99%), glucose (BioXtra, ≥99.5%). Activity assay kits of invertase and glucose oxidase were bought from BioVision (Catalog #K674-100). MilliQ water was used throughout all experiments.

3.4.2 General Characterization Methods and Instruments

DLS measurements were performed on the LS Instruments NanoLab 3D at 25 °C operating with a red laser (λ = 685 nm) and a scattering angle of Θ = 90 ° using standard disposable PS cuvettes (BRAND GmbH & Co. KG). The distributions of the hydrodynamic radii were obtained by a CONTIN mode analysis.

ζ-potential of microgels was measured using a Zetasizer Nano-ZS (Malvern Panalytical GmbH) at 25 ° C. All samples were measured in triplicate in disposable folded capillary cells. pH was maintained using a 907 Titrando auto-titrator (Metrohm, Switzerland), and titrations were performed using 0.1 M NaOH and 0.1 M HCl at 25 °C.

Confocal laser scanning microscopy (CLSM) was performed on Leica Stellaris 5 microscope with four laser lines and three HyD S detectors using plan-apochromat objectives (63×, 1.40 numerical aperture, oil immersion).

The evolutions of the pH profiles were recorded on a 12-channel pH monitoring system by EA Instruments at 25 °C. Electrodes were calibrated by calibration buffers (pH= 4, 7, 10) each time before using them.

The temperature-controlled fluorescence measurements were performed on a TECAN (Spark model) microplate plate reader using Costar® 96-Well black polystyrene plate.

p values are calculated by performing a t-Test (Two-Sample Assuming Equal Variances) in Microsoft excel using a built-in Data analysis tool pack.

3.4.3 Methods

3.4.3.1 Synthesis of surfactant-free, poly(2,2,2-trifluoroethyl methacrylate)-Rhodamine labeled core particles:

Divinylbenzene (DVB) and 2,2,2-trifluoroethyl methacrylate (tFMA) were purified using column chromatography (Al_2O_3, neutral). The initiator 2,2'-azobis(2-methylpropionamidine) dihydrochloride (V50, 160

mg, 590 µmol) was dissolved in deionized water (44 mL), degassed (25 min) and thermostated at 70 °C for 15 min. To a solution of DVB (15.4 mg, 118 µmol, 1 mol %) and TFMA (1.98 g, 11.8 mmol), a solution of acryloxyethyl thiocarbamoyl Rhodamine B (1.5 mg) and *N*-isopropylacrylamide (NIPAM, 150 mg, 1.3 mmol) in water (4.3 mL) were added. The mixture was ultrasonicated for 2 minutes and degassed (10 min). The resulting mixture was added dropwise (over a period of 5 min) to the initiator solution starting the polymerization. The reaction mixture was stirred at 70 °C for 6 h (stirring rate = 600 rpm). The resulting dispersion was filtered while hot and dialyzed against deionized water (MWCO 8000 Da), and dispersion with a solid content of 35.6 mg/mL was observed upon freeze-drying.

3.4.3.2 Synthesis of the PNIPAM shell to yield PtFMA-Rhodamine labelled-core-PNIPAM-co-GMA-shell microgel (MGs) particles:

NIPAM (1.4g, 12.8 mmol, 80.5 wt %) was dissolved in deionized water (100 mL) together with the cross-linker *N*,*N*'-methylenebis(acrylamide) (MBA, 12.6 mg, 81.7 µmol, 1.0 wt %). The core particles (4.7 mL, 35.6 mg/mL, 166 mg solids content, 9.5 wt %) were added and the mixture was degassed for 30 min and heated to 72 °C. The initiator V50 (75.9 mg, 0.3 mmol) was dissolved in water (30 mL) and degassed (15 min). The polymerization was initiated by dropwise addition of initiator solution to heated reaction mixture and stirred (stirring rate = 350 rpm). After 10 minutes, degassed Glycidyl methacrylate (GMA, 162 mg, 150.7 µL, 1.1 mmol, 9 wt %) after purification by column chromatography (Al_2O_3, neutral) was added dropwise into the reaction mixture. The stirring rate was increased to 600 rpm and reaction was allowed to run for 4 hours. The resulting core/shell MG particles (amount of GMA moieties assuming full conversion = 633.8 µmol per g of MG) were filtered while hot and purified by dialysis (MWCO 8000 Da) against deionized water. The resulting core-shell MGs were further purified via centrifugation (5 x 25 min, 11000 rpm, 15 °C replacement of the supernatant with Milli Q water per centrifugation step).

3.4.3.3 Synthesis of Guest, AZ-PEG-NH_2:

Step I: Azobenzene-4-sulfonyl chloride (1.3 g, 4.6 mmol) in DCM (dichloromethane) solution (65 mL) was dropped slowly (0.5 h) to a vigorously stirred 165 mL DCM solution containing 1-(*t*-Butyloxycarbonyl-amino)-4,7,10-trioxa-13-tridecanamine (Boc-TOTA, 3.0 g, 9.3 mmol, 2 eq.) and triethylamine (TEA, 0.5 g, 0.6 mL, 4.6 mmol) mixture in an ice bath, and then stirred at room temperature overnight. Subsequently, DCM was removed by a rotary evaporator, and the residue was dissolved into ethyl acetate. The solution was washed with a saturated $NaHCO_3$ solution, and the solvent was removed under reduced pressure. The resulting oil (AZ-PEG-NHBoc) was purified using column chromatography (SiO_2, DCM/MeOH, 8:2, R_f = 0.8), and the product (2.3 g) was obtained as an orange oil. ^{1}H NMR (300 MHz, DMSO-d6): d (ppm) = 7.96 (4H); 7.89 (2H); 7.48 (3H); 5.75 (1H); 4.85 (1H); 3.59 (6H); 3.47 (6H); 3.11 (4H); 1.67 (4H) and 1.35 (9H).

Step II: AZ-PEG-NHBoc (2.3 g, 4.1 mmol) was dissolved in DCM (12 mL), and the solution was cooled to 0 °C. Trifluoroacetic acid (TFA, 11.8 g, 103.6 mmol, 25 eq.) was added dropwise and the solution was stirred at RT for 3 h. Afterward, the solvent was removed under reduced pressure and the resulting oil was dissolved in

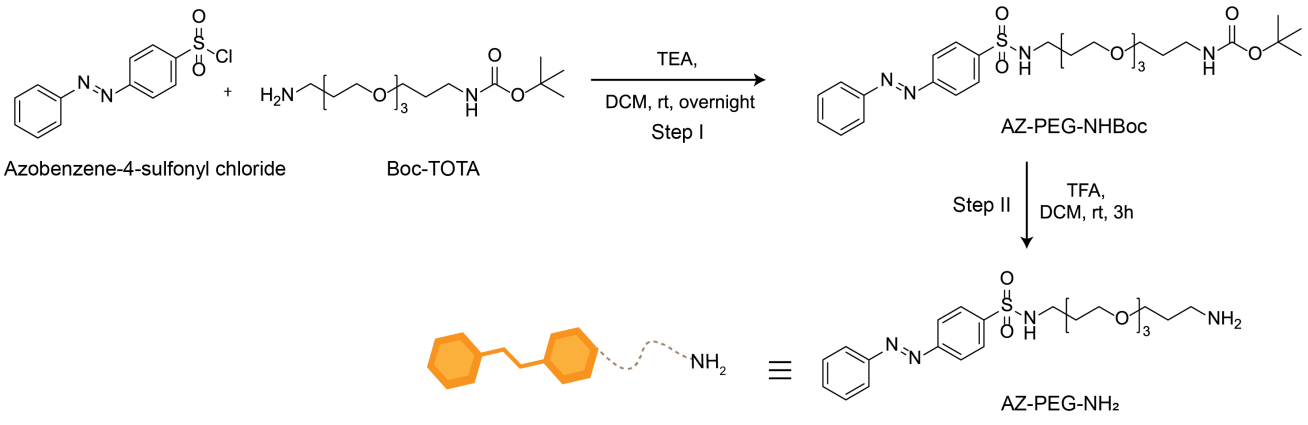

water (40 mL) and washed with ethyl acetate (3 × 10 mL). The aqueous solution was freeze-dried, and the desired product was obtained as a deep orange liquid. ^{1}H NMR (300 MHz, DMSO-d6): d (ppm) = 8.01 (6H); 7.58 (3H); 6.82 (1H); 3.66 (12 H); 3.26 (2H); 3.13 (2H); 2.01 (2H) and 1.62 (2H). HRMS (ESI) calculated for $[M + H]^+$ $C_{22}H_{33}N_4O_5S$ 465.2166, found 465.2165.

3.4.3.4 Functionalization reactions on parent MG

Functionalization of parent MG with *N, N*-dimethylethylenediamine (DMEDA) to produce $MG_{N(Me)_2}$.

First, 34.1 mg of DMEDA (ca. 10-fold excess with respect to GMA moieties in the MG shell) was dissolved in 5 mL of N-ethylmorpholine (NEM) buffer (200 mM, pH = 8.2). To this, 5 mL of parent MG suspension (12.2 mg/mL) was added. The mixture was stirred overnight at room temperature. The resulting modified core-shell MGs, $MG_{N(Me)_2}$ were purified via centrifugation (3 x 10 min, 11000 rpm, 15 °C replacement of the supernatant with 5 mL Milli Q water per centrifugation step).

Sequential functionalization of parent MG to produce MG_{AZ} and $MG_{AZ/N(Me)_2}$.

First, 215.7 mg of AZ-PEG-NH_2 (ca. 12-fold excess with respect to GMA moieties in the MG shell) was dissolved in 5 mL of N-ethylmorpholine (NEM) buffer (200 mM, pH = 8.2). To this, 5 mL of parent MG suspension (12.2 mg/mL) was added. The mixture was stirred overnight at room temperature. The resulting modified core-shell MGs, MG_{AZ} were purified via centrifugation (3 x 10 min, 11000 rpm, 15 °C replacement of the supernatant with 5 mL Milli Q water per centrifugation step). The change in the color of the precipitated MG from light pink (from Rhodamine B in the cores) to orange/peach after functionalization with AZ provides macroscopic proof for the successful linkage (**Figure 3-7**). 2.5 mL of MG_{AZ} was reserved for further experiments, and the rest 2.5 mL was further functionalized with DMEDA (ca. 10-fold excess with respect to GMA moieties in the MG shell) as described in section 4.4.1 to produce $MG_{AZ/N(Me)_2}$.

Sequential functionalization of parent MG to produce MG_{CD} and $MG_{CD/N(Me)2}$.

First, 451.5 mg of 3A-Amino-3A-deoxy- (2A *S*, 3A *S*) -α-cyclodextrin (α-CD, ca. 12-fold excess with respect to GMA moieties in the MG shell) was dissolved in 5 mL of N-ethylmorpholine (NEM) buffer (200mM, pH = 8.2). To this, 5 mL of parent MG suspension (12.2 mg/mL) was added. The mixture was stirred overnight at room temperature. The resulting modified core-shell MGs, MG_{CD} were purified via centrifugation (3 x 10 min, 11000 rpm, 15 °C replacement of the supernatant with 8 mL Milli Q water per centrifugation step). 2.5 mL of MG_{CD} was reserved for further experiments, and the rest 2.5 mL was further functionalized with DMEDA (ca. 10-fold excess with respect to GMA moieties in the MG shell) as described in section 4.4.1 to produce $MG_{CD/N(Me)_2}$. There is no color change in precipitates of MG_{CD} since α-CD is a colorless solid.

For preparing CLSM samples, MG_{CD} was functionalized with Atto-488-amine in the shell. 0.1 equivalent of Atto-488-amine (4 mg/mL, stock solution prepared in DMSO) with respect to GMA moieties in the MG shell was dispersed in PBS buffer (pH = 7.4), to which respective MG suspension was added. The reaction mixture was stirred overnight at 25 °C. The resulting dye-labeled core-shell MGs were purified via centrifugation (3 x 10 min, 11000 rpm, 15 °C replacement of the supernatant with Milli Q water per centrifugation step). Further functionalization reaction with DMEDA was performed as described in Section 4.4.1.

It is important to mention that an exact quantification of functionalizations at each step is hardly feasible due to the small contents and overlap in elemental analysis or spectroscopic techniques. However, all reaction protocols maintain 12 equivalents of CD/AZ pairs and 10 equivalents of DMEDA with respect to GMA in the MG shell to achieve identical functionalizations.

3.4.3.5 Enzyme Immobilization:

Immobilization of Invertase (INV) on MGs (MG).[2,28,29]

The stock solution of INV (2 g/L) was freshly prepared as needed in the citric acid/sodium citrate (CA/Na_3CA) buffer (1.5 mM, pH = 5.5). Enzyme functionalization was done on core-shell beads, bearing epoxide groups in their shell. First, 5 mg of the INV was dissolved in 3 mL of respective buffer. Next, 1 mL of MG suspension (12.2 mg/mL) was added to 2 mL of respective buffer. To this mixture, 1 mL of enzyme solution was added, and the reaction was stirred overnight at room temperature. The functionalized core-shell MGs were purified via centrifugation (3 x 10 min, 11000 rpm, 15 °C, replacement of the supernatant with Milli Q water per centrifugation step).

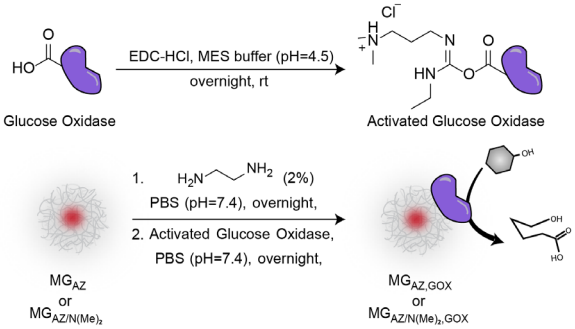

Immobilization of Glucose Oxidase (GOX) on MG.

A three-step reaction achieves the spacer-mediated immobilization of GOX on MGs. In the first step, a spacer arm was introduced on the MGs for which 1 mL of MG suspension was stirred in phosphate buffer solution (PBS, 10 mM, pH = 7.4) containing 0.1 equivalent of ethylenediamine (with respect to GMA groups on MGs) overnight at 25°C. After the completion of reaction, MGs were purified via centrifugation (3 x 10 min, 11000 rpm, replacement of the supernatant with PBS buffer per centrifugation step). Next, activation of carboxyl acid groups in GOX (6 mg) was carried out by stirring with 1-ethyl-3-(3-dimethylaminopropyl) carbodiimide hydrochloride (EDC, 1.5 mg) in 2.4 mL of 2-(N-morpholino) ethane sulfonic acid buffer (MES, 10 mM, pH = 4.5) for 25 minutes at 25 °C. Finally, 1.2 mL solution of activated enzyme is added to aminated MGs prepared in first step and mixture is stirred overnight at 25 °C. The GOX immobilized MGs were purified via centrifugation (3 x 10 min, 11000 rpm, 15 °C, replacement of the supernatant with Milli Q water per centrifugation step).

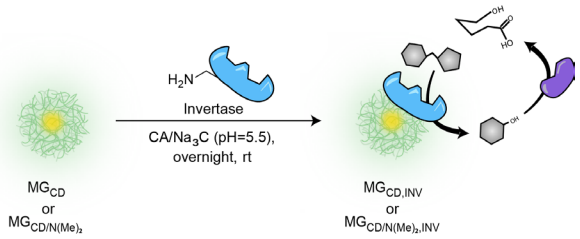

3.4.3.6 Activity determination of immobilized enzymes by fluorometric assay

INV activity measurement

INV activity assay kit from Bio Vision (Catalog #K674-100) was adopted to measure the activity of immobilized INV, $M_{CD,INV}$ and $MG_{CD/N(Me)2,INV}$. We followed the protocol of the assay kit but did not take background control as it was insignificant for our samples. The assay kit has the following components: INV hydrolysis buffer, INV assay buffer, INV stop solution, OxiRed™ probe in DMSO, INV enzyme mix, INV substrate, glucose standard (100 mM), and positive control.

Calibration curve: 1 mM glucose standard solution was prepared by diluting 10 µL 100 mM glucose standard with 990 µL MilliQ water. 1 mM glucose standard solution was further diluted with MilliQ water to make 0.1 mM stock solution of glucose standard. 0, 2, 4, 6, 8, and 10 µL of 0.1 mM glucose standard solution was

pipetted to a 96-well plate, INV hydrolysis buffer was added to adjust the total volume to 50 µL. 10 µL INV stop solution, 36 µL INV assay buffer, 2 µL INV enzyme mix, and 2 µL probe were added to the glucose solution to make a total volume of 100 µL. The well plate was incubated at 25 °C for 30 min in dark place, then the fluorescence (Ex/Em = 535/585 nm) was measured with a plate reader. Zero standard record was subtracted from all records and calibration curves were plotted. The calibration curve is shown in **Figure 3-9a**.

INV activity measurement: I) Preparation of INV sample: 250 µL of respective MG suspension (0.2 mg/mL) was centrifuged (5 min, 11000 rpm) and the Milli Q water was replaced with INV hydrolysis buffer to make a final volume of 40 µL. Positive control of INV sample: 4 µL positive control solution was diluted with 36 µL hydrolysis buffer. ii) Substrate hydrolysis: 10 µL of INV substrate was added into wells containing INV sample and positive control. Then the plate was incubated at 25 °C (same as the temperature at which all experiments in the main text were carried out) for 30 min. After the incubation, 10 µL of INV stop solution, a mixture of 36 µL assay buffer, 2 µL Inv enzyme mix, and 2 µL probe was sequentially added to each well, including INV sample and positive control. The well plate was incubated at 25 °C for 30 min in a dark place, then fluorescence (Ex/Em = 535/585 nm) was measured with a plate reader. iv) Calculation: Zero standard record was subtracted from all records and the calibration curve was plotted. The fluorescence record of INV sample was applied to calibration curves to get the amount of glucose generated by sample INV during the incubation at 25 °C. The activity of sample INV was calculated using the following equation:

$$\text{Activity}=n/(m*t)\ \text{nmol}/(\text{min}*\text{mg})$$

where: n is the amount of glucose generated by sample INV (nmol); m is the amount of sample INV added into the well plate (mg); t is the incubation time at 25 °C (min). **Figure 3-3** in the main text presents the activity of $MG_{CD,INV}$ and $MG_{CD/N(Me)_2,INV}$.

GOX activity measurement

GOX activity assay kit from BioVision (Catalog #K788-100) was used to measure the activity of immobilized GOX, $MG_{AZ,GOX}$ and $MG_{AZ/N(Me)_2,GOX}$. We followed the assay kit protocol but did not take background control as it was insignificant for our samples. The assay kit has the following components: GOX assay buffer, OxiRed™ probe, GOX substrate, GOX developer, GOX positive control, and H_2O_2 standard (0.88 M).

Calibration curve: 10 µL of 0.8 M H_2O_2 standard was added to 870 µL MilliQ water to make an H_2O_2 solution with a concentration of 10 mM. Then 5 µL 10 mM H_2O_2 solution was diluted with 45 µL assay buffer to a concentration of 1 mM. 1mM glucose standard solution was further diluted with MilliQ water to make 0.1 mM stock solution of H_2O_2 standard. 0, 2, 4, 6, 8, and 10 µL of 0.1 mM H_2O_2 standard solution was pipetted to a 96-well plate, and assay buffer was added to each well to adjust the volume to 50 µL. A mixture of 36 µL assay buffer, 2 µL GOX developer, 2 µL OxiRed™ probe, and 10 µL GOX substrate was added to the H_2O_2 solution and homogeneously mixed. The plate was incubated at 25 °C for 5 min and then the fluorescence (Ex/Em = 535/585 nm) was measured with a plate reader. The zero standard record was subtracted from all records and the calibration curve was plotted. Calibration curves is shown in **Figure 3-9b**.

GOX activity measurement: i) Preparation of GOX sample: 250 µL of respective MG suspension (0.2 mg/mL) was centrifuged (5 min, 11000 rpm) and the Milli Q water was replaced with GOX assay buffer to make a final volume of 40 µL. Positive control: 4 µL of positive control solution was diluted with 46 µL GOX assay buffer. ii) Kinetics measurement: A mixture of 36 µL assay buffer, 2 µL GOX developer, 2 µL OxiRed™ probe, and 10 µL GOX substrate was added to GOX sample and positive control, and homogeneously mixed. The well plate was incubated for 30 min, 25 °C. The fluorescence (Ex/Em = 535/585 nm) of GOX sample and positive control was measured after incubation at 25 °C iii) Calculation: Zero standard record was subtracted from all records and calibration curve was plotted. The fluorescence record of GOX sample was applied to calibration curves to get

the amount of H_2O_2 generated by sample GOX during the incubation at 25 °C. The activity of GOX sample can be calculated using the following equation:

$$\text{Activity} = n/(m*t) \text{ nmol}/(\text{min}*\text{mg})$$

where: n is the amount of H_2O_2 generated by GOX sample (nmol); m is the amount of GOX sample added into the well plate (mg); t is the incubation period at 25 °C (min). **Figure 3-3d** in main text presents the activity of $MG_{AZ,GOX}$ and $MG_{AZ/N(Me)_2,GOX}$.

3.4.3.7 Qualitative assessment of immobilized enzymes by pH assay

pH assay for INV

250 µL (0.2 mg/mL) of INV immobilized MG ($MG_{CD,\ INV}$ and $MG_{CD/N(Me)_2,\ INV}$) was first diluted with 250 µL of MilliQ water. To this suspension, 750 µL of CA/Na_3CA buffer (1.5 mM, pH = 3.5) containing 0.2 mg of GOX was added. pH-assay was initiated by addition of 500 µL of tris buffer (20mM, pH 8.8) containing 200 mM sucrose. pH profiles are recorded to observe any change in the pH (**Figure 3-3e** in main text). All pH-profiles are an average of two measurements recorded simultaneously.

pH assay for GOX

250 µL (0.2 mg/mL) of GOX immobilized MG ($MG_{AZ,\ GOX}$ and $MG_{AZ/N(Me)_2,\ GOX}$) was first diluted with 250 µL of MilliQ water. To this suspension, 750 µL of CA/ Na_3CA buffer (1.5 mM, pH = 3.5) was added. pH-assay was initiated by addition of 500 µL of tris buffer (20 mM, pH 8.8) containing 200 mM sucrose. pH-profiles are recorded to observe any change in the pH (**Figure 3-3f** in main text). All pH-profiles are an average of two measurements recorded simultaneously.

3.4.3.8 Supporting Figures

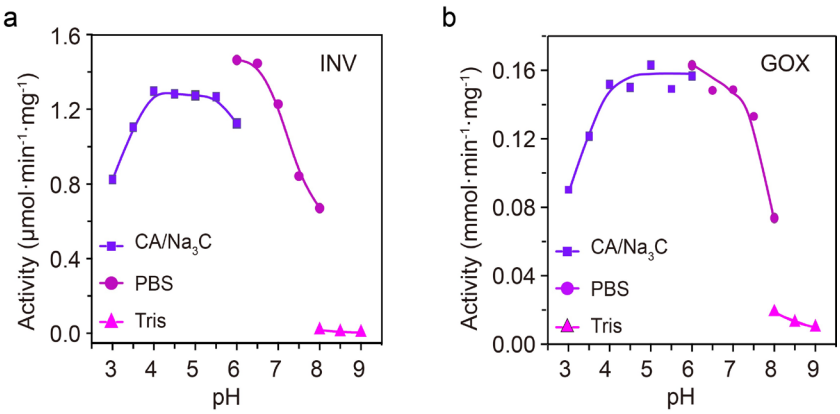

Figure 3-5. pH-dependent enzyme activities. Both INV (a) and GOX (b) have bell-shaped pH-dependent activity curves with weak activity at high pH (8-9), which increases rapidly as the pH decreases below 7. Thereafter, the activity remains nearly constant until pH 4, and decreases again at lower pH. Therefore, the formation of gluconic acid during the deactivation pathway first exerts a positive feedback loop, self-accelerating the metabolic chain of the EC, and ultimately provides a negative feedback loop to the enzymatic activity, flattening off the pH response.

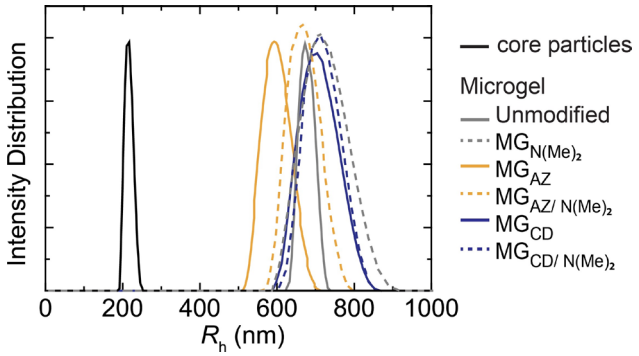

Figure 3-6. DLS CONTIN plots of: poly(2,2,2-trifluoroethyl methacrylate) (PtFMA) core, parent MG, $MG_{N(Me)_2}$, MG_{AZ}, $MG_{AZ/N(Me)_2}$, MG_{CD}, $MG_{CD/N(Me)_2}$. Due to its hydrophobicity, azobenzene when embedded in microgels (MG_{AZ}) leads to water expulsion and subsequent shrinking exhibiting lower z-average radius, $\langle R_h \rangle_z$ than unmodified MG. The suspensions were prepared in MilliQ water with a final concentration of 0.05 mg/mL.

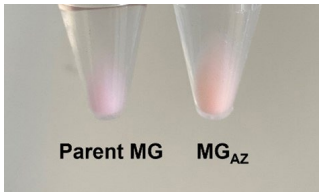

Figure 3-7. Photographs of the centrifuged samples. (a) Parent MG and (b) MG_{AZ}, obtained after functionalization of parent MG with AZ-PEG-NH_2. The change in the color of the suspensions from pink to orange/peach is a macroscopic proof for a successful linkage.

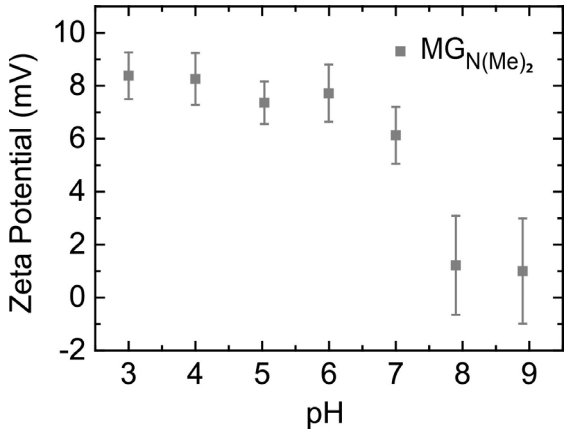

Figure 3-8. pH-dependent surface ζ-potential values of $MG_{N(Me)_2}$. The electrostatic repulsions decrease upon increasing the pH from 3 to 9. The error bars represent the standard deviation from three independent measurements.

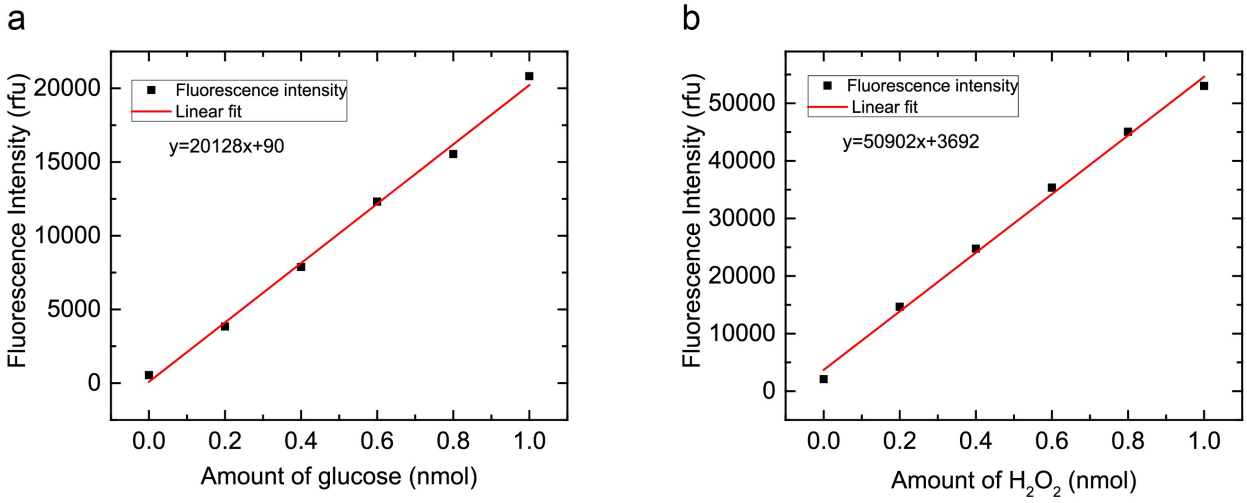

Figure 3-9. Calibration curves of: (a) glucose standard solutions and (b) H_2O_2 solutions.

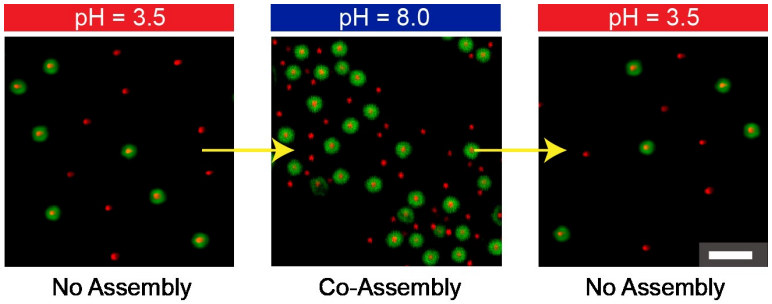

Figure 3-10. pH-dependent CLSM images of 1:1 mixture of $MG_{CD/N(Me)_2}$ and $MG_{AZ/N(Me)_2}$. Co-assemblies only occur at pH 8.0 and disassemble reversibly at acidic pH. Scale bar, 3 µm. The final concentration of MGs in the suspensions is 0.0064 wt%.

3.5 References

1 Han, K. *et al.* Social Self-Sorting of Colloidal Families in Co-Assembling Microgel Systems. *Angew. Chem. Int. Ed.* **56**, 2176-2182, doi:https://doi.org/10.1002/anie.201612196 (2017).

2 Heuser, T., Steppert, A. K., Lopez, C. M., Zhu, B. & Walther, A. Generic concept to program the time domain of self-assemblies with a self-regulation mechanism. *Nano Lett.* **15**, 2213-2219, doi:10.1021/nl5039506 (2015).

3 Maiti, S., Fortunati, I., Ferrante, C., Scrimin, P. & Prins, L. J. Dissipative self-assembly of vesicular nanoreactors. *Nat. Chem.* **8**, 725-731, doi:10.1038/nchem.2511 (2016).

4 Pezzato, C. & Prins, L. J. Transient signal generation in a self-assembled nanosystem fueled by ATP. *Nat. Commun.* **6**, 7790, doi:10.1038/ncomms8790 (2015).

5 Boekhoven, J. *et al.* Dissipative Self-Assembly of a Molecular Gelator by Using a Chemical Fuel. *Angew. Chem. Int. Ed.* **49**, 4825-4828, doi:https://doi.org/10.1002/anie.201001511 (2010).

6 Boekhoven, J., Hendriksen, W. E., Koper, G. J., Eelkema, R. & van Esch, J. H. Transient assembly of active materials fueled by a chemical reaction. *Science* **349**, 1075-1079, doi:10.1126/science.aac6103 (2015).

7 Heckel, J., Loescher, S., Mathers, R. T. & Walther, A. Chemically Fueled Volume Phase Transition of Polyacid Microgels. *Angew. Chem. Int. Ed.* **60**, 7117-7125, doi:https://doi.org/10.1002/anie.202014417 (2021).

8 Heinen, L. & Walther, A. Programmable dynamic steady states in ATP-driven non-equilibrium DNA systems. *Sci. Adv.* **5**, eaaw0590, doi:10.1126/sciadv.aaw0590 (2019).

9 Suzuki, D., Taniguchi, H. & Yoshida, R. Autonomously oscillating viscosity in microgel dispersions. *J. Am. Chem. Soc.* **131**, 12058-12059, doi:10.1021/ja904677g (2009).

10 Plamper, F. A. & Richtering, W. Functional Microgels and Microgel Systems. *Acc. Chem. Res.* **50**, 131-140, doi:10.1021/acs.accounts.6b00544 (2017).

11 Scheffold, F. Pathways and challenges towards a complete characterization of microgels. *Nat. Commun.* **11**, 4315, doi:10.1038/s41467-020-17774-5 (2020).

12 Harada, A., Kobayashi, R., Takashima, Y., Hashidzume, A. & Yamaguchi, H. Macroscopic self-assembly through molecular recognition. *Nat. Chem.* **3**, 34-37, doi:10.1038/nchem.893 (2011).

13 Moratz, J., Samanta, A., Voskuhl, J., Mohan Nalluri, S. K. & Ravoo, B. J. Light-Triggered Capture and Release of DNA and Proteins by Host–Guest Binding and Electrostatic Interaction. *Chem. Eur. J.* **21**, 3271-3277, doi:https://doi.org/10.1002/chem.201405936 (2015).

14 Li, Q.-L., Gu, W.-X., Gao, H. & Yang, Y.-W. Self-assembly and applications of poly(glycidyl methacrylate)s and their derivatives. *Chem. Commun.* **50**, 13201-13215, doi:10.1039/C4CC03036B (2014).

15 Daly, E. & Saunders, B. R. Temperature–dependent electrophoretic mobility and hydrodynamic radius measurements of poly(N-isopropylacrylamide) microgel particles: structural insights. *Phys. Chem. Chem. Phys.* **2**, 3187-3193, doi:10.1039/B002678F (2000).

16 Jia, F., Narasimhan, B. & Mallapragada, S. Materials-based strategies for multi-enzyme immobilization and co-localization: A review. *Biotechnol. Bioeng.* **111**, 209-222, doi:10.1002/bit.25136 (2014).

17 Castellana, M. *et al.* Enzyme clustering accelerates processing of intermediates through metabolic channeling. *Nat. Biotechnol.* **32**, 1011-1018, doi:10.1038/nbt.3018 (2014).

18 Wong, C. M., Wong, K. H. & Chen, X. D. Glucose oxidase: natural occurrence, function, properties and industrial applications. *Appl. Microbiol. Biotechnol.* **78**, 927-938, doi:10.1007/s00253-008-1407-4 (2008).

19 Mansour, E. H. & Dawoud, F. M. Immobilization of invertase on celite and on polyacrylamide by an absorption procedure. *J. Sci. Food Agric.* **83**, 446-450, doi:https://doi.org/10.1002/jsfa.1390 (2003).

20 Peng, G., Hou, X., Liu, B., Chen, H. & Luo, R. Stabilized enzyme immobilization on micron-size PSt–GMA microspheres: different methods to improve the carriers' surface biocompatibility. *RSC Adv.* **6**, 91431-91439, doi:10.1039/C6RA18126K (2016).

21 Gau, E. *et al.* Sortase-Mediated Surface Functionalization of Stimuli-Responsive Microgels. *Biomacromolecules* **18**, 2789-2798, doi:10.1021/acs.biomac.7b00720 (2017).

22 Jonkheijm, P., Weinrich, D., Schroder, H., Niemeyer, C. M. & Waldmann, H. Chemical strategies for generating protein biochips. *Angew. Chem. Int. Ed.* **47**, 9618-9647, doi:10.1002/anie.200801711 (2008).
23 Nussinov, R., Tsai, C.-J. & Jang, H. Allostery, and how to define and measure signal transduction. *Biophys. Chem.* **283**, 106766, doi:https://doi.org/10.1016/j.bpc.2022.106766 (2022).
24 della Sala, F., Neri, S., Maiti, S., Chen, J. L. Y. & Prins, L. J. Transient self-assembly of molecular nanostructures driven by chemical fuels. *Curr. Opin. Biotechnol.* **46**, 27-33, doi:https://doi.org/10.1016/j.copbio.2016.10.014 (2017).
25 van Ravensteijn, B. G. P., Voets, I. K., Kegel, W. K. & Eelkema, R. Out-of-Equilibrium Colloidal Assembly Driven by Chemical Reaction Networks. *Langmuir* **36**, 10639-10656, doi:10.1021/acs.langmuir.0c01763 (2020).
26 Walther, A. Viewpoint: From Responsive to Adaptive and Interactive Materials and Materials Systems: A Roadmap. *Adv. Mater.* **32**, 1905111, doi:https://doi.org/10.1002/adma.201905111 (2020).
27 Levin, A. *et al.* Biomimetic peptide self-assembly for functional materials. *Nat. Rev. Chem.* **4**, 615-634, doi:10.1038/s41570-020-0215-y (2020).
28 Cingil, H. E., Meertens, N. C. H. & Voets, I. K. Temporally Programmed Disassembly and Reassembly of C3Ms. *Small* **14**, e1802089, doi:10.1002/smll.201802089 (2018).
29 Parolini, L., Kotar, J., Di Michele, L. & Mognetti, B. M. Controlling Self-Assembly Kinetics of DNA-Functionalized Liposomes Using Toehold Exchange Mechanism. *ACS Nano* **10**, 2392-2398, doi:10.1021/acsnano.5b07201 (2016).

4 DNA-based Signaling Networks for Transient Colloidal Co-Assemblies

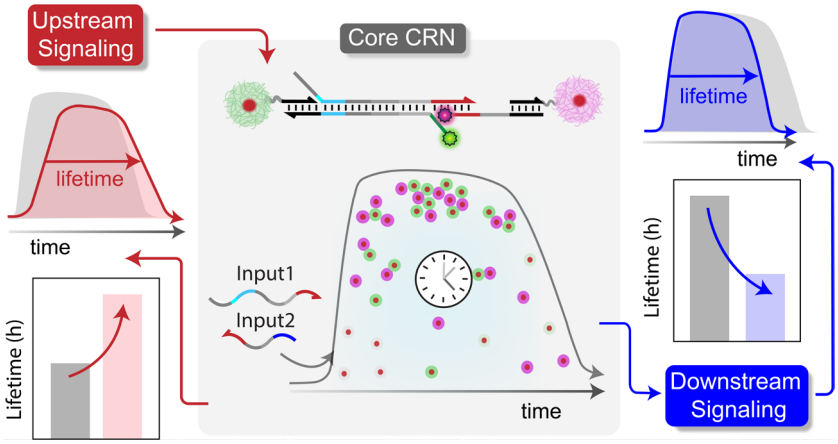

Preliminary note: *This chapter is based on the journal article published in J. Am. Chem. Soc. 145, 17819-17830, doi:10.1021/jacs.3c04807 (2023) by* ***C. Sharma, A. Samanta, R. S. Schmidt,*** *and A. Walther. Minor changes have been made concerning formatting style.*

Author contributions: C.S. and A.W. conceptualized the project. C.S. conceived, designed, and performed the free solution and particle experiments, and analyzed the respective data. C.S. and A.S. performed flow cytometry experiments together and analyzed respective results. R.S. provided help with DNA synthesis and analysis. A.W. conceived and supervised the project. C.S. and A.W. discussed and analyzed the results. C.S. wrote the first draft, C.S., A.S., R.S., and A.W edited and finalized the article.

I acknowledge support by the IMB Flow Cytometry Core Facility for providing access to flow cytometer.

Abstract: Programmable chemical circuits inspired by the signaling networks in living cells are a promising approach for the development of adaptive and autonomous self-assembling molecular systems and material functions. Progress has been made at the molecular level, but connecting molecular control circuits to self-assembling larger elements such as colloids that enable real-space studies and access to functional materials is sparse and can suffer from kinetic traps, flocculation, or difficult system integration protocols. Here we report a toehold-mediated DNA strand displacement reaction network capable of autonomously directing two different microgels into transient and self-regulating co-assemblies. The microgels are functionalized with DNA and become elemental components of the network. The flexibility of the circuit design allows the installation of delay phases or accelerators by chaining additional circuit modules upstream or downstream of the core circuit. The design provides an adaptable and robust route to regulate other building blocks for advanced biomimetic functions.

4.1 Introduction

In cells, advanced functions such as cell division, motility, motor-mediated organelle transport, and maintenance of cell shape are performed by cytoskeletal structures that exist dynamically in space and time and derive energy for operation from chemical fuel. Depending on the cellular function to be performed, cytoskeletal structures break down and reorganize, changing their life cycles and turnover. At the molecular level, such microscopic functions are regulated by signal transduction from one (upstream) node to another (downstream) in well-defined chemical reaction networks (CRNs), where the signal can be triggered by either extracellular or intracellular events.[2-4]

Mimicking such dynamic structure formation pathways in a bottom up approach to develop fuel-driven autonomous material systems out-of-equilibrium is an emerging pursuit across the fields of systems chemistry and synthetic biology. Diverse building blocks on different length scales like peptides, block copolymers,[9] liposomes,[10] emulsion droplets,[11] DNA,[12-15] and nanoparticles have been engineered in the recent past for non-equilibrium self-assemblies. Synthetic non-equilibrium self-assembling systems can be realized either by designing the structural elements that are themselves energy dissipating, or by coupling responsive structural elements to energy dissipating environments or signaling networks and feedback loops in which the self-assemblies act as a system load for the active environment. Selected examples include pH feedback systems,[23,24] ATP degradation in ATP-co-assembling systems, DNA strand displacement (DSD) circuits, Polymerase-Exonuclease-Nickase (PEN) toolbox, DNA/RNA genelet circuits, and gene regulatory networks.

Colloidal nano- and microparticles are versatile building blocks for the development of functional materials, for instance, for applications in photonics and sensing.[16] However, the most challenging task while dealing with colloidal assembly/disassembly is maintaining their overall stability in solution which is usually achieved by balancing van der Waals attraction with electrostatic and steric repulsion. Especially large colloids are prone to excessive flocculation. The integration of colloids with CRNs further requires judicious tuning of activation and deactivation rates to avoid non-dissipative kinetically trapped structures.[30-32] These limitations explain the scarcity of examples showing autonomous micro(scale) colloidal self-assembly. Addressing this gap in knowledge, we, for instance, recently coupled pH-responsive microparticles to pH feedback systems to reach transient colloidal co-assembling system featuring a chemo-structural feedback.[34] Dehne et al. showed transient clustering using antagonistic enzymatic reactions of RNA transcription and degradation.[35,36]

Charting a path forward for autonomous colloidal assemblies requires to think of multicomponent colloidal systems and of chemical circuits with enhanced regulatory capacity. Toehold-mediated DNA strand displacement (TMSD) CRNs exhibit such advantages and feature high programmability, implementation of feedback loops, predictability via computational models, and tunable operational conditions. Such TMSD CRNs have previously been exploited for transient self-sorting self-assemblies of DNA origami, or for communication between large coacervate droplets. The intermediate colloidal scale remains to be explored. It is relevant

because it allows both Brownian dynamics and real space imaging by fluorescence microscopy, and neither the macroscopic droplet system nor the nanoscopic origami system address the challenges regarding colloidal stability.

We herein demonstrate how to integrate a TMSD CRN with colloidal-scale core-shell microgel (MG) particles to autonomously regulate the first transient co-assembly of two building blocks. The particles are elementary components of the TMSD CRN and transduce the input strands with time delays due to the colloidal scale. Due to the versatility of such networks, we show how additional upstream and downstream TMSD modules can be connected to modulate the onset and lifetime of the transient co-assemblies. In addition, the inherent properties of the co-assemblies like assembly size distribution etc., can be regulated temporally. We discuss in detail how to design such CRNs, how to integrate upstream and downstream modules, and use simulations and experiments to shed light on details about their operation and coupling to colloidal co-assembly. We envision that our design strategies for building a modular and robust DNA-based CRN with integrable subnetworks can provide a customizable route to regulate the non-equilibrium behavior of other building blocks and ultimately for developing advanced biomimetic functions.

4.2 Results and Discussion

4.2.1 System design for the self-regulation of colloidal co-assemblies using modular DNA-based reaction networks.

We use DNA-functionalized micron-sized core-shell MGs as building blocks. Before discussing the rationale behind their use and details of their structure and synthesis, we first introduce the TMSD CRN and its integration with the co-assembling particles, termed Particle1 and Particle2 (**Figure 4-1a**). The starting point of the system is a set of gated particles, Gated Particle1 and Gated Particle2, which carry gating modules that prevent assembly in the starting state (State A). The gating modules also carry fluorophore and quencher pairs, and the corresponding fluorescence signals are quenched in State A. The starting mixture also contains a Dormant Inhibitor. Note that all modules carry loops in their structures, which serve as toeholds or energy reservoirs needed to drive the TMSD circuit. Simultaneous addition of Input1 and Input2 to the mixture of Gated Particle1 and Gated Particle2 opens their gates via TMSD and allows them to co-assemble into hetero-complementary structures through interaction of the i/i* domains (State B).

The activation can be tracked by the increase of different fluorescent signals (Particle1 turns green; Particle2 turns magenta). While co-assembly takes place, the Deactivator released from the gating module of Gated Particle1 triggers the release of an Inhibitor from the Dormant Inhibitor, present in the medium (shown to the right in **Figure 4-1a**). This Inhibitor eventually reacts with the linkage domain between Particle1 and Particle2 (note the “a*” toehold) in the co-assemblies and induces the disassembly of the co-assembled structures (State C). Critically, due to optimization of the sequence space, only the Inhibitor can efficiently break the co-assemblies, whereas other strands containing an a* domain are engineered to be inefficient in this TMSD (see below). Time delays occur due to multivalent binding scenarios and the soft and colloidal nature of the MG system.[37,40] The disassembly leads to a decrease in green fluorescence on Particle1 because the green-labeled strand is hybridized with a quencher labeled Inhibitor during the disassembly process. In contrast, the corresponding magenta fluorescence signal on Particle2 remains unaltered. These processes can be tracked by fluorescence measurements, Confocal Laser Scanning Microscopy (CLSM) and Flow Cytometry.

The modularity of TMSD CRNs allows to increase the regulator capacity of the autonomous system surrounding this Core CRN. We introduce two additional control modules: (1) a downstream accelerator module (**Figure 4-1b**), and (2) an upstream signaling module (**Figure 4-1c**). For instance, a Regenerator strand, already present in the starting mixture, can recycle the waste produced in the Core CRN and regenerate the Deactivator to increase Inhibitor concentration to accelerate the deactivation and ultimately the disassembly

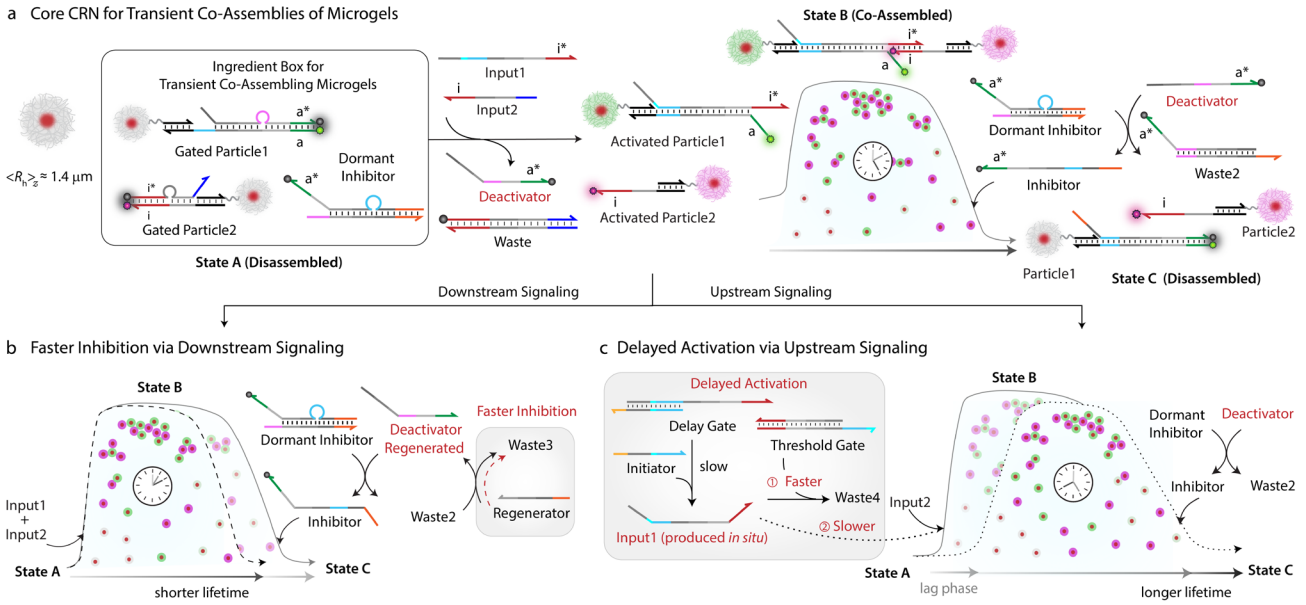

Figure 4-1. System design for autonomous control of microgel co-assemblies via DNA-based reaction networks. (a) Ingredient box with all the components required to set-up Core CRN. Addition of Input1 and Input2 triggers the transient co-assembly between Particle1 and Particle2. (b) Programming faster inhibition in co-assemblies in response to downstream signaling. (c) Programming the onset time, delay, and an increased lifetime of the co-assemblies by integrating Core CRN with an upstream subnetwork.

speed (**Figure 4-1**). This leads to shorter lifetimes for State B. Instead of providing Input1 extrinsically to the system, it can be produced *in situ* via an upstream module connected to the Core CRN (**Figure 4-1c**). The upstream subnetwork contains a Delay Gate slowly generating Input1 and a Threshold Gate that shares the same sequence as Gated Particle1 but with a longer toehold. The slow production of Input1 and its competitive consumption between Threshold Gate and Gated Particle1 introduces a delay in the activation step. This integration in the Core CRN on a molecular level increases the lifetime of the co-assembled state on a structural level with a pre-defined onset time.

4.2.2 DNA functionalized MGs and their hetero-complementary co-assembly.

Core-shell MGs are our particles of choice as they are well dispersible in aqueous medium and can be functionalized within their shell. The core is composed of a brightly red fluorescent hydrophobic material which is refractive index-matched to water ($\langle R_h \rangle_z \approx 230$ nm, synthesis in Supporting Information section 3.1). The shell contains a lightly crosslinked PNIPAM-*co*-AA hydrogel contributing 90.5 wt% of the MG (80.5 wt% N-isopropylacrylamide (NIPAM); 9 wt% acrylic acid (AA); 1 wt% N,N'-methylenebis(acrylamide) (MBA)). This composition allows functionalization with NH_2-ssDNA (**Figure 4-2a**, synthesis in Supporting Information section 3.2). The core-shell MGs have a total $\langle R_h \rangle_z \approx 1.4$ µm and can be well visualized in CLSM (**Figure 4-6**). Functionalization by ssDNA can be achieved by EDC-mediated coupling of NH_2-ssDNA (e.g., NH_2-x* and NH_2-z*; EDC = 1-Ethyl-3-(3-dimethylaminopropyl)carbodiimide = 25 equiv. with respect to COOH groups on MG), leading to a typical DNA grafting density of $3.43 \pm 0.03 \times 10^4$ strands per MG or 13.6 ± 0.2 µmol strands per g of MG (Supporting Information section 3.3, **Figure 4-7**). Such grafting densities agree with previous literature for DNA-mediated colloidal assembly. It is important to mention that this grafting density was optimized to the extent that it allows reversible co-assembly. **Figure 4-8** shows that higher coverage leads to kinetically trapped co-assemblies, whereas lower coverage decreased the propensity for co-assembly.

By using two different NH_2-ssDNA, we prepared an x*-functionalized Particle1 and a z*-functionalized Particle2. The domains x* and z* have no crosstalk to avoid non-specific interactions between Particle1 and Particle2 (NUPACK[42] simulation in **Figure 4-9**). Subsequently, we assembled the individual components of the gating modules on each of the particles. For instance, Particle1 was first incubated with equimolar amount of

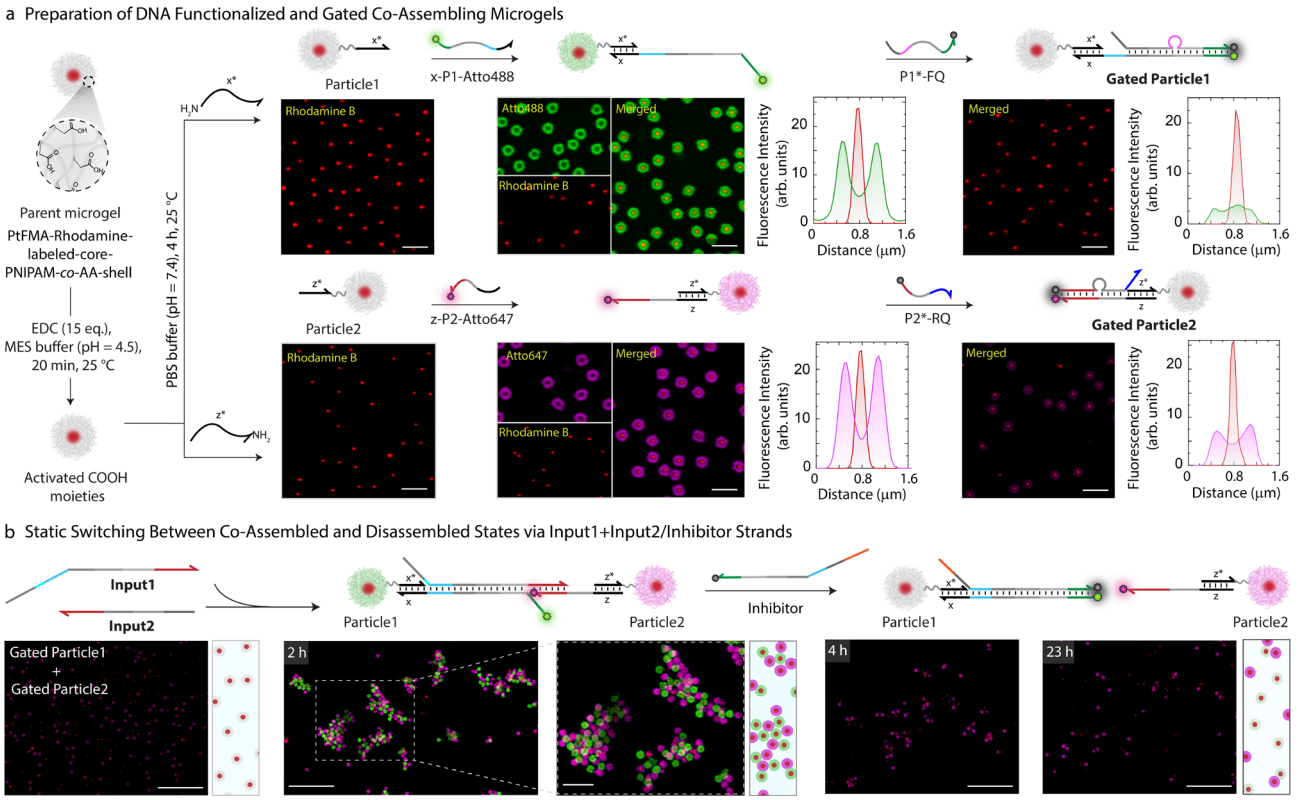

Figure 4-2. Fabrication and characterization of DNA functionalized co-assembling microgels. (a) Step-wise preparation of a set of Gated Particle1 and Gated Particle2 from a parent microgel. The first step involves covalent functionalization of DNA and consequent annealing with x-P1-Atto488, P1*-FQ on Particle1 and z-P2-Atto647 and P2*-RQ on Particle2. Each step is monitored with CLSM imaging, and the particles are quantitatively analyzed by line segment analysis. Experimental conditions: Particle1 and Particle2 suspended in TE buffer (pH = 8.0) at a final concentration of 0.05 wt%, to which 4.3 μM (1 equiv. with respect to functionalized DNA) of respective annealing strands are added at 15 °C. (b) Monitoring the Gated Particle1 and Gated Particle2 for potential co-assembly by addition of 2 equiv. of Input1 and Input2 and for reversible disassembly by consequent addition of 1 equiv. of Inhibitor. The sample was first checked for co-assembly after 2 h of Input addition with *ex situ* CLSM imaging. After addition of Inhibitor strand, sample was again visualized after 4 h and 23 h. Experimental conditions: Gated Particle1 and Gated Particle2 suspended in TE buffer (pH = 8.0), 50 mM NaCl, 1.5 mM $MgCl_2$ at a final MG concentration of 0.05 wt% at 28 °C. All CLSM images in b are represented as merged composite compiled as a *z*-projection. Scale bars: (a) 2 μm, (b) 10 μm, inset: 3 μm.

complementary x-P1-Atto488 (4.3 μM), and thereafter with P1*-FQ (4.3 μM; FQ = quencher). The gate on Particle2 (composed of z-P2-Atto647 and P2*-RQ strands) was assembled in a similar way. Step-wise assembly of the gates offers the advantage of visualizing successful functionalization by CLSM as the particles first turn fluorescent, and then the fluorescence is quenched.

4.2.3 Establishing the Core CRN to mediate transient co-assemblies of MGs.

After confirming that particle mixtures can form reversible co-assemblies, we integrated them into the Core CRN. **Figure 4-3a** shows this network in greater detail with specific hybridization regions. The system at initial State A contains a stochiometric mixture of Gated Particle1 and Gated Particle2, as well as Dormant Inhibitor in TE buffer (pH = 8.0, 50 mM NaCl, 1.5 mM $MgCl_2$). Simultaneous addition of Input1 and Input2 in equimolar ratio removes the gates on both particles. Input1 displaces the P1- FQ* strand breaking the fluorophore-quencher pair and increasing Atto488 fluorescence on Activated Particle1. Simultaneously, Input2 releases Activated Particle2 from Gated Particle2 and increases Atto647 fluorescence at the shell. During these activation steps, an "i*" domain on Activated Particle1 and a complementary "i" domain on Activated Particle2 are exposed which bind the two particles together via i/i* hybridization. The domain, "i" is designed for a higher binding strength (11 nucleotides (nt), 36.4% CG content, T_m = 30 °C) as compared to other domains used in the CRN. This hybridization gradually results in the formation of co-assemblies (State B) owing to

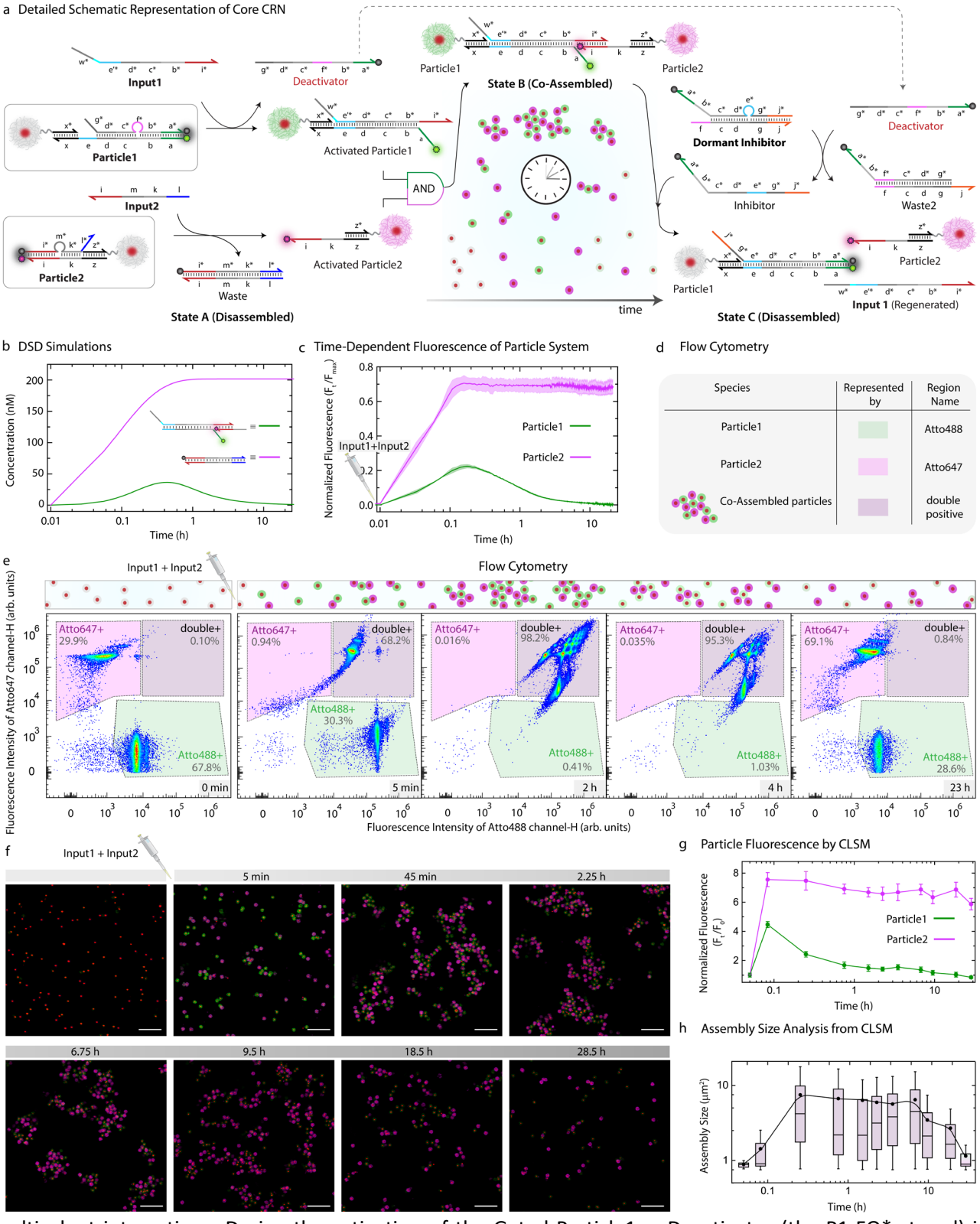

multivalent interactions. During the activation of the Gated Particle1, a Deactivator (the P1-FQ* strand) is released which in turn displaces an Inhibitor strand from Dormant Inhibitor by hybridizing to toehold “f” (8 nt).

The Inhibitor triggers the negative feedback and breaks the co-assembled complex in the co-assembly by displacing the Input1 strand via toehold “a” (10 nt). This ultimately leads to the disassembly of all particles from the formed co-assemblies. The disassembly step brings the system to a new State C which is marked by

Figure 4-3. Core Chemical Reaction Network (Core CRN) used to mediate transient co-assemblies of microgels. (a) Schematic representation of the design and operation of Core CRN. (b) DSD Simulations of the Core CRN predicting the time-dependent behavior of: 1) co-assembled complex (P1-Atto488/Input1/P2-Atto647; green curve), and 2) Waste (Input2/P2*-RQ; magenta curve) produced from the activation step of P2-Atto647/P2*-RQ module. The concentration of the starting modules: P1-Atto488/P1*-FQ, P2-Atto647/P2*-RQ and Dormant Inhibitor is set at 0.25 µM with 2 equiv. of Input1 and Input2. (c) Time-resolved normalized fluorescence of Atto488 and Atto647 dye on Gated Particle1 and Gated Particle2 suspended as equimolar mixture in TE buffer (pH = 8.0), 50 mM NaCl, 1.5 mM $MgCl_2$ at a final MG concentration of 0.005 wt%, 0.25 µM (1 equiv. with respect to DNA gates on particles) of Dormant Inhibitor at 28 ºC. The network is initiated with 2 equiv. each of Input1 and Input2. Atto488 and Atto647 fluorescence is normalized with respect to two separate systems containing pre-annealed Activated Particle1 and Activated Particle2 under same experimental conditions. The results represent an average contribution from 2 independent measurements, the shaded region depicts the standard deviation (SD). (d), (e) *ex situ* Flow Cytometric analysis of the Core CRN showing density plots with Atto488 and Atto647 channels on x and y axis respectively where the H denotes the height of the pulse. Three different regions i.e., green, magenta, and purple outlined with dotted boundary represent the gates which are used to isolate Gated Particle1, Gated Particle2 and their co-assembly events respectively from each other. An overhead panel schematically represents the state of the system over the course of experimental investigation. The experiments are performed as described in (c) but at a final MG concentration of 0.05 wt% and 1.5 µM (0.7 equiv.) of Dormant Inhibitor. The network initiated with 2 equiv. each of Input1 and Input2. The aliquots were withdrawn as needed from the reaction mixture and diluted with TE buffer (pH = 8.0) by 100 times before injecting into the Cytometer. (f) *ex situ* CLSM imaging of Core CRN. All CLSM images are represented as merged composite compiled as a *z*-projection. Experimental conditions: same as described in e), aliquots were withdrawn as needed and visualized without any dilution. (g) Fluorescence on Gated Particle1 and Gated Particle2 obtained from CLSM images, each data point represents an average from 15 particles. (h) Assembly size analysis on the particles obtained from two different regions at each time interval. The box represents 25-75 % of data, whiskers represent 5-95 % of data, a solid circle represents the mean, and horizontal bar the median of the assembly size distribution in box charts. A solid line provides a guide to the eye. Scale bars: 5 µm.

the decrease in the Atto488 fluorescence on Particle1 whereas the Atto647 fluorescence on Particle2 remains unaltered. Note that regardless of the complementary toehold "a*" on Dormant Inhibitor and Deactivator, only Inhibitor can energetically favor the disassembly of co- assemblies (**Figure 4-10**). The system follows a complex trajectory with a transient state to perform such autonomous functions and overall approaches thermodynamic equilibrium. The energy for the overall execution is supplied by the successive use of toeholds and the opening of bulge loops. In addition, these bulge loops provide steric constraints and protect the toeholds from side reactions during the DSD operation.[43,44]

To establish and validate the Core CRN design, we performed computer simulations using Visual DSD of all modules in absence of the particles (**Figure 4-3b**, representative codes are available in **Supplementary Notes 4.4.6 S2, S3,** and **S4**). The simulations were performed at the same concentrations of DNA modules used for the experiments. Visual DSD does not allow to take immobilization effects into account, but we consider them to be of low importance as we are dealing with a flexible microgel shell and not with a hard sphere colloid. The green curve corresponds to the emergence and disappearance of co-assembled complex (P1-Atto488/Input1/P2-Atto647) which is considered as an indirect measure of the increase of Atto488 fluorescence from the P1-Atto488 strand in the co-assembled complex and a consequent decrease in Atto488 fluorescence due to hybridization of P1-Atto488 strand with the quencher-labeled Inhibitor strand in the disassembled complex (P1-Atto488/Inhibitor-FQ). The magenta curve corresponds to the Waste (Input2/P2*-RQ) produced from the activation step of P2-Atto647/P2*-RQ module which is considered as an indirect measure for the change of Atto647 fluorescence from the P2-Atto647 strand. The simulations clearly show that both modules get activated and that a transient co-assembled complex is formed. We first verified the simulations by time-dependent fluorescence measurements on free DNA modules, P1-Atto488/P1*-FQ and P2-Atto647/P2*-RQ (**Figure 4-11a**) in solution and then on the particle-based system (**Figure 4-3c**). Indeed, when the gated particles are treated with both Inputs, the Atto488 fluorescence reaches a transient state (with a maximum yield of 22%) at 11.5 min whereas Atto647 fluorescence saturates to a maximum yield of ~70% within 10.5 min. This confirms the validity of the simulations and hints to a transient self-regulating co-assembly. CLSM monitoring of the process indeed confirms the transient co-assembly and autonomous operation of the coupled Core CRN/particle system (**Figure 4-3f**, **Figure 4-12a**). Before Input addition, the Gated Particle1 and Gated Particle2 are present in well dispersed state. In a control experiment, no transient

co-assemblies are observed in the absence of Input1 and Input2 (**Figure 4-13**). After 5 min of Input addition, both particles are activated and form small co-assembled clusters. The average fluorescence intensity on Particle1 increases to ~4.2-fold (green color) and that on Particle2 to ~7.5-fold (magenta color) of their corresponding initial values (**Figure 4-3g)**. The recorded *z*-projection CLSM images were also analyzed quantitatively for their change in assembly size over time (**Figure 4-3h**, **Figure 4-14**). The fluorescence intensity on Particle1 already starts to decrease after 5 min whereas that on Particle2 reaches a plateau. The size of the co-assemblies however continues to increase as suggested by assembly size distribution analysis which reaches a maximum value after 15 min and stays the same until 6.75 h. This means even though the fluorescence intensity on Particle1 decreases significantly after 1 hour, more time is required for the complete dissociation of the co-assemblies. This suggests that the quenching of fluorescence on Particle1 (which can occur as soon as the a/a* domains bind to each other) happens faster than the complete dissociation of the co-assembled complex, which requires complete melting of the i/i* domain in the multivalent, potentially interdigitated, and crowded state of the gel-like interface of the colloidal co-assemblies. After 7 h, the structures begin to disassemble and dissolve completely after 28 h.

To further quantify the behavior on a population ensemble level, we used flow cytometry that is able to identify particle species according to their fluorescence and the state of assembly according to their scattering (**Figure 4-3d,e**). We injected aliquots of an autonomously developing particle co-assembly system into the cytometer at different time intervals after Input addition (5 min, 2 h, 4 h, and 23 h). At 0 min, Particle1 and Particle2 can be clearly identified in their regions. 5 minutes after addition of Input1 and Input2, majorly two distinct populations of Particle1 and Particle2 can still be observed, but they exhibit a higher fluorescence intensity originating from an increased activation by removing the respective quencher strands. This is consistent with the fluorescence increase observed in solution spectroscopic analysis (**Figure 4-3c**). The subsequent co-assembly is evident at 2 h, as the two distinct populations of Particle1 and Particle2 merge into the double positive area (98% of all particles). Interestingly, the observation of distinct patterns in the co-assembly population indicates the presence of co-assemblies with gradual increase in particle numbers (see **Figure 4-15**, **Figure 4-16**, **Supplementary Note 4.4.6 S9** for details). After 4 h, degradation of the co-assembly occurs, as the population in the double positive region starts to decrease. Complete degradation of the co-assembled state and return of the system to the initial state (dispersed population) is observed after 23 h. The populations also show that the Atto488 fluorescence (Particle1) returns to its quenched state, while the Atto647 fluorescence (Particle2) remains in its activated state. Again, this conforms to expectations of the CRN and to the fluorescence spectroscopic measurements (**Figure 4-3c**). The consistent evolution of cytometry data underscores the transient co-assemblies triggered by the CRN and confirms the robustness of our design.

4.2.4 Faster inhibition of co-assemblies by installing a downstream signaling module.

After successfully establishing the Core CRN/particle system, we wondered if we could modulate the kinetics and size of the co-assemblies in response to an additional external signal. Specifically, could we accelerate the destruction of the co-assemblies and decrease the overall lifetime of the co-assemblies? To achieve this, we developed a Regenerator strand (1 equiv. with respect to Gated Particle1 and Gated Particle2) that regenerates the Deactivator from Waste2. Overall, no extra waste is produced in the process, old waste (Waste2) is recycled to generate Waste3 (**Figure 4-4a**). Simulations suggest that the co-assembled complex in the presence of Regenerator disassembles faster whereas the activation on Particle2 shows no change (see change to dotted green line in **Figure 4-4b**, **Supplementary Notes 4.4.6, S5** and **S6**). In the Core CRN, the Inhibitor is produced following a slight lag from the Deactivator generation (**Figure 4-17**) and the co-assembled complex starts to dissociate once the Inhibitor acquires a threshold yield of 7% at 14 min. However, in the presence of Regenerator, the Inhibitor reaches the same threshold within 8 min (**Figure 4-17**). This leads to an earlier dissociation of the co-assembled complex. Fluorescence profiles of free DNA modules, P1-Atto488/P1*-FQ and P2-Atto647/P2*-RQ in the presence of a Regenerator agree with the simulations (**Figure 4-11b**). When

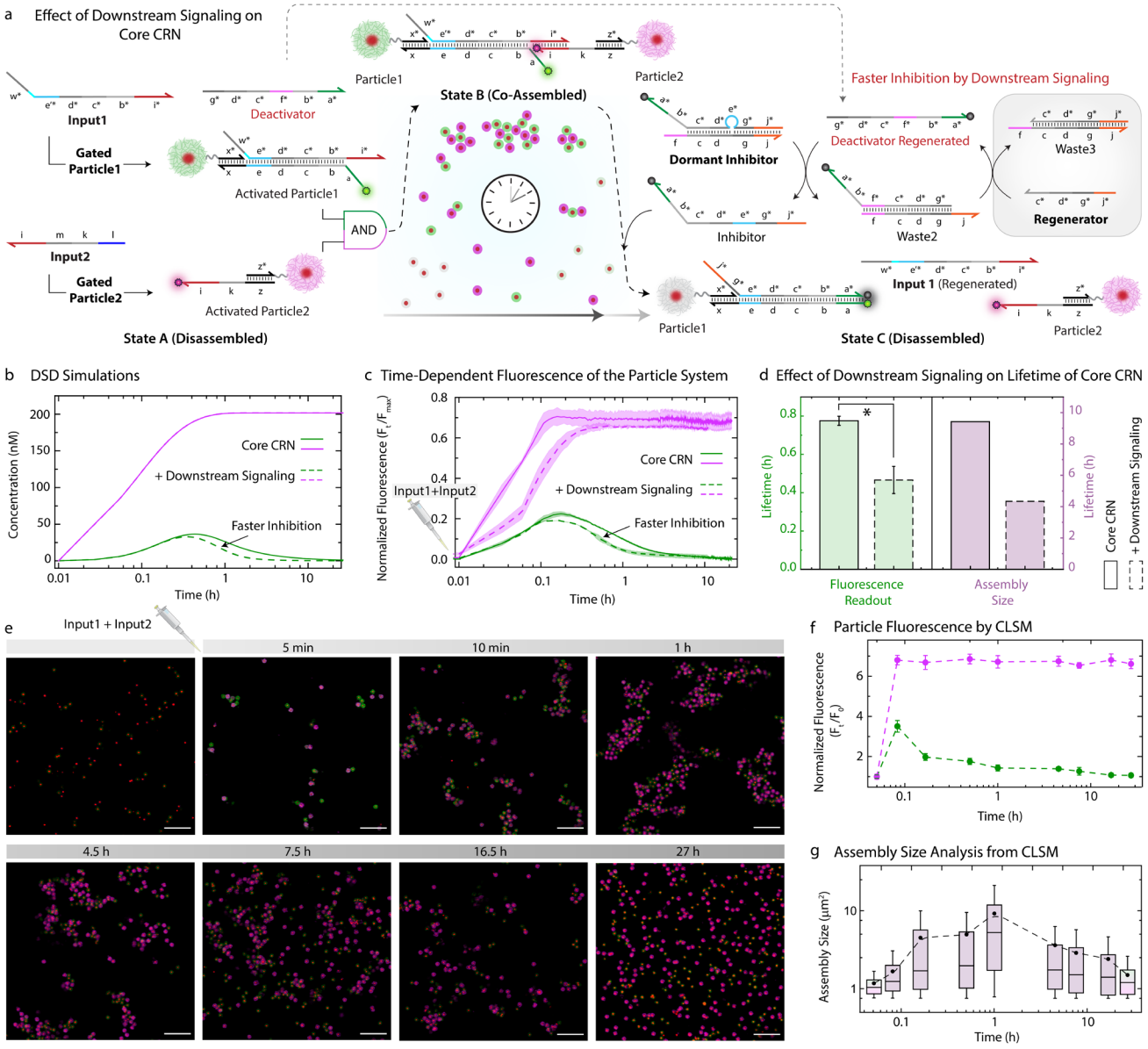

Figure 4-4. Effect of faster inhibition on Core CRN via downstream signaling. (a) Schematic representation of the design and operation of Core CRN in the presence of a downstream module consisting of Regenerator. (b) DSD Simulations predicting the behavior of co-assembled complex (green curve) and Waste (magenta curve), the effect of a Regenerator is represented by dashed curves. The concentration of both modules is set at 0.25 μM with 0.25 μM of Dormant Inhibitor, Regenerator and 2 equiv. each of Input1 and Input2. (c) Time-resolved normalized fluorescence of Atto488 and Atto647 dye on Particle1 and Particle2 suspended as equimolar mixture in TE buffer (pH = 8.0), 50 mM NaCl, 1.5 mM $MgCl_2$ at a final MG concentration of 0.005 wt%, 0.25 μM (1 equiv.) Dormant Inhibitor and, 0.25 μM (1 equiv.) Regenerator at 28 °C. The network is initiated with 2 equiv. each of Input1 and Input2. The effect of Regenerator strand is plotted with dashed lines. Atto488 and Atto647 fluorescence is normalized with respect to two separate systems containing pre-annealed Activated Particle1 and Activated Particle2 under same experimental conditions. The results represent an average contribution from 2 independent measurements, the shaded region depicts the SD. (d) The lifetime comparison of the transient state obtained from time-dependent fluorescence measurements and, assembly size analysis from *ex situ* CLSM between Core CRN with (bars with dashed boundaries) and without (bars with solid boundaries) downstream signaling. * indicate that $p < 0.05$. (e) *ex situ* CLSM imaging of Core CRN in the presence of Regenerator. All CLSM images are represented as merged composite compiled as a *z*-projection. Experimental conditions: same as described in (c) but at a final MG concentration of 0.05 wt%, 1.5 μM (0.7 equiv.) of Dormant Inhibitor and Regenerator strand at 28 °C. The network is initiated with 2 equiv. each of Input1 and Input2. Aliquots were withdrawn as needed and visualized without any dilution. (f) Fluorescence on Gated Particle1 and Gated Particle2 obtained from CLSM images, each data point represents an average from 15 particles. (g) Assembly size analysis on the particles obtained from two different *z*-projections at each time interval. The box represents 25-75 % of data, whiskers represent 5-95 % of data, a solid circle represents the mean, and horizontal bar the median of the assembly size distribution in box charts. A dashed line provides a guide to the eye. Scale bars: 5 μm.

implemented with the particle system, a similar trend of faster inhibition in the Atto488 fluorescence on Gated Particle1 is observed (green line in **Figure 4-4c**). The Atto647 fluorescence on Gated Particle2 levels off at 65% yield within 30 min (magenta line in **Figure 4-4c**). The Atto647 fluorescence in presence of a Regenerator shows a slight delay regarding its increase as compared to the Core CRN without Regenerator (dotted vs solid magenta line in **Figure 4-4c**). This should however not be overinterpreted on this part of the logarithmic scale (1-2 min difference for systems running 1-3 h), and critically, the overall faster inhibition is well reflected in the spectroscopic analysis (dotted vs solid green line in **Figure 4-4c**).

The transient profiles can be easily compared through their lifetimes, which is the time period that the fluorescence profile takes to decrease to the level corresponding to the half of the initial and the maximum fluorescence. As anticipated, the lifetime of the fluorescence profile corresponding to the Activated Particles in Core CRN (~46.2 min) can be reduced by 1.7 times in the presence of downstream signaling (~27.6 min) (**Figure 4-4d**).

To check whether the shorter lifetime observed in the fluorescence profiles can be translated for reduced lifetime of the co-assembled structures, we monitored the system via CLSM (**Figure 4-4e**, **Figure 4-12b**). Without Input addition, Gated Particle1 and Gated Particle2 continue to remain well dispersed and inactivated until 48h (**Figure 4-18**). Within only 5 minutes of Input 1 and 2 addition, Particle1 and Particle2 are activated (**Figure 4-4f**). But this time, Atto488 fluorescence on Particle1 increases to only 3.5 times of its initial value compared to 4.2 times increase in case of Core CRN.

This is to be expected according to the simulations: Faster inhibition in the presence of Regenerator compromises the overall yield of activated modules (x-P1-Atto488/Input1) on Particle1. The increase in the Atto647 fluorescence on Particle2 however remains the same (~7 times). The activation thereby triggers co-assembly of Particle1 and Particle2 reaching their maximum size (10 μm^2) slowly after 1 h (**Figure 4-4g**). The structures start to disassemble soon after that, with a lifetime of only ~4 h compared to the Core CRN without Regenerator (~9 h). The reduced lifetime confirms the faster destruction of the co-assembled structures in the presence of Regenerator. The above results validate the robustness of the Core CRN even when integrated with downstream signal. The shorter lifetime of the co-assembled structures proves that a simple change in the network can bring out advance changes on the system level without hampering the overall performance of the original network.

4.2.5 Introduction of a delay and threshold for co-assembly via an upstream signaling module.

Next, we asked whether we can further modulate the Core CRN to process a signal wired through upstream reactions to induce a programmed delay time with a signal thresholding function into the lifecycle. To demonstrate the concept, we first designed a Delay Gate bearing a toehold containing only 3 nt (CTC) through which Input1 is generated upon addition of an Initiator (**Figure 4-5a**). Under the same conditions, reactions mediated by 3 nt toeholds proceed approximately 10-100 times slower than 7-8 nt long toeholds which are used in other parts of the CRN.[46] In most cellular processes, an output is generated when the input concentration reaches above a threshold concentration which creates a presence/absence interpretation associated with the thresholding unit.[27,47] Thresholding can be adapted in TMSD by designing a Threshold Gate to possess a longer toehold than the competing target gate such that the incoming Input is preferentially consumed by the Threshold Gate, only after which the Input becomes available for target gate on Gated Particle1.

Without making any amendments in the Core CRN, we built a Threshold Gate that shares the same sequence as P1-Atto488/P1*-FQ module (toehold sequence, e = GTGTAATA, $k_b \approx 3.3 \times 10^{-6}$ $nM^{-1}s^{-1}$) but with a longer toehold containing 3 extra nt (TCC) at the end (toehold sequence at Threshold Gate, e´ = GTGTAATATCC, $k_b \approx 7 \times 10^{-6}$ $nM^{-1}s^{-1}$). In this case, it is not the increase in the toehold length alone (from 8 to 11 nt), but the 15%

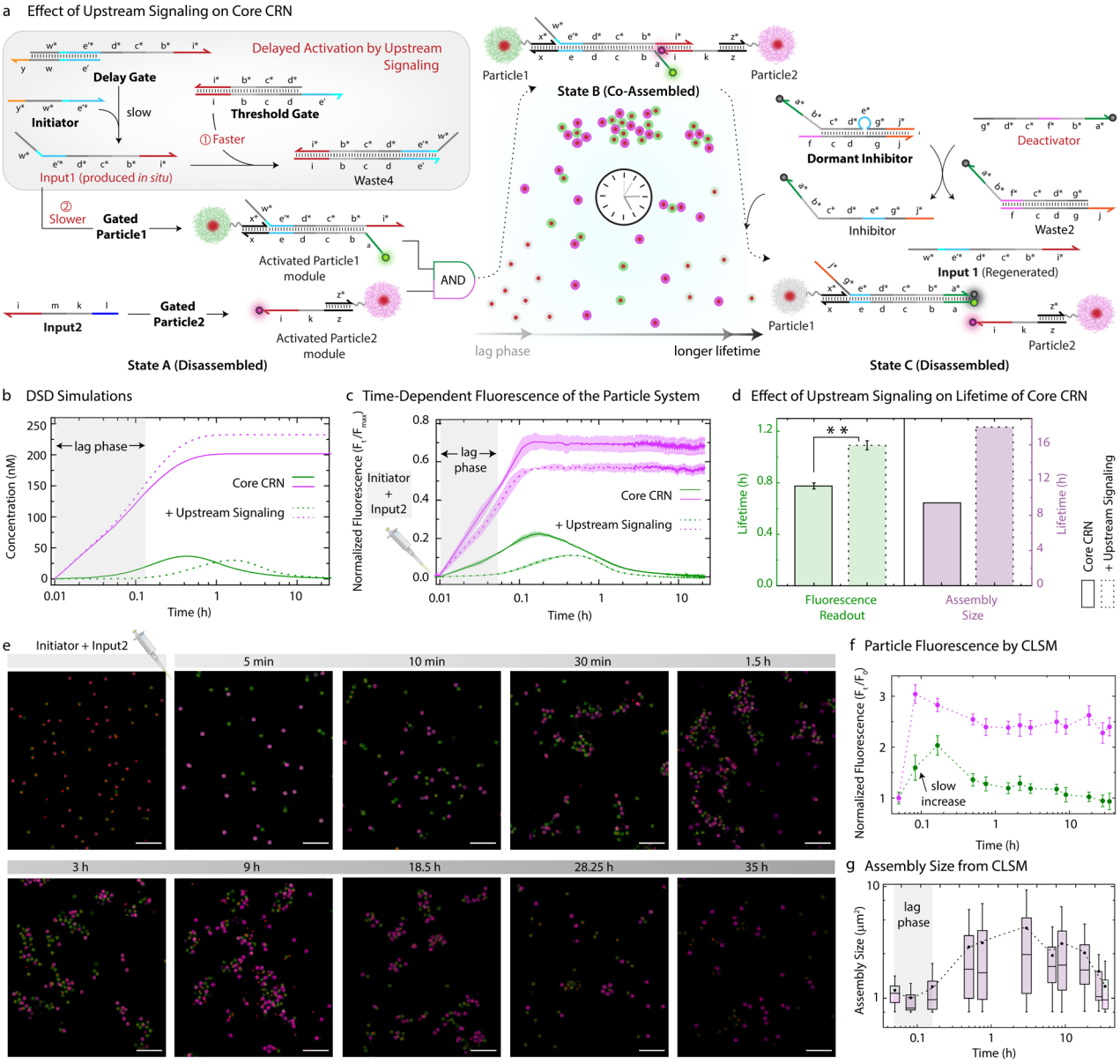

Figure 4-5. Effect of delayed activation on Core CRN via upstream signaling. (a) Schematic representation of the design and operation of Core CRN in the presence of an upstream module consisting of a Delay Gate and a Threshold Gate. The concentration of both modules is set at 0.25 μM with 0.25 μM of Dormant Inhibitor, Threshold Gate, 0.5 μM of Delay Gate, 4 equiv. of Initiator and 2 equiv. of Input2. (b) DSD Simulations predicting the behavior of co-assembled complex (green curve) and Waste (magenta curve), the effect of upstream module is represented by dotted curves. (c) Time-resolved normalized fluorescence of Atto488 and Atto647 dye on Particle1 and Particle2 suspended as equimolar mixture in TE buffer (pH = 8.0), 50 mM NaCl, 1.5 mM $MgCl_2$ at a final MG concentration of 0.005 wt%, 0.25 μM (1 equiv.) Dormant Inhibitor, 0.25 μM (1 equiv.) Threshold Gate, 0.5 μM (2 equiv.) Delay Gate at 28 °C. The network is initiated with 4 equiv. of Initiator and 2 equiv. of Input2. The effect of upstream module is plotted with dotted lines. Atto488 and Atto647 fluorescence is normalized with respect to two separate systems containing pre-annealed Activated Particle1 and Activated Particle2 under same experimental conditions. The results represent an average contribution from 2 independent measurements, the shaded region depicts the SD. (d) The lifetime comparison of the transient state obtained from time-dependent fluorescence measurements and, area distribution analysis from *ex situ* CLSM between Core CRN with (bars with dotted boundaries) and without (bars with solid boundaries) upstream signaling. ** indicate that $p < 0.01$. (e) *ex situ* CLSM measurements of Core CRN integrated with upstream signaling. All CLSM images are represented as merged composite compiled as a *z*-projection. Experimental conditions: same as described in c) but at a final MG concentration of 0.05 wt%, 1.5 μM (0.7 equiv.) Dormant Inhibitor, 1.5 μM (0.7 equiv.) Threshold Gate, 3 μM (1.4 equiv.) Delay Gate at 28 °C. The network is initiated with 4 equiv. of Initiator and 2 equiv. of Input2. Aliquots were withdrawn as needed and visualized without any dilution. (f) Fluorescence on Gated Particle1 and Gated Particle2 obtained from CLSM images, each data point represents an average from 15 particles. (g) Assembly size analysis on the particles obtained from two different *z*-projections at each time interval. The box represents 25-75 % of data, whiskers represent 5-95 % of data, a solid circle represents the mean, and horizontal bar the median of the assembly size distribution in box charts. A dotted line provides a guide to the eye. Scale bars: 5 μm.

increase in the overall G-C content (25% for "e" and 40% for "e´") which allows the Input1 to react with Threshold Gate ~2 times faster than the P1-Atto488/P1*-FQ module.[49]

Simulations confirm that there is a strong competition between the reaction of Input1 with Threshold Gate versus P1-Atto488/P1*-FQ module where both of them follow two-phase exponential decay (**Figure 4-19**). As anticipated, the rate of consumption or the decay rate of Threshold Gate ($k_{decay,Threshold\ Gate}$ ≈ 1.4 h^{-1}) is higher than that of P1-Atto488/P1*-FQ module ($k_{decay,P1/P1*}$ ≈ 0.9 h^{-1}). The combined effect of (i) slow *in situ* production of Input1 through a Delay Gate based on adding the Initiator and (ii) a subsequent competition for Input1 between Threshold Gate versus P1-Atto488 /P1*-FQ module generates a well-defined lag time of ~5 min as determined from simulations (**Figure 4-5b**, **Supplementary Notes 4.4.6, S7** and **S8**). Moreover, an overall delay of ~1 h is expected for the Atto488 fluorescence to achieve its maximum yield of 12%. Experimentally, the lag phase and an associated delay in Atto488 fluorescence from Atto488-P1 is confirmed with time-dependent fluorescence measurement on free DNA modules (**Figure 4-11c**).

Similar fluorescence trends are observed when the system is implemented with the particles (**Figure 4-5b**). Upon simultaneous addition of Initiator and Input2, activation on Particle1 is observed after a well-defined lag of ~4 min with a jump in the lifetime from 0.77 h to 1.09 h (**Figure 4-5c,d**). Atto647 fluorescence on Particle2 reaches its saturated state within ~ 4 min, similar to that observed in the absence of upstream signaling, but with a reduced yield of 60% which can be explained because of local fluctuations in the environment of the fluorophore.[35] The observed trend in the Atto488 and Atto647 fluorescence confirms the efficiency of the Core CRN in the presence of an upstream module. This lag time and delay come however on the expense of reduced activation on Particle1 and Particle2.

To check whether 11% maximum yield (only half of the original network, 22%) of the activated Particle1 is sufficient to induce co-assemblies, we performed CLSM experiments. The gated particles stay inactivated and well dispersed before providing any Initiator and Input2 (**Figure 4-20**). However, upon simultaneous addition of Initiator and Input2 to an equimolar mixture of Gated Particle1 and Gated Particle2, a ~3-fold increase in the Atto647 fluorescence on the Particle2 is observed within 5 min (**Figure 4-5e**). Atto488 fluorescence on Particle1 increases to 2 times of its initial value, which is only half the increase observed in Core CRN (4.3 times increase) after 10 min (**Figure 4-5f**). The slow increase and the low yield of activation of Particle1 gate does not induce any co-assemblies within 10 min, unlike for the Core CRN/particle system (**Figure 4-5g**, **Figure 4-12c**, 3 h). However, after 30 min, the co-assembled structures are finally observed and gradually grow in size and reach their maximum average size of 8 μm^2 after 3 h. The overall time taken by the co-assemblies to reach their maximum average size is delayed by 2.75 h with a relative decrease of 2 μm^2 in the average size of the co-assemblies. The relatively less activated strands on Particle1 and Particle2 reduce the multivalency strength for co-assembly and thereby explain the reduced co-assembly size. Beyond this point, Atto488 fluorescence on Particle1 continues to decrease, and the co-assembled structures slowly begin to disassemble and complete disassembly is only observed after 35 h. It is important to note that the relatively slow production of Input1 in this case also slows down the Deactivator and hence the Inhibitor generation in the downstream processes. This directly influences the disassembly step, which increases the lifetime of the transient co-assembled state from 9.42 to 18 h (**Figure 4-5d**).

4.3 Conclusion

In this work, we presented the first example of a transient co-assembling system that uses micron-scale soft colloids as primary building blocks carrying molecular information relays for signal acquisition, processing, and transduction through a series of concatenated TMSD reactions. Our approach combines the concepts of polymer chemistry in the form of the design and synthesis of DNA-decorated monodisperse microgels with a cornerstone of dynamic DNA nanotechnology in the form of TMSD-based CRNs that enable rational design of

signaling and feedback loops. The micrometer-sized building blocks facilitate distinction and monitoring of the transient assembly process by CLSM and Flow Cytometry.

Owing to the versatility and programmability of the TMSD-based CRN, the lifetime of the co-assembled state could be shortened by amplifying the negative feedback through the addition of a Regenerator or extended by delaying the activation signal through the introduction of a Threshold and Delay Gate. The inhibition and delay rate can further be modulated by tuning the length and composition of the toeholds responsible for the certain strand displacement reaction. In fact, co-assembly can be programmed to be delayed from hours to days by decreasing the length of toehold "y" from 3 nt to 1 nt. Alternatively, "y" can be completely removed from Delay gate and "y*" from Initiator. For this case, Input1 will be released from Delay Gate facilitated by the spontaneous binding and unbinding of the bases on the ends of the Delay complex, i.e., a process known as fraying.[35]

In addition, *in silico* optimization of DNA modules provides essential guidance for experimental design and analysis. Next to the temporal property of the DSD circuits, we designed our two populations of microgel particles carrying the respective modules in a way that two distinct fluorescence signals emanate from each population over the course of the CRN. The distinguishability of the particle populations allows us not only to monitor the transient pathway of co-assemblies using CLSM and cytometric analysis but also to quantify the respective size distribution of the resulting co-assemblies. It also allows link molecular activation/deactivation reactions to colloidal scale processes that experience obvious delays. Our optimized DNA sequences for the Core CRN operate smoothly and confirm our expectations despite the spatial confinement and steric factors associated with immobilized DNA on the microgel surface. Moreover, the programmability of the TMSD reactions also provides the opportunity to optimize the transient self-assembly systems to avoid non-dissipative, kinetically trapped aggregates by simply changing the binding strength and nucleotide composition of the toeholds and other domains.

The TMSD circuit demonstrated here in the microparticle systems provides a starting point to extend the systems engineering to more sophisticated systems, such as ATP-driven TMSD circuits,[33] catalytic TMSD circuits,[37] or even the inclusion of additional functions that arise in the co-assembled state of the microparticles. The energy stored in such non-equilibrium assemblies can be further transduced into mechanical energy to achieve advanced functions such as shape-change control/maintenance and movement.[50] The size of these particles enables their use in the development of interactive materials for photonics, sensing, and delivery systems. In fact, the sensing and processing properties of these particles demonstrated in this study can be an essential parameter for communication with living cells leading to bioactive materials.[7]

4.4 Experimental

4.4.1 Materials

All chemicals and reagents are purchased from Sigma Aldrich or Merck and used without further purification unless otherwise stated:

2,2,2-trifluoroethyl methacrylate (ABCR GMBH, 99 %), N-isopropylacrylamide (97 %), 2,2'-azobis(2-methylpropionamidine) dihydrochloride (ABCR GMBH, 96 %), N,N'-methylenebis(acrylamide) (99%), divinylbenzene (DVB, 80 %), acryloxyethyl thiocarbamoyl Rhodamine B (POLYSCIENCES, INC.), Al_2O_3 90 neutral (CARL ROTH GMBH), 1-Ethyl-3-(3-dimethylaminopropyl)carbodiimide (ABCR GMBH, 98%), potassium persulfate (≥99%), acrylic acid (Acros Organics, 99.5 %), disodium ethylenediaminetetraacetate dehydrate (biology grade), tris(hydroxymethyl)aminomethane hydrochloride (Trizma buffer substance pH=8), 2-(N-morpholino)ethanesulfonic acid, sodium chloride (99%), magnesium chloride (99%), phosphate buffered saline (PBS, pH = 7.4). MilliQ water was used throughout all experiments unless otherwise stated.

All oligonucleotides (except amine-modified oligonucleotides) were purchased from Integrated DNA Technologies Inc. (IDT) and Biomers GmbH (as listed below in Table S1). The oligonucleotides as received were dissolved in 1X TE buffer, pH = 8.0 (Thermo Fischer). Amine-modified oligonucleotides were synthesized following a well-defined procedure (as described in **section 4.4.3.4**).

4.4.2 General Characterization Methods and Instruments

DLS measurements were performed on the LS Instruments NanoLab 3D at 25 °C operating with a red laser (λ = 685 nm) and a scattering angle of Θ = 90 ° using standard disposable PS cuvettes (BRAND GmbH & Co. KG). The distributions of the hydrodynamic radii were obtained by a CONTIN mode analysis.

Confocal laser scanning microscopy (CLSM) was performed on Leica Stellaris 5 microscope (LasX v4.3.0.24308) with four laser lines and three HyD S detectors using plan-apochromat objectives (63×, 1.40 numerical aperture, oil immersion).

Thermal annealing and temperature ramps were programmed on Mastercycler® nexus GX2 (Eppendorf).

DNA concentrations were determined using a DeNovix-S-06873 (DeNovix OS 0.8.1 v4.1.5) spectrophotometer with a standard value of 33 µg/OD_{260}.

The temperature-controlled fluorescence measurements were performed on a TECAN (SPARK control v3.1) microplate plate reader using Corning® 384-Well black polystyrene plate with non-binding surface. Excitation and emission wavelengths for Atto488 are 485 nm and 535 nm and for Atto647N are 620 nm and 679 nm respectively.

Flow Cytometry experiments were performed on a Novocyte Quanteon (Agilent, NovoExpress v.1.6.0) with 4 excitation lasers (violet 405 nm, blue 488 nm, yellow-green 561 nm and red 640 nm) and 16 fluorescence detectors. Flow Cytometry data was analyzed using FLOWJO (v10.8.1) software.

***p* values** are calculated by performing a t-Test (Two-Sample Assuming Equal Variances) in Microsoft excel using a built-in Data analysis tool pack.

The amine-modified oligonucleotides were synthesized on a H-8 custom LNA, DNA/RNA automatic synthesizer from K&A Laborgeräte. The synthesized oligonucleotides were purified by **High Performance Liquid Chromatography (HPLC)** on a Dionex Ultimate 3000 (Thermo Fischer Scientific).

4.4.3 Methods

4.4.3.1 Synthesis of surfactant-free, poly(2,2,2-trifluoroethyl methacrylate)-Rhodamine labeled core particles.

Divinylbenzene (DVB) and 2,2,2-trifluoroethyl methacrylate (tFMA) were purified using column chromatography (Al_2O_3, neutral). The initiator potassium persulfate (KPS, 159.49 mg, 590 µmol) was dissolved in deionized water (45 mL), degassed by bubbling with nitrogen gas (25 min) and thermostated at 70 °C for 15 min. To a solution of DVB (46.2 mg, 354.9 µmol) and tFMA (1.98 g, 11.8 mmol), a solution of acryloxyethyl thiocarbamoyl Rhodamine B (1 mg) and N-isopropylacrylamide (NIPAM, 150 mg, 1.3 mmol) in water (4.5 mL) were added. The mixture was ultrasonicated for 2 minutes and degassed by bubbling with nitrogen gas (10 min). The resulting mixture was added dropwise (over a period of 5 min) to the initiator solution starting the polymerization. The reaction mixture was stirred at 70 °C for 6 h (stirring rate = 600 rpm). The resulting dispersion was filtered while hot and dialyzed against deionized water (MWCO 8000 Da). The dispersion with a solid content of 35.6 mg/mL was observed upon freeze-drying.

4.4.3.2 Synthesis of the PNIPAM shell to yield PtFMA-Rhodamine labelled-core-PNIPAM-co-GMA-shell microgel (MGs) particles.

NIPAM (1.49 g, 13.2 mmol, 80.5 wt%) was dissolved in deionized water (100 mL) together with the cross-linker *N*,*N*'-methylenebis(acrylamide) (MBA, 18.2 mg, 81.7 µmol, 1.0 wt%). The core particles (4.7 mL, 35 mg/mL, 157.2 mg solid content, 9.5 wt%) were added and the mixture was degassed for 30 min and heated to 72 °C. The initiator KPS (76.2 mg, 0.28 mmol) was dissolved in water (30 mL) and degassed (15 min). The polymerization was initiated by dropwise addition of initiator solution to a heated reaction mixture and stirred (stirring rate = 350 rpm). After 10 minutes, degassed acrylic acid (AA, 153 mg, 150 µL, 2.1 mmol, 9 wt%) after purification by column chromatography (Al_2O_3, neutral) was added dropwise into the reaction mixture. The stirring rate was increased to 600 rpm and reaction was allowed to run for 4 hours. The resulting core/shell MG particles (amount of AA moieties assuming full conversion = 1250 µmol per g of MG) were filtered while hot and purified by dialysis (MWCO 8000 Da) against deionized water. The resulting core-shell MGs were further purified via centrifugation (5 x 25 min, 11000 rpm, 15 °C, replacement of the supernatant with Milli Q water per centrifugation step).

4.4.3.3 Functionalization of MG with amine-modified DNA.

The MG suspension was redispersed in 2-(N-morpholino)ethanesulfonic acid (MES) buffer (10 mM, pH = 4.5) via centrifugation (20 min, 9000 rpm, 15 °C, replacement of the supernatant with MES buffer). A two-step reaction achieves the functionalization of DNA on MGs. In the first step, activation of carboxyl acid groups in MG shell (120 µL, 1.943 mg/mL, 0.29 µmol of COOH groups) was carried out by stirring with EDC (1.1 mg, 7.2 µmol, 25 equiv. with respect to COOH groups) dissolved in 40 µL of MES buffer (10 mM MES, pH = 4.5) for 15 minutes at 25 °C. Finally, amine-modified DNA (0.15 µmol, 0.5 equiv.) dispersed in PBS buffer (pH = 7.4) was added to activated MGs prepared in first step and mixture is stirred for 4.5 h at 25 °C. The DNA functionalized MGs were purified via centrifugation (2 x 3 min, 8000 rpm, 25 °C, replacement of the supernatant with TE buffer (pH = 8.0), per centrifugation step).

4.4.3.4 Functionalization of MG with amine-modified DNA.

The oligonucleotides were synthesized at 10 µmol scale employing the standard solid phase β-cyanoethyl-phosphoramidite chemistry in trityl-on mode. The DNA phosphoramidites (DMT (dimethoxytrityl)-dT, DMT-dA(bz), DMT-dG(dmf) and DMT-dC(ac)) were diluted to 50 mM with dry acetonitrile and synthesis occurred from the 3' towards the 5' end of the oligonucleotides on packed solid phase columns.

Cleavage of the oligonucleotides (DMT-on) from the solid support and base deprotection was achieved in one step to ensure optimal yields. The 34 µmol/g controlled pore glass (CPG) solid support was treated with 10 mL of ice-cold ammonia solution (30-32% NH_3) overnight at room temperature to detach the DNA from the CPG support. The cleaved DNA (DMT-on) in ammonia was diluted with 10 mL of disodium phosphate buffer (75 mM containing 1 mM EDTA, pH = 8.3) and the crude product was obtained upon freeze drying. The obtained DNA was redispersed in MilliQ water and purified by preparative reverse phase-HPLC (RP-HPLC) followed by freeze drying to remove the solvent.

The DMT group was cleaved from the purified product by making a 2 wt% solution of the dry DNA in NaOAc/HOAc buffer (200 mM, pH 4.0, 200 mM NaCl) and heating the mixture to 50 °C for one hour. After neutralizing the reaction mixture with disodium phosphate buffer (750 mM, 10 mM EDTA), the synthesized DNA was precipitated into a 5-fold excess of isopropanol to remove contaminants and to exchange the counterions to sodium. The precipitate was dissolved in MiliQ water, freeze dried. The synthesized and purified strands were stored at -20 °C until further use.

The purity of the obtained oligonucleotides was confirmed with analytical HPLC.

4.4.3.5 CLSM image treatment and analysis.

All CLSM images were processed using ImageJ (Fiji). All images except in **Figure 4-2a** were acquired as a *z*-stack. Atto488, Atto647 and Rhodamine B channels were merged together to form a composite image and then compiled as a *z*-projection for representation purposes. The size of the co-assemblies was determined by thresholding the compiled images. The masks obtained upon thresholding were analyzed in terms of size and total amount.[51]

4.4.3.6 Lifetime Calculation

The lifetime of the transient state is defined as the time that a transient profile (either obtained from time-dependent fluorescence measurements or assembly size analysis) takes to decrease to half of the initial and maximum value.

4.4.4 Supplementary Tables

Table S1. DNA sequences for the oligonucleotides synthesized following a well-defined procedure (**section 4.4.3.4**) with their abbreviations and modifications.

Name	Sequence 5'→ 3'	Purification	Modification
NH2-x* (T_{20}-x*)	TTTTTTTTTTTTTTTTTTTT GAACCCGTATATCTATCCTA	HPLC	5' Amino Modifier C6 dT
NH2-z* (z*-T_{20})	GATAGAGATCGTGTGTTAC TTTTTTTTTTTTTTTTTTTT	HPLC	3' Amino Modifier C6

Table S2. DNA sequences for the oligonucleotides purchased from IDT with their abbreviations and modifications.

Name	Sequence 5'→ 3'	Purification	Modification
x-P1-Atto488 (a b c d e x)	TGTAGTACTA GATTA GTGTAG TTAGTTAGGTGTAATA TAGGATAGATATACGGGTTC	HPLC	5' ATTO™ 488 (NHS Ester)
P1*-FQ (g*d*c*f*b*a*)	TTCA CTAACTAA CTACAC ATACTTAC TAATC TAGTACTACA	HPLC	3' Iowa Black ® FQ
z-P2-Atto647 (z k i)	GTAACACACGATCTCTATC GGAACTGT GATGAAGATAC	HPLC	3' ATTO™ 647N (NHS Ester)
P2*-RQ (i*m*k*l*)	GTATCTTCATC TGAAACCG ACAGTTCC CATTCATA	HPLC	5' Iowa Black ® RQ
Inhibitor (j*g*e*d*c*b*a*)	CAACTCT TTCA TATTACAC CTAACTAA CTACAC TAATC TAGTACTACA	HPLC	3' Iowa Black ® FQ
Inhibitor Gate (f c d g j)	GTAAGTAT GTGTAG TTAGTTAG TGAA AGAGTTG	Standard Desalting	None
Input2 (l k m i)	TATGAATG GGAACTGT CGGTTTCA GATGAAGATAC	Standard Desalting	None
Regenerator (j*g*d*c*)	CAACTCT TTCA CTAACTAA CTACAC	Standard Desalting	None

Table S3. DNA sequences for the oligonucleotides purchased from Biomers with their abbreviations and modifications.

Name	Sequence 5'→ 3'	Purification	Modification
Input1 (w*e*d*c*b*i*)	CCACCAAACTTCA TATTACAC CTAACTAA CTACAC TAATC GTATCTTCATC	Standard Desalting	None
Delay Up (e w y)	GTGTAATATCC TGAAGTTTGGTGG CTC	HPLC	None
Threshold Up (i b c d e)	GATGAAGATAC GATTA GTGTAG TTAGTTAG GTGTAATATCC	HPLC	None
Threshold Down (d*c*b*i*)	CTAACTAA CTACAC TAATC GTATCTTCATC	HPLC	None
Initiator (y*w*e*)	GAG CCACCAAACTTCA GGATATTACAC	HPLC	None

4.4.5 Supplementary Figures

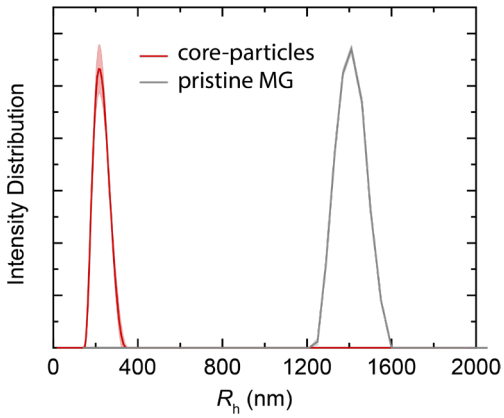

Figure 4-6. DLS CONTIN plots of: poly(2,2,2-trifluoroethyl methacrylate) (PtFMA) core-particles and pristine MG. The suspensions were prepared in MilliQ water with a final concentration of 0.06 mg/mL.

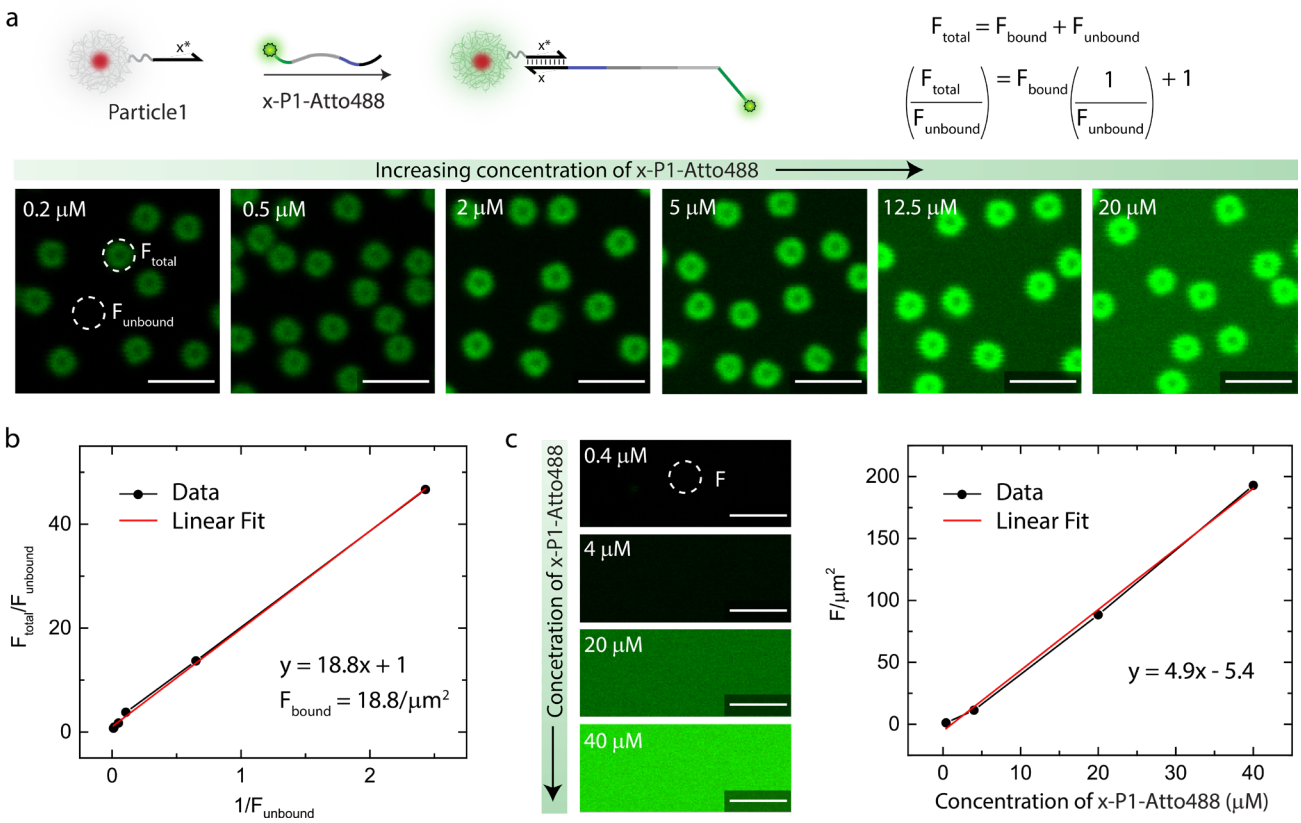

Figure 4-7. Measurement of DNA grafting density on Particle1. (a) The binding capacity of x-P1-Atto488 onto Particle1 via x/x* hybridization is measured as a proxy for the DNA grafting density. The mean fluorescence intensity per µm² over the particle (F_{total}, includes the contribution from both x-P1-Atto488 bound on Particle1 and free x-P1-Atto488 in the suspension) and in the background ($F_{unbound}$, includes only free x-P1-Atto488 in the suspension) is measured for increasing amounts of x-P1-Atto488 via CLSM. Experimental conditions: Particle1 is incubated with increasing concentrations of x-P1-Atto488 (0.2-20 µM) in TE buffer (pH = 8.0) at 15 °C at a final MG concentration of 0.05 wt%. F_{total} and $F_{unbound}$ represent average fluorescence intensity measured from 10 different regions. (b) The data is fitted with linear equation where the slope provides fluorescence contribution from x-P1-Atto488 on the particle (F_{bound}). (c) With the help of calibration curve between mean fluorescence intensity per µm² (F, measured via CLSM) and concentration of free x-P1-Atto488, a corresponding DNA concentration for F_{bound} is calculated to be 4.9 ± 0.1 µM accounting for 3.43 ± 0.03 x 10^4 strands/MG. Experimental conditions: Increasing concentrations of x-P1-Atto488 (0.4-40 µM) dispersed in TE buffer. F represents an average fluorescence intensity from 5 different regions. Scale bars: (a), (c) 2 µm.

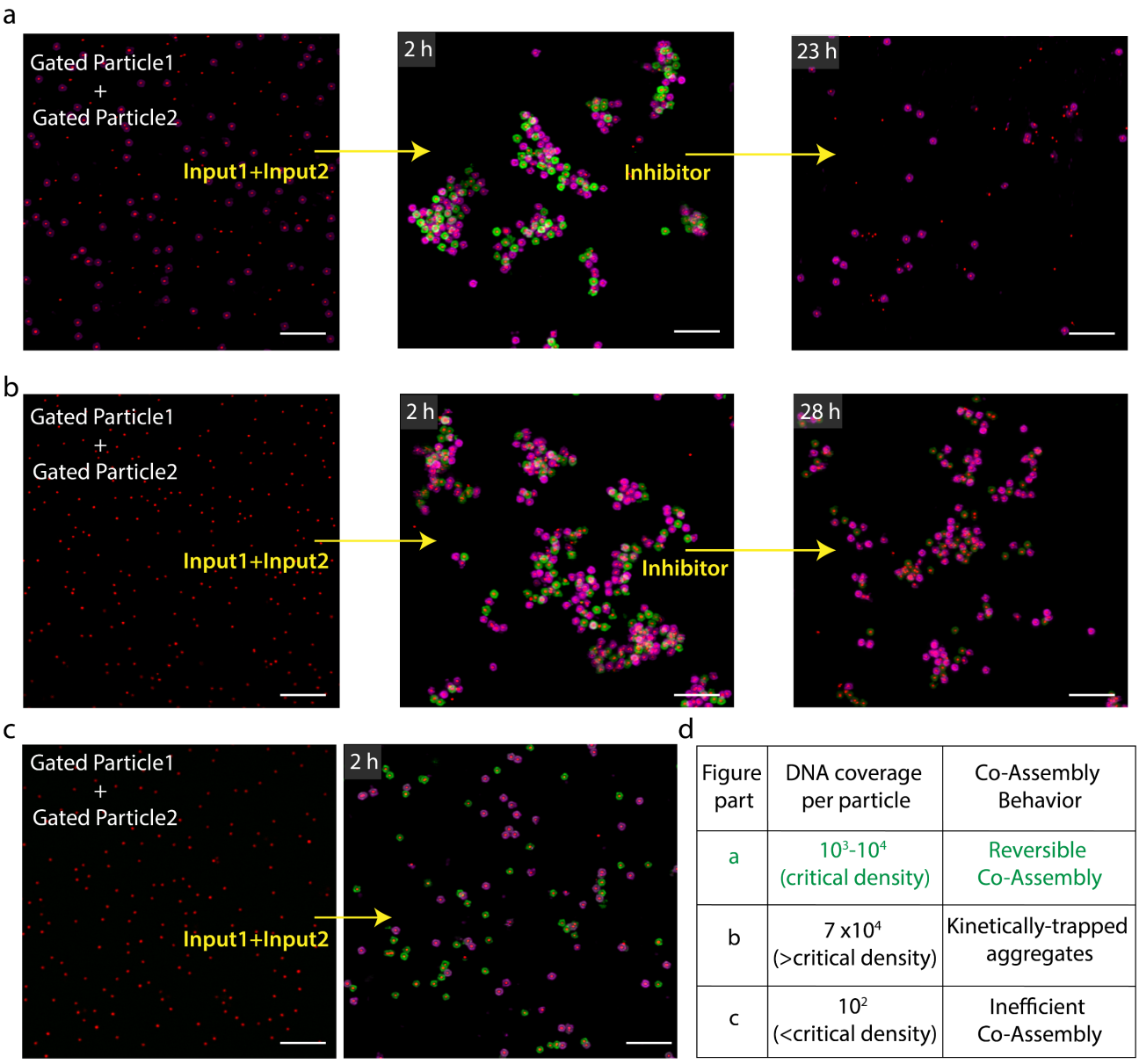

d

Figure part	DNA coverage per particle	Co-Assembly Behavior
a	10^3-10^4 (critical density)	Reversible Co-Assembly
b	7 x10^4 (>critical density)	Kinetically-trapped aggregates
c	10^2 (<critical density)	Inefficient Co-Assembly

Figure 4-8. Co-assembly behavior as a function of DNA coverage on MG particle. (a) At a critical density of DNA coverage (**Figure 4-2b**, procedure described in **Figure 4-7**), 1:1 mixture of Gated Particle1 and Gated Particle2 form reversible co-assembly. (b) Above the critical density of DNA coverage, kinetically trapped aggregates are observed, which do not disassemble even after 28 h of Inhibitor addition. (b) Below the critical density of DNA coverage, co-assembly process is inefficient. (d) Table summarizing the co-assembly behavior as a function of DNA coverage. Experimental conditions: Gated Particle1 and Gated Particle2 suspended in TE buffer (pH = 8.0), 50 mM NaCl, 1.5 mM $MgCl_2$ at a final MG concentration of 0.05 wt% at 28 °C. Co-assembly and disassembly triggered by sequential addition of 2 equiv. of Input1 and Input2 (with respect to critical density on particle) and 1 equiv. of Inhibitor respectively. No inhibitor was added in part c. All CLSM images are represented as merged composite compiled as a *z*-projection. Scale bars: 5 µm.

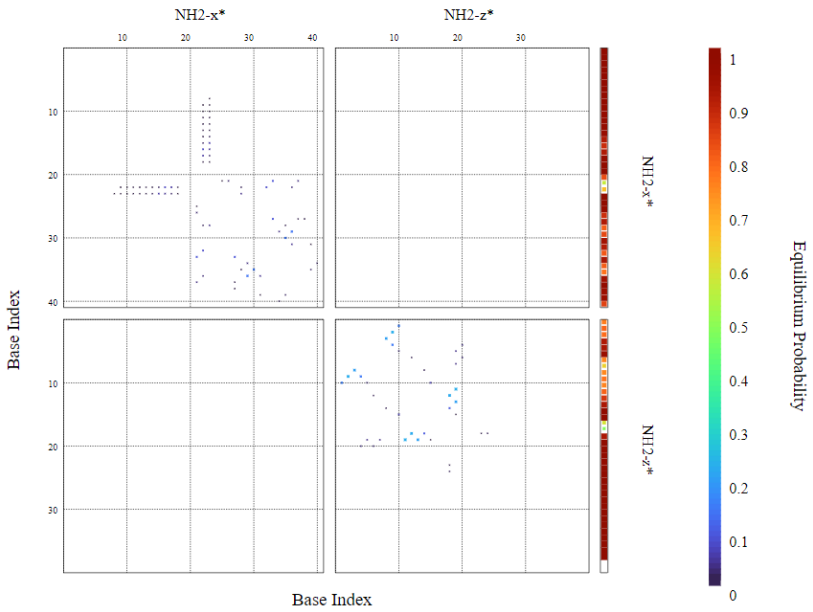

Figure 4-9. Ensemble pair fractions between NH_2-x* and NH_2-z* calculated with NUPACK simulations. Temperature is set at 28 °C with salt concentrations as 50 mM NaCl, 1.5 mM $MgCl_2$. No appreciable crosstalk between the two strands is observed.

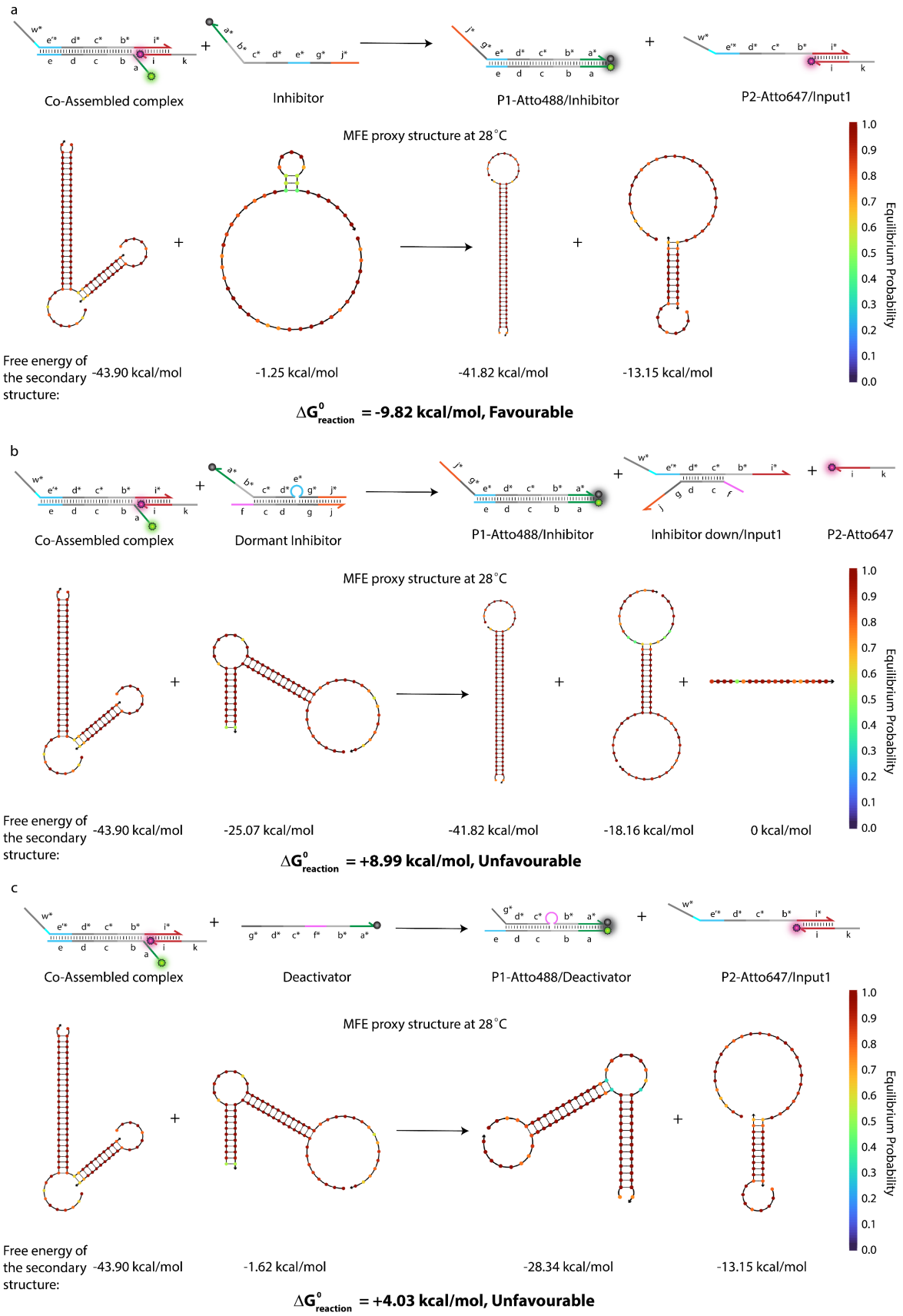

Figure 4-10. Free energy change in the reaction between (a) Co-Assembled complex and Inhibitor, (b) Co-Assembled complex and Dormant Inhibitor, (c) Co-Assembled complex and Deactivator calculated with NUPACK simulations setting the temperature at 28 °C and salt concentrations at 50 mM NaCl, 1.5 mM $MgCl_2$. **Only the reaction between Co-Assembled complex and Dormant Inhibitor is energetically favored.**

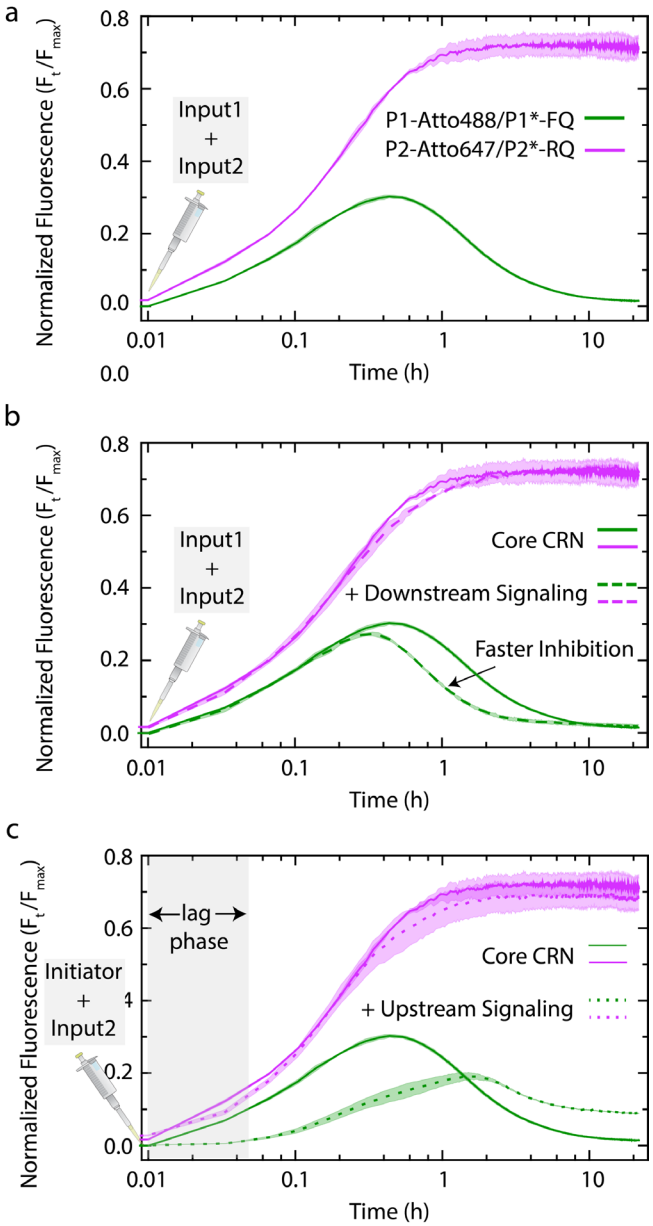

Figure 4-11. Time-resolved normalized fluorescence of Atto488 and Atto647 dye on modules: P1-Atto488/P1*-FQ and P2-Atto647/P2*-RQ (without particles) in (a) Core CRN, (b) Core CRN with downstream signaling, and (c) Core CRN with upstream signaling. Experimental conditions: (a) The two modules are dispersed at an equimolar concentration of 0.25 µM with 0.25 µM Dormant Inhibitor in TE buffer (pH = 8.0), 50 mM NaCl, 1.5 mM $MgCl_2$ at 28 °C. The network is initiated with 2 equiv. of Input1 and Input2. (b) Same as described in (a) but with additional 0.25 µM of Regenerator strand. (c) same as described in (a) but with 0.25 µM Threshold Gate, 0.5 µM Delay Gate. The network is initiated with 4 equiv. of Initiator and 2 equiv. of Input2. Atto488 and Atto647 fluorescence is normalized with respect to 0.25 µM of P1-Atto488 and P2-Atto647 strands respectively under same experimental conditions. The results represent an average contribution from 2 independent measurements, the shaded region depicts the standard deviation.

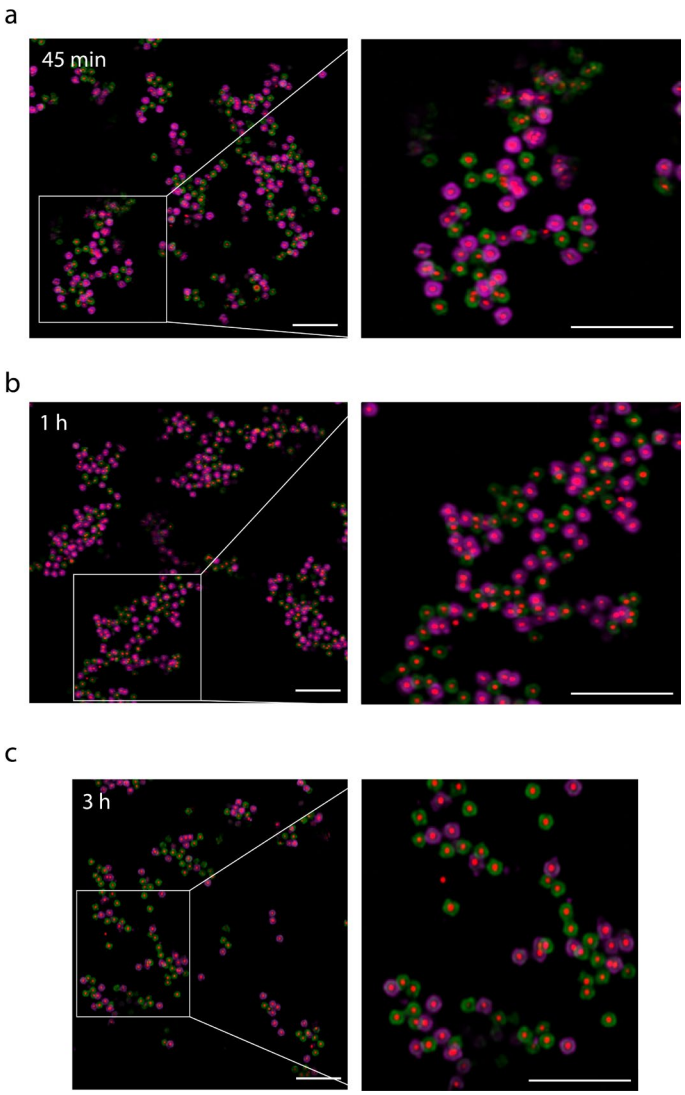

Figure 4-12. Zoomed-in CLSM images at time-point where maximum sizes of the co-assemblies are observed for (a) Core CRN, (b) Core CRN with downstream signaling, and (c) Core CRN with upstream signaling. All CLSM images are represented as merged composite images compiled as a z-projection. Scale bars: 5 µm.

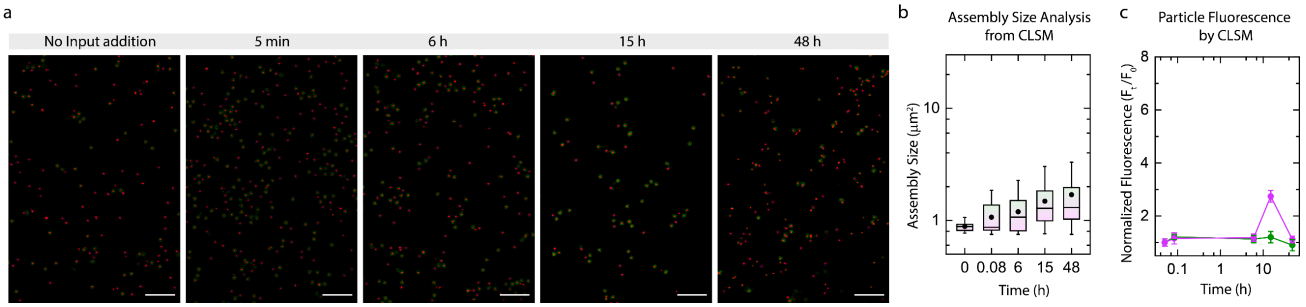

Figure 4-13. Control for Core CRN without Input1 and Input2 addition. (a) ex situ CLSM imaging of Core CRN. All CLSM images are represented as merged composite obtained from a z-projection. Experimental conditions: Gated Particle1 and Gated Particle2 suspended as an equimolar mixture in TE buffer (pH = 8.0), 50 mM NaCl, 1.5 mM $MgCl_2$ at a final MG concentration of 0.05 wt%, 1.5 μM (0.7 equiv. with respect to DNA on Gated Particle1 and Gated Particle2) of Dormant Inhibitor at 28 °C. (b) Assembly size analysis on the particles obtained from two different *z*-projections at each time interval. (c) Fluorescence on Gated Particle1 and Gated Particle2 obtained from CLSM images, each data point represents an average from 10 particles. Overall, no fluorescence activation on the Gated Particle1 and Gated Particle2 is observed. Scale bars: 5 μm.

The mean size of the particle population is increased to two times of its initial value indicating formation of small clusters only after 48 h of monitoring the system. This might result because of salt-induced non-specific aggregation of MGs.[52]

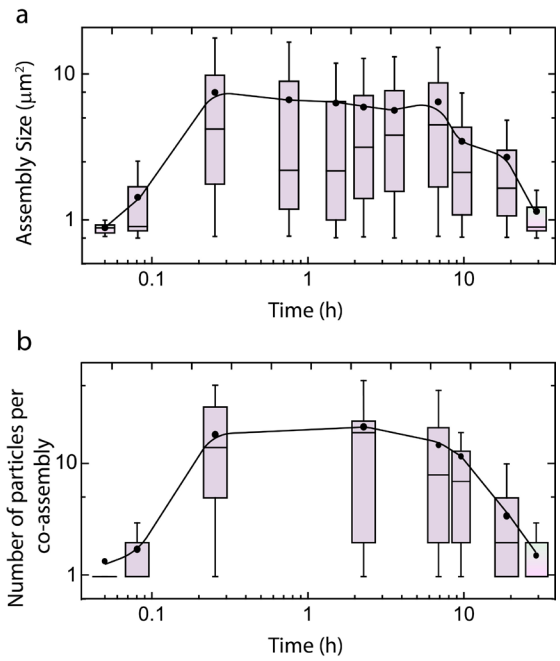

Figure 4-14. Comparison of the assembly size analysis from the CLSM images of Core CRN by (a) determining the average size of the co-assemblies upon thresholding the images (section 3.5), and (b) determining the average number of particles per co-assembly. The particles were counted manually to obtain the average count per co-assembly for each time-point. The box represents 25-75 % of data, whiskers represent 5-95 % of data, a solid circle represents the mean, and horizontal bar the median of the assembly size distribution in box charts. A solid line provides a guide to the eye. **Both characterization methods demonstrate similar trends of transient co-assembly.**

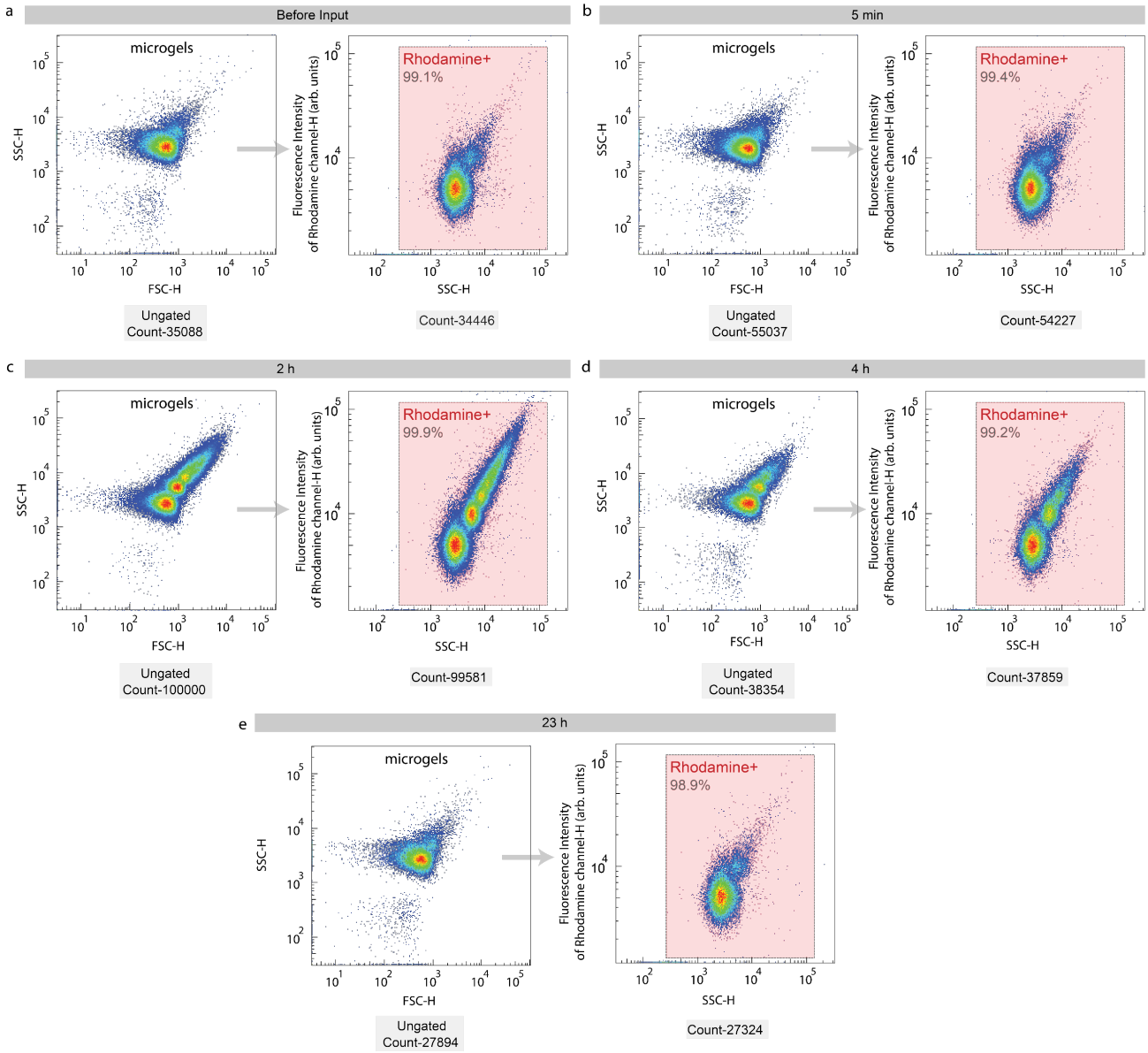

Figure 4-15. ex situ Flow Cytometric analysis of the Core CRN at different time intervals. (a-e) Initial identification of the MGs through forward (FSC, size)-height of the pulse (H) and side scattering (SSC, granularity/complexity)-height of the pulse (H). To isolate true MG events from the non-colloidal/non-labelled matter, MGs are gated (red boxes) using SSC intensity and the fluorescence intensity from the Rhodamine labelled core. The experiments are performed with an equimolar mixture of Gated Particle1 and Gated Particle2 at a final MG concentration of 0.05 wt% and 1.5 μM of Dormant Inhibitor dispersed in TE buffer (pH = 8.0), 50 mM NaCl, 1.5 mM $MgCl_2$ at 28 °C. The network was initiated with 2 equiv. each of Input1 and Input2. The aliquots were withdrawn as needed from the reaction mixture and diluted with TE buffer (pH = 8.0) by 100 times before injecting into the Cytometer.

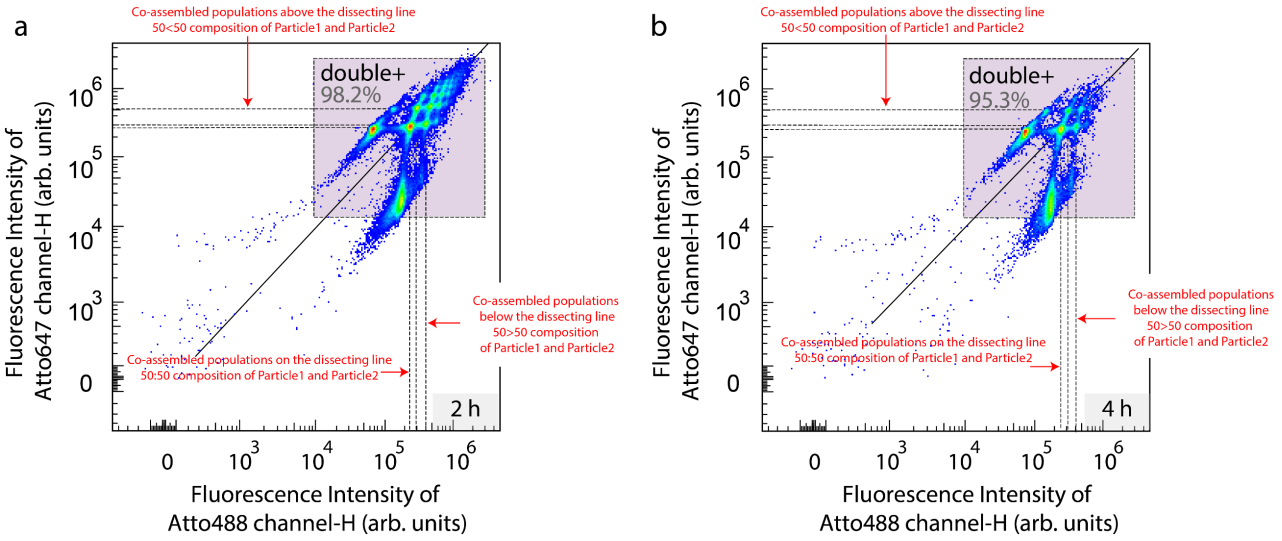

Figure 4-16. Processing of the ex situ Flow Cytometric results for Core CRN showing density plots with fluorescence from Atto488 and Atto647 channels on x and y axis respectively for aliquots derived at (a) 2 h and (b) 4 h. For simplicity only purple gate is shown. The ordered patterns observed are dissected with a solid black line which symmetrically divides the pattern into two halves. All the populations are compared for their Atto488 and Atto647 fluorescence intensity values by drawing black dotted lines along the axis.

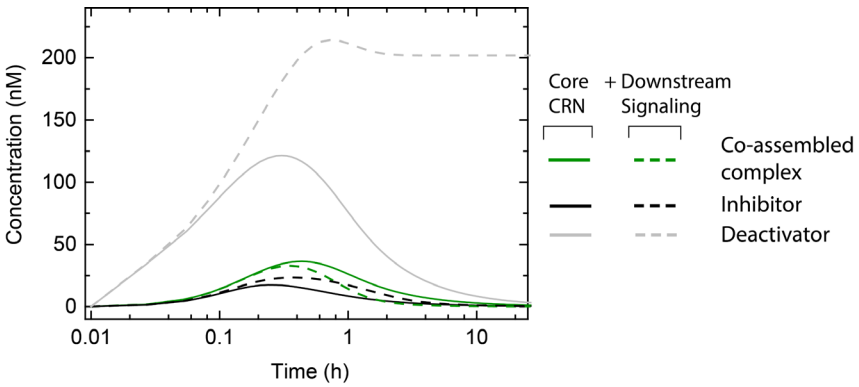

Figure 4-17. DSD Simulations predict the behavior of Co-assembled complex, Waste, Inhibitor and Deactivator strand for Core CRN with Regenerator (dashed curves) and without Regenerator (solid curves). The concentration of the starting modules: P1-Atto488/P1*-FQ, P2-Atto647/P2*-RQ, Dormant Inhibitor and Regenerator is set at 0.25 µM with 2 equiv. of Input1 and Input2.

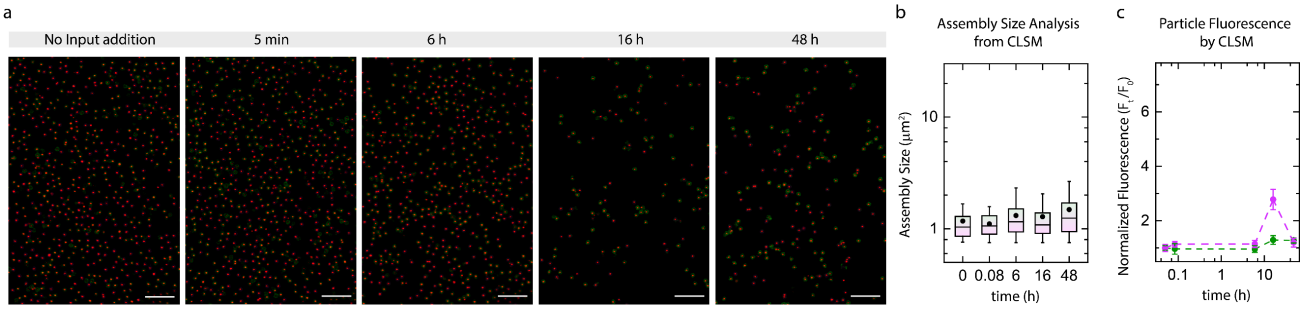

Figure 4-18. Control for Core CRN in presence of downstream signaling without Input1 and Input2 addition. (a) ex situ CLSM imaging of Core CRN. All CLSM images are represented as merged composite obtained from a z-projection. Experimental conditions: Gated Particle1 and Gated Particle2 suspended as equimolar mixture in TE buffer (pH = 8.0), 50 mM NaCl, 1.5 mM $MgCl_2$ at a final MG concentration of 0.05 wt%, 1.5 µM (0.7 equiv. with respect to DNA on Particle1 and Particle2) of Dormant Inhibitor, 1.5 µM of Regenerator strand at 28 °C. (b) Assembly size analysis on the particles obtained from two different z-projections at each time interval. No appreciable increase in the mean size of the particle population is observed even after 48h of monitoring the system. (c) Fluorescence on Gated Particle1 and Gated Particle2 obtained from CLSM images, each data point represents an average from 10 particles. Overall, no fluorescence activation on the Gated Particle1 and Gated Particle2 is observed. Scale bars: 5 µm.

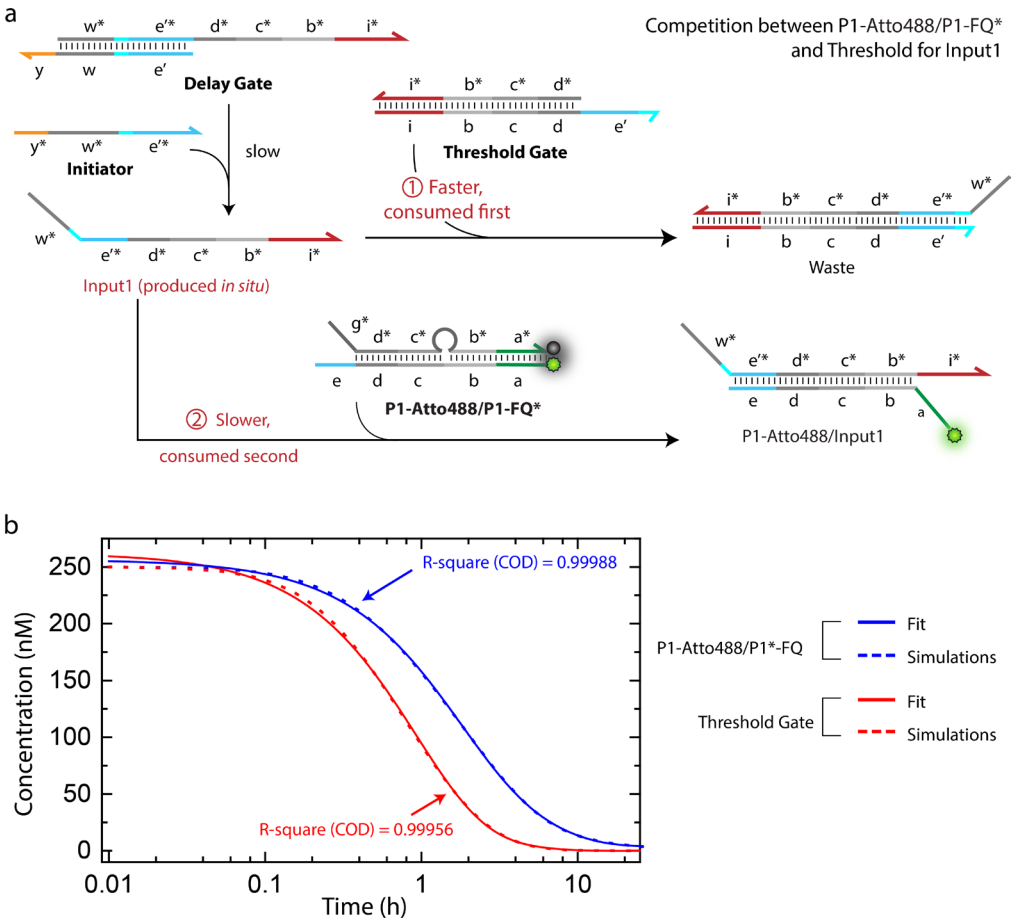

For P1-Atto488/P1*-FQ, $y = y_0 + A1 * exp^{\frac{-(x-x_0)}{t_1}} + A2 * exp^{\frac{-(x-x_0)}{t_2}}$;

$$y = 3.9 + 161 * exp^{\frac{-(x-0.1)}{1.5}} + 80 * exp^{\frac{-(x-0.1)}{4.6}};$$

Time constants, $t_1 =$ 1.5 h and $t_2 =$ 4.6 h

Rate constants, $k_1 =$ 0.7 h^{-1} and $k_2 =$ 0.2 h^{-1}, Combined Rate constant, $\boldsymbol{k_{decay,P1/P1*}} =$ **0.9 h^{-1}**

For Threshold Gate, $y = y_0 + A1 * exp^{\frac{-(x-x_0)}{t_1}} + A2 * exp^{\frac{-(x-x_0)}{t_2}}$;

$$y = 209 * exp^{\frac{-(x-0.1)}{0.9}} + 23 * exp^{\frac{-(x-0.1)}{2.8}};$$

Time constants, $t_1 =$ 1.1 h and $t_2 =$ 0.3 h

Rate constants, $k_1 =$ 0.7 h^{-1} and $k_2 =$ 0.2 h^{-1}, Combined Rate constant, $\boldsymbol{k_{decay,Threshold\ Gate}} =$ **1.4 h^{-1}**

$$\boldsymbol{k_{decay,Threshold\ Gate} > k_{decay,P1/P1*}}$$

Figure 4-19. (a) DSD simulations predicting the consumption of P1-Atto488/P1*-FQ and Threshold Gate when Input1 is produced in situ during the operation of Core CRN with upstream signaling. The concentration of modules: P1-Atto488/P1*-FQ, Threshold Gate is set at 0.25 µM, 0.5 µM of Delay Gate, 4 equiv. of Initiator and 2 equiv. of Input2. (b) The simulation results for both curves are fitted with a two-phase exponential decay model which provides two rate constants which when summed together provides the combined rate constant of the decaying species. R-square value or coefficient of determination (COD) measures the quality of the linear regression. **The rate of consumption or the decay rate of Threshold Gate is faster than P1-Atto488/P1*-FQ in presence of Input1.**

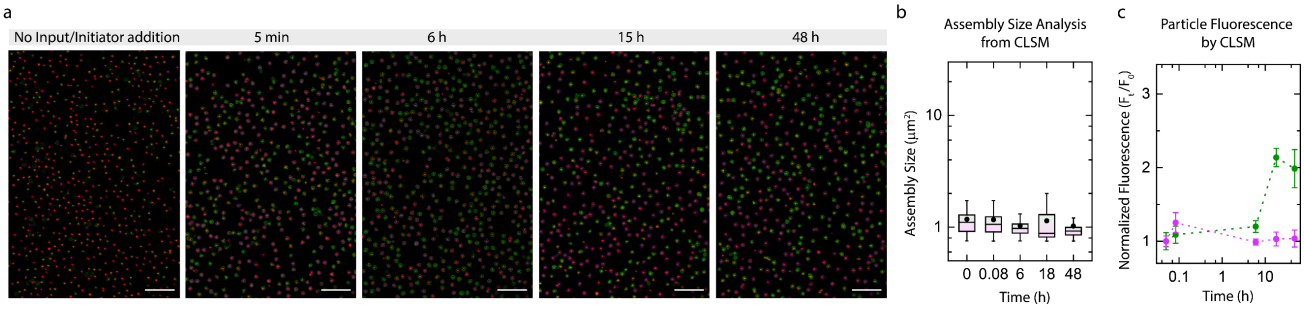

Figure 4-20. Control for Core CRN in presence of upstream signaling without Initiator and Input2 addition. (a) ex situ CLSM imaging of Core CRN. All CLSM images are represented as merged composite obtained from a z-projection. Experimental conditions: Gated Particle1 and Gated Particle2 suspended as an equimolar mixture in TE buffer (pH = 8.0), 50 mM NaCl, 1.5 mM $MgCl_2$ at a final MG concentration of 0.05 wt%, 1.5 μM (0.7 equiv. with respect to DNA on Gated Particle1 and Gated Particle2) of Dormant Inhibitor, 1.5 μM of Threshold Gate, 3 μM of Delay Gate at 28 °C. (b) Assembly size analysis on the particles obtained from two different z-projections at each time interval. No appreciable increase in the mean size of the particle population is observed even after 48 h of monitoring the system. (c) Fluorescence on Gated Particle1 and Gated Particle2 obtained from CLSM images, each data point represents an average from 10 particles. Scale bars: 5 μm.

No appreciable activation on Gated Particle1 is observed until 6 h, after which it increases to twice its initial value within 18 h and levels off beyond that. This leakage might stem from the partial fraying of the Delay Gate where 35% of the bases are unpaired at 28 °C (**Figure 4-21**).[13,50] However, the slow non-specific activation of Gated Particle1 does not induce any transient effects in the system. No activation on Gated Particle2 is observed throughout the experimental investigation.

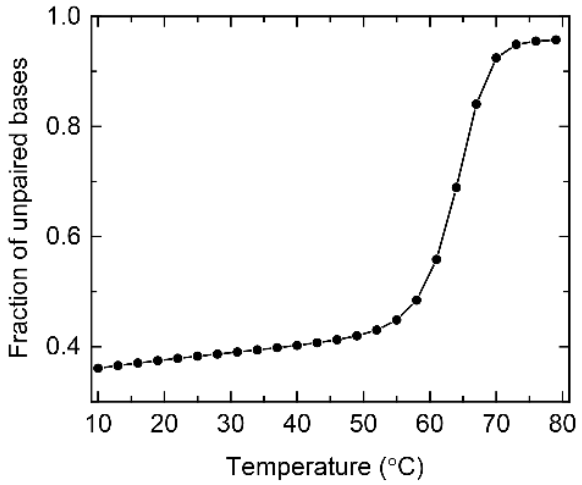

Figure 4-21. Melt profile for Delay Gate generated using NUPACK simulations. At 28 °C, 35% of the bases are unpaired at equilibrium. Parameters used for simulation: 3 μM of Delay Gate, 50 mM NaCl, 1.5 mM of $MgCl_2$.

4.4.6 Supplementary Notes

Note S1. Rate determination for Visual DSD Simulations.

All the simulations were carried out on software Visual DSD using the programming language reported by Phillips and co-workers. The codes are mentioned in the Supplementary Notes S2-S7.

The binding rate constant, k_b, defines the rate of hybridization of two complementary domains, while the unbinding rate constant, k_u, defines the rate of dissociation of these two hybridized domains. The two parameters (k_b and k_u) are specific to the length and composition of the domain/toehold sequence and are required to define the kinetics in the Visual DSD software.[51] Assuming a standard k_u of 0.012 s^{-1}, the k_b of all toeholds and other domains are calculated from the equilibrium composition of the species acquired at 50 mM NaCl, 1.5 mM $MgCl_2$, 28 °C from NUPACK.[52] The binding rate for toehold "y" (3nt, CTC) and "j" (7nt, AGAGTTG) cannot be calculated using the defined method because of its short length, unsupported by NUPACK and hence the binding rate was predicted based on previous literature to fit best with the results.[1-3]

$$A + A' \rightleftharpoons A\text{-}A'$$

$$K_{eq} = \frac{k_b}{k_u} = \frac{[A - A']}{[A] * [A']}$$

$$k_b = \frac{[A - A']}{[A] * [A']} * k_u$$

Note S2. Visual DSD Code for Core CRN.

```
directive rules {
// Classic DSD rules
bind(P1,P2,Q,D!i) :-
  P1 = C1 [D@X], compl(D, D'), P2 = C2 [D'@Y],
  Q = C1 [D!i] | C2 [D'!i], freshBond(D!i, P1|P2),
  not hidden(D@X, P1),
  not hidden(D'@Y, P2).
  bind(P,Q,D!i) :-
  P = C [D@X][D'@Y], compl(D, D'),
  Q = C [D!i] [D'!i], freshBond(D!i, P),
  not hidden(D@X, P),
  not hidden(D'@Y, P).
displace(P,Q,E!j,D!i) :-
  P = C [E!j D] [D!i] [D'!i E'!k], junction(E!j, E'!k, P),
  Q = C [E!j D!i] [D] [D'!i E'!k].
displaceL(P,Q,E!j,D!i) :-
  P = C [D!i] [D E!j] [E'!k D'!i], junction(E!j, E'!k, P),
  Q = C [D] [D!i E!j] [E'!k D'!i].
unbind(P,Q,D!i) :-
  P = C [D!i] [D'!i], toehold(D),
  Q = C [D] [D'], not adjacent(D!i,_,P).
adjacent(D!i,E!j,P) :- P = C [D!i E!j] [E'!j D'!i].
adjacent(D!i,E!j,P) :- P = C [E!j D!i] [D'!i E'!j].
bind(P1,P2,Q,D!i) :-
  P1 = C1 [D], P2 = C2 [D'], compl(D, D'),
  Q = C1 [D!i] | C2 [D'!i], freshBond(D!i, P1|P2).

displace(P,Q,E!j,D!i) :-
  P = C [E!j D] [D!i] [D'!i E'!j],
  Q = C [E!j D!i] [D] [D'!i E'!j].
```

```
displaceL(P,Q,E!j,D!i) :-
  P = C [D!i] [D E!j] [E'!j D'!i],
  Q = C [D] [D!i E!j] [E'!j D'!i].
cover(P,Q,E!j,D!i) :-
  P = C [E!j D] [D' E'!j], compl(D, D'),
  Q = C [E!j D!i] [D'!i E'!j], freshBond(D!i,P).
coverL(P,Q,E!j,D!i) :-
  P = C [D E!j] [E'!j D'], compl(D, D'),
  Q = C [D!i E!j] [E'!j D'!i], freshBond(D!i,P).

binds(P1,P2,R,D!i,[D#L]) :- bind(P1,P2,Q,D!i), not coverL(Q,_,D!i,_), covers(Q,R,D!i,L).
binds(P1,P2,Q,D!i,[D]) :- bind(P1,P2,Q,D!i), not coverL(Q,_,D!i,_), not cover(Q,_,D!i,_).
displaces(P,R,E!j,[D#L]) :- displace(P,Q,E!j,D!i), displaces(Q,R,D!i,L).
displaces(P,Q,E!j,[D]) :- displace(P,Q,E!j,D!i), not displace(Q,_,D!i,_).
displacesL(P,R,E!j,[D#L]) :- displaceL(P,Q,E!j,D!i), displacesL(Q,R,D!i,L).
displacesL(P,Q,E!j,[D]) :- displaceL(P,Q,E!j,D!i), not displaceL(Q,_,D!i,_).
covers(P,R,E!j,[D#L]) :- cover(P,Q,E!j,D!i), covers(Q,R,D!i,L).
covers(P,Q,E!j,[D]) :- cover(P,Q,E!j,D!i), not cover(Q,_,D!i,_).
coversL(P,R,E!j,[D#L]) :- coverL(P,Q,E!j,D!i), coversL(Q,R,D!i,L).
coversL(P,Q,E!j,[D]) :- coverL(P,Q,E!j,D!i), not coverL(Q,_,D!i,_).
unbinds(P,R,D!i,[D#L]) :-
  P = C [D!i E!j] [E'!j D'!i], toehold(D), not boundL(D!i,_,P),
  Q = C [D E!j] [E'!j D'], unbinds(Q,R,E!j,L).
boundL(D!i,E!j,P) :- P = C [E!j D!i] [D'!i E'!j].
unbinds(P,Q,D!i,[D]) :- unbind(P,Q,D!i).
find(D,Type,Rate):- rate(D,Type,Rate).
find(D,Type,Rate):- default(D,Type,Rate), not rate(D,Type,_).
//order of find and binds clauses could be reversed.
slow(P1, P2, Rate, Q) :- find(L, "bind", Rate), binds(P1,P2,Q,_,L). //, productive(Q,_,_!i,L).
fast(P, Rate, Q) :- displaces(P,Q,_,L), find(L, "displace", Rate).
fast(P, Rate, Q) :- displacesL(P,Q,_,L), find(L, "displace", Rate).
fast(P, Rate, Q) :- covers(P,Q,_,L), find(L, "cover", Rate).
fast(P, Rate, Q) :- coversL(P,Q,_,L), find(L, "cover", Rate).
fast(P, Rate, Q) :- unbinds(P,Q,_,L), find(L, "unbind", Rate).
productive(P,Q,E!j,L) :- displaces(P,Q,E!j,L).
productive(P,Q,E!j,L) :- displacesL(P,Q,E!j,L).
productive(P,Q,E!j,L) :- covers(P,Q,E!j,L).
productive(P,Q,E!j,L) :- coversL(P,Q,E!j,L).
mergestep(P,Q,V) :- fast(P,_,Q), not member(Q,V).
merge(P,P,V) :- not fast(P,_,_).
merge(P,R,V) :- mergestep(P,Q,V), merge(Q,R,[Q#V]).
infinite([P1; P2], Rate, R) :- slow(P1, P2, Rate, Q), merge(Q,R,[(P1|P2);Q]).
infinite([P], Rate, R) :- slow(P, Rate, Q), merge(Q,R,[P;Q]).
detailed([P1; P2], Rate, Q):- slow(P1, P2, Rate, Q).
detailed([P], Rate, Q) :- slow(P, Rate, Q).
detailed([P], Rate, Q) :- fast(P, Rate, Q).
default([_],"unbind",0.012).
default(_,"bind",0.00003).
default(_,"displace",1.0).
default(_,"cover",1.0).
//The following specifies infinite compilation mode
reaction([P1; P2], Rate, R) :- infinite([P1; P2], Rate, R).
reaction([P], Rate, R) :- infinite([P], Rate, R).
rate([e^*], "bind", 0.0000033).
rate([f^*], "bind", 0.0000033).
rate([a^*], "bind", 0.00003).
rate([l^*], "bind", 0.000005).
rate([i], "bind", 0.00011).
}
directive simulator deterministic
```

```
directive deterministic {stiff = true}
directive simulation {final = 100000}
(500 [<w* e^* d* c* b* i*>]
|250 [<a^!1 b!2 c!3 d!4 e^>
|<g^* d*!4 c*!3 f^* b*!2 a^*!1>]
|250 [<f^ c!11 d!12 g^!13 j^!14>
|<j^*!14 g^*!13 e^* d*!12 c*!11 b* a^*>]
|250 [<k!15 i!16>|<i*!16 m* k*!15 l^*>]
|500 [<l^ k m i>]
)
```

Note S3. Code explanation for code used for Core CRN.

We now illustrate how this language can be used to define logic predicates that automatically generate the behavior of DNA strand displacement systems.

```
directive rules {
// Classic DSD rules
```

The following logic predicate defines the conditions that need to be satisfied in order for processes P1 and P2 to bind, producing the resulting process Q. The predicate is satisfied if P1 matches a context C1[D] and P2 matches a context C2[D'], such that D is complementary to D', as specified by the built-in predicate compl(D,D'). The resulting process Q is obtained by replacing D with D!i in context C1, and replacing D' with D'!i in context C2, written C1[D!i] | C2[D'!i]. Furthermore, we require that the bond i is fresh in the sense that it should not occur anywhere in processes P1 and P2. This is enforced by the built-in predicate fresh Bond(D!i, P1 | P2):

```
bind(P1,P2,Q,D!i) :-
 P1 = C1 [D@X], compl(D, D'), P2 = C2 [D'@Y],
 Q = C1 [D!i] | C2 [D'!i], freshBond(D!i, P1|P2),
```

The presence of the hidden constraint prohibits complexes to bind on domains hidden in a loop structure.

```
 not hidden(D@X, P1),
 not hidden(D'@Y, P2).
```

The following logic predicate defines the conditions that need to be satisfied in order for processed P to intramolecularly bind such that D is complementary to D', producing a resulting process Q. This is the unimolecular version of the binding reaction, to model phenomena such as the binding of domains in a bulge or the formation of hairpins.

```
 bind(P,Q,D!i) :-
 P = C [D@X][D'@Y], compl(D, D'),
 Q = C [D!i] [D'!i], freshBond(D!i, P),
 not hidden(D@X, P),
 not hidden(D'@Y, P).
```

Similarly, the following predicate defines the conditions that need to be satisfied in order for process P to perform a strand displacement step, resulting in process Q. The displacement rule is generalized to branches with the junction predicate:

```
displace(P,Q,E!j,D!i) :-
 P = C [E!j D] [D!i] [D'!i E'!k], junction(E!j, E'!k, P),
 Q = C [E!j D!i] [D] [D'!i E'!k].
```

Note that this predicate only allows displacement to take place in the 5' to 3' direction. As a result, we also need to define a symmetric *displaceL* predicate for the 3' to 5' direction:

```
displaceL(P,Q,E!j,D!i) :-
 P = C [D!i] [D E!j] [E'!k D'!i], junction(E!j, E'!k, P),
 Q = C [D] [D!i E!j] [E'!k D'!i].
```

Finally, the following predicate defines the conditions for unbinding:

```
unbind(P,Q,D!i) :-
  P = C [D!i] [D'!i], toehold(D),
  Q = C [D] [D'], not adjacent(D!i,_,P).
```

This encodes the assumption that only the toehold domains are short enough to unbind, as specified by the built-in predicate *toehold(D)*, and relies on an additional predicate to check that there are no bound domains adjacent to domain D:

```
adjacent(D!i,E!j,P) :- P = C [D!i E!j] [E'!j D'!i].
adjacent(D!i,E!j,P) :- P = C [E!j D!i] [D'!i E'!j].
```

Note that this predicate takes the site D!i as an argument, which contains both the domain D and its corresponding bond i. Since the bond can only occur twice in a well-formed process, this allows the inference system to pinpoint the specific domain on which unbinding occurs in order to test for adjacent bound domains, even if there are multiple occurrences of domain D in the system.

```
bind(P1,P2,Q,D!i) :-
  P1 = C1 [D], P2 = C2 [D'], compl(D, D'),
  Q = C1 [D!i] | C2 [D'!i], freshBond(D!i, P1|P2).

displace(P,Q,E!j,D!i) :-
  P = C [E!j D] [D!i] [D'!i E'!j],
  Q = C [E!j D!i] [D] [D'!i E'!j].
displaceL(P,Q,E!j,D!i) :-
  P = C [D!i] [D E!j] [E'!j D'!i],
  Q = C [D] [D!i E!j] [E'!j D'!i].
```

In order to account for the case in which adjacent complementary domains can bind to each other, a *cover* predicate is defined.

```
cover(P,Q,E!j,D!i) :-
  P = C [E!j D] [D' E'!j], compl(D, D'),
  Q = C [E!j D!i] [D'!i E'!j], freshBond(D!i,P).
coverL(P,Q,E!j,D!i) :-
  P = C [D E!j] [E'!j D'], compl(D, D'),
  Q = C [D!i E!j] [E'!j D'!i], freshBond(D!i,P).
```

In order to assure that displace, cover, and bind predicates are extended to occur on a maximal sequence of consecutive domains, they are defined using recursive encoding. There are two cases for the predicate: the base case and the recursive case. The base case displaces(P,Q,E!j,[D]) holds if the single displacement predicate displace(P,Q,E! j,D!i) also holds, where E!j and D!i denote the sites at the beginning and end of the displacement, respectively, and no further displacement is possible starting from site D!i. The list [D] contains the consecutive domains on which the displacement takes place, where the list contains only a single domain D in the base case. The recursive case displaces(P,R,E!j, [D#L]) holds if process P can perform a single displacement to become process Q, beginning at site E!j and ending at site D!i, and furthermore if process Q can itself perform multiple displacements starting at site D!i along the list of domains L to produce process R. The list [D#L] adds the domain D to the list of domains L. Similar recursive predicates for the symmetric case of the displace rule and for the cover and bind rules are defined.

```
binds(P1,P2,R,D!i,[D#L]) :- bind(P1,P2,Q,D!i), not coverL(Q,_,D!i,_), covers(Q,R,D!i,L).
binds(P1,P2,Q,D!i,[D]) :- bind(P1,P2,Q,D!i), not coverL(Q,_,D!i,_), not cover(Q,_,D!i,_).
displaces(P,R,E!j,[D#L]) :- displace(P,Q,E!j,D!i), displaces(Q,R,D!i,L).
displaces(P,Q,E!j,[D]) :- displace(P,Q,E!j,D!i), not displace(Q,_,D!i,_).
displacesL(P,R,E!j,[D#L]) :- displaceL(P,Q,E!j,D!i), displacesL(Q,R,D!i,L).
displacesL(P,Q,E!j,[D]) :- displaceL(P,Q,E!j,D!i), not displaceL(Q,_,D!i,_).
covers(P,R,E!j,[D#L]) :- cover(P,Q,E!j,D!i), covers(Q,R,D!i,L).
covers(P,Q,E!j,[D]) :- cover(P,Q,E!j,D!i), not cover(Q,_,D!i,_).
```

```
coversL(P,R,E!j,[D#L]) :- coverL(P,Q,E!j,D!i), coversL(Q,R,D!i,L).
coversL(P,Q,E!j,[D]) :- coverL(P,Q,E!j,D!i), not coverL(Q,_,D!i,_).
unbinds(P,R,D!i,[D#L]) :-
  P = C [D!i E!j] [E'!j D'!i], toehold(D), not boundL(D!i,_,P),
  Q = C [D E!j] [E'!j D'], unbinds(Q,R,E!j,L).
boundL(D!i,E!j,P) :- P = C [E!j D!i] [D'!i E'!j].
unbinds(P,Q,D!i,[D]) :- unbind(P,Q,D!i).
find(D,Type,Rate):- rate(D,Type,Rate).
find(D,Type,Rate):- default(D,Type,Rate), not rate(D,Type,_).
```

The behavior of the reaction can be defined to be fast or slow. Sufficiently fast reactions are merged into a single step. This predicate assumes that only unimolecular reactions involving a single species can be considered fast, since bimolecular reactions are limited by the relatively slow rate of molecular diffusion. The list V stores the list of processes corresponding to each step of the merge. This is used to ensure that the same process is not revisited twice, in order to avoid getting trapped in an infinite cycle of fast reactions.

```
//order of find and binds clauses could be reversed.
slow(P1, P2, Rate, Q) :- find(L, "bind", Rate), binds(P1,P2,Q,_,L). //, productive(Q,_,_!i,L).
fast(P, Rate, Q) :- displaces(P,Q,_,L), find(L, "displace", Rate).
fast(P, Rate, Q) :- displacesL(P,Q,_,L), find(L, "displace", Rate).
fast(P, Rate, Q) :- covers(P,Q,_,L), find(L, "cover", Rate).
fast(P, Rate, Q) :- coversL(P,Q,_,L), find(L, "cover", Rate).
fast(P, Rate, Q) :- unbinds(P,Q,_,L), find(L, "unbind", Rate).
```

Productive predicate ensures that toehold binding only takes place if a subsequent branch migration is possible.

```
productive(P,Q,E!j,L) :- displaces(P,Q,E!j,L).
productive(P,Q,E!j,L) :- displacesL(P,Q,E!j,L).
productive(P,Q,E!j,L) :- covers(P,Q,E!j,L).
productive(P,Q,E!j,L) :- coversL(P,Q,E!j,L).
mergestep(P,Q,V) :- fast(P,_,Q), not member(Q,V).
merge(P,P,V) :- not fast(P,_,_).
merge(P,R,V) :- mergestep(P,Q,V), merge(Q,R,[Q#V]).
infinite([P1; P2], Rate, R) :- slow(P1, P2, Rate, Q), merge(Q,R,[(P1|P2);Q]).
infinite([P], Rate, R) :- slow(P, Rate, Q), merge(Q,R,[P;Q]).
detailed([P1; P2], Rate, Q):- slow(P1, P2, Rate, Q).
detailed([P], Rate, Q) :- slow(P, Rate, Q).
detailed([P], Rate, Q) :- fast(P, Rate, Q).
```

The following predicates allow default rates to be assigned to all toehold:

```
default([_],"unbind",0.012).
default(_,"bind",0.00003).
default(_,"displace",1.0).
default(_,"cover",1.0).
```

Above predicates are combined automatically to generate the behavior of a nucleic acid system, i.e., a CRN, defined as a set of reactions, where each reaction consists of a multiset of reactant species, reaction rate and a multiset of product species. This is achieved by defining a built-in *species* predicate that converts a process P to a multiset of species, where a species is a set of one or more strands that form a connected component, and by allowing the programmer to define one or more custom reaction predicates of the form *reaction*([P1;⋯;PN], R, Q). The reaction predicate takes as input a list of one or more processes [P1;⋯;PN] denoting the reactant species, together with a reaction rate R, and produces as output the product of the reaction, specified as a process Q. The system then takes care of splitting the process Q into individual products species, using the built-in species predicate. Applying this approach to our example, we can encode the rules of DNA strand displacement by defining reaction predicates for binding, displacement, and unbinding of strands, using our previously defined predicates. The compilation mode is chosen to be *infinite* where the concentration of species is assumed to be sufficiently low that the rates of unbinding and migration reactions are infinite compared to the rates of binding reactions. As a result, strand displacement is assumed to take place in a single step that merges binding, migration, and unbinding.

```
//The following specifies infinite compilation mode
reaction([P1; P2], Rate, R) :- infinite([P1; P2], Rate, R).
reaction([P], Rate, R) :- infinite([P], Rate, R).
```

Following predicates allow specific rates to be assigned to distinct toeholds”

```
rate([e^*], "bind", 0.0000033).
rate([f^*], "bind", 0.0000033).
rate([a^*], "bind", 0.00003).
rate([l^*], "bind", 0.000005).
rate([i], "bind", 0.00011).
}
directive simulator deterministic
directive deterministic {stiff = true}
directive simulation {final = 100000}
(500 [<w* e^* d* c* b* i*>]
|250 [<a^!1 b!2 c!3 d!4 e^>
|<g^* d*!4 c*!3 f^* b*!2 a^*!1>]
|250 [<f^ c!11 d!12 g^!13 j^!14>
|<j^*!14 g^*!13 e^* d*!12 c*!11 b* a^*>]
|250 [<k!15 i!16>|<i*!16 m* k*!15 l^*>]
|500 [<l^ k m i>]
)
```

Note S4. CRN code for Core CRN.

```
directive simulation {final=100000; plots=[sp_0; sp_1; sp_2; sp_3; sp_4; sp_5; sp_6; sp_7; sp_8; sp_9; sp_10; sp_11; sp_12; sp_13; sp_14; sp_15; sp_16; sp_17]; }
directive simulator deterministic
directive deterministic {stiff=true}

| 500 sp_0
| 250 sp_1
| 250 sp_2
| 250 sp_3
| 500 sp_4
| sp_4 + sp_3 ->{5E-06} sp_17 + sp_16
| sp_1 + sp_0 ->{3.3E-06} sp_15 + sp_14
| sp_15 + sp_4 ->{0.00011} sp_12
| sp_15 + sp_17 ->{0.00011} sp_13
| sp_2 + sp_14 ->{3.3E-06} sp_11 + sp_10
| sp_12 + sp_3 ->{5E-06} sp_9
| sp_1 + sp_11 ->{3.3E-06} sp_14 + sp_8
| sp_15 + sp_11 ->{3E-05} sp_8 + sp_0
| sp_13 + sp_11 ->{3E-05} sp_8 + sp_6
| sp_12 + sp_11 ->{3E-05} sp_8 + sp_7
| sp_9 + sp_11 ->{3E-05} sp_8 + sp_5
| sp_7 + sp_3 ->{5E-06} sp_5
| sp_1 + sp_7 ->{3.3E-06} sp_12 + sp_14
| sp_1 + sp_6 ->{3.3E-06} sp_13 + sp_14
| sp_1 + sp_5 ->{3.3E-06} sp_9 + sp_14
```

Note S5. Visual DSD code for the effect of downstream signaling on Core CRN.

```
directive rules {
// Classic DSD rules
bind(P1,P2,Q,D!i) :-
  P1 = C1 [D@X], compl(D, D'), P2 = C2 [D'@Y],
  Q = C1 [D!i] | C2 [D'!i], freshBond(D!i, P1|P2),
  not hidden(D@X, P1),
```

```
  not hidden(D'@Y, P2).
  bind(P,Q,D!i) :-
  P = C [D@X][D'@Y], compl(D, D'),
  Q = C [D!i] [D'!i], freshBond(D!i, P),
  not hidden(D@X, P),
  not hidden(D'@Y, P).
displace(P,Q,E!j,D!i) :-
  P = C [E!j D] [D!i] [D'!i E'!k], junction(E!j, E'!k, P),
  Q = C [E!j D!i] [D] [D'!i E'!k].
displaceL(P,Q,E!j,D!i) :-
  P = C [D!i] [D E!j] [E'!k D'!i], junction(E!j, E'!k, P),
  Q = C [D] [D!i E!j] [E'!k D'!i].
unbind(P,Q,D!i) :-
  P = C [D!i] [D'!i], toehold(D),
  Q = C [D] [D'], not adjacent(D!i,_,P).
adjacent(D!i,E!j,P) :- P = C [D!i E!j] [E'!j D'!i].
adjacent(D!i,E!j,P) :- P = C [E!j D!i] [D'!i E'!j].
bind(P1,P2,Q,D!i) :-
  P1 = C1 [D], P2 = C2 [D'], compl(D, D'),
  Q = C1 [D!i] | C2 [D'!i], freshBond(D!i, P1|P2).

displace(P,Q,E!j,D!i) :-
  P = C [E!j D] [D!i] [D'!i E'!j],
  Q = C [E!j D!i] [D] [D'!i E'!j].
displaceL(P,Q,E!j,D!i) :-
  P = C [D!i] [D E!j] [E'!j D'!i],
  Q = C [D] [D!i E!j] [E'!j D'!i].
cover(P,Q,E!j,D!i) :-
  P = C [E!j D] [D' E'!j], compl(D, D'),
  Q = C [E!j D!i] [D'!i E'!j], freshBond(D!i,P).
coverL(P,Q,E!j,D!i) :-
  P = C [D E!j] [E'!j D'], compl(D, D'),
  Q = C [D!i E!j] [E'!j D'!i], freshBond(D!i,P).

binds(P1,P2,R,D!i,[D#L]) :- bind(P1,P2,Q,D!i), not coverL(Q,_,D!i,_), covers(Q,R,D!i,L).
binds(P1,P2,Q,D!i,[D]) :- bind(P1,P2,Q,D!i), not coverL(Q,_,D!i,_), not cover(Q,_,D!i,_).
displaces(P,R,E!j,[D#L]) :- displace(P,Q,E!j,D!i), displaces(Q,R,D!i,L).
displaces(P,Q,E!j,[D]) :- displace(P,Q,E!j,D!i), not displace(Q,_,D!i,_).
displacesL(P,R,E!j,[D#L]) :- displaceL(P,Q,E!j,D!i), displacesL(Q,R,D!i,L).
displacesL(P,Q,E!j,[D]) :- displaceL(P,Q,E!j,D!i), not displaceL(Q,_,D!i,_).
covers(P,R,E!j,[D#L]) :- cover(P,Q,E!j,D!i), covers(Q,R,D!i,L).
covers(P,Q,E!j,[D]) :- cover(P,Q,E!j,D!i), not cover(Q,_,D!i,_).
coversL(P,R,E!j,[D#L]) :- coverL(P,Q,E!j,D!i), coversL(Q,R,D!i,L).
coversL(P,Q,E!j,[D]) :- coverL(P,Q,E!j,D!i), not coverL(Q,_,D!i,_).
unbinds(P,R,D!i,[D#L]) :-
  P = C [D!i E!j] [E'!j D'!i], toehold(D), not boundL(D!i,_,P),
  Q = C [D E!j] [E'!j D'], unbinds(Q,R,E!j,L).
boundL(D!i,E!j,P) :- P = C [E!j D!i] [D'!i E'!j].
unbinds(P,Q,D!i,[D]) :- unbind(P,Q,D!i).
find(D,Type,Rate):- rate(D,Type,Rate).
find(D,Type,Rate):- default(D,Type,Rate), not rate(D,Type,_).
//order of find and binds clauses could be reversed.
slow(P1, P2, Rate, Q) :- find(L, "bind", Rate), binds(P1,P2,Q,_,L). //, productive(Q,_,_!i,L).
fast(P, Rate, Q) :- displaces(P,Q,_,L), find(L, "displace", Rate).
```

```
fast(P, Rate, Q) :- displacesL(P,Q,_,L), find(L, "displace", Rate).
fast(P, Rate, Q) :- covers(P,Q,_,L), find(L, "cover", Rate).
fast(P, Rate, Q) :- coversL(P,Q,_,L), find(L, "cover", Rate).
fast(P, Rate, Q) :- unbinds(P,Q,_,L), find(L, "unbind", Rate).
productive(P,Q,E!j,L) :- displaces(P,Q,E!j,L).
productive(P,Q,E!j,L) :- displacesL(P,Q,E!j,L).
productive(P,Q,E!j,L) :- covers(P,Q,E!j,L).
productive(P,Q,E!j,L) :- coversL(P,Q,E!j,L).
mergestep(P,Q,V) :- fast(P,_,Q), not member(Q,V).
merge(P,P,V) :- not fast(P,_,_).
merge(P,R,V) :- mergestep(P,Q,V), merge(Q,R,[Q#V]).
infinite([P1; P2], Rate, R) :- slow(P1, P2, Rate, Q), merge(Q,R,[(P1|P2);Q]).
infinite([P], Rate, R) :- slow(P, Rate, Q), merge(Q,R,[P;Q]).
detailed([P1; P2], Rate, Q):- slow(P1, P2, Rate, Q).
detailed([P], Rate, Q) :- slow(P, Rate, Q).
detailed([P], Rate, Q) :- fast(P, Rate, Q).
default([_],"unbind",0.012).
default(_,"bind",0.00003).
default(_,"displace",1.0).
default(_,"cover",1.0).
//The following specifies infinite compilation mode
reaction([P1; P2], Rate, R) :- infinite([P1; P2], Rate, R).
reaction([P], Rate, R) :- infinite([P], Rate, R).
rate([e^*], "bind", 0.0000033).
rate([f^*], "bind", 0.0000033).
rate([a^*], "bind", 0.00003).
rate([l^*], "bind", 0.000005).
rate([i], "bind", 0.00011).
rate([j^], "bind", 0.000058).
}
directive simulator deterministic
directive deterministic {stiff = true}
directive simulation {final = 100000}
(500 [<w* e^* d* c* b* i*>]
|250 [<a^!1 b!2 c!3 d!4 e^>
|<g^* d*!4 c*!3 f^* b*!2 a^*!1>]
|250 [<f^ c!11 d!12 g^!13 j^!14>
|<j^*!14 g^*!13 e^* d*!12 c*!11 b* a^*>]
|250 [<k!15 i!16>|<i*!16 m* k*!15 l^*>]
|500 [<l^ k m i>]
|250 [<j^* g^* d* c*>]
)
```

Note S6. CRN code for the effect of downstream signaling on Core CRN.

```
directive simulation {final=100000; plots=[sp_0; sp_1; sp_2; sp_3; sp_4; sp_5; sp_6; sp_7; sp_8; sp_9; sp_10; sp_11; sp_12; sp_13; sp_14; sp_15; sp_16; sp_17; sp_18; sp_19]; }
directive simulator deterministic
directive deterministic {stiff=true}

| 500 sp_0
| 250 sp_1
| 250 sp_2
| 250 sp_3
| 500 sp_4
```

```
| 250 sp_5
| sp_4 + sp_3 ->{5E-06} sp_19 + sp_18
| sp_1 + sp_0 ->{3.3E-06} sp_17 + sp_16
| sp_17 + sp_4 ->{0.00011} sp_14
| sp_17 + sp_19 ->{0.00011} sp_15
| sp_2 + sp_16 ->{3.3E-06} sp_13 + sp_12
| sp_14 + sp_3 ->{5E-06} sp_11
| sp_1 + sp_13 ->{3.3E-06} sp_16 + sp_10
| sp_17 + sp_13 ->{3E-05} sp_10 + sp_0
| sp_15 + sp_13 ->{3E-05} sp_10 + sp_8
| sp_14 + sp_13 ->{3E-05} sp_10 + sp_9
| sp_11 + sp_13 ->{3E-05} sp_10 + sp_6
| sp_9 + sp_3 ->{5E-06} sp_6
| sp_1 + sp_9 ->{3.3E-06} sp_14 + sp_16
| sp_1 + sp_8 ->{3.3E-06} sp_15 + sp_16
| sp_5 + sp_12 <->{5.8E-05}{3.3E-06} sp_7 + sp_16
| sp_1 + sp_6 ->{3.3E-06} sp_11 + sp_16
```

Note S7. Visual DSD code for the effect of upstream signaling on Core CRN.

```
directive rules {
// Classic DSD rules
bind(P1,P2,Q,D!i) :-
  P1 = C1 [D@X], compl(D, D'), P2 = C2 [D'@Y],
  Q = C1 [D!i] | C2 [D'!i], freshBond(D!i, P1|P2),
  not hidden(D@X, P1),
  not hidden(D'@Y, P2).
  bind(P,Q,D!i) :-
  P = C [D@X][D'@Y], compl(D, D'),
  Q = C [D!i] [D'!i], freshBond(D!i, P),
  not hidden(D@X, P),
  not hidden(D'@Y, P).
displace(P,Q,E!j,D!i) :-
  P = C [E!j D] [D!i] [D'!i E'!k], junction(E!j, E'!k, P),
  Q = C [E!j D!i] [D] [D'!i E'!k].
displaceL(P,Q,E!j,D!i) :-
  P = C [D!i] [D E!j] [E'!k D'!i], junction(E!j, E'!k, P),
  Q = C [D] [D!i E!j] [E'!k D'!i].
unbind(P,Q,D!i) :-
  P = C [D!i] [D'!i], toehold(D),
  Q = C [D] [D'], not adjacent(D!i,_,P).
adjacent(D!i,E!j,P) :- P = C [D!i E!j] [E'!j D'!i].
adjacent(D!i,E!j,P) :- P = C [E!j D!i] [D'!i E'!j].
bind(P1,P2,Q,D!i) :-
  P1 = C1 [D], P2 = C2 [D'], compl(D, D'),
  Q = C1 [D!i] | C2 [D'!i], freshBond(D!i, P1|P2).

displace(P,Q,E!j,D!i) :-
  P = C [E!j D] [D!i] [D'!i E'!j],
  Q = C [E!j D!i] [D] [D'!i E'!j].
displaceL(P,Q,E!j,D!i) :-
  P = C [D!i] [D E!j] [E'!j D'!i],
  Q = C [D] [D!i E!j] [E'!j D'!i].
cover(P,Q,E!j,D!i) :-
  P = C [E!j D] [D' E'!j], compl(D, D'),
```

```
  Q = C [E!j D!i] [D'!i E'!j], freshBond(D!i,P).
coverL(P,Q,E!j,D!i) :-
  P = C [D E!j] [E'!j D'], compl(D, D'),
  Q = C [D!i E!j] [E'!j D'!i], freshBond(D!i,P).

binds(P1,P2,R,D!i,[D#L]) :- bind(P1,P2,Q,D!i), not coverL(Q,_,D!i,_), covers(Q,R,D!i,L).
binds(P1,P2,Q,D!i,[D]) :- bind(P1,P2,Q,D!i), not coverL(Q,_,D!i,_), not cover(Q,_,D!i,_).
displaces(P,R,E!j,[D#L]) :- displace(P,Q,E!j,D!i), displaces(Q,R,D!i,L).
displaces(P,Q,E!j,[D]) :- displace(P,Q,E!j,D!i), not displace(Q,_,D!i,_).
displacesL(P,R,E!j,[D#L]) :- displaceL(P,Q,E!j,D!i), displacesL(Q,R,D!i,L).
displacesL(P,Q,E!j,[D]) :- displaceL(P,Q,E!j,D!i), not displaceL(Q,_,D!i,_).
covers(P,R,E!j,[D#L]) :- cover(P,Q,E!j,D!i), covers(Q,R,D!i,L).
covers(P,Q,E!j,[D]) :- cover(P,Q,E!j,D!i), not cover(Q,_,D!i,_).
coversL(P,R,E!j,[D#L]) :- coverL(P,Q,E!j,D!i), coversL(Q,R,D!i,L).
coversL(P,Q,E!j,[D]) :- coverL(P,Q,E!j,D!i), not coverL(Q,_,D!i,_).
unbinds(P,R,D!i,[D#L]) :-
  P = C [D!i E!j] [E'!j D'!i], toehold(D), not boundL(D!i,_,P),
  Q = C [D E!j] [E'!j D'], unbinds(Q,R,E!j,L).
boundL(D!i,E!j,P) :- P = C [E!j D!i] [D'!i E'!j].
unbinds(P,Q,D!i,[D]) :- unbind(P,Q,D!i).
find(D,Type,Rate):- rate(D,Type,Rate).
find(D,Type,Rate):- default(D,Type,Rate), not rate(D,Type,_).
//order of find and binds clauses could be reversed.
slow(P1, P2, Rate, Q) :- find(L, "bind", Rate), binds(P1,P2,Q,_,L). //, productive(Q,_,_!i,L).
fast(P, Rate, Q) :- displaces(P,Q,_,L), find(L, "displace", Rate).
fast(P, Rate, Q) :- displacesL(P,Q,_,L), find(L, "displace", Rate).
fast(P, Rate, Q) :- covers(P,Q,_,L), find(L, "cover", Rate).
fast(P, Rate, Q) :- coversL(P,Q,_,L), find(L, "cover", Rate).
fast(P, Rate, Q) :- unbinds(P,Q,_,L), find(L, "unbind", Rate).
productive(P,Q,E!j,L) :- displaces(P,Q,E!j,L).
productive(P,Q,E!j,L) :- displacesL(P,Q,E!j,L).
productive(P,Q,E!j,L) :- covers(P,Q,E!j,L).
productive(P,Q,E!j,L) :- coversL(P,Q,E!j,L).
mergestep(P,Q,V) :- fast(P,_,Q), not member(Q,V).
merge(P,P,V) :- not fast(P,_,_).
merge(P,R,V) :- mergestep(P,Q,V), merge(Q,R,[Q#V]).
infinite([P1; P2], Rate, R) :- slow(P1, P2, Rate, Q), merge(Q,R,[(P1|P2);Q]).
infinite([P], Rate, R) :- slow(P, Rate, Q), merge(Q,R,[P;Q]).
detailed([P1; P2], Rate, Q):- slow(P1, P2, Rate, Q).
detailed([P], Rate, Q) :- slow(P, Rate, Q).
detailed([P], Rate, Q) :- fast(P, Rate, Q).
default([_],"unbind",0.012).
default(_,"bind",0.00003).
default(_,"displace",1.0).
default(_,"cover",1.0).
//The following specifies infinite compilation mode
reaction([P1; P2], Rate, R) :- infinite([P1; P2], Rate, R).
reaction([P], Rate, R) :- infinite([P], Rate, R).
rate([y^], "bind", 0.00000029).
rate([e^], "bind", 0.000007).
rate([e^*], "bind", 0.0000033).
rate([f^*], "bind", 0.0000033).
rate([a^*], "bind", 0.00003).
rate([l^*], "bind", 0.000005).
```

```
rate([i], "bind", 0.00011).
}
directive simulator deterministic
directive deterministic {stiff = true}
directive simulation {final = 100000}
(500 [<e^!2 w!1 y^>|<w*!1 e^*!2 d* c* b* i*>]
|1000 [<y^* w* e^*>]
|250 [<a^!1 b!2 c!3 d!4 e^>|<g^* d*!4 c*!3 f^* b*!2 a^*!1>]
|250 [<d*!4 c*!3 b*!2 i*!7>|<i!7 b!2 c!3 d!4 e^>]
|250 [<f^ c!11 d!12 g^!13 j^!14>
|<j^*!14 g^*!13 e^* d*!12 c*!11 b* a^*>]
|250 [<k!15 i!16>|<i*!16 m* k*!15 l^*>]
|500 [<l^ k m i>]
)
```

Note S8. CRN code for the effect of upstream signaling on Core CRN.

```
directive simulation {final=100000; plots=[sp_0; sp_1; sp_2; sp_3; sp_4; sp_5; sp_6; sp_7; sp_8; sp_9; sp_10; sp_11; sp_12; sp_13; sp_14; sp_15; sp_16; sp_17; sp_18; sp_19; sp_20; sp_21; sp_22; sp_23; sp_24; sp_25; sp_26]; }
directive simulator deterministic
directive deterministic {stiff=true}

| 500 sp_0
| 1000 sp_1
| 250 sp_2
| 250 sp_3
| 250 sp_4
| 250 sp_5
| 500 sp_6
| sp_6 + sp_5 ->{5E-06} sp_26 + sp_25
| sp_1 + sp_0 ->{2.9E-07} sp_24 + sp_23
| sp_24 + sp_3 ->{7E-06} sp_20 + sp_19
| sp_2 + sp_24 ->{3.3E-06} sp_22 + sp_21
| sp_22 + sp_6 ->{0.00011} sp_17
| sp_22 + sp_26 ->{0.00011} sp_18
| sp_4 + sp_21 ->{3.3E-06} sp_16 + sp_15
| sp_20 + sp_6 ->{0.00011} sp_13
| sp_20 + sp_26 ->{0.00011} sp_14
| sp_17 + sp_5 ->{5E-06} sp_12
| sp_2 + sp_16 ->{3.3E-06} sp_21 + sp_11
| sp_22 + sp_16 ->{3E-05} sp_11 + sp_24
| sp_18 + sp_16 ->{3E-05} sp_11 + sp_9
| sp_17 + sp_16 ->{3E-05} sp_11 + sp_10
| sp_13 + sp_5 ->{5E-06} sp_8
| sp_12 + sp_16 ->{3E-05} sp_11 + sp_7
| sp_10 + sp_5 ->{5E-06} sp_7
| sp_2 + sp_10 ->{3.3E-06} sp_17 + sp_21
| sp_2 + sp_9 ->{3.3E-06} sp_18 + sp_21
| sp_2 + sp_7 ->{3.3E-06} sp_12 + sp_21
```

Note S9. Flow Cytometry Analysis of the Core CRN.

To achieve MG population-based insights throughout the operating network we performed Flow Cytometry experiments (**Figure 4-3d,e**). MGs are initially identified through FSC-H versus SSC-H plot. To isolate true MG

events from the non-colloidal/non-labelled matter, MGs are gated (red boxes) using SSC intensity and the fluorescence intensity from the Rhodamine labelled core (**Figure 4-15**).

Before Input addition, only one major MG population in the SSC-H versus Rhodamine fluorescence intensity density plot can be observed which more or less remains the same for the aliquot tested after 5 min of Input addition (**Figure 4-15**). However, for the aliquot taken after 2 h, multiple populations with progressively increasing FSC, SSC and Rhodamine signals are clearly observed which indicate bigger size and higher complexity/granularity. The scattering and fluorescence signals start to decrease soon after 4 h and ultimately demonstrate single major population again for aliquot taken after 23 h. It is important to mention that individual participation from Particle1 and Particle2 cannot be differentiated based on the above results because being prepared from the same parent microgel, these particles have same size. But they carry orthogonal set of dyes-Atto488 and Atto647, the signals from the respective channels were then plotted against each other to find two distinct MG populations. The two particle populations are separated by two secondary-level gates - Particle1 is enclosed within green box contributing 67.8% of the MG population and Particle2 within a magenta box accounts for 29.9% of the MG population. A deviation from the 50:50 ratio of Particle1 and Particle2 arises from the gating regions chosen and minimal experimental errors.

Within 5 min of Input addition, Particle1 and Particle2 shift towards the higher fluorescence range, Particle2 enters into a new gated region (purple box), leaving only 0.94% of the events in the magenta gate. However, for Particle1, only 30.3% of the events can be traced in green gate, the rest events lie in the new purple region. This indicates that individual fluorescence on two populations of particles is increased, and they are activated for co-assembly. Indeed, for the aliquot observed after 2 h, the two distinct populations have converged into the purple region with a total contribution of 98.2% leaving only 0.016% events in the magenta region and 0.41% events in the green region, meaning 98.2% of the MG population is participating in the formation of a converged pattern. Interestingly, this highly ordered and symmetric pattern directs multiple population distributions. If we compare these results, with the SSC-H vs Rhodamine fluorescence intensity-H plot at 2 h, we can conclude that these different MG distributions correspond to distinct co-assemblies with different numbers. To understand the pattern in a simpler way, we dissected it in two halves (**Figure 4-16**). The MG distributions lying on the dissecting line have similar Atto488 and Atto647 fluorescence intensity values, which might indicate the 50:50 composition of Particle1 and Particle2 in co-assemblies. As we progress on the line towards higher fluorescence intensity values, more particles seem to contribute towards co-assemblies increasing their overall size and granularity, however regions become less intense which means, intensity of co-assemblies with bigger size is less. Now, if we look at the upper side of the dissecting line, the distributions indicate co-assemblies with an overall higher composition of Particle2. Alternatively, the distributions on the lower side of the dissecting line suggest co-assemblies with a higher composition of Particle1. Overall, these results confirm the formation of co-assemblies and that also with distinguishable distribution after 2 h of Input addition.

For an aliquot derived after 4 h, the hotspots with the higher fluorescence intensity values are dissolved which means disassembly process is initiated already where bigger co-assemblies are breaking down first. However, purple region still contributes 95.3% of the MG population with only 1.03% and 0.035% events in the green and magenta regions. Finally, when the system is observed after 23 h, the pattern was completely dissolved, only 0.84% events in the purple region and two distinct scatter plots reappear again in the magenta and green regions which clearly indicates the successful disassembly of the transiently formed co-assemblies. The overall fluorescence intensity of the Particle1 population decreases again and that of Particle2 stays in the higher region as anticipated from the design of the network.

4.5 References

1 Zhang, Y. *et al.* Sequential self-assembly of DNA functionalized droplets. *Nat. Commun.* **8**, 21, doi:10.1038/s41467-017-00070-0 (2017).

2 Heinen, L. & Walther, A. Temporal control of i-motif switch lifetimes for autonomous operation of transient DNA nanostructures. *Chem. Sci.* **8**, 4100-4107, doi:10.1039/c7sc00646b (2017).

3 Sharma, C. & Walther, A. Self-Regulating Colloidal Co-Assemblies That Accelerate Their Own Destruction via Chemo-Structural Feedback. *Angew. Chem. Int. Ed.* **61**, e202201573, doi:https://doi.org/10.1002/anie.202201573 (2022).

4 Laramy, C. R., O'Brien, M. N. & Mirkin, C. A. Crystal engineering with DNA. *Nat. Rev. Mater.* **4**, 201-224, doi:10.1038/s41578-019-0087-2 (2019).

5 Mirkin, C. A., Letsinger, R. L., Mucic, R. C. & Storhoff, J. J. A DNA-based method for rationally assembling nanoparticles into macroscopic materials. *Nature* **382**, 607-609, doi:10.1038/382607a0 (1996).

6 Alivisatos, A. P. *et al.* Organization of 'nanocrystal molecules' using DNA. *Nature* **382**, 609-611, doi:10.1038/382609a0 (1996).

7 Merindol, R. & Walther, A. Materials learning from life: concepts for active, adaptive and autonomous molecular systems. *Chem. Soc. Rev.* **46**, 5588-5619, doi:10.1039/C6CS00738D (2017).

8 Schwarz, P. S., Tena-Solsona, M., Dai, K. & Boekhoven, J. Carbodiimide-fueled catalytic reaction cycles to regulate supramolecular processes. *Chem. Commun.* **58**, 1284-1297, doi:10.1039/d1cc06428b (2022).

9 Boekhoven, J., Hendriksen, W. E., Koper, G. J., Eelkema, R. & van Esch, J. H. Transient assembly of active materials fueled by a chemical reaction. *Science* **349**, 1075-1079, doi:10.1126/science.aac6103 (2015).

10 Heinen, L. & Walther, A. Programmable dynamic steady states in ATP-driven non-equilibrium DNA systems. *Sci. Adv.* **5**, eaaw0590, doi:10.1126/sciadv.aaw0590 (2019).

11 Deng, J. & Walther, A. ATP-powered molecular recognition to engineer transient multivalency and self-sorting 4D hierarchical systems. *Nat. Commun.* **11**, 3658, doi:10.1038/s41467-020-17479-9 (2020).

12 Deng, J. & Walther, A. Autonomous DNA nanostructures instructed by hierarchically concatenated chemical reaction networks. *Nat. Commun.* **12**, 5132, doi:10.1038/s41467-021-25450-5 (2021).

13 Sharma, C., Maity, I. & Walther, A. pH-feedback systems to program autonomous self-assembly and material lifecycles. *Chem. Commun.* **59**, 1125-1144, doi:10.1039/D2CC06402B (2023).

14 Maiti, S., Fortunati, I., Ferrante, C., Scrimin, P. & Prins, L. J. Dissipative self-assembly of vesicular nanoreactors. *Nat. Chem.* **8**, 725-731, doi:10.1038/nchem.2511 (2016).

15 Mishra, A., Dhiman, S. & George, S. J. ATP-Driven Synthetic Supramolecular Assemblies: From ATP as a Template to Fuel. *Angew. Chem. Int. Ed.* **60**, 2740-2756, doi:10.1002/anie.202006614 (2021).

16 Joesaar, A. *et al.* DNA-based communication in populations of synthetic protocells. *Nat. Nanotechnol.* **14**, 369-378, doi:10.1038/s41565-019-0399-9 (2019).

17 Groeer, S., Schumann, K., Loescher, S. & Walther, A. Molecular communication relays for dynamic cross-regulation of self-sorting fibrillar self-assemblies. *Sci. Adv.* **7**, eabj5827, doi:doi:10.1126/sciadv.abj5827 (2021).

18 Srinivas, N., Parkin, J., Seelig, G., Winfree, E. & Soloveichik, D. Enzyme-free nucleic acid dynamical systems. *Science* **358**, eaal2052, doi:doi:10.1126/science.aal2052 (2017).

19 Gines, G. *et al.* Microscopic agents programmed by DNA circuits. *Nat. Nanotechnol.* **12**, 351-359, doi:10.1038/nnano.2016.299 (2017).

20 Zambrano, A. *et al.* Programmable synthetic cell networks regulated by tuneable reaction rates. *Nat. Commun.* **13**, 3885, doi:10.1038/s41467-022-31471-5 (2022).

21 Qin, Z., Liu, Y., Zhang, L., Liu, J. & Su, X. Programming Dissipation Systems by DNA Timer for Temporally Regulating Enzyme Catalysis and Nanostructure Assembly. *ACS Nano* **16**, 14274-14283, doi:10.1021/acsnano.2c04405 (2022).

22 Green, L. N. *et al.* Autonomous dynamic control of DNA nanostructure self-assembly. *Nat. Chem.* **11**, 510-520, doi:10.1038/s41557-019-0251-8 (2019).
23 Gentile, S. *et al.* Spontaneous Reorganization of DNA-Based Polymers in Higher Ordered Structures Fueled by RNA. *J. Am. Chem. Soc.* **143**, 20296-20301, doi:10.1021/jacs.1c09503 (2021).
24 Schaffter, S. W. & Schulman, R. Building in vitro transcriptional regulatory networks by successively integrating multiple functional circuit modules. *Nat. Chem.* **11**, 829-838, doi:10.1038/s41557-019-0292-z (2019).
25 Dupin, A. & Simmel, F. C. Signalling and differentiation in emulsion-based multi-compartmentalized in vitro gene circuits. *Nat. Chem.* **11**, 32-39, doi:10.1038/s41557-018-0174-9 (2019).
26 Cai, Z. *et al.* From colloidal particles to photonic crystals: advances in self-assembly and their emerging applications. *Chem. Soc. Rev.* **50**, 5898-5951, doi:10.1039/D0CS00706D (2021).
27 Dehne, H., Reitenbach, A. & Bausch, A. R. Transient self-organisation of DNA coated colloids directed by enzymatic reactions. *Sci. Rep.* **9**, 7350, doi:10.1038/s41598-019-43720-7 (2019).
28 Dalchau, N. *et al.* Computing with biological switches and clocks. *Nat Comput* **17**, 761-779, doi:10.1007/s11047-018-9686-x (2018).
29 Seeman, N. C. DNA in a material world. *Nature* **421**, 427-431, doi:10.1038/nature01406 (2003).
30 Han, K., Go, D., Hoenders, D., Kuehne, A. J. C. & Walther, A. Switchable Supracolloidal Coassembly of Microgels Mediated by Host/Guest Interactions. *ACS Macro Lett.* **6**, 310-314, doi:10.1021/acsmacrolett.7b00053 (2017).
31 Wang, Y. *et al.* Synthetic Strategies Toward DNA-Coated Colloids that Crystallize. *J. Am. Chem. Soc.* **137**, 10760-10766, doi:10.1021/jacs.5b06607 (2015).
32 Hennig, A. *et al.* Scope and Limitations of Surface Functional Group Quantification Methods: Exploratory Study with Poly(acrylic acid)-Grafted Micro- and Nanoparticles. *J. Am. Chem. Soc.* **134**, 8268-8276, doi:10.1021/ja302649g (2012).
33 Zadeh, J. N. *et al.* NUPACK: Analysis and design of nucleic acid systems. *J. Comput. Chem.* **32**, 170-173, doi:10.1002/jcc.21596 (2011).
34 Sullivan, R., Adams, M. C., Naik, R. R. & Milam, V. T. Analyzing Secondary Structure Patterns in DNA Aptamers Identified via CompELS. *Molecules* **24**, 1572 (2019).
35 Lakin, M. R., Youssef, S., Polo, F., Emmott, S. & Phillips, A. Visual DSD: a design and analysis tool for DNA strand displacement systems. *Bioinformatics* **27**, 3211-3213, doi:10.1093/bioinformatics/btr543 (2011).
36 Petersen, R. L., Lakin, M. R. & Phillips, A. A strand graph semantics for DNA-based computation. *Theor. Comput. Sci.* **632**, 43-73, doi:10.1016/j.tcs.2015.07.041 (2016).
37 Zhang, D. Y. & Winfree, E. Control of DNA Strand Displacement Kinetics Using Toehold Exchange. *J. Am. Chem. Soc.* **131**, 17303-17314, doi:10.1021/ja906987s (2009).
38 Mannan, A. A., Liu, D., Zhang, F. & Oyarzún, D. A. Fundamental Design Principles for Transcription-Factor-Based Metabolite Biosensors. *ACS Synth. Biol.* **6**, 1851-1859, doi:10.1021/acssynbio.7b00172 (2017).
39 Qian, L., Winfree, E. & Bruck, J. Neural network computation with DNA strand displacement cascades. *Nature* **475**, 368-372, doi:10.1038/nature10262 (2011).
40 Jung, J. K., Archuleta, C. M., Alam, K. K. & Lucks, J. B. Programming cell-free biosensors with DNA strand displacement circuits. *Nat. Chem. Biol.* **18**, 385-393, doi:10.1038/s41589-021-00962-9 (2022).
41 Schirripa Spagnolo, C. & Luin, S. Choosing the Probe for Single-Molecule Fluorescence Microscopy. *Int. J. M. Sci.* **23**, 14949 (2022).
42 Fern, J. *et al.* DNA Strand-Displacement Timer Circuits. *ACS Synth. Biol.* **6**, 190-193, doi:10.1021/acssynbio.6b00170 (2017).
43 Deng, J. & Walther, A. Fuel-Driven Transient DNA Strand Displacement Circuitry with Self-Resetting Function. *J. Am. Chem. Soc.* **142**, 21102-21109, doi:10.1021/jacs.0c09681 (2020).
44 Zhang, D. Y., Turberfield, A. J., Yurke, B. & Winfree, E. Engineering entropy-driven reactions and networks catalyzed by DNA. *Science* **318**, 1121-1125, doi:10.1126/science.1148532 (2007).

45 Prasad, A. & Alizadeh, E. Cell Form and Function: Interpreting and Controlling the Shape of Adherent Cells. *Trends Biotechnol.* **37**, 347-357, doi:10.1016/j.tibtech.2018.09.007 (2019).

46 Caldwell, A. S., Aguado, B. A. & Anseth, K. S. Designing Microgels for Cell Culture and Controlled Assembly of Tissue Microenvironments. *Adv. Funct. Mater.* **30**, 1907670, doi:https://doi.org/10.1002/adfm.201907670 (2020).

47 Routh, A. F. & Vincent, B. Salt-Induced Homoaggregation of Poly(N-isopropylacrylamide) Microgels. *Langmuir* **18**, 5366-5369, doi:10.1021/la011869d (2002).

48 Thachuk, C., Winfree, E. & Soloveichik, D. 133-153 (Springer International Publishing).

49 Spaccasassi, C., Lakin, M. R. & Phillips, A. A Logic Programming Language for Computational Nucleic Acid Devices. *ACS Synth. Biol.* **8**, 1530-1547, doi:10.1021/acssynbio.8b00229 (2019).

50 van Ravensteijn, B. G. P., Voets, I. K., Kegel, W. K. & Eelkema, R. Out-of-Equilibrium Colloidal Assembly Driven by Chemical Reaction Networks. *Langmuir* **36**, 10639-10656, doi:10.1021/acs.langmuir.0c01763 (2020).

51 della Sala, F., Neri, S., Maiti, S., Chen, J. L. Y. & Prins, L. J. Transient self-assembly of molecular nanostructures driven by chemical fuels. *Curr. Opin. Biotechnol.* **46**, 27-33, doi:https://doi.org/10.1016/j.copbio.2016.10.014 (2017).

52 Hess, H. & Ross, J. L. Non-equilibrium assembly of microtubules: from molecules to autonomous chemical robots. *Chem. Soc. Rev.* **46**, 5570-5587, doi:10.1039/C7CS00030H (2017).

5 Transient Co-Assemblies of Micron-Scale Colloids Regulated by ATP-Fueled Reaction Networks

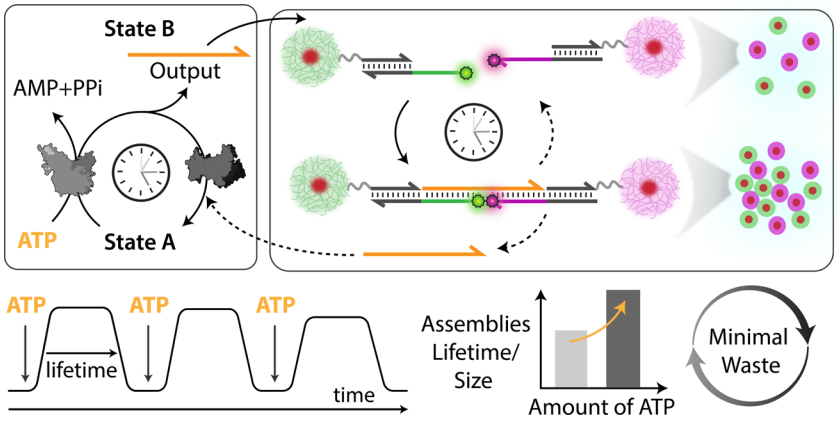

Preliminary note: *This chapter is based on the journal article published in Chem. Sci., Accepted Manuscript, doi:10.1039/D3SC04017H (2022) by C. Sharma and A. Walther. Minor changes have been made concerning formatting style.*

Author contributions: C.S., A.S., and A.W. conceptualized the project. C.S. and A.S. performed the free solutions. C.S. performed the DNA synthesis and carried out particle studies. A.W. conceived and supervised the project. C.S. and A.W. discussed and analyzed the results. C.S. wrote the first draft, C.S, A.S., and A.W edited and finalized the article.

I thank Dr. L. Heinen and Dr. J. Deng for establishing ATP-driven networks.

Abstract: Self-assembly of colloidal particles offers an attractive bottom-up approach to functional materials. Current design strategies for colloidal assemblies are mostly based on thermodynamically-controlled principles and lack autonomous behavior. The next advance in the properties of colloidal assemblies will come from coupling these structures to out-of-equilibrium chemical reaction networks furnishing them with autonomous and dynamic behavior. This, however, constitutes a major challenge of carefully modulating the interparticle potentials on a temporal circuit program and avoiding kinetic trapping and irreversible aggregation. Herein, we report the coupling of a fuel-driven DNA-based enzymatic reaction network (ERN) to micron-sized colloidal particles to achieve their transient co-assembly. The ERN operating on the molecular level transiently releases an Output strand which links two DNA functionalized microgel particles together into co-assemblies with a programmable assembly lifetime. The system generates minimal waste and recovers all components of the ERN after the consumption of the ATP fuel. The system can be reactivated by addition of new fuel as shown for up to three cycles. The design can be applied to organize other building blocks into hierarchical structures and materials with advanced biomimetic properties.

5.1 Introduction

Self-assembly of synthetic building blocks (molecular or colloidal) is an extremely powerful tool for the development of complex systems and materials in a bottom-up fashion. The past decade has experienced a gradual evolution in their properties from being classic responsive to adaptive and life-like in nature. On a conceptual level, such systems often take inspiration from biological self-assemblies such as microtubules and actin filaments which operate out of equilibrium via hierarchically concatenated chemical reaction networks (CRNs) and regulate advanced cellular functions including cell-division, motility, transport, and proliferation.[5] Being able to translate such behavior into present-day synthetic self-assemblies remains a challenging goal to create dynamic and adaptive materials unachievable by conventional equilibrium principles. This can be achieved by either coupling the responsive building blocks to the energy-dissipating environments or designing the building blocks to be energy dissipating themselves.[6-10] The first strategy provides a more generic approach, whereas the latter one typically requires judicious design and tuning of the CRN for each building block.

Choosing appropriate synthetic analogues to emulate biological self-assemblies is essential to obtain emergent life-like behavior. This has been demonstrated for various building blocks from different chemical origins and domains such as small molecules, colloids, DNA, peptides, surfactants[27,28] up to molecular machines. Colloids especially can give rise to functional materials with unique catalytic, photonic, magnetic, and electronic properties. These properties originate not only from the positional or dimensional order of these building blocks, but also from the type of material bulk (metallic, polymeric, semiconductor, inorganic). Employing biocompatible material for their fabrication can even pave the way into biomedical applications such as drug delivery and diagnostics.[9,13]

Imprinting transient behavior into colloidal particles requires precise control over the interparticle potentials such that the repulsive contributions (steric/electrostatic) dominate the attractive van der Waals interactions in the deactivated or disassembled state of the particles. A slight disbalance can otherwise compromise the overall stability of the particles and result in irreversible aggregation. Only in the activated state should the fuel-induced attractions sufficiently overcome repulsion to induce assembly. Limiting the magnitude of attractions between the particles by either reducing the binding strengths or the number of activated sites is essential to avoid the system falling into kinetic traps and promote spontaneous disintegration of assemblies after fuel depletion. Another challenge involves fine tuning of a fuel-consuming CRN in terms of its activation and deactivation rates to match the colloidal dynamics which are significantly slower than their molecular counterparts. Naturally, the challenges become more evident when larger colloids are used. Because of which the majority of transient colloidal systems demonstrated till date rely on relatively small (*z*-average diameter,

D_z ≈ 5-50 nm),[9,11-13] nanoparticle-sized building blocks while examples for micrometer-sized particles are scarce.

For instance, van Ravensteijn and Hendriksen et al. demonstrated the first example for the transient clustering of sub micrometer-sized (D_z ≈ 750 nm) colloidal particles by modulating the hydrophobicity of the grafted polymers in response to a limited supply of chemical fuel.[12] The system, however, lacks selectivity and cannot be utilized further for multicomponent systems. We recently coupled pH-feedback system to pH-responsive microparticles to achieve transient co-assembling systems.[31,32] The excessive salt accumulation in these systems can disbalance the interparticle potentials and thereby the colloidal stability after each fueling cycle. In this respect, DNA coated colloids may offer better structural control due to high programmability and selectivity of DNA hybridization. Particularly this allows design of DNA-based out-of-equilibrium CRNs emulating complex signaling networks found in nature. In this direction, DNA-based CRNs coupled to DNA-coated particles with transient and oscillatory behavior were reported. Dehne et al. showed transient assembly of DNA-coated colloids (D_z ≈ 1 μm) using antagonistic enzymatic CRN of RNA formation and degradation.[33] They also programmed oscillation of these colloids by coupling them to polymerase, exonuclease and nickase (PEN)-based enzymatic CRNs.[34,35] In both cases, the transiently generated linker strand is based on nucleotide monomers that are degraded to waste. This equals an energetically downhill process opposed to what is found in nature where a chemical fuel is processed and the building components themselves are not degraded. We recently integrated a toehold-mediated DNA strand displacement reaction network with micron-sized colloids and DNA origami nanoparticles to regulate the transient co-assembly and self-sorting of two building blocks. The system however reaches a new thermodynamic state at the end and cannot be refueled. Therefore, examples where fuel-driven DNA-based out-of-equilibrium reaction networks can be utilized for temporal and spatial control over DNA-coated colloidal co-assemblies remain very scarce.

Over the past few years, we have developed ATP-driven enzymatic reaction network (ERN) to achieve dynamic behavior in systems ranging from polymer level to nanostructures[34,35] up to multicomponent self-sorted colloids (D_z ≈ 1 μm) and coacervates. Herein, we build on our ATP-mediated dissipative strand displacement cascade whereby a linker strand is made transiently available in the system by ATP-powered ligation and restriction of DNA components to operate a temporally controlled downstream co-assembly of larger micron-sized core-shell microgels (MGs). The linker strand is recovered after the consumption of the ATP fuel allowing it to be reused for subsequent cycles. We discuss in detail how to modulate such ERNs, how to fabricate and couple particles to these ERNs to exclusively achieve non-equilibrium structures avoiding irreversible aggregation and kinetic traps. Our strategy offers design principles for an unattended dimension of particles and can practically be adopted for building blocks of different chemical origin and varied dimensions. We envisage that upon appropriate modification of colloids or materials, their interactions with cells can be programmed in a temporal fashion in their co-assembled state.[40]

5.2 Results and Discussion

5.2.1 System design for transient colloidal co-assemblies using ATP-fueled ERN

Building on our previous design, we customized ATP-fueled ERNs of antagonistic ATP-powered ligation and restriction for an easy concatenation with colloidal particles (**Figure. 5-1**). The ATP-fueled ERN operates on the molecular level and functions as a control program for the autonomous co-assembly of particles at the structural level. The upstream ERN in its initial deactivated State A is composed of two double-stranded (ds) complexes (Complex 1 and Substrate 1) and two single stranded DNAs (ssDNA; Input1 and Input 2) as shown in Figure. . In this state, Input 1 and Input 2 are incapable of kicking out Output from Substrate 1 due to unstable hybridization of Input 1 (melting temperature (T_m) = 32 °C < experimental temperature (T_{exp}) = 37 °C, determined by NUPACK[17,34]) and Input 2 (T_m = 22 °C < T_{exp} = 37 °C) with the longer strand of Substrate 1. However, the addition of ATP powers the covalent ligation of Substrate 1 with two molecules of Complex 1 (4

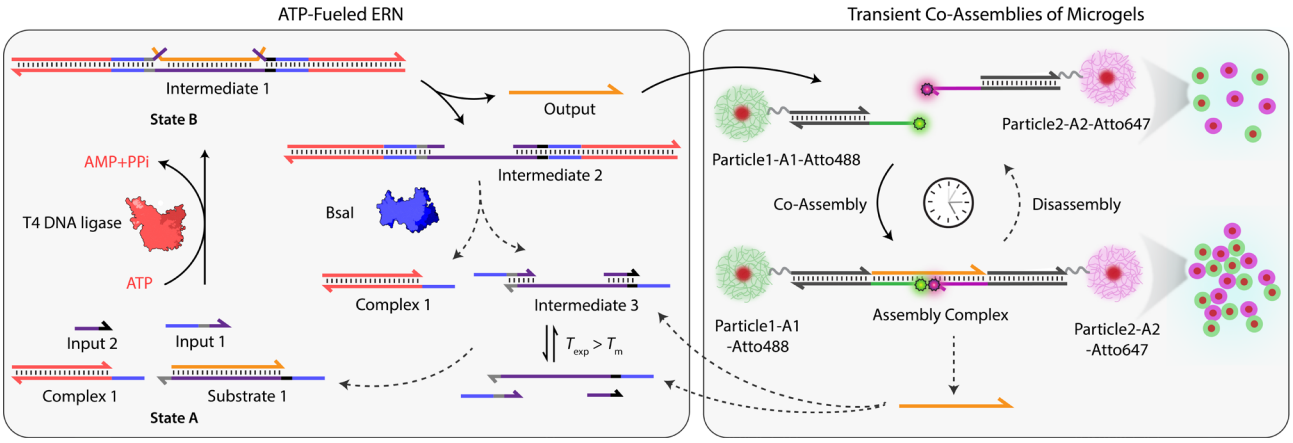

Figure. 5-1 System design for ATP-driven transient co-assemblies of MGs regulated by upstream ATP-fueled ERN.

equivalents used with respect to Substrate 1) and one molecule each of Input 1 and Input 2 with the help of T4 DNA ligase, generating Intermediate 1. The system is pushed towards an activated State B, where the chain migration from two sides provides a strong thermodynamic push to release Output from Intermediate 1, finally generating Intermediate 2. The dual inversion strategy is essential for releasing an Output strand long enough to link two particles together in a ternary Assembly Complex (*vide infra*). Concurrently, BsaI cleaves Intermediate 2 to regenerate Complex 1 and Intermediate 3. Because of the low T_m (32 °C < T_{exp} = 37 °C), Intermediate 3 dissociates into Input 1 and Input 2 and reproduces Substrate 1 after re-hybridization with Output returning the system back to State A. Faster ligation than cleavage (Supplementary Note 4.1) satisfies the kinetic boundary conditions required for the system to achieve a dynamic steady state with an ATP-dependent lifetime before the restriction overtakes and brings the system back to its initial state. Output is therefore generated in an uphill fashion and is transiently available in the system to perform downstream functions before its ultimately reassociated within Substrate 1. The co-assemblies are thereby maintained by an ATP-driven dynamic steady state where the lifetime and the size of the hierarchical structures can be programmed by the amount of ATP introduced in the system.

5.2.2 Characterization of the ATP-fueled ERN

Before coupling the ATP-fueled ERN to particles, we first sought to construct the ATP-driven ERN in solution (**Figure 5-2a**). Fluorophore-functionalized A1-Atto488 and quencher-functionalized A2-BMNQ535 which will be later annealed on the particles are dissolved in solution together with the other components of the upstream ERN. The released Output strand, powered by ATP-fueled ligation, will couple A1-Atto488 and A2-BMNQ535 into an Assembly Complex, resulting in a decrease in fluorescence intensity (FI) due to close proximity between the fluorophore and quencher. Subsequently, once BsaI controlled restriction takes over, the Assembly Complex will be dissociated resulting in the recovery of the fluorescence signal. For the successful functioning of the system at both upstream and downstream nodes, two conditions are mandatory: (1) In the initial State A, Output must remain bound within Substrate 1 without showing crosstalk with A1-Atto488 and A2-BMNQ535. This condition is also essential for the system to regenerate Substrate 1 and return back to State A after consumption of ATP. Overall, the hybridization of Output within Substrate 1 should be more favorable than formation of the Assembly Complex with A1-Atto488 and A2-BMNQ535 in State A; (2) In State B (ATP-fueled), binding of Output with A1-Atto488 and A2-BMNQ535 must be more favorable than its tendency to remain bound within Intermediate 1. For both of these conditions to be met, the length and composition of Output play critical roles. For instance, a longer Output strand with higher binding affinity is essential to drive the ternary Assembly Complex formation between A1-Atto488 and A2-BMNQ535, and Output. On the other hand, the increased length of the Output can pose difficulty during its expulsion from Intermediate 1. As a trade-off, we added 2 nucleotides (nt) at the 3'-end of Output (Supplementary Table S2)

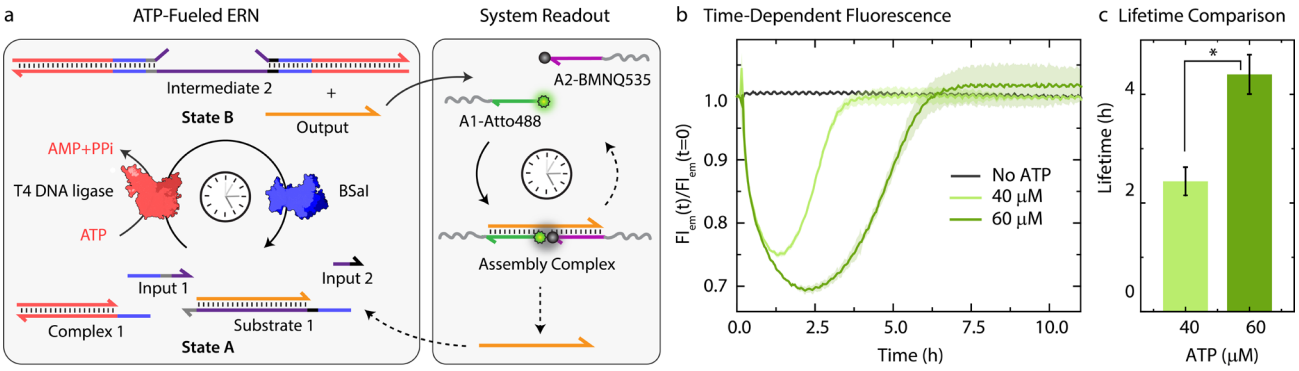

Figure 5-2. In situ detection of transiently released Output strand from an ATP-fueled DNA-based ERN. (a) Schematic representation for the in situ readout of transiently released Output strand via FRET interaction between A1-Atto488 and A2-BMNQ535. (b) Time-dependent FI changes demonstrating programmable transient complexation between A1-Atto488, A2-BMNQ535, and Output with different ATP equivalent. (c) Corresponding lifetime obtained from Figure. 5-2b shows an increase with higher ATP equivalent. Experimental conditions: A1-Atto488 and A2-BMNQ535 at an equimolar concentration of 5 µM are dissolved in 1X NEB CutSmart buffer containing 20 µM Complex 1, 5 µM Substrate 1, 10 µM Input 1 and Input 2 at 37 °C, initiated by different ATP concentrations. The results represent an average contribution from two measurements, the shaded region in (b) and error bars in (c) depict the standard deviation (SD). * indicate that $p < 0.05$.

which are non-complementary to the long strand of Substrate 1 and hence, do not affect the release of Output from Intermediate 1. However, this 2 nt extension successfully induces the formation of the Assembly Complex by strengthening the binding of Output with A1-Atto488 and A2-BMNQ535 (**Figure 5-6**).

Next, with the designed strands we assembled the ERN in solution at 37 °C with 20 µM Complex 1, 5 µM Substrate 1, 5 µM A1-Atto488 and A2-Atto647, 10 µM Input 1 and Input 2 using 0.8 Weiss units (WU) μL^{-1} of T4 DNA ligase and 0.8 units (U) μL^{-1} of BsaI. The ERN was initiated by ATP addition, which immediately resulted in a decrease in fluorescence signifying the formation of the Assembly Complex between A1-Atto488, A2-BMNQ535 and Output. Once ATP reaches a subcritical level, the restriction of Intermediate 2 via BsaI overtakes ligation and leads to regeneration of Substrate 1 returning the system back to State A with the full recovery of FI. The time-dependent FI measurements confirm the ATP-powered ERN with transient population of the Assembly Complex between A1-Atto488, A2-BMNQ535 and Output (**Figure 5-2b**). No such change in the FI is observed in the absence of ATP. The lifetime of the ERN reaction can be further modulated using a higher ATP concentrations which allow ligation to dominate restriction process for longer period.[42-44] Because of this (a) dynamic steady state is even more populated with Output strand thereby increasing the maximum dynamic yield of the Assembly Complex which can be explained by the 32% decrease in FI at 60 µM ATP as opposed to 25% decrease in case of 40 µM ATP (**Figure 5-2b**), and (b) dynamic steady state is acquired later than usual which increases the lifetimes of the Assembly Complex from ~2.4 to ~4.3 h (**Figure 5-2c**). Through control experiments, we found that mixing 5 µM each of A1-Atto488, A2-BMNQ535 and Output generates 2.6 µM (52%) of Assembly Complex in equilibrium (**Figure 5-7b,c**). NUPACK simulation suggests a similar yield of 54.8% (**Figure 5-7a**). Hence, we can conclude that fueling the system with 40 µM ATP furnishes ~1.16 µM (23%) of Assembly Complex (check **Figure 5-8** for detailed explanation). Similarly, for 60 µM ATP, ~1.48 µM (29%) of Assembly Complex is formed.

An interesting calculation regarding the question on how often building blocks are reactivated can be made. Substrate 1 is present at 5 µM and requires 4 ligation steps (**Figure. 5-1**) that will consume 4 ATP molecules to eject one Output strand with highest efficiency. That means that each Output can at maximum be transduced 3 times in the cyclic ERN at 60 µM ATP. In reality, this will be lower as the restriction can already set in at the hemi-ligated intermediate (e.g., Substrate 1, Complex 1 and only one of the Inputs) without completing to the fully ligated state that is the condition for expulsion of Output (**Figure 5-8**). The system can be successfully reactivated up to 3 times (**Figure 5-9**). However, we noted that for subsequent cycles of ATP addition, the decrease and increase of FI is slowed down, increasing the lifetime of the Assembly Complex by more than 3

times (6th cycle) compared to the previous cycles. This might occur due to gradual loss of enzymes activities over time.

5.2.3 DNA-functionalized MGs and their hetero-complementary co-assembly

With successful demonstration of the ATP-powered ERN and transient formation of Assembly Complex between A1-Atto488, A2-BMNQ535, and Output, we next attempted the translation to transient co-assemblies between DNA-functionalized core-shell MGs. For this, we employ DNA-functionalized micron-sized core-shell MGs as building blocks as they are well dispersible in aqueous medium and can be functionalized within their hydrogel shell. The core is composed of a brightly red fluorescent hydrophobic material, refractive index-matched to water ($\langle R_h \rangle_z \approx 230$ nm, synthesis in **Experimental section 5.4.3.1**). The shell contains a lightly crosslinked PNIPAM-*co*-AA hydrogel constituting 90.5 wt% of the MG (80.5 wt% N-isopropylacrylamide (NIPAM); 9 wt% acrylic acid (AA); 1 wt% N,N'- methylenebis(acrylamide) (MBA)). The core-shell MGs have a total $\langle R_h \rangle_z \approx 1.4$ µm and can be well visualized in Confocal Laser Scanning Microscopy (CLSM, **Figure 5-3**, and **Figure 5-10**). The AA groups in the shell allow functionalization with NH_2-ssDNA (**Figure 5-3a**, synthesis in Experimental **section 5.4.3.2**). This can be achieved by EDC-mediated coupling of NH_2-ssDNA (e.g., NH_2-x* and NH_2-z*; EDC = 1-Ethyl-3-(3-dimethylaminopropyl)carbodiimide = 25 equiv. with respect to COOH groups on MG), leading to a typical DNA grafting density of 2.7×10^3 strands per MG or 1.26 ± 0.2 µmol strands per g of MG (Experimental **section 5.4.3.3**, **Figure 5-11**). Such grafting densities agree with previous literature for DNA-mediated colloidal assembly. By using two different NH_2-ssDNA, we prepared an x*-functionalized Particle1 and a z*-functionalized Particle2. Subsequently, we annealed the potential binding components on each of the particles. Particle1 at a final concentration of 0.05 wt% was incubated with equimolar amount of complementary x-A1-Atto488 (0.63 µM). Similarly, Particle2 at a final concentration of 0.05 wt% was incubated with equimolar amount of z-A2-Atto647 (0.63 µM). Please note that the concentration of DNA is comparable to the concentration of Assembly Complex (**Figure 5-2b**) which is formed in the transient state.

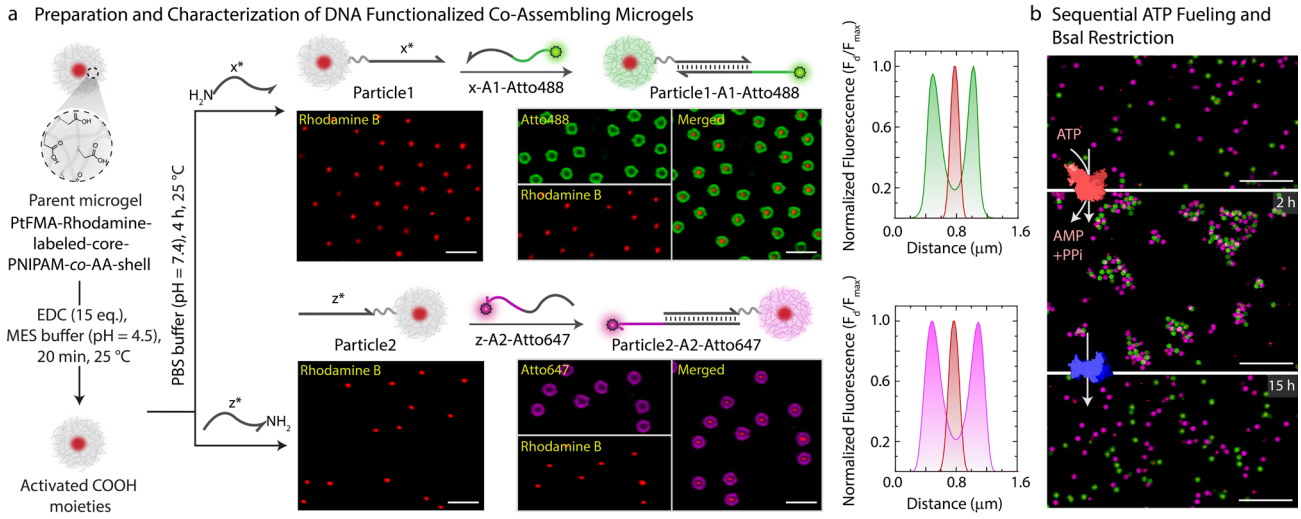

Figure 5-3. Fabrication and characterization of DNA-functionalized co-assembling MGs. (a) Schematic and CLSM images depicting step-wise preparation of Particle1-A1-Atto488 and Particle2-A2-Atto647 from a parent microgel. The first step involves covalent functionalization of DNA and consequent annealing with x-A1-Atto488 on Particle1 and z-A2-Atto647 on Particle2. Each step is monitored with CLSM imaging, and the particles are quantitatively analyzed by line segment analysis. Experimental conditions: Particle1 and Particle2 suspended in TE buffer (pH = 8.0) at a final concentration of 0.05 wt%, to which 0.63 µM (1 equiv. with respect to functionalized DNA) of respective annealing strands are added at 15 °C. (b) CLSM images of sequential assembly and disassembly of Particle1-A1-Atto488 and Particle2-A2-Atto647 using ATP-driven ligation and disassembly using subsequent addition of BsaI. The sample was first checked for co-assembly after 2 h of 40 µM ATP addition with ex situ CLSM imaging. After addition of BsaI strand, sample was again visualized after 15 h. Experimental conditions: Particle1-A1-Atto488 and Particle2-A2-Atto647 suspended in 1X NEB CutSmart buffer at a final MG concentration of 0.05 wt% with 5 µM Substrate 1, 20 µM Complex 1, 10 µM Input 1, 10 µM Input 2, 0.8 WU μL^{-1} T4 DNA ligase followed by addition of 0.8 U μL^{-1} of BsaI at 37 °C. All CLSM images in b are represented as merged composite compiled as a z-projection. Scale bars: (a) 2 µm, (b) 10 µm.

The post-annealing with the dye labeled strands (x-A1-Atto488, and z-A2-Atto647) offers the advantage of visualizing successful functionalization by CLSM as both Particle1-A1-Atto488 and Particle2-A2-Atto647 turn fluorescent with orthogonal emission profiles (**Figure 5-3a**).

We hypothesized that the transient release of Output from the upstream ATP-fueled ERN should bring Particle1-A1-Atto488 and Particle2-A2-Atto647 together into the co-assemblies. But for consistency and setting a reference, we first investigated the sequential co-assembly using T4 DNA ligase and disassembly using BsaI.

The system contains an equimolar mixture of Particle1-A1-Atto488 and Particle2-A2-Atto647 at a final concentration of 0.05 wt% dispersed in medium containing all the DNA components of the ERN, 20 μM Complex 1, 5 μM Substrate 1, 10 μM Input 1 and Input 2 and 0.8 WU μL^{-1} of T4 DNA ligase. CLSM images confirm the co-assemblies between the particles after 2 h of introducing 40 μM of ATP in absence of the restriction enzyme BsaI (**Figure 5-3b**). The co-assemblies achieve an average size of 9 μm^2 as confirmed by automated image analysis (**Figure 5-12**). Subsequent introduction of 0.8 U μL^{-1} of BsaI into the system recovers the Output strand from the formed structures and induces disassembly into individual particles after 15 h.

5.2.4 ATP-fueled autonomous co-assemblies of MGs

Moving beyond the classical step-by-step switching by sequential addition of ligation and restriction components, we next targeted the ATP-fueled ERN with Particle1-A1-Atto488 and Particle2-A2-Atto647 to achieve transient self-regulating co-assemblies (**Figure 5-4a**).

We decided to probe the co-assemblies of the particles using both time-dependent FI changes as well as CLSM microscopy. To monitor the transient co-assemblies using time-dependent fluorescence changes we annealed Particle2 with z-A2-BMNQ535. The presence of a quencher on Particle2-A2- BMNQ535 will *in situ* report any formation of co-assemblies between Particle1-A1-Atto488 and Particle2-A2-BMNQ535 owing to the FRET mechanism. With the fluorophore and quencher modified particles in hand, we constructed the ATP-fueled ERN by combining 20 μM Complex 1, 5 μM Substrate 1, 10 μM Input 1 and Input 2, 0.8 WU μL^{-1} of T4 DNA ligase and 0.8 units (U) μL^{-1} of BsaI containing an equimolar mixture of Particle1-A1-Atto488 and Particle2-A2-BMNQ535. Before adding ATP, the system shows high FI because there are no interactions between the two particles (**Figure 5-4b**). However, the addition of ATP activates the ligation-induced transient release of Output which links Particle1-A1-Atto488 and Particle2-A2-BMNQ535 together to quench Atto488 fluorescence due to the formation of the Assembly Complex. A FI decrease of ~12% occurs. Once ATP is consumed, the restriction reaction dominates, leading to the disassembly of the transiently formed co-assemblies marked by the complete recovery of the FI. The linker-mediated transient co-assembly between the particles can be further temporally controlled by increasing the concentration of ATP from 40 to 60 μM, which leads to an increase in the lifetime from 6 to 10 h (**Figure 5-4c**). Much higher ATP concentrations lead to more pronounced decrease in FI suggesting an increased yield of Assembly Complex with an ATP-dependent lifetime (**Figure 5-13**).

Moreover, a variation in the enzyme concentration also changes the lifetime and yield of the Assembly complex. Towards this, we used a two-fold excess of T4 DNA ligase (1.6 WU μL^{-1}) as compared to BsaI (0.8 U μL^{-1}), while keeping the concentrations of DNA species and ATP fixed (**Figure 5-14**). This leads to two main effects: (1) a faster and greater decrease in FI (32 %) compared to the original system (12 %) indicates a faster establishment of dynamic steady state with an increased fraction of Assembly Complex; (2) a shorter lifetime (2.4 h) indicates a faster ATP consumption during ligation allowing restriction to overtake ligation much earlier. However, no transient state is observed in the absence of BsaI. A parallel experiment with two-fold excess units of BsaI (1.6 U μL^{-1}) as compared to T4 DNA ligase (0.8 WU μL^{-1}) at fixed concentrations of DNA species and ATP favors restriction more than ligation. More frequent cleavage events lead to decrease in both the

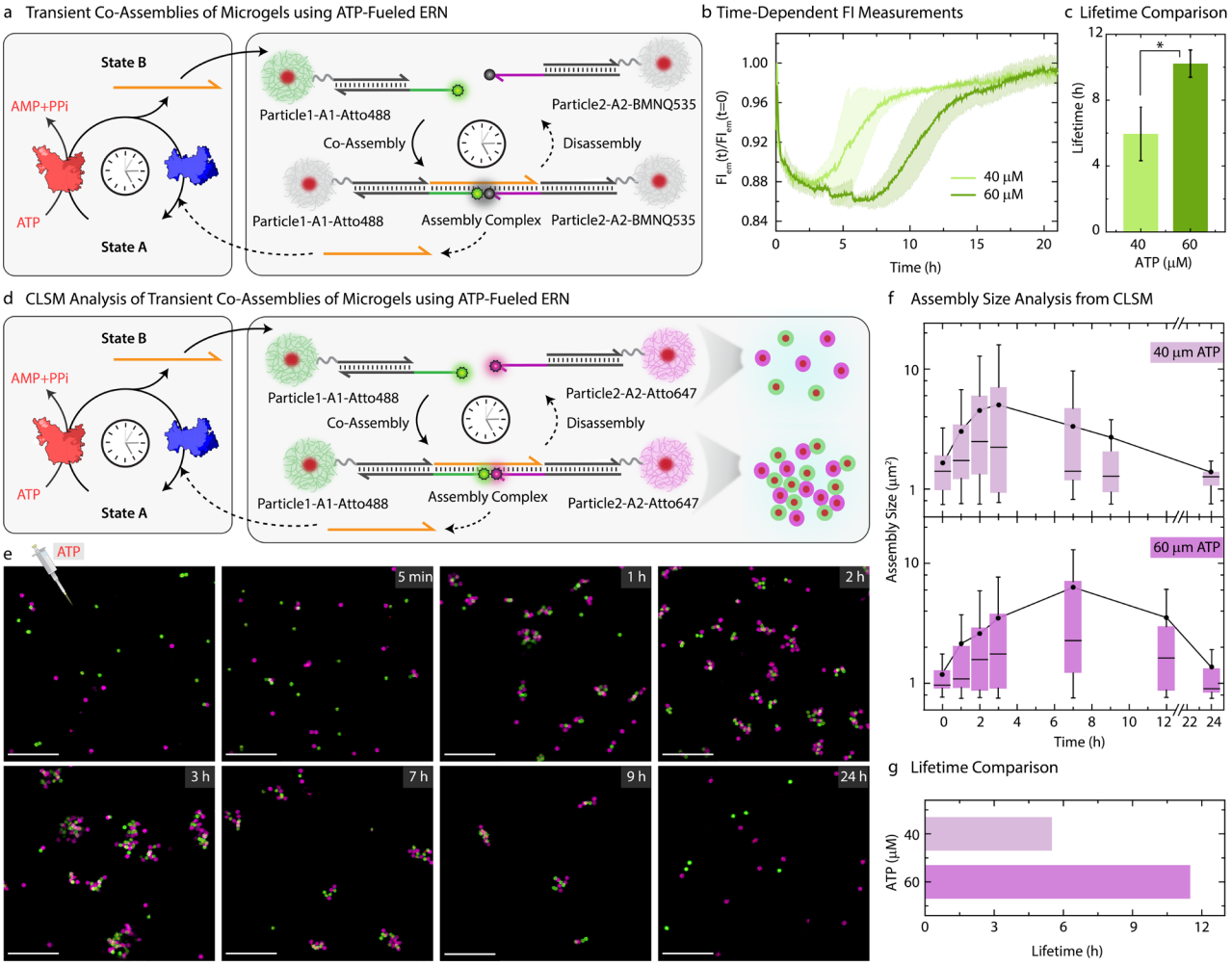

Figure 5-4. Self-regulating co-assembling MGs with transient lifetimes. (a) Schematic representation showing transient co-assembly between Particle1-A1-Atto488 and Particle2-A2-BMNQ535 due to transiently released Output strand from ATP driven enzymatic reaction network. (b) Time-dependent FI changes demonstrating transient co-assembly of dye functionalized Particle1-A1-Atto488 and quencher functionalized Particle2-A2-BMNQ535 upon ATP addition (c) Lifetime comparison of the ATP driven transient co-assembly of Particle1-A1-Atto488 and Particle2-A2-BMNQ535 with different ATP equivalent demonstrating an increase in lifetime with increase in ATP equivalent. Experimental conditions: Particle1-A1-Atto488 and Particle2-A2-BMNQ535 are suspended as an equimolar mixture in 1X NEB CutSmart buffer at a final MG concentration of 0.05 wt% containing 20 µM Complex 1, 5 µM Substrate 1, 10 µM Input 1 and Input 2 at 37 °C, fueled by different ATP concentrations. The results represent an average contribution from two measurements, the shaded region in (b) and error bars in (c) depict the SD. * indicate that $p < 0.05$. (d) Schematic representation for CLSM analysis of the transient co-assemblies between Particle1-A1-Atto488 and Particle2-A2-Atto647. (e) ex situ CLSM imaging of transient co-assemblies at 40 µM ATP concentration. All CLSM images are represented as merged composite compiled as a z-projection. Experimental conditions: same as described in (b) except using Particle2-A2-Atto647 instead of Particle2-BMNQ535. Aliquots were withdrawn as needed and visualized without any dilution. (f) Assembly size analysis on the particles obtained from two different z-stacks at each time interval observed at two different ATP concentrations. The box represents 25-75 % of data, whiskers represent 5-95 % of data, a solid circle represents the mean, and horizontal bar the median of the assembly size distribution in box charts. A solid line provides a guide to the eye. (g) ATP-dependent lifetime of the transient co-assemblies obtained from the assembly size analysis. Scale bars: 10 µm.

lifetime (1.9 h) as well as the yield of the Assembly Complex. This is evident from a relatively less decrease in FI on ATP addition (9 %) compared to pristine system with 1:1 ratio of the BsaI and T4 DNA ligase.

Since the particles can be easily labelled with fluorophore-conjugated DNA species, the transient co-assembly can be convincingly visualized using CLSM. For this, we annealed z-A2-Atto647 on the Particle2 instead of using Particle2-A2BMNQ (**Figure 5-4d,e**). The assembled ERN/MG mixture prior to ATP addition showed well dispersed green and pink MGs (**Figure 5-15**). However, within 1 h of ATP addition, small co-assembled clusters are observed which eventually grow and reach a steady plateau (average assembly size ≈ 5 µm²) after 3 h

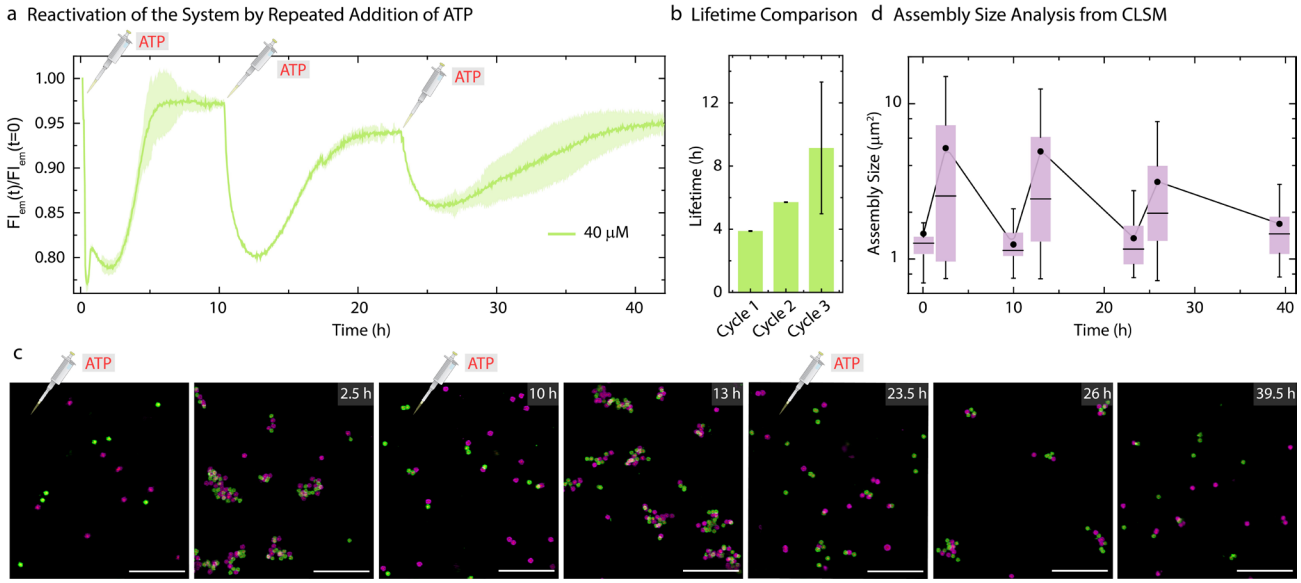

Figure 5-5. Reactivation of the system by repeated addition of ATP. (a) Time-dependent FI changes demonstrating transient co-assembly of dye functionalized Particle1-A1-Atto488 and quencher functionalized Particle2-A2-BMNQ535 upon repeated ATP addition. (b) Corresponding lifetimes for each consecutive cycle obtained from Figure. 5-5a. Experimental conditions: Particle1-A1-Atto488 and Particle2-A2-BMNQ535 are suspended as an equimolar mixture in 1X NEB CutSmart buffer at a final MG concentration of 0.05 wt% containing 20 µM Complex 1, 5 µM Substrate 1, 10 µM Input 1 and Input 2 at 37 °C, fueled by repetitive addition of 40 µM ATP. The results represent an average contribution from two measurements, the shaded region in (a) and error bars in (b) depict the SD. (c) ex situ CLSM imaging of transient co-assemblies between Particle1-A1-Atto488 and Particle2-A2-Atto647 at 40 µM ATP concentration. All CLSM images are represented as merged composite compiled as a z-projection. Experimental conditions: same as described in (a,b) except using Particle2-A2-Atto647 instead of Particle2-BMNQ535. Aliquots were withdrawn as needed and visualized without any dilution. (d) Assembly size analysis on the particles obtained from two different z-stacks at each time interval. The box represents 25-75 % of data, whiskers represent 5-95 % of data, a solid circle represents the mean, and horizontal bar the median of the assembly size distribution in box charts. A solid line provides a guide to the eye. Scale bars: 10 µm.

beyond which they begin to disassemble into individual MGs when observed until 24 h (**Figure 5-4f**) confirmed by automated image analysis. This clearly suggests transient formation of co-assemblies. However, for a higher ATP concentration, the co-assemblies grow in size and reach their maximum average size of ~6.4 µm^2 after 7h (**Figure 5-16**, **Figure 5-4f,g**). This clearly confirms the effect of increasing ATP concentrations on the size and lifetime of the co-assembled structures.

As the present system returns back to the initial state after consumption of ATP, this offered us the opportunity to reactivate the system with a fresh batch of fuel. Thus, we attempted refueling the system with three batches of ATP addition (**Figure 5-5**). The time-dependent FI measurements (**Figure 5-5a**) and CLSM analysis (**Figure 5-5c**) demonstrates successful formation of co-assemblies between the particles which dissolve over time for each cycle. A quantitative analysis of the lifetimes using the time-dependent FI changes show an increase for subsequent fueling cycle (**Figure 5-5a,b**). This is in line with the observations made for the pure ERN (**Figure 5-9**) and can be attributed to some loss of enzyme activities. Moreover, FI decreases by only 10 % for the third cycle as compared to a 20 % decrease for the first two cycles. This decrease in yield of the Assembly Complex associated with the transient co-assemblies is also reflected in the decreased size of the co-assemblies in the final cycle (**Figure 5-5c**). The mean assembly size increases by only ~2.3 times after the third batch of ATP addition as opposed to ~4 times for the first two cycles (**Figure 5-5d**).

5.3 Conclusion

In conclusion, we have demonstrated a generic design strategy for programming self-regulating co-assemblies of micron-sized particles when coupled to an ATP-driven ERN. Transient release of an Output strand from the upstream ERN acts as a linker for a pair of potentially co-assembling particles that indirectly pushes the co-assembled structures away from equilibrium. The key component is realized to be the length and composition

of Output strand. It must be short enough to be easily ejected by the dual inversion strategy, but at the same time must have higher binding strength to bring two particles together. To achieve this, Output was strategically extended with a short domain (2 nt) which is only complementary to the co-assembling units but does not affect the release rate from the upstream ERN. This extra domain can be customized depending on the building blocks required to be programmed.

The system's properties can be tuned by simply changing the ATP concentration. For example, higher ATP concentration forces ligation to dominate restriction for longer periods which populates more Output strands in the dynamic steady state assuring bigger size of co-assemblies sustained for longer periods. The second advantage stems from the resetting ability of the ERN because of which system can be successfully reactivated for at least three subsequent batches of ATP addition. The only waste accumulated in the system is the equivalent amount of AMP and PPi generated from ATP used. Adding 40 µM of ATP accumulates 120 µM of AMP and PPi over three cycles which is well below the limit above which these components can affect MG or enzyme stability. Such conditions further favor the reactivation of the system.

Since the length of the linker can be further adjusted according to the strategy presented in this work, the system can be generalized for any building block based on DNA hybridization to produce materials with dynamic and tunable properties which can be sustained over multiple cycles. The presented colloidal particles can be grafted with biologically active molecules or ligands for communication with living cells opening up avenues for biomedical applications of fuel-driven matter.

5.4 Experimental

5.4.1 Materials

All chemicals and reagents were purchased from Sigma Aldrich or Merck and used without further purification unless otherwise stated:

2,2,2-trifluoroethyl methacrylate (ABCR GMBH, 99 %), N-isopropylacrylamide (97 %), 2,2'-azobis(2-methylpropionamidine) dihydrochloride (ABCR GMBH, 96 %), N,N'-methylenebis(acrylamide) (99%), divinylbenzene (DVB, 80 %), acryloxyethyl thiocarbamoyl Rhodamine B (POLYSCIENCES, INC.), Al_2O_3 90 neutral (CARL ROTH GMBH), 1-Ethyl-3-(3-dimethylaminopropyl)carbodiimide (ABCR GMBH, 98 %), potassium persulfate (≥99 %), acrylic acid (Acros Organics, 99.5 %), disodium ethylenediaminetetraacetate dehydrate (biology grade), tris(hydroxymethyl)aminomethane hydrochloride (Trizma buffer substance pH=8), 2-(N-morpholino) ethanesulfonic acid, sodium chloride (99 %), magnesium chloride (99 %), phosphate buffered saline (PBS, pH = 7.4).

T4 DNA Ligase Storage Buffer (Promega): 10 mM Tris-HCl (pH 7.4 at 25 °C), 50 mM KCl, 1 mM dithiothreitol (DTT), 0.1 mM EDTA, 50 % glycerol. BsaI-HF® v2 storage buffer (*NEB*): 10 mM Tris-HCl, 200 mM NaCl, 1 mM DTT, 0.1 mM EDTA, 200 µg/mL BSA, 50% glycerol. 1X *NEB* CutSmart® Buffer: 50 mM potassium acetate, 20 mM Tris-acetate, 10 mM magnesium acetate, 100 µg mL-1 BSA. Annealing Buffer: 10 mM Tris-HCl (pH 8.0), 50 mM NaCl, 10 mM $MgCl_2$. MilliQ water was used throughout all experiments unless otherwise stated.

All oligonucleotides (except amine-modified oligonucleotides) were purchased from Integrated DNA Technologies Inc. (IDT) and Biomers GmbH (as listed below in Table S1). The oligonucleotides as received were dissolved in 1X TE buffer, pH = 8.0 (Thermo Fischer). Amine-modified oligonucleotides were synthesized following a well-defined procedure (as described in **Experimental section 5.4.3.4**).

5.4.2 General Characterization Methods and Instruments

DLS measurements were performed on the LS Instruments NanoLab 3D at 25 °C operating with a red laser (λ = 685 nm) and a scattering angle of Θ = 90 ° using standard disposable PS cuvettes (BRAND GmbH & Co. KG). The distributions of the hydrodynamic radii were obtained by a CONTIN mode analysis.

Confocal laser scanning microscopy (CLSM) was performed on Leica Stellaris 5 microscope (LasX v4.3.0.24308) with four continuous wave laser lines (λ = 488 nm, power = 20 mW; λ = 561 nm, power = 20 mW; λ = 638 nm, power = 30 mW) and three HyD S detectors using plan-apochromat objectives (63×, 1.40 numerical aperture, oil immersion).

DNA concentrations were determined using a DeNovix-S-06873 (DeNovix OS 0.8.1 v4.1.5) spectrophotometer with a standard value of 33 µg/OD_{260}.

The temperature-controlled fluorescence measurements were performed on a TECAN (SPARK control v3.1) microplate plate reader using Corning® 384-Well black polystyrene plate with non-binding surface. Excitation and emission wavelengths for Atto488 are 485 nm and 535 nm and for Atto647N are 620 nm and 679 nm respectively.

***p* values** were calculated by performing a t-Test (Two-Sample Assuming Equal Variances) in Microsoft excel using a built-in Data analysis tool pack.

The amine-modified oligonucleotides were synthesized on a H-8 custom LNA, DNA/RNA automatic synthesizer from K&A Laborgeräte. The synthesized oligonucleotides were purified by **High Performance Liquid Chromatography (HPLC)** on a Dionex Ultimate 3000 (Thermo Fischer Scientific).

5.4.3 Methods

5.4.3.1 Synthesis of surfactant-free, poly(2,2,2-trifluoroethyl methacrylate)-Rhodamine labeled core particles.

The synthesis is analogous to a previous report. Divinylbenzene (DVB) and 2,2,2-trifluoroethyl methacrylate (tFMA) were purified using column chromatography (Al_2O_3, neutral). The initiator potassium persulfate (KPS, 159.49 mg, 590 µmol) was dissolved in deionized water (45 mL), degassed by bubbling with nitrogen gas (25 min) and thermostated at 70 °C for 15 min. To a solution of DVB (46.2 mg, 354.9 µmol) and tFMA (1.98 g, 11.8 mmol), a solution of acryloxyethyl thiocarbamoyl Rhodamine B (1 mg) and N-isopropylacrylamide (NIPAM, 150 mg, 1.3 mmol) in water (4.5 mL) was added. The mixture was ultrasonicated for 2 minutes and degassed by bubbling with nitrogen gas (10 min). The resulting mixture was added dropwise (over a period of 5 min) to the initiator solution starting the polymerization. The reaction mixture was stirred at 70 °C for 6 h (stirring rate = 600 rpm). The resulting dispersion was filtered while hot and dialyzed against deionized water (MWCO 8000 Da; solid content = 35.6 mg/mL by freeze-drying).

5.4.3.2 Synthesis of the NIPAM shell to yield PtFMA-Rhodamine labeled-core-PNIPAM-co-Acrylic Acid-shell microgel (MGs) particles.

The synthesis was adapted from a previous report[49]: NIPAM (1.49 g, 13.2 mmol, 80.5 wt %) was dissolved in deionized water (100 mL) together with the cross-linker *N*,*N*'-methylenebis(acrylamide) (MBA, 18.2 mg, 81.7 µmol, 1.0 wt %). The core particles (4.7 mL, 35 mg/mL, 157.2 mg solid content, 9.5 wt %) were added and the mixture was degassed for 30 min and heated to 72 °C. The initiator KPS (76.2 mg, 0.28 mmol) was dissolved in water (30 mL) and degassed (15 min). The polymerization was initiated by dropwise addition of initiator solution to a heated reaction mixture and stirred (stirring rate = 350 rpm). After 10 minutes, degassed acrylic acid (AA, 153 mg, 150 µL, 2.1 mmol, 9 wt%) after purification by column chromatography (Al_2O_3, neutral) was added dropwise into the reaction mixture. The stirring rate was increased to 600 rpm and reaction was allowed to run for 4 hours. The resulting core/shell MG particles (amount of AA moieties assuming full conversion =

1250 µmol per g of MG) were filtered while hot and purified by dialysis (MWCO 8000 Da) against deionized water. The resulting core-shell MGs were further purified via centrifugation (5 × 25 min, 11000 rpm, 15 °C, replacement of the supernatant with Milli Q water per centrifugation step).

5.4.3.3 Functionalization of MG with amine-modified DNA.

The MG suspension was redispersed in 2-(N-morpholino)ethanesulfonic acid (MES) buffer (10 mM, pH = 4.5) via centrifugation (20 min, 9000 rpm, 15 °C, replacement of the supernatant with MES buffer). A two-step reaction achieves the functionalization of DNA on MGs. In the first step, activation of carboxyl acid groups in MG shell (120 µL, 1.943 mg/mL of MGs, 0.29 µmol of COOH groups) was carried out by stirring with EDC (1.1 mg, 7.2 µmol, 25 equiv. with respect to COOH groups) dissolved in 40 µL of MES buffer (10 mM MES, pH = 4.5) for 15 minutes at 25 °C. Finally, amine-modified DNA (0.1 µmol, 0.35 equiv.) dispersed in 350 µL PBS buffer (pH = 7.4) was added to activated MGs prepared in first step and the mixture was stirred for 4.5 h at 25 °C. The DNA functionalized MGs were purified via centrifugation (2 × 3 min, 8000 rpm, 25 °C, replacement of the supernatant with TE buffer (pH = 8.0), per centrifugation step).

5.4.3.4 Synthesis and purification of amine-modified oligonucleotide sequences.

The oligonucleotides were synthesized at 10 µmol scale employing the standard solid phase β-cyanoethyl-phosphoramidite chemistry in trityl-on mode. The DNA phosphoramidites (DMT (dimethoxytrityl)-dT, DMT-dA(bz), DMT-dG(dmf) and DMT-dC(ac)) were diluted to 50 mM with dry acetonitrile and synthesis occurred from the 3' towards the 5' end of the oligonucleotides on packed solid phase columns.

Cleavage of the oligonucleotides (DMT-on) from the solid support and base deprotection was achieved in one step to ensure optimal yields. The 34 µmol/g controlled pore glass (CPG) solid support was treated with 10 mL of ice-cold ammonia solution (30-32 % NH_3) overnight at room temperature to detach the DNA from the CPG support. The cleaved DNA (DMT-on) in ammonia was diluted with 10 mL of disodium phosphate buffer (75 mM containing 1 mM EDTA, pH = 8.3) and the crude product was obtained upon freeze drying. The obtained DNA was redispersed in MilliQ water and purified by preparative reverse phase-HPLC (RP-HPLC) followed by freeze drying to remove the solvent.

The DMT group was cleaved from the purified product by making a 2 wt % solution of the dry DNA in NaOAc/HOAc buffer (200 mM, pH 4.0, 200 mM NaCl) and heating the mixture to 50 °C for one hour. After neutralizing the reaction mixture with disodium phosphate buffer (750 mM, 10 mM EDTA), the synthesized DNA was precipitated into a 5-fold excess of isopropanol to remove contaminants and to exchange the counterions to sodium. The precipitate was dissolved in MiliQ water and freeze dried. The synthesized and purified strands were stored at -20 °C until further use.

The purity of the obtained oligonucleotides was confirmed with analytical HPLC.

5.4.3.5 DNA annealing

All DNA strands were used as received. All the sequences are provided in Supplementary Table S1 and Table S2. The DNA strands received from IDT and Biomers were dissolved in TE buffer (10 mM Tris-HCl, pH = 8.0) to prepare a stock solution of 1 mM and stored at -20 °C for further use. The complementary DNA strands intended for double stranded complexes, i.e., Complex 1 and Substrate 1 were dissolved in annealing buffer (10 mM Tris-HCl, 50 mM NaCl, 10 mM $MgCl_2$, pH = 8.0) with the same stoichiometry at -20 °C overnight to prepare a stock solution of 0.125 mM.

5.4.3.6 CLSM image treatment and analysis

All CLSM images were processed using ImageJ (Fiji). All images except in **Figure 5-3a** were acquired as a *z*-stack. Atto488, Atto647 and Rhodamine B channels were merged together to form a composite image and then compiled as a *z*-projection for representation purposes. The size of the co-assemblies was determined

by thresholding the compiled images. The masks obtained upon thresholding were analyzed in terms of size and total amount.[1]

5.4.3.7 Lifetime Calculation

The lifetime of the transient state is defined as the time that a transient profile (either obtained from time-dependent fluorescence measurements or assembly size analysis) takes to decrease to half of the initial and maximum value.

5.4.4 Supplementary Notes

5.4.4.1 Definition of activity units of both enzymes

Definition of the Weiss Unit to describe the activity of T4 DNA ligase: 0.01 Weiss Unit [WU] of T4 DNA Ligase is the amount of enzyme required to catalyze the ligation of greater than 95 % of 1 µg of λ/HindIII fragments at 16 °C in 20 minutes.

Unit definition to describe the activity of BsaI: One Unit [U] is defined as the amount of enzyme required to completely digest 1 µg of pXba DNA in one hour at 37 °C in 50 µl assay buffer containing acetylated BSA added to a final concentration of 0.1 g/L.

5.4.5 Supplementary Tables

Table S1. DNA sequences for the oligonucleotides synthesized following a well-defined procedure (section 3.4) with their abbreviations and modifications.

Name	Sequence 5'→ 3'	Figure	Modification
NH2-x* (T_{20}-x*)	TTTTTTTTTTTTTTTTTTTT GAACCCGTATATCTATCCTA	Fig. 5-3 – 5-4	5' Amino Modifier C6 dT
NH2-z* (z*-T_{20})	GATAGAGATCGTGTGTTAC TTTTTTTTTTTTTTTTTTTT	Fig. 5-3 – 5-4	3' Amino Modifier C6

Table S2. DNA sequences for the oligonucleotides with their abbreviations, sequence, and modifications. 5' Phosphorylated DNA strands were purchased from IDT. All other DNA sequences were purchased from Biomers.

Name	Sequence 5'→ 3'	Figure	Modification
Substrate	CGGATTGGTATTGTATTACC	Fig. 5-2 – 5-4	None
	AATCTTTAATACAATACCAATCCGATT	Fig. 5-2 – 5-4	5' Phos
Complex	CATGAGAATTCCATTCACGGTCTCT	Fig. 5-2 – 5-4	None
	GATTAGAGACCGTGAATGGAATTCTCATG	Fig. 5-2 – 5-4	5' Phos
Input 1	AATCAATCGGA	Fig. 5-2 – 5-4	5' Phos
Input 2	GTATTAAA	Fig. 5-2 – 5-4	None
A1-Atto488	ACCAATCCG TTTTTTTTTTTTTTTTTTTT	Fig. 5-2	5' ATTO 488
A2-Atto647	TTTTTTTTTTTTTTTTTTTT GGTAATACAAT	Fig. 5-2	3' BMN Q535
x-A1-Atto488	ACCAATCCG TAGGATAGATATACGGGTTC	Fig. 5-3,5-4	5' ATTO 488
z-A2-BMNQ535	GTAACACACGATCTCTATC GGTAATACAAT	Fig. 5-4a,5-4b,5-4c	3' BMN Q535
z-A2-Atto647	GTAACACACGATCTCTATC GGTAATACAAT	Fig. 5-3,5-4d,5-4e,5-4f,5-4g	3' ATTO 647N

5.4.6 Supplementary Figures

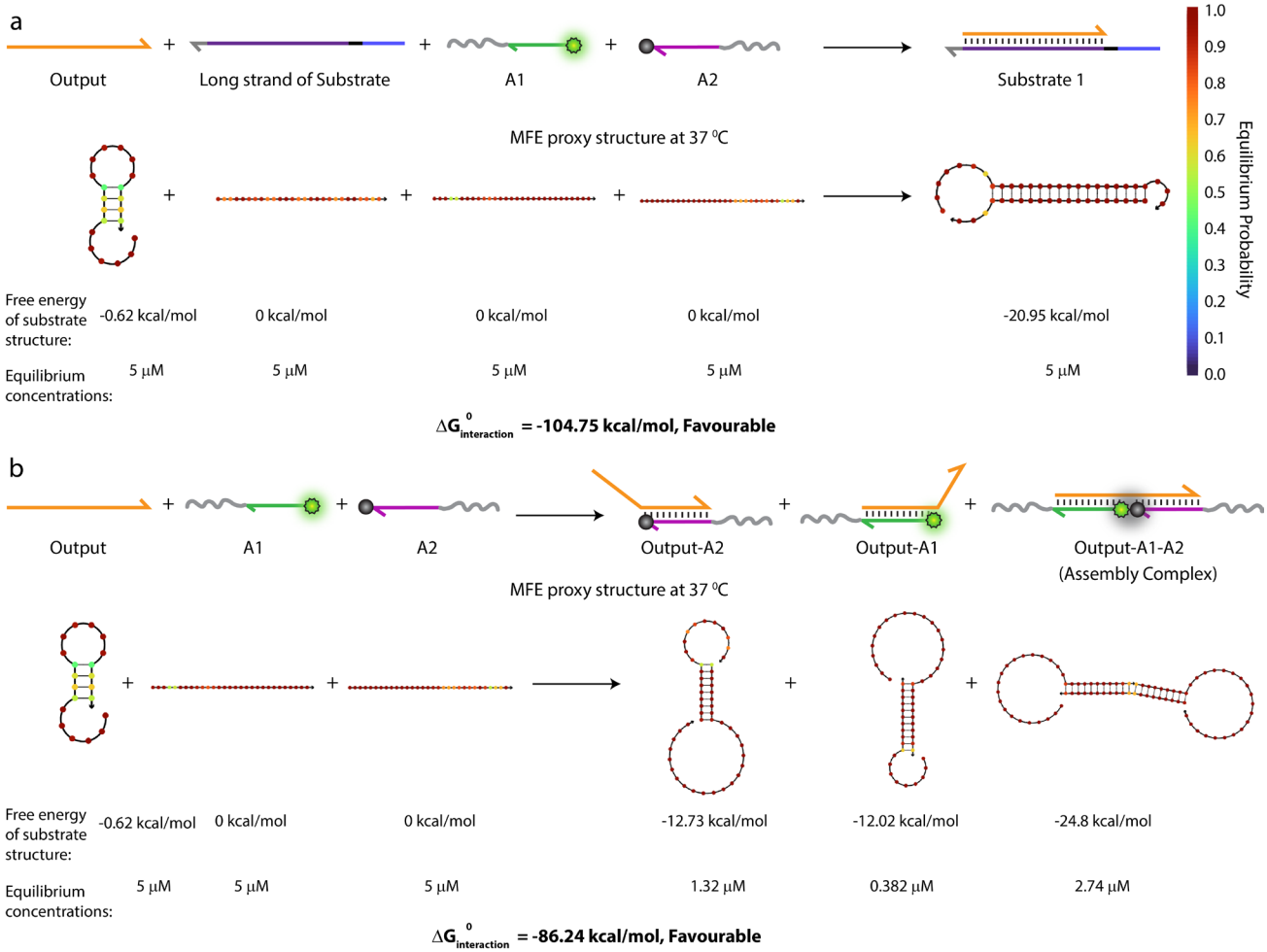

Figure 5-6. Free energy change for the interaction between (a) Output and long strand of Substrate in the presence of A1 and A2 in the State A of the system, (b) Output and A1 and A2 in the absence of long strand of Substrate 1 in the State B of the system calculated with NUPACK simulations setting the temperature at 37 °C and salt concentrations at 50 mM NaCl, 10 mM $MgCl_2$. Output preferably remains bound within Substrate 1 and does not show any interaction with A1 or A2 in State A of the system. Only in State B of the system in the absence of long strand of Substrate, Output forms Assembly Complex with A1 and A2.

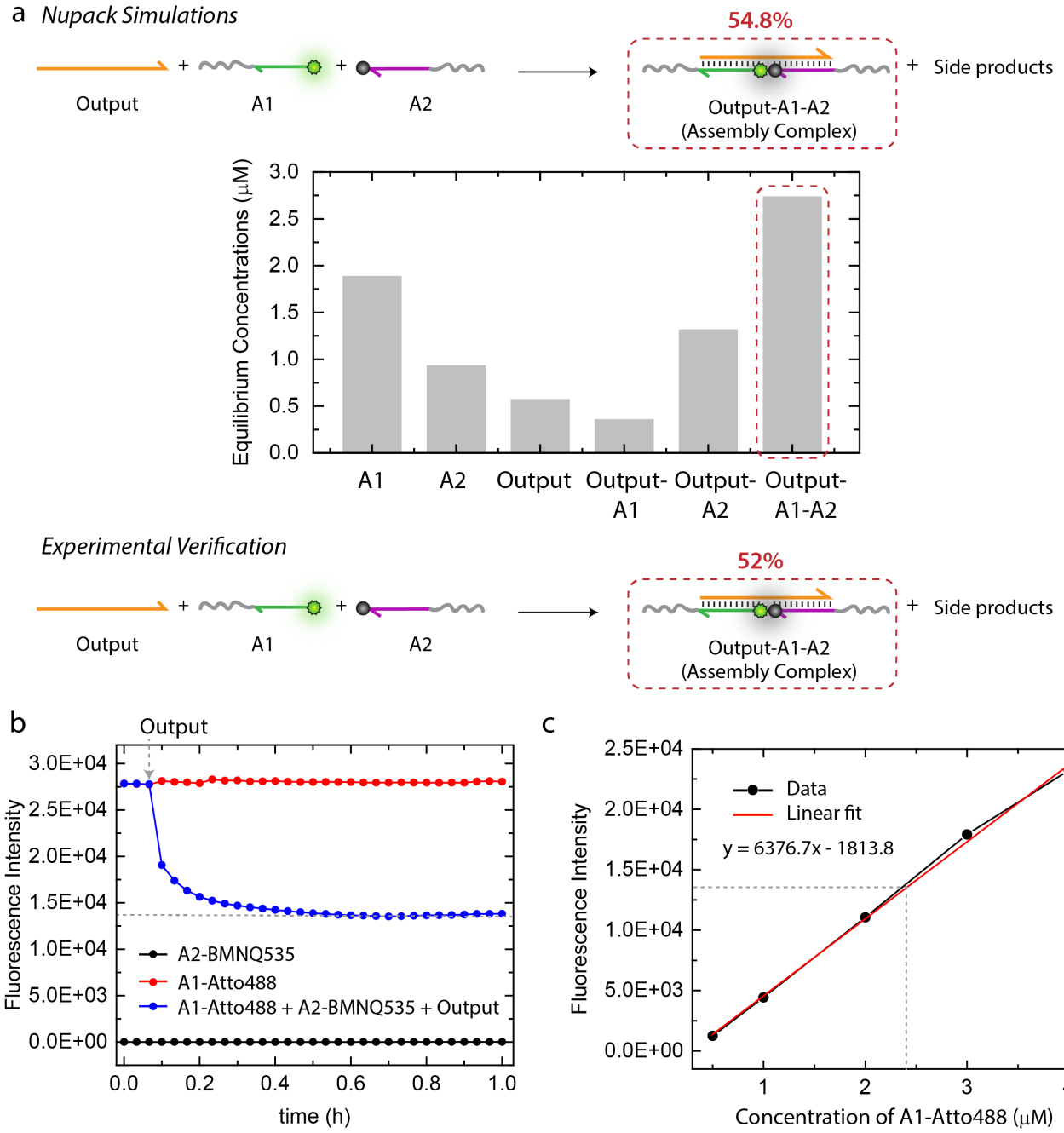

Figure 5-7. (a) Equilibrium concentrations of all the components obtained from NUPACK[1-3] simulations upon mixing 5 μM each of Output, A1 and A2 setting the temperature at 37 °C and salt concentrations at 50 mM NaCl, 10 mM $MgCl_2$. The desired Assembly Complex between Output, A1 and A2 is formed in 54.8 % yield. (b), (c) Experimental verification of the equilibrium concentration of desired Assembly Complex between Output, A1-Atto488 and A2-ABMNQ535. (b) Time-dependent fluorescence intensity measurements of A1-Atto488 (red), A2-ABMNQ535 (black), and a 1:1 mixture of A1-Atto488, A2-ABMNQ535 upon introduction of Output in the system (blue). The remaining fluorescence (blue) corresponds to the uncomplexed or free A1-Atto488. (c) With the help of calibration curve between fluorescence Intensity and concentration of free A1-Atto488, the amount of uncomplexed A1-Atto488 in the equivalent mixture of A1-Atto488, A2-ABMNQ535, and Output can be calculated as 2.4 μM. Assuming a 100% quenching efficiency between Atto488 and BMNQ535 and zero fluorescence contribution from BMNQ535, the equilibrium concentration of Assembly complex can be calculated as 2.6 μM accounting for 52% yield. This means the experimental yield shows only 5% deviation from simulated yield (NUPACK, 54.8%). Experimental conditions: all species present at 5 μM concentration in 1X *NEB* CutSmart buffer at 37 °C.

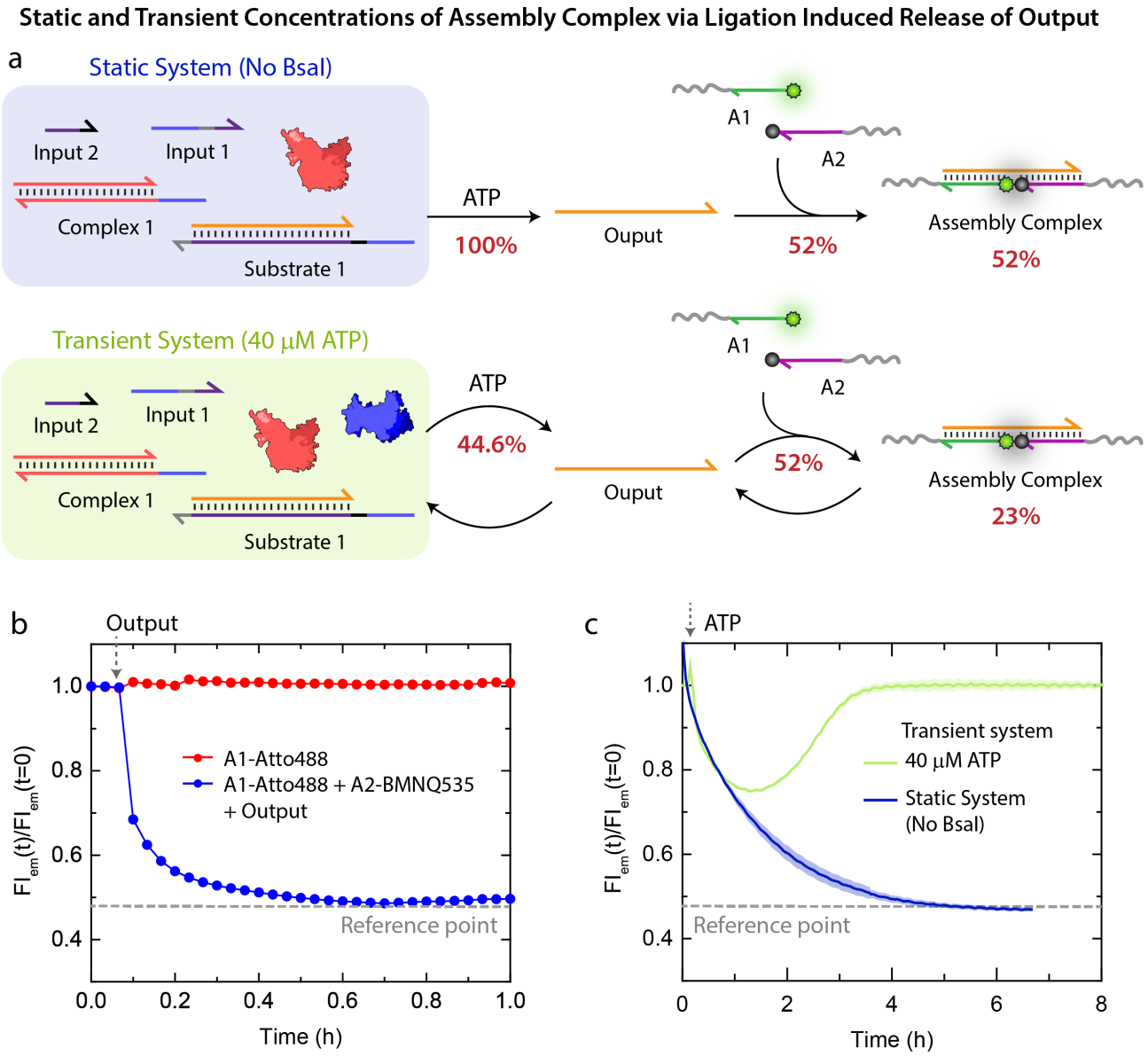

Figure 5-8. (a) Schematics for experimental verification of percentage yield of Assembly Complex in Static and Transient systems. (b) Time-dependent fluorescence intensity measurements of A1-Atto488 and a 1:1 mixture of A1-Atto488, A2-ABMNQ535 upon introduction of Output in the system. The percentage of fluorescence decrease (grey, dotted line) provides a Reference point which indicates the minimum fluorescence that can be observed in the system. Experimental conditions: all species present at 5 μM concentration in 1X *NEB* CutSmart buffer at 37 °C. (c) Time-dependent fluorescence intensity changes demonstrating static and transient complexation of A1-Atto488 and A2-BMNQ535 upon ATP-fueled ligation induced release of Output. For the Static system, in the absence of BsaI, fluorescence intensity decreases approximately to the Reference point. This clearly indicates that Output must have released with 100% efficiency. But, in case of transient system, restriction can set in already at the hemi-ligated intermediate (e.g., Substrate 1, Complex 1 and only one of the Inputs) without completing to the fully ligated state which is the condition for expulsion of Output. Because of this, fluorescence intensity decreases by only 25% which indicates that Output is released with 44.6% efficiency with respect to Reference point. Since only 52% of Output released can form Assembly Complex (Fig. S2b), a final yield of 23% can be attributed to Assembly Complex. Experimental conditions: A1-Atto488 and A2-BMNQ535 at an equimolar concentration of 5 μM are dissolved in 1X *NEB* CutSmart buffer containing 20 μM Complex 1, 5 μM Substrate 1, 10 μM Input 1 and Input 2 at 37 °C. For transient system (green curve), 0.8 WU μL^{-1} of T4 DNA ligase and 0.8 U μL^{-1} of BsaI was used and system was fueled by 40 μM ATP; static system (blue curve) was carried out only with 0.8 WU μL^{-1} of T4 DNA ligase and fueled with 40 μM ATP.

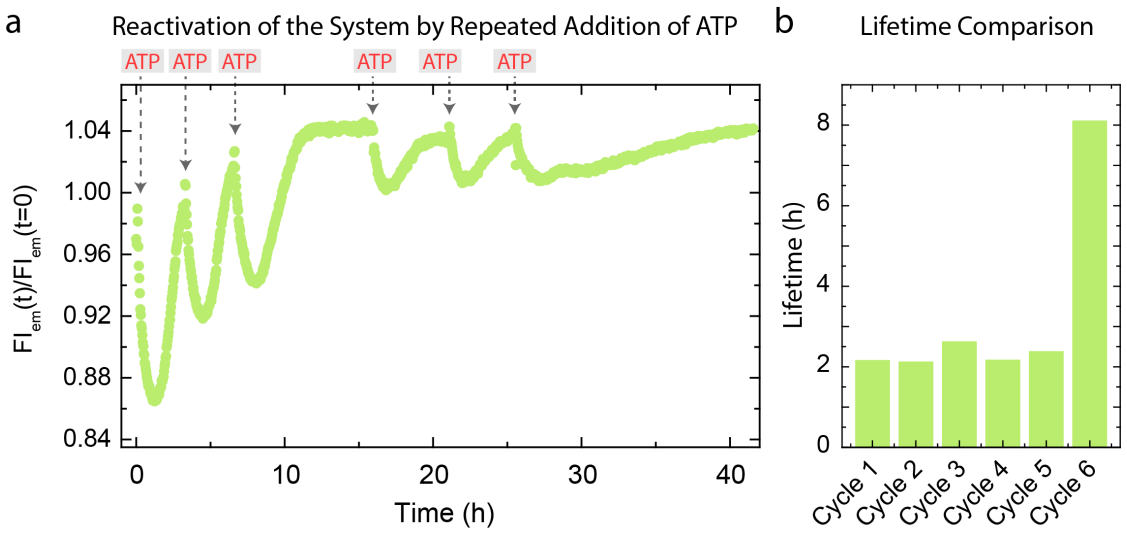

Figure 5-9. Multiple activations of the system by repetitive addition of ATP. (a) Time-dependent fluorescence intensity changes upon three times addition of 40 µM ATP. (b) Corresponding lifetimes for each consecutive cycle obtained from Fig. S4a. Experimental conditions: A1-Atto488 and A2-BMNQ535 at an equimolar concentration of 5 µM are dissolved in 1X *NEB* CutSmart buffer containing 20 µM Complex 1, 5 µM Substrate 1, 10 µM Input 1, Input 2, 0.8 WU μL^{-1} T4 DNA ligase, and 0.8 U μL^{-1} BsaI at 37 °C, initiated by repetitive addition of 40 µM ATP.

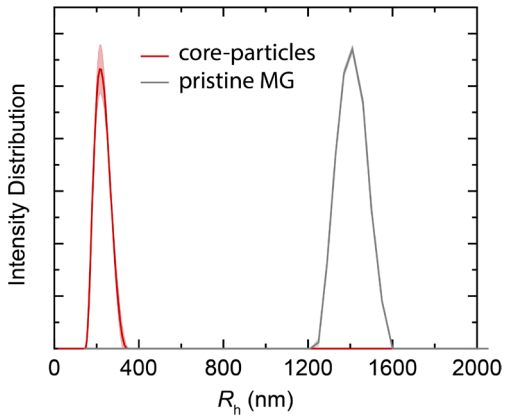

Figure 5-10. DLS CONTIN plots of: poly(2,2,2-trifluoroethyl methacrylate) (PtFMA) core-particles and pristine MG. The suspensions were prepared in MilliQ water with a final concentration of 0.06 mg/mL.

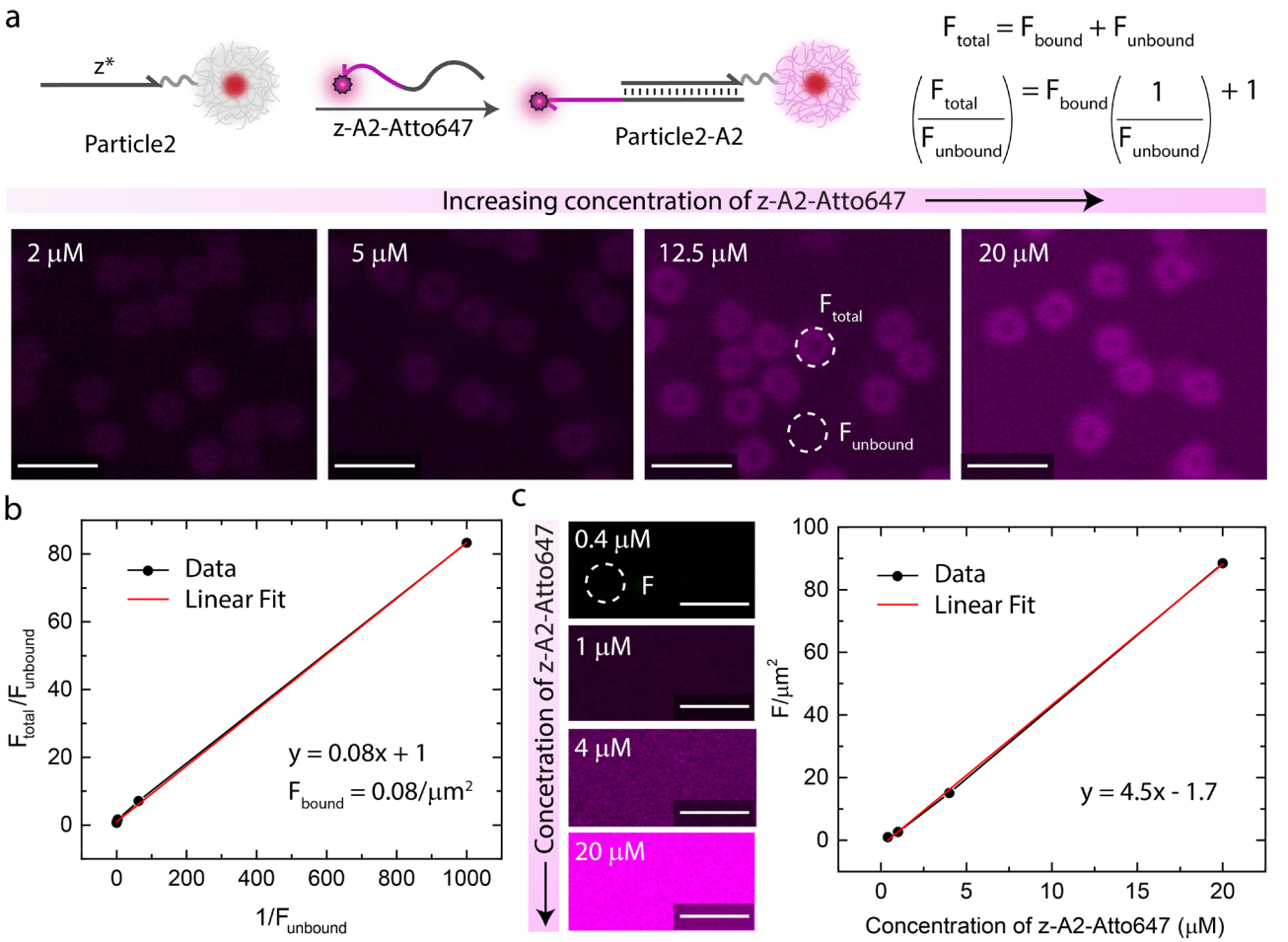

Figure 5-11. Measurement of DNA grafting density on Particle2. (a) The binding capacity of z-A2-Atto647 onto Particle2 via z/z* hybridization is measured as a proxy for the DNA grafting density. The mean fluorescence intensity per μm² over the particle (F_{total}, includes the contribution from both z-A2-Atto647 bound on Particle2 and free z-A2-Atto647 in the suspension) and in the background ($F_{unbound}$, includes only free z-A2-Atto647 in the suspension) is measured for increasing amounts of z-A2-Atto647 via CLSM. Experimental conditions: Particle1 is incubated with increasing concentrations of z-A2-Atto647 (0.2-20 μM) in TE buffer (pH = 8.0) at 15 °C at a final MG concentration of 0.05 wt %. F_{total} and $F_{unbound}$ represent average fluorescence intensity measured from 10 different regions. (b) The data is fitted with linear equation where the slope provides fluorescence contribution from z-A2-Atto647 on the particle (F_{bound}). (c) With the help of calibration curve between mean fluorescence intensity per μm² (F, measured via CLSM) and concentration of free z-A2-Atto647, a corresponding DNA concentration for F_{bound} is calculated to be 4.5 ± 0.1 μM accounting for 2.7 × 10^3 strands/MG. Experimental conditions: Increasing concentrations of z-A2-Atto647 (4-40 μM) dispersed in TE buffer. F represents an average fluorescence intensity from 5 different regions. A laser with λ = 638 nm and power of 30 mW was used at 2% intensity throughout the experiment. Scale bars: (a), (c) 2 μm.

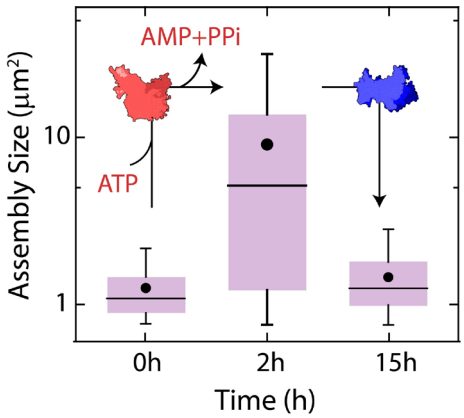

Figure 5-12. Assembly size analysis on the particles from the CLSM images (Figure. 5-3b) obtained during sequential ATP fueling and BsaI restriction (i.e., static system) The co-assemblies achieve a maximum average size of 9 μm² after 2h of ATP addition. The formed structures disassemble again after 15h of BsaI addition. The box represents 25-75 % of data, whiskers represent 5-95 % of data, a solid circle represents the mean, and horizontal bar the median of the assembly size distribution in box charts.

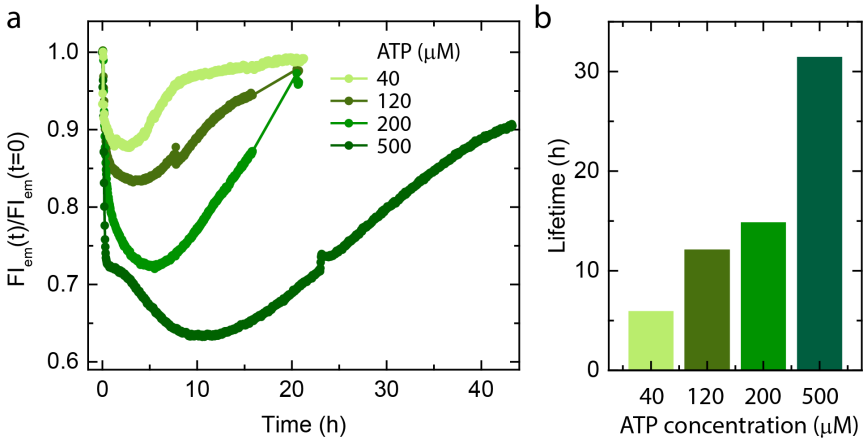

Figure 5-13. (a) Time-dependent fluorescence intensity changes demonstrating transient co-assembly of dye-functionalized Particle1-A1-Atto488 and quencher-functionalized Particle2-A2-BMNQ535 at different ATP concentrations. (b) Lifetime comparison of the ATP-driven transient co-assembly of Particle1-A1-Atto488 and Particle2-A2-BMNQ535 with increasing ATP equivalents demonstrate consequent increase in lifetime. Experimental conditions: Particle1-A1-Atto488 and Particle2-A2-BMNQ535 are suspended as an equimolar mixture in 1X NEB CutSmart buffer at a final MG concentration of 0.05 wt% containing 20 μM Complex 1, 5 μM Substrate 1, 10 μM Input 1 and Input 2 at 37 °C, fueled by different ATP concentrations.

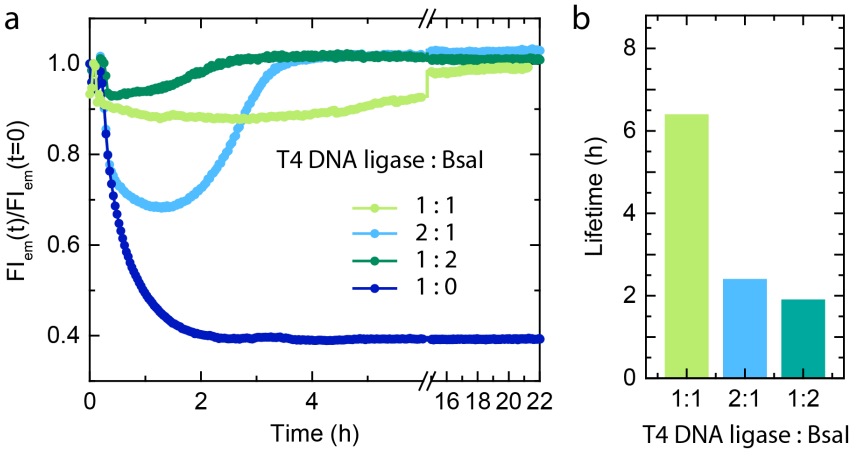

Figure 5-14. (a) Time-dependent fluorescence intensity changes demonstrating transient co-assembly of dye-functionalized Particle1-A1-Atto488 and quencher-functionalized Particle2-A2-BMNQ535 upon ATP addition at different ratios of T4 DNA ligase and BsaI. Please note that a 1:1 ratio of T4 DNA ligase and BsaI is used in all other experiments (standard conditions of the MS). (b) Corresponding lifetime comparison of the ATP-driven transient co-assembly of Particle1-A1-Atto488 and Particle2-A2-BMNQ535. Experimental conditions: Particle1-A1-Atto488 and Particle2-A2-BMNQ535 are suspended as an equimolar mixture in 1X *NEB* CutSmart buffer at a final MG concentration of 0.05 wt% containing 20 µM Complex 1, 5 µM Substrate 1, 10 µM Input 1 and Input 2 at 37 °C, fueled by 40 µM ATP.

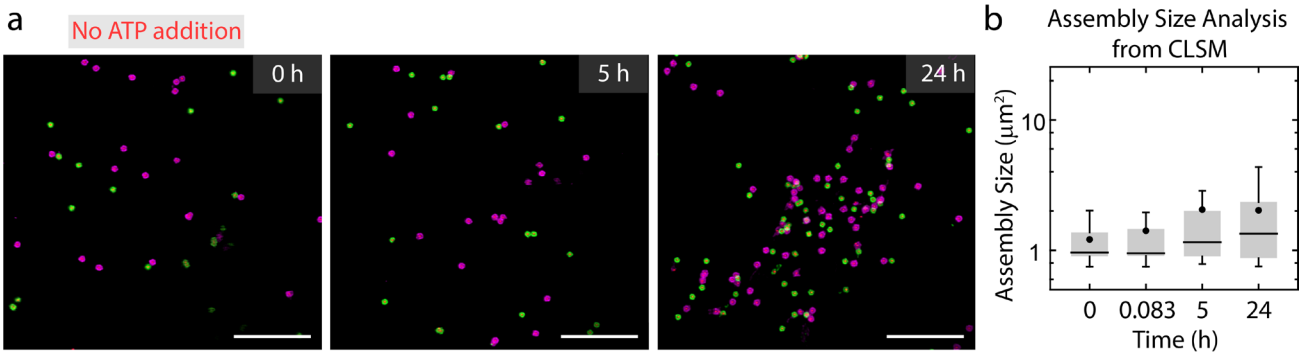

Figure 5-15. Control for transient co-assemblies of MGs regulated by upstream ATP-fueled ERN without ATP addition. (a) Time dependent ex situ CLSM imaging shows absence of any co-assembly between Particle1-A1-Atto488 and Particle2-A2-Atto647 without ATP addition. All CLSM images are represented as merged composite compiled as a z-projection. Experimental conditions: Particle1-A1-Atto488 and Particle2-A2-Atto647 suspended as an equimolar mixture in 1X *NEB* CutSmart buffer at a final MG concentration of 0.05 wt %, 20 µM Complex 1, 5 µM Substrate 1, 10 µM Input 1 and Input 2 at 37 °C. (b) Assembly size analysis on the particles obtained from two different *z*-projections at each time interval. The box represents 25-75 % of data, whiskers represent 5-95 % of data, a solid circle represents the mean, and horizontal bar the median of the assembly size distribution in box charts. Scale bars: 10 µm.

The average assembly size increased to 2.5 times of its initial value indicating formation of small clusters only after 24 h of monitoring the system. This might result because of salt-induced non-specific aggregation of MGs.[2]

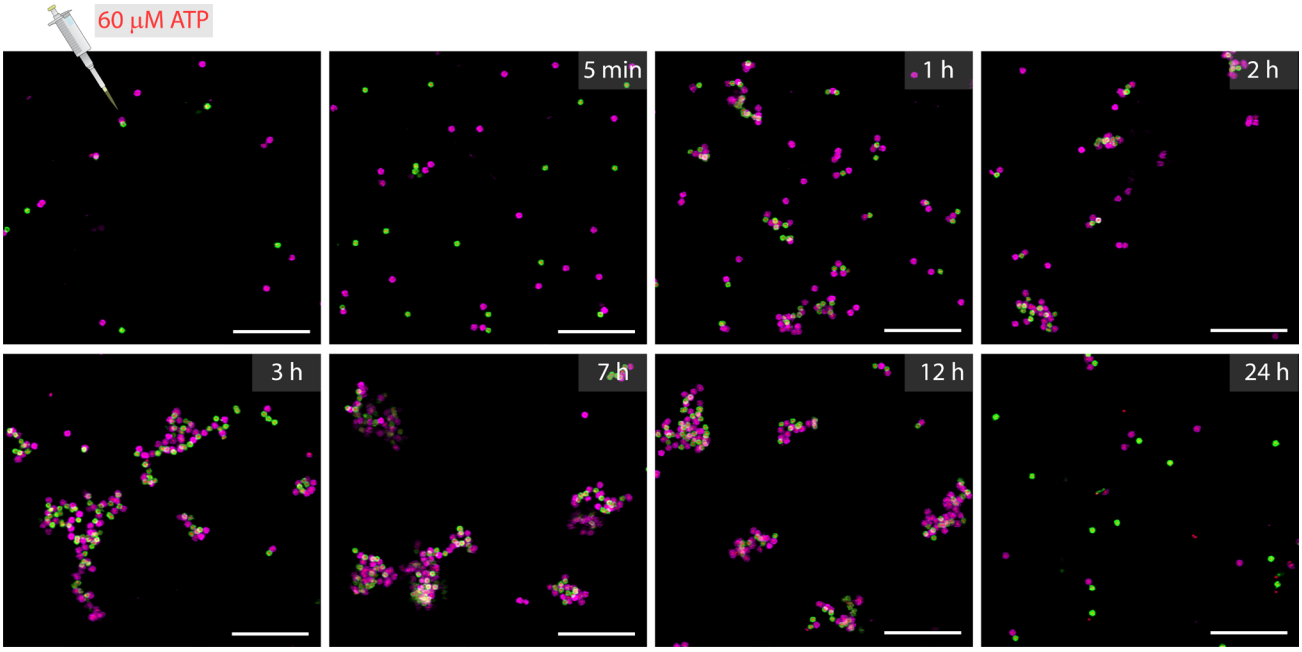

Figure 5-16. Time dependent ex situ CLSM imaging shows transient co-assembly of MGs regulated by ATP-fueled upstream ERN. Experimental conditions: Particle1-A1-Atto488 and Particle2-A2-Atto647 suspended as an equimolar mixture in 1X CutSmart buffer at a final MG concentration of 0.05 wt%, 20 µM Complex 1, 5 µM Substrate 1, 10 µM Input 1 and Input 2 fueled by 60 µM of ATP at 37 °C. All CLSM images are represented as merged composite compiled as a z-projection. Scale bars: 10 µm.

5.5 References

1 Zadeh, J. N. *et al.* NUPACK: Analysis and design of nucleic acid systems. *J. Comput. Chem.* **32**, 170-173, doi:10.1002/jcc.21596 (2011).

2 van Ravensteijn, B. G. P., Voets, I. K., Kegel, W. K. & Eelkema, R. Out-of-Equilibrium Colloidal Assembly Driven by Chemical Reaction Networks. *Langmuir* **36**, 10639-10656, doi:10.1021/acs.langmuir.0c01763 (2020).

3 Merindol, R. & Walther, A. Materials learning from life: concepts for active, adaptive and autonomous molecular systems. *Chem. Soc. Rev.* **46**, 5588-5619, doi:10.1039/C6CS00738D (2017).

4 della Sala, F., Neri, S., Maiti, S., Chen, J. L. Y. & Prins, L. J. Transient self-assembly of molecular nanostructures driven by chemical fuels. *Curr. Opin. Biotechnol.* **46**, 27-33, doi:https://doi.org/10.1016/j.copbio.2016.10.014 (2017).

5 Hess, H. & Ross, J. L. Non-equilibrium assembly of microtubules: from molecules to autonomous chemical robots. *Chem. Soc. Rev.* **46**, 5570-5587, doi:10.1039/C7CS00030H (2017).

6 Sharma, C., Maity, I. & Walther, A. pH-feedback systems to program autonomous self-assembly and material lifecycles. *Chem. Commun.* **59**, 1125-1144, doi:10.1039/D2CC06402B (2023).

7 Mishra, A. *et al.* Biomimetic temporal self-assembly via fuel-driven controlled supramolecular polymerization. *Nat. Commun.* **9**, 1295, doi:10.1038/s41467-018-03542-z (2018).

8 Dhiman, S., Jalani, K. & George, S. J. Redox-Mediated, Transient Supramolecular Charge-Transfer Gel and Ink. *ACS Appl. Mater. Interfaces* **12**, 5259-5264, doi:10.1021/acsami.9b17481 (2020).

9 Mishra, A., Dhiman, S. & George, S. J. ATP-Driven Synthetic Supramolecular Assemblies: From ATP as a Template to Fuel. *Angew. Chem. Int. Ed.* **60**, 2740-2756, doi:10.1002/anie.202006614 (2021).

10 Sharko, A., Livitz, D., De Piccoli, S., Bishop, K. J. M. & Hermans, T. M. Insights into Chemically Fueled Supramolecular Polymers. *Chem. Rev.* **122**, 11759-11777, doi:10.1021/acs.chemrev.1c00958 (2022).

11 Rieß, B., Grötsch, R. K. & Boekhoven, J. The Design of Dissipative Molecular Assemblies Driven by Chemical Reaction Cycles. *Chem* **6**, 552-578, doi:https://doi.org/10.1016/j.chempr.2019.11.008 (2020).

12 Boekhoven, J., Hendriksen, W. E., Koper, G. J., Eelkema, R. & van Esch, J. H. Transient assembly of active materials fueled by a chemical reaction. *Science* **349**, 1075-1079, doi:10.1126/science.aac6103 (2015).

13 Samanta, D. & Klajn, R. Aqueous Light-Controlled Self-Assembly of Nanoparticles. *Adv. Opt. Mater.* **4**, 1373-1377, doi:https://doi.org/10.1002/adom.201600364 (2016).

14 Sharma, C. & Walther, A. Self-Regulating Colloidal Co-Assemblies That Accelerate Their Own Destruction via Chemo-Structural Feedback. *Angew. Chem. Int. Ed.* **61**, e202201573, doi:https://doi.org/10.1002/anie.202201573 (2022).

15 Grötsch, R. K. *et al.* Pathway Dependence in the Fuel-Driven Dissipative Self-Assembly of Nanoparticles. *J. Am. Chem. Soc.* **141**, 9872-9878, doi:10.1021/jacs.9b02004 (2019).

16 van Ravensteijn, B. G. P., Hendriksen, W. E., Eelkema, R., van Esch, J. H. & Kegel, W. K. Fuel-Mediated Transient Clustering of Colloidal Building Blocks. *J. Am. Chem. Soc.* **139**, 9763-9766, doi:10.1021/jacs.7b03263 (2017).

17 Dehne, H., Reitenbach, A. & Bausch, A. R. Reversible and spatiotemporal control of colloidal structure formation. *Nat. Commun.* **12**, 6811, doi:10.1038/s41467-021-27016-x (2021).

18 Dehne, H., Reitenbach, A. & Bausch, A. R. Transient self-organisation of DNA coated colloids directed by enzymatic reactions. *Sci. Rep.* **9**, 7350, doi:10.1038/s41598-019-43720-7 (2019).

19 Heuser, T., Steppert, A. K., Lopez, C. M., Zhu, B. & Walther, A. Generic concept to program the time domain of self-assemblies with a self-regulation mechanism. *Nano Lett.* **15**, 2213-2219, doi:10.1021/nl5039506 (2015).

20 Deng, J. & Walther, A. ATP-powered molecular recognition to engineer transient multivalency and self-sorting 4D hierarchical systems. *Nat. Commun.* **11**, 3658, doi:10.1038/s41467-020-17479-9 (2020).

21 Heinen, L. & Walther, A. Temporal control of i-motif switch lifetimes for autonomous operation of transient DNA nanostructures. *Chem. Sci.* **8**, 4100-4107, doi:10.1039/c7sc00646b (2017).

22 Heinen, L. & Walther, A. Programmable dynamic steady states in ATP-driven non-equilibrium DNA systems. *Sci. Adv.* **5**, eaaw0590, doi:10.1126/sciadv.aaw0590 (2019).

23 Gentile, S., Del Grosso, E., Prins, L. J. & Ricci, F. Autonomous and Programmable Reorganization of DNA-Based Polymers Using Redox Chemistry**. *Chem. Eur. J.* **29**, e202300394, doi:https://doi.org/10.1002/chem.202300394 (2023).

24 Del Grosso, E., Ragazzon, G., Prins, L. J. & Ricci, F. Fuel-Responsive Allosteric DNA-Based Aptamers for the Transient Release of ATP and Cocaine. *Angew. Chem. Int. Ed.* **58**, 5582-5586, doi:https://doi.org/10.1002/anie.201812885 (2019).

25 Panja, S., Patterson, C. & Adams, D. J. Temporally-Programmed Transient Supramolecular Gels. *Macromol. Rapid Commun.* **40**, 1900251, doi:https://doi.org/10.1002/marc.201900251 (2019).

26 Kumar, M. *et al.* Amino-acid-encoded biocatalytic self-assembly enables the formation of transient conducting nanostructures. *Nat. Chem.* **10**, 696-703, doi:10.1038/s41557-018-0047-2 (2018).

27 Maiti, S., Fortunati, I., Ferrante, C., Scrimin, P. & Prins, L. J. Dissipative self-assembly of vesicular nanoreactors. *Nat. Chem.* **8**, 725-731, doi:10.1038/nchem.2511 (2016).

28 Mao, X., Liu, M., Li, Q., Fan, C. & Zuo, X. DNA-Based Molecular Machines. *JACS Au* **2**, 2381-2399, doi:10.1021/jacsau.2c00292 (2022).

29 Mondal, A., Toyoda, R., Costil, R. & Feringa, B. L. Chemically Driven Rotatory Molecular Machines. *Angew. Chem. Int. Ed.* **61**, e202206631, doi:https://doi.org/10.1002/anie.202206631 (2022).

30 Fan, X. & Walther, A. 1D Colloidal chains: recent progress from formation to emergent properties and applications. *Chem. Soc. Rev.* **51**, 4023-4074, doi:10.1039/D2CS00112H (2022).

31 Heuser, T., Merindol, R., Loescher, S., Klaus, A. & Walther, A. Photonic Devices Out of Equilibrium: Transient Memory, Signal Propagation, and Sensing. *Adv. Mater.* **29**, 1606842, doi:https://doi.org/10.1002/adma.201606842 (2017).

32 Talapin, D. V., Lee, J.-S., Kovalenko, M. V. & Shevchenko, E. V. Prospects of Colloidal Nanocrystals for Electronic and Optoelectronic Applications. *Chem. Rev.* **110**, 389-458, doi:10.1021/cr900137k (2010).

33 Diez-Pascual, A. M. & Rahdar, A. Functional Nanomaterials in Biomedicine: Current Uses and Potential Applications. *ChemMedChem* **17**, e202200142, doi:https://doi.org/10.1002/cmdc.202200142 (2022).
34 Heckel, J., Loescher, S., Mathers, R. T. & Walther, A. Chemically Fueled Volume Phase Transition of Polyacid Microgels. *Angew. Chem. Int. Ed.* **60**, 7117-7125, doi:https://doi.org/10.1002/anie.202014417 (2021).
35 Groeer, S., Schumann, K., Loescher, S. & Walther, A. Molecular communication relays for dynamic cross-regulation of self-sorting fibrillar self-assemblies. *Sci. Adv.* **7**, eabj5827, doi:doi:10.1126/sciadv.abj5827 (2021).
36 Sharma, C., Samanta, A., Schmidt, R. S. & Walther, A. DNA-Based Signaling Networks for Transient Colloidal Co-Assemblies. *J. Am. Chem. Soc.* **145**, 17819-17830, doi:10.1021/jacs.3c04807 (2023).
37 Deng, J. & Walther, A. Pathway Complexity in Fuel-Driven DNA Nanostructures with Autonomous Reconfiguration of Multiple Dynamic Steady States. *J. Am. Chem. Soc.* **142**, 685-689, doi:10.1021/jacs.9b11598 (2020).
38 Deng, J. & Walther, A. Fuel-Driven Transient DNA Strand Displacement Circuitry with Self-Resetting Function. *J. Am. Chem. Soc.* **142**, 21102-21109, doi:10.1021/jacs.0c09681 (2020).
39 Deng, J. & Walther, A. Autonomous DNA nanostructures instructed by hierarchically concatenated chemical reaction networks. *Nat. Commun.* **12**, 5132, doi:10.1038/s41467-021-25450-5 (2021).
40 Deng, J. & Walther, A. Programmable ATP-Fueled DNA Coacervates by Transient Liquid-Liquid Phase Separation. *Chem* **6**, 3329-3343, doi:https://doi.org/10.1016/j.chempr.2020.09.022 (2020).
41 Caldwell, A. S., Aguado, B. A. & Anseth, K. S. Designing Microgels for Cell Culture and Controlled Assembly of Tissue Microenvironments. *Adv. Funct. Mater.* **30**, 1907670, doi:https://doi.org/10.1002/adfm.201907670 (2020).
42 Rossi, R., Montecucco, A., Ciarrocchi, G. & Biamonti, G. Functional characterization of the T4 DNA ligase: a new insight into the mechanism of action. *Nucleic Acids Res.* **25**, 2106-2113, doi:10.1093/nar/25.11.2106 (1997).
43 Cao, Y., Gabrielli, L., Frezzato, D. & Prins, L. J. Persistent ATP-Concentration Gradients in a Hydrogel Sustained by Chemical Fuel Consumption. *Angew. Chem. Int. Ed.* **62**, e202215421, doi:https://doi.org/10.1002/anie.202215421 (2023).
44 Han, K., Go, D., Hoenders, D., Kuehne, A. J. C. & Walther, A. Switchable Supracolloidal Coassembly of Microgels Mediated by Host/Guest Interactions. *ACS Macro Lett.* **6**, 310-314, doi:10.1021/acsmacrolett.7b00053 (2017).
45 Han, K. *et al.* Social Self-Sorting of Colloidal Families in Co-Assembling Microgel Systems. *Angew. Chem. Int. Ed.* **56**, 2176-2182, doi:https://doi.org/10.1002/anie.201612196 (2017).
46 Wang, Y. *et al.* Synthetic Strategies Toward DNA-Coated Colloids that Crystallize. *J. Am. Chem. Soc.* **137**, 10760-10766, doi:10.1021/jacs.5b06607 (2015).
47 Hennig, A. *et al.* Scope and Limitations of Surface Functional Group Quantification Methods: Exploratory Study with Poly(acrylic acid)-Grafted Micro- and Nanoparticles. *J. Am. Chem. Soc.* **134**, 8268-8276, doi:10.1021/ja302649g (2012).
48 do Nascimento Marques, N., Curti, P. S., da Silva Maia, A. M. & Balaban, R. d. C. Temperature and pH effects on the stability and rheological behavior of the aqueous suspensions of smart polymers based on N-isopropylacrylamide, chitosan, and acrylic acid. *J. Appl. Polym. Sci.* **129**, 334-345, doi:https://doi.org/10.1002/app.38750 (2013).
49 RAAE, A. J., KLEPPE, R. K. & KLEPPE, K. Kinetics and Effect of Salts and Polyamines on T4 Polynucleotide Ligase. *Eur. J. Biochem.* **60**, 437-443, doi:https://doi.org/10.1111/j.1432-1033.1975.tb21021.x (1975).
50 Caldwell, A. S., Campbell, G. T., Shekiro, K. M. T. & Anseth, K. S. Clickable Microgel Scaffolds as Platforms for 3D Cell Encapsulation. *Adv. Healthc. Mater.* **6**, 1700254, doi:https://doi.org/10.1002/adhm.201700254 (2017).
51 Routh, A. F. & Vincent, B. Salt-Induced Homoaggregation of Poly(N-isopropylacrylamide) Microgels. *Langmuir* **18**, 5366-5369, doi:10.1021/la011869d (2002).

6 ATP-Fueled Delivery of DNA in Living Cells

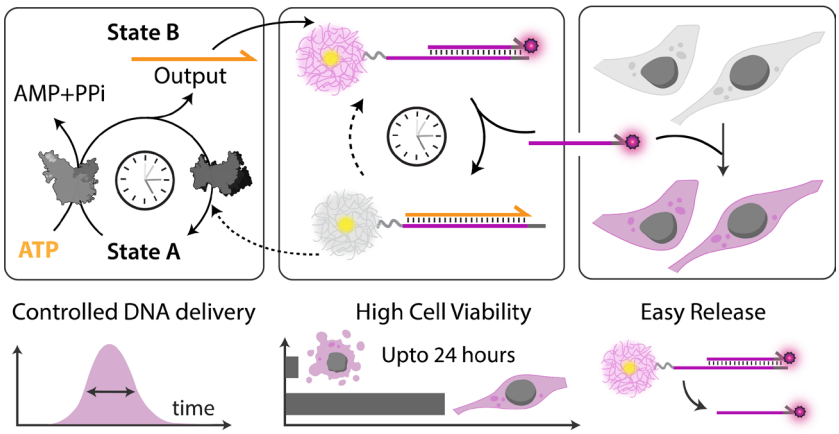

Preliminary note: *This chapter is based on a manuscript draft prepared by* ***C. Sharma,*** *S. Sethi, and A. Walther. The draft is not submitted for publication yet.*

Author contributions: C.S., S.S., and A.W. conceptualized the project. C.S. and S.S. conceived, designed, and performed the experiments, and analyzed the data. A.W. conceived and supervised the project. C.S. and S.S. discussed and analyzed the results. C.S. wrote the first draft, C.S., S.S., and A.W edited and finalized the chapter.

I thank Dr. C. Drees (cell lab manager), Dr. L Driessen, and Ms. M. Miller (cell lab technician) for setting up the cell lab and making it ready to be used.

Abstract: Development of highly specific and selective drugs with minimum side effects is an overarching goal in cancer research. Some of the current strategies involve taking advantage of the extracellular environment and natural transmembrane transport mechanisms of diseased tissues to stimulate immune response and/or suppress tumor growth. For instance, ATP, which is one of the main biochemical components of the tumor microenvironment has currently been suggested as a suitable target for cancer therapy. This opens up possibilities to exploit the increased ATP levels in the tumor microenvironment for selective delivery. Towards this, we propose a model approach for an ATP-induced delivery of DNA in cancer cells. An ATP-driven reaction network that transiently releases a Signal (DNA) strand is installed in the extracellular medium of cancer cells. The appropriate modification of Signal strand with a fluorophore enables successful uptake by cells and allows to monitor the uptake kinetics via confocal laser scanning microscopy. Signal strands are immobilized on a microgel particle which prevents non-specific internalization by cells in the absence of ATP and recaptures excess Signal strands from the medium after ATP consumption. The strategy presented in this study can further be extended to deliver therapeutic oligonucleotides such as small interfering (siRNA) and microRNA (miRNA) for future applications in gene therapy and gene silencing. We anticipate that potential installation of these delivery systems in the tumor microenvironment can exploit the naturally increased ATP levels to induce selective delivery of therapeutic oligonucleotides.

6.1 Introduction

An overarching goal in cancer research is to develop selective agents for targeting cancer cells while minimizing collateral damage to the surrounding healthy tissue. To this end, currently used strategies interfere with critical intracellular mechanisms particularly those involved in cellular metabolism, gene regulation, cell proliferation, some drugs directly interact with DNA.[1,2] The second limitation is imposed by the efficient delivery of these drugs to the intracellular targets. As a result of which, a considerable effort has been devoted towards investigating strategies to enhance cell penetration. This includes the use of nanomaterials to encapsulate drugs[3,4] and facilitate their delivery via passive diffusion and/or use of electrical membrane disruption (chemotherapy)[5].

Two alternative and potentially less invasive approaches include (i) direct modulation of the extracellular components (such as ATP) of tumor microenvironment (TME) to promote immune response (immunotherapy) or suppress tumor growth or (ii) utilization of natural transmembrane transport mechanisms of cell to move anticancer drugs to the cell interior[6,7].

ATP is recognized as one of the main biochemical components of TME with concentrations detected in the range of 50-200 µM. Depending on its concentration in the extracellular space and the presence of ecto-nucleotidases (ATP-hydrolyzing enzymes) and receptors expressed by cancer and immune cells, ATP can either promote tumor cell proliferation or trigger tumor suppression.[8] With increased understanding of such information exchange in TME, new therapeutic approaches are developed to directly target extracellular ATP (eATP) in TME. Such increased ATP levels in TME also open up possibilities to use ATP as a natural trigger for selective drug delivery from the extracellular environment to the diseased tissues. This requires a biocompatible delivery system that can release drug molecules of choice in response to ATP.

Towards this, we designed an ATP-fueled DNA delivery system that transiently releases a Signal (DNA) strand into the extracellular media of cancer cells. The delivery system is composed of an ATP-driven enzymatic reaction network (ERN) and a microgel (MG) particle bearing the Signal strand to be delivered to the target cells. The appropriate modification of Signal strand with a fluorophore enables their uptake within cells and allows to monitor the uptake process via confocal laser scanning microscopy (CLSM, both qualitatively and quantitatively). Signal strands are initially immobilized (non-covalently) on an MG particle to prevent any non-specific internalization by cells. Once ATP reaches suboptimal amounts in the extracellular medium, the ATP-ERN resets the entire delivery system to its initial state which involves recapturing of the excess Signal strands by the particle. This allows to deliver controlled amounts of Signal strand in an ATP-dependent fashion.

Essentially the strategy offers a model approach to deliver therapeutic oligonucleotides (such as anti-sense oligonucleotides (ODNs),[9] siRNAs,[10] miRNAs,[11] or DNA-peptide conjugates[12]) to control cell physiology and providing aid in gene therapy and gene silencing. Direct integration of the proposed delivery system with eATP in the TME can provide a potential approach to deliver therapeutic oligonucleotides to diseased tissues. Critically, such an ATP-driven system actively consumes the ATP and offers routes for self-regulating delivery that adapts to the levels of ATP in the TME.

6.2 Results and Discussion

6.2.1 System design for controlled delivery of DNA in living cells via ATP-fueled reaction network.

The entire system can be divided into three different layers. Layer 1 contains an ATP-fueled ERN which operates on the molecular level and functions as a control program for the transient release of Signal from a Particle in Layer 2 and uptake of Signal by living cells in Layer 3. Both Layers 2 and 3 operate at the structural level.

Layer 1: The upstream ERN in its initial deactivated State A is composed of two double-stranded (ds) complexes (Complex 1 and Substrate 1) and two single stranded DNAs (ssDNA; Input 1 and Input 2) as shown in **Figure 6-1**. In this state, Input 1 and Input 2 are incapable of kicking out Output from Substrate 1 due to unstable hybridization of Input 1 (melting temperature (T_m) = 32 °C < experimental temperature (T_{exp}) = 37 °C, determined by NUPACK[13]) and Input 2 (T_m = 22 °C < T_{exp} = 37 °C) with the longer strand of Substrate 1. However, the addition of ATP powers the covalent ligation of Substrate 1 with two molecules of Complex 1 (4 equivalents used with respect to Substrate 1) and one molecule each of Input 1 and Input 2 with the help of T4 DNA ligase, generating Intermediate 1. The system is pushed towards an activated transient state, where the chain migration from two sides provides a strong thermodynamic push to release Output from Intermediate 1, finally generating Intermediate 2. The dual inversion strategy is essential for releasing an Output strand long enough to displace Signal strand in Layer 2.[14,15] Concurrently, BsaI cleaves Intermediate 2 to regenerate Complex 1 and Intermediate 3. Because of the low T_m (32 °C < T_{exp} = 37 °C), Intermediate 3 dissociates into Input 1 and Input 2, and reproduces Substrate 1 after re-hybridization with Output returning the system back to State A. Faster ligation than cleavage (**Supplementary Note 6.4.3.1**) satisfies the kinetic boundary conditions required for the system to achieve a dynamic steady state with an ATP-dependent lifetime before the restriction overtakes and brings the system back to its initial

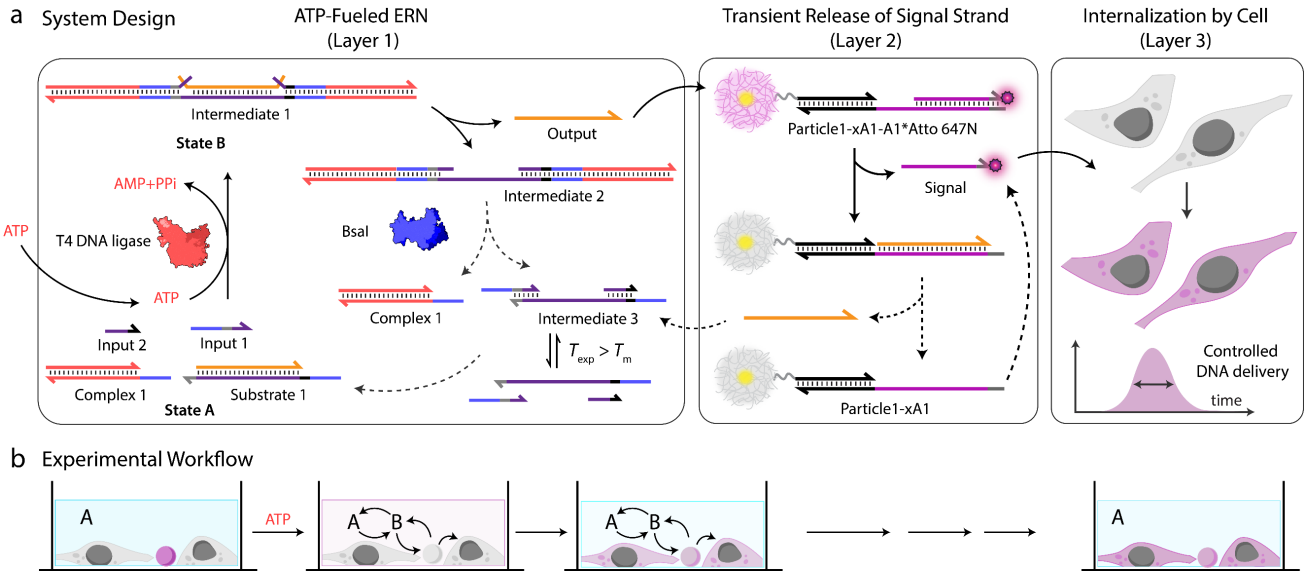

Figure 6-1. System design for controlled delivery of DNA in living cells via out-of-equilibrium extracellular medium.

state. Output is therefore generated in an uphill fashion and is transiently available in the system to perform downstream functions before its ultimately reassociated within Substrate 1.

Layer 2: The transiently released Output displaces the Signal strand from Particle1 in a dissipative manner. The ATP-dependence of Layer 1 is indirectly linked to the Layer 2 because once restriction overtakes ligation, Output prefers to regenerate Substrate 1 rather than residing within Particle1. As a result, Particle1 is again available for Signal strand which reforms the initial state of the system. The lifetime and amount of Signal strand released in the dynamic steady state depends not only on the ATP concentration but is also limited by the transient Output yield.

Layer 3: Signal strand released from Layer 2 is designed to be internalized by living cells. This indeed causes uptake of DNA in the cytoplasm of the cells. The percentage amount and release kinetics of Signal strand can essentially be controlled via Layer 1 and 2 operating upstream to Layer 3.

6.2.2 Dye selection to enable cellular uptake and monitoring oligonucleotide delivery in living cells.

We first designed a Signal strand that is able to cross the cell membrane to enter cell cytoplasm in experimentally detectable amounts. Regardless of the anionic nature of DNA, DNA-nanodevices are shown to enter cells with decent efficiency, particularly when additional modifications are present to enhance uptake or increase stability.[16-18] For instance, insertion of a fluorophore in DNA (nucleobase, backbone, 3'- and 5'-end modifications) can reduce nuclease degradation and enhance cellular uptake while providing a visual aid for DNA uptake and location within cells via fluorescence-based assays.[19]

Therefore, we first screened appropriately modified DNA strands for their successful internalization into cells, more specifically HeLa Cells. The Signal strand labeled with the corresponding fluorophore (Atto 647N/Cy5/Atto 488, Supplementary Table S2) was added to insulin-transferrin-selenium (ITS)-containing media (Cell buffer) of HeLa cells (**Figure 6-2**). Replacing commonly used fetal bovine serum (FBS)-containing cell culture medium with ITS-containing medium maintains DNA stability at least in the cell environment. This is because nucleases contained in FBS can cause degradation of DNA.[20]

We incubated HeLa cells with the respective Signal strand at 1 µM and 5 µM followed by their comparison with confocal laser scanning microscopy (CLSM, **Figure 6-2a, Figure 6-5**). The uptake kinetics were overall faster for the higher concentration (5 µM) of Atto 647N/Cy5-labeled Signal strand (**Figure 6-5b,d**). Within 2 h of incubation, the fluorescent signal within the cells increased to 115 times for 1 µM and 137 times for 5 µM of Atto 647N-labeled Signal strand as compared to its initial value (**Figure 6-5a,b**). At the same time point, the fluorescence increase (88 times for 1 µM and 128 times for 5 µM of Signal strand) for Cy5-labeled Signal strands was comparatively less (**Figure 6-5c,d**). For the final time point of 20 h, cells incubated with 1 µM Atto 647N-labeled Signal strands demonstrated a final 290 fold increase in fluorescence. In contrast, the Cy5-labeled Signal strand (1 µM) only led to a 120 fold increase of its initial value. Both dye modifications clearly localize the DNA strand to the elongated mitochondria resulting in long filamentous fluorescent signals.[19] In contrast, no internalization was observed for a Atto 488-labeled Signal strand, even after 20 h of incubation with the cells (**Figure 6-5e**, **Figure 6-2b**).

Differences in the uptake can be explained as follows: The lipophilic nature of the cytoplasmic membrane enables the passage of lipophilic molecules through the barrier, but only specific transport systems can mediate and regulate the entry of hydrophilic substances. Lipophilic molecules such as cyanine dyes, carbopyronine-based dyes, and some Alexa dyes are known to diffuse readily across the cell membrane.[21,22] The above facts explain the successful internalization of both Atto 647N and Cy5-labeled Signal strands. Atto 647N has a carbopyronine core and Cy5 belongs to the cyanine family which is why the respective Signal strands penetrate the cell membrane. In contrast, the strongly hydrophilic and negatively charged Atto 488

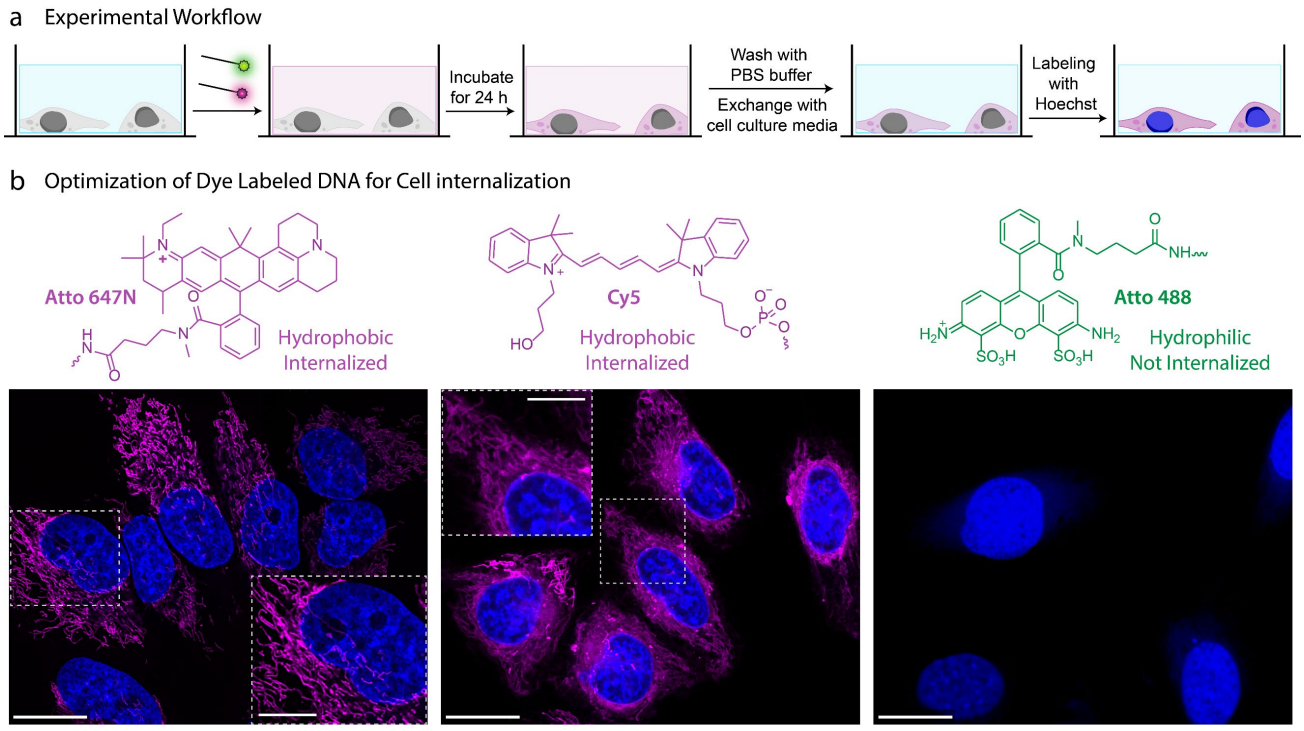

Figure 6-2. Screening of different dye labelled A1* (Signal) strand for internalization in living HeLa cells. (a) Schematic representation of the experimental workflow where HeLa cells are incubated with respective Signal strands in DNA-Cell buffer for 24 h after which the medium is exchanged with PBS buffer and cells are stained with Hoechst (nucleus staining dye). (b) Final CLSM images acquired after the final step in (a) for samples containing (from left to right) Atto 647N, Cy5 and Atto 488 modified Signal strands. Experimental conditions: HeLa cells at a concentration of 10^4 cells/mL incubated in DNA-Cell buffer at 37 °C with 1 µM of respective dye labelled A1* (Signal) strand. Hoechst added following the guidelines of the supplier. Scale bars: (b) 20 µm, inset 10 µm.

dye is repelled by the negatively charged, hydrophobic tails of the phospholipid bilayer and cannot easily enter the cell.[23] This means that regardless of the strongly anionic nature of the 20 nucleotide (nt) long Signal strand, appropriate dye modification can effectively modulate internalization behavior across cell membrane.

With this, we standardized a fluorophore labeled Signal strand which can successfully enter cells in appreciable amounts within only 2 h of incubation. We used Atto 647N-labeled Signal for further experiments because of the (i) two-fold higher uptake as compared to Cy5-labeled Signal strands and (ii) better photostability and quantum efficiency of Atto 647N.[24] Using Atto 647N-labeled Signal strand, we designed a two-layer upstream network which transiently releases Signal strand at a rate matching the kinetics of cell internalization.

6.2.3 Extracellular two-layer reaction network for transient release of Signal

After finding the appropriate Signal strand to be introduced into the cells, we non-covalently immobilized it on a particle. This constitutes Layer 2 of the network and is later coupled to ATP-fueled Layer 1. The immobilization of Signal on the particle serves two purposes: first, it prevents unwanted internalization ensuring on-demand release and availability in the medium, and second, after the fuel is consumed i.e., after completion of the cycle, non-internalized Signal will be recovered by the particle. The particles thus also assist in recapture and analysis of the system.

For this, we employed DNA-functionalized micron-sized core-shell MGs as they are well dispersible in aqueous medium and can be functionalized within their hydrogel shell.[25,26] The core is composed of a brightly fluorescent hydrophobic material ($\langle R_h \rangle_z \approx 230$ nm, synthesis in Experimental section **6.4.2.1**). The shell contains a lightly crosslinked PNIPAM-*co*-AA hydrogel constituting 95.6 wt% of the MG (84.2 wt% N-isopropylacrylamide (NIPAM); 10.4 wt% acrylic acid (AA); 1 wt% N,N'- methylenebis(acrylamide) (MBA), synthesis in Experimental section **6.4.2.2**). The core-shell MGs have a total $\langle R_h \rangle_z \approx 2.3$ µm and can be well

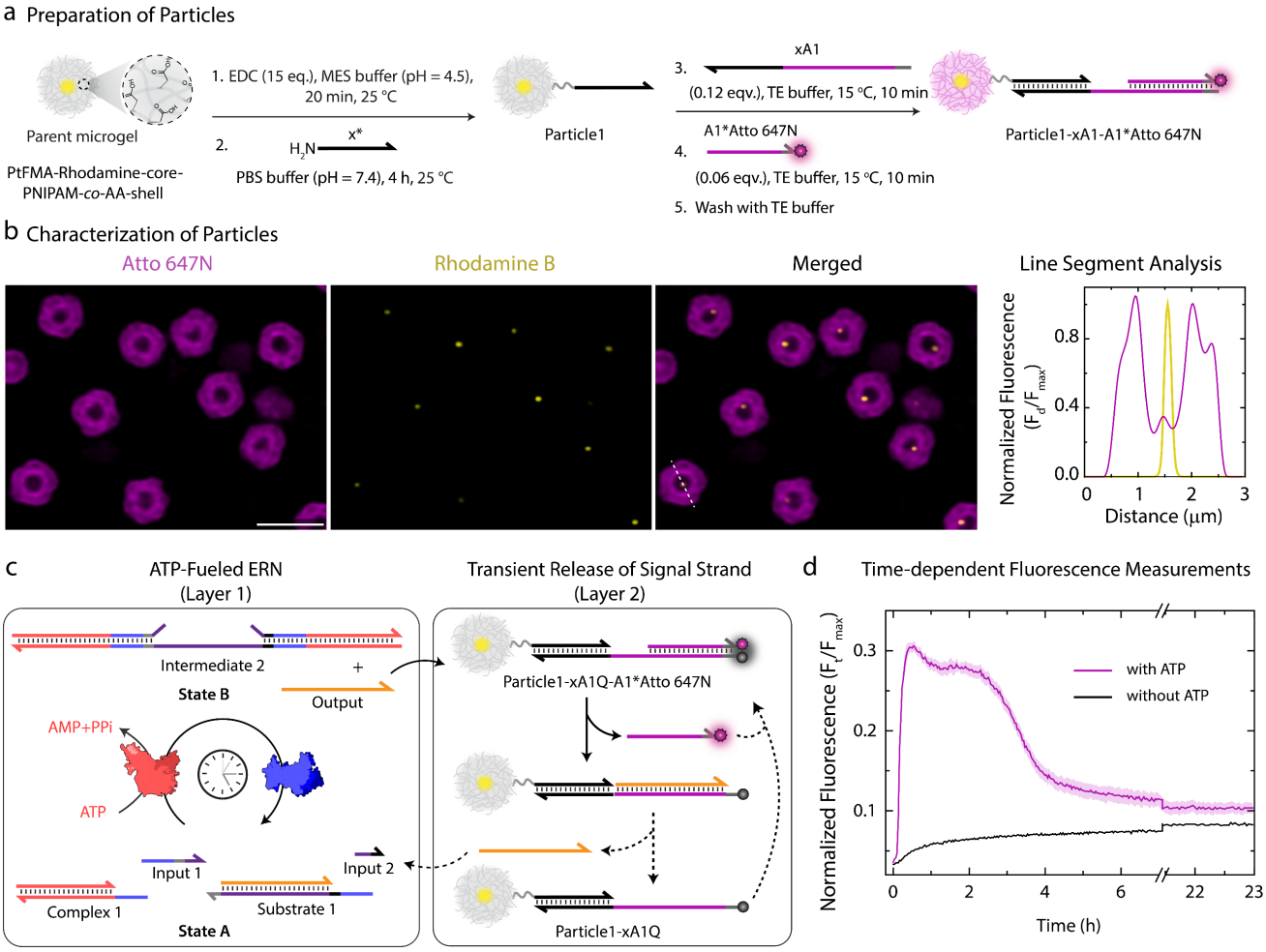

Figure 6-3. Preparation of DNA-functionalized MGs for transient release of Signal strand. (a) Schematics depicting step wise preparation of Particle1-xA1-A1*Atto 647N from a parent MG. The first step involves covalent functionalization of DNA and consequent annealing with xA1and A1*Atto 647N. (b) The final step is monitored with CLSM imaging and particles are quantitatively analyzed by line segment analysis. Experimental conditions: Particle1-xA1-A1*Atto 647N suspended in TE buffer (pH = 8.0) at a final concentration of 0.05 wt%, to which 7.5 µM of xA1 (0.12 equiv. with respect to functionalized DNA) and 3.75 µM of A1*Atto 647N (0.06 equiv. with respect to functionalized DNA) annealing strands are added at 15 °C. (c) Schematic representation of the transient release of Signal strand from Particle1-xA1Q-A1*Atto 647N via ATP-fueled ERN. (d) Time dependent FI changes demonstrating transient increase of fluorescence because of Signal strand release into the medium upon ATP addition. The results are normalized with respect to 3.75 µM of A1*Atto 647N (Signal) strands dissolved in DNA-Cell buffer which corresponds to the maximum fluorescence that can be observed in the system. The results represent an average contribution from two measurements and shaded region depict the standard deviation (SD). Experimental conditions: Particle1-xA1Q-A1*Atto 647N is employed for checking FI changes by using xA1Q instead of xA1 while keeping all conditions for annealing same as (a), (b). Particle1-xA1Q-A1*Atto 647N is suspended in DNA-Cell buffer at a final MG concentration of 0.05 wt% containing 20 µM Complex 1, 5 µM Substrate 1, 10 µM Input 1 and Input 2, 0.8 WU μL^{-1} of T4 DNA ligase and 0.8 U μL^{-1} of BsaI at 37 °C fueled by 40 µM ATP (b, d). Scale bars: (b) 3 µm.

visualized in CLSM (**Figure 6-3**, and **Figure 6-6**). The AA groups in the shell allow functionalization by EDC-mediated coupling with NH_2-ssDNA (**Figure 6-3a**, synthesis in Experimental section **6.4.2.3**; NH_2-x* and NH_2-z*; EDC = 1-Ethyl-3-(3-dimethylaminopropyl)carbodiimide = 25 equiv. with respect to COOH groups on MG), leading to a typical DNA grafting density of 3.3×10^6 strands per MG or 132 ± 5 µmol strands per g of MG (**Figure 6-7**). Due to the strong negative zeta potential of MGs (ζ = -18 ± 2 mV), no MG internalization is observed within cells after 24 h of incubation (**Figure 6-8**).

The Signal strand is immobilized on Particle1 with the help of a Linking strand (xA1). By using NH_2-ssDNA, we first prepared an x*-functionalized Particle1. At a final concentration of 0.05 wt%, Particle1 was incubated with 0.12 equivalents (equiv.) of complementary Linker strand (xA1, 7.5 µM). A1 domain now available on Particle1 through Linker strand allows to assemble 0.06 equiv. (3.75 µM) of Signal strand (A1*Atto 647N) on

Particle1. CLSM images confirm the successful functionalization of Linker and Atto 647N-labeled Signal strand as Particle1 turn fluorescent (**Figure 6-3b**). This strategy offers easy tuning of the amount of Signal strands on Particle1.

Next, we coupled Signal-functionalized Particle1 to an ATP-fueled ERN to control the transient release of Signal in a dissipative fashion (**Figure 6-3c**). For the successful functioning of the system at Layer 1 and Layer 2, two conditions are mandatory: (1) In the Initial State, Output must remain bound within Substrate 1 without showing crosstalk with Particle1-xA1Q-A1*Atto 647N. This condition is also essential for the system to regenerate Substrate 1 and return back to Initial State after consumption of ATP. Overall, the hybridization of Output within Substrate 1 should be more favorable than formation of Particle1-xA1Q-Output in Initial State; (2) In State B (ATP-fueled), displacement of Signal by Output and formation of Particle1-xA1Q-Output must be more favorable than its tendency to remain bound within Intermediate 1. A traditional DNA strand displacement reaction between Output and Particle1-xA1Q-A1*Atto 647N would have not allowed the return of Initial State because of the extra energy gained from 3 extra base pairs during the formation of Particle1-xA1Q-Output (**Figure 6-9**). However, in the presence of ATP-dependent Layer 1, Output is only favored to interact with Particle1-xA1Q-A1*Atto 647N when longer strand of Substrate 1 is involved in Intermediate 1. As soon as the longer strand of Substrate 1 dissociates from Intermediate 3, Output prefers to reside within Substrate 1 rather than staying bound on Particle1 as Particle1-xA1Q-Output.

Experimentally, ATP-fueled ERNs are optimized to operate at maximum efficiency in 1X Cut Smart buffer prepared in MilliQ water.[15,27] But Layer 1 and Layer 2 in this system will be finally combined and installed in the cell culture media (Cell buffer) of HeLa cells which is critical for cell growth and sustainability (Layer 3). The main challenge at this point is to find the right compromise between these two completely different media conditions so that neither cell viability nor ERN performance is affected. For this, we simply prepared the 1X Cut Smart buffer in Cell buffer (instead of using MilliQ water) and term it DNA-Cell buffer. First, we checked the performance of Layer1 and Layer 2 in DNA-Cell buffer.

To be able to track the process of transient Signal release with time-dependent fluorescence intensity (FI) changes, we used a quencher-labeled Linker (xA1*Q). With the designed Particle1-xA1Q-A1*Atto 647N at a concentration of 0.05 wt%, we combined Layer 1 and Layer 2 together in DNA-Cell buffer at 37 °C with 20 µM Complex 1, 5 µM Substrate 1, 5 µM A1-Atto 488 and A2-Atto 647N, 10 µM Input 1 and Input 2 using 0.8 Weiss units (WU) μL^{-1} of T4 DNA ligase and 0.8 units (U) μL^{-1} of BsaI. Due to close proximity between fluorophore of Signal strand and quencher of Linker strand in the assembled complex on Particle1-xA1Q-A1*Atto 647N, the initial fluorescence is low (**Figure 6-3d**).The ERN was initiated by ATP addition, which immediately resulted in an increase in FI by~30% signifying the dissociation of FRET pair between Signal and Linker strand in Particle1-xA1Q-A1*Atto 647N and release of free Signal. Subsequently, once BsaI-controlled restriction takes over, the Output, temporarily functionalized on Particle1-xA1Q-Output, returns back to Layer 1 reforming Initial State A. This makes Particle1-xA1Q available for Signal again causing the ultimate drop of FI. Through NUPACK simulations, we found that mixing Output (5 µM) with NH_2-x (7.5 µM), xA1Q (7.5 µM) and A1*Atto 647N (3.75 µM) releases 3.5 µM (94%) of free Signal strand (**Figure 6-9**). From this we can conclude that fueling the system with 40 µM ATP furnishes ~1.47 µM (39%) of Signal strand (check **Figure 6-10** for detailed explanation). The dynamic steady state with ~1.47 µM of Signal strands sustains for 2.5 h. This transient concentration of Signal strand is sufficiently enough to saturate cells within 2.5 h of its lifetime as checked previously (**Figure 6-2**, **Figure 6-5**). A minimal increase of ~6% in the absence of ATP is caused by unavoidable leakage between Substrate 1 and Particle1-xA1Q-A1*Atto 647N (**Figure 6-9**), however this increase in fluorescence is slow and insufficient to cause any observable cellular internalization.

6.2.4 Out-of-equilibrium extracellular medium controls cellular internalization.

Until now we have separately shown the successful internalization of fluorophore-labeled Signal strand in HeLa cells (Layer 3) and its transient release from Particle1 via ATP-fueled network (Layer 1 and Layer 2). We finally combined all three Layers together and installed Layer 1 and Layer 2 in the extracellular medium of HeLa cells (**Figure 6-4a**).

We decided to probe the controlled delivery of Signal strand (A1*Atto 647 N) in cells using CLSM microscopy (**Figure 6-4**). Towards this, we prepared Particle1-xA1-A1*Atto 647N by annealing xA1 (Linker strand) and Signal strand on Particle1. We did not use any quencher on Linker strand as this will allow us to qualitatively track the transfer of Signal strands from Particle1-xA1-A1*Atto 647N to the cells all the way through the medium upon ATP addition. With the prepared Particle in hand, we integrated the ATP-fueled ERN (Layer 1) with Layer 2 by combining 20 µM Complex 1, 5 µM Substrate 1, 10 µM Input 1 and Input 2, 0.8 WU μL^{-1} of T4

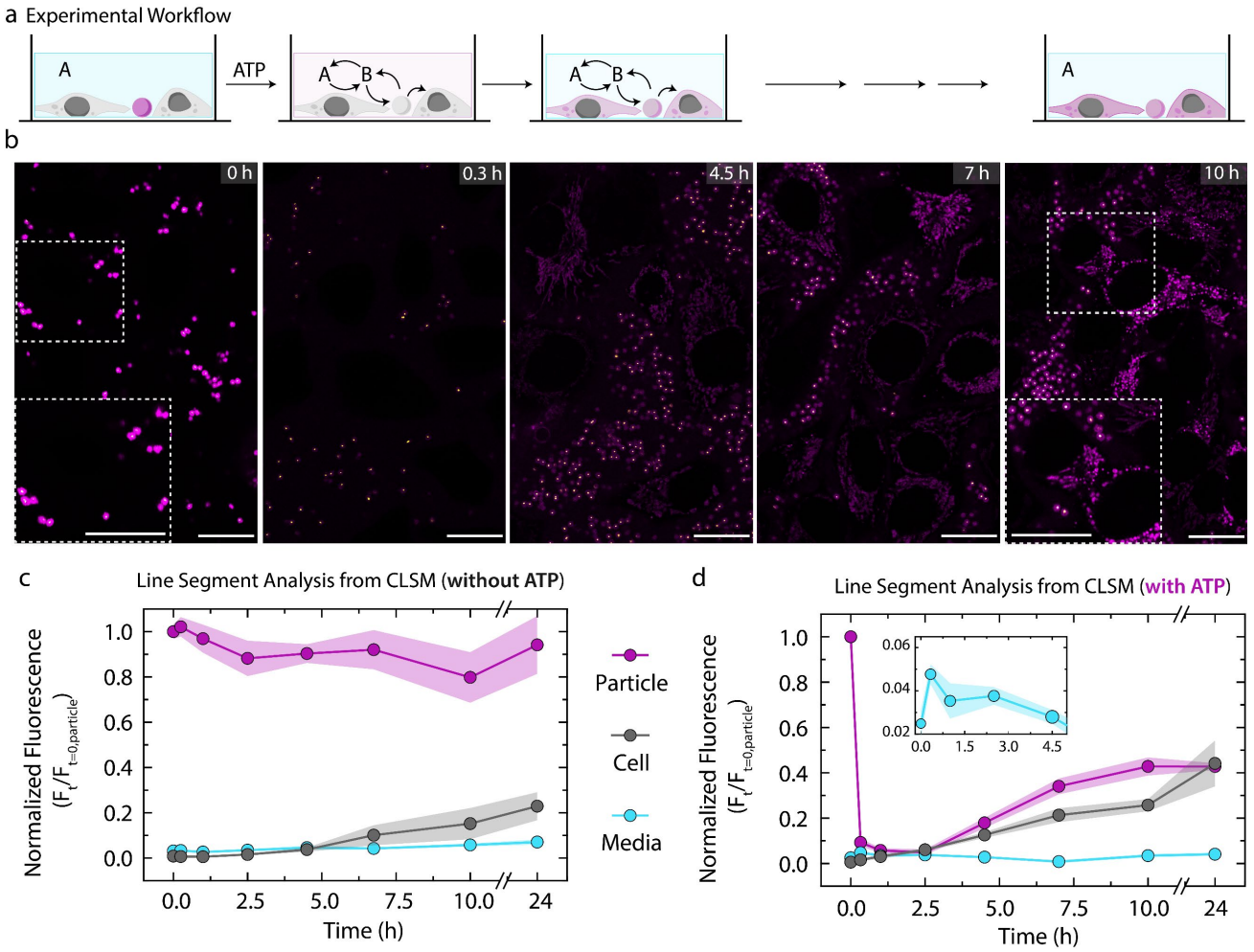

Figure 6-4. Out-of-equilibrium extracellular medium controls cellular internalization. (a) Schematic representation of the experimental workflow where Layer1 and Layer2 are installed within the extracellular medium of cells marked by the initial State A. State B is acquired upon ATP addition which marks the transient release of Signal strands from particle into the medium to be uptaken by cells. (b) CLSM imaging of the controlled delivery of Signal strands into living cells through out-of-equilibrium extracellular medium. (c), (d) Time-dependent FI changes on the particle, in the medium and within cells without ATP (c) and with ATP addition (d). The inset in (d) shows the zoomed in region of FI changes in media. The fluorescence values represent the maximum intensity acquired from the line segment analysis and normalized with respect to maximum fluorescence observed on the particle. The results represent an average contribution from 5 different regions. The shaded region in (c), (d) depict the SD. Experimental conditions: Particle1-xA1-A1*Atto 647N suspended in DNA-Cell buffer at a final MG concentration of 0.05 wt% containing 20 µM Complex 1, 5 µM Substrate 1, 10 µM Input 1 and Input 2, 0.8 WU μL^{-1} of T4 DNA ligase and 0.8 U μL^{-1} of BsaI and HeLa cells at a concentration of 10^4 cells/mL incubated together at 37 °C and fueled by 40 µM ATP (b, d). Scale bars: (b) 20 µm.

DNA ligase and 0.8 units (U) μL^{-1} of BsaI with Particle1-xA1-A1*Atto 647N at a concentration of 0.05 wt%. Before adding ATP, MG shows high fluorescence because all Signal strands are bound on the MG. Moreover, no fluorescence can be detected within the cells (**Figure 6-11, Figure 6-4c**).

However, within 18 minutes of ATP addition, FI on the particle decreases by 90% also causing an increase in the FI of the medium which in fact attains the maximum fluorescence value (**Figure 6-4d**). By the next 2.5 h, MG fluorescence continues to decrease reaching a minimum point with FI change of 95%. But the medium fluorescence instead of increasing further, starts to decrease already. This clearly indicates that during this time, the internalization of Signal strands within cells has begun, also marked by the increase in their FI change. Beyond this point, particles begin to recover their fluorescence by recapturing the excess Signal strands. A partial recovery of only 37% in fluorescence intensity on particle confirms the partial internalization of Signal strands by the cells. Upon comparing the fluorescence decrease on the particle with the fluorescence increase of the medium at 24 h of ATP addition, we estimated the amount of Signal strand internalized within the cells during this time to be 2.06 µM or 1.24×10^{11} Signal strands per cell (check **Figure 6-13** for further details).

We also measured the viability of living cells during the experiment at different time points (**Figure 6-12**). When cells are incubated with all components of ATP-ERN and Particle1-xA1-A1*Atto 647N in DNA-Cell buffer, a cell viability of 92% is observed before adding ATP which remains the same for next 7 h, and decreases to 85% after 24 h (**Figure 6-12a**). A total loss of 7% in cell viability is observed over 24 h (**Figure 6-4c, Figure 6-12**). Furthermore, for the system where ATP is introduced, an overall decrease of only 12% is observed after 24 h (**Figure 6-12b**).

6.3 Conclusion

In summary, we have demonstrated a design strategy to program an out-of-equilibrium extracellular medium of living cells for ATP-induced release of fluorophore labeled DNA. Two layers are combined to form the extracellular medium and the cells themselves form the third layer. An ATP-fueled ERN (Layer 1), which acts as the control program of the system transiently releases an invading strand (Output) which further displaces a Signal strand functionalized on a particle (Layer 2). The Signal strand is specifically designed to be taken up by cells. The dissipative nature of the upstream ATP-fueled ERN enables the restoration of the system's initial state once the fuel is depleted. The transient availability of Signal strand provides greater control in terms of quantity and timing of release. The medium is customized to maintain the stability of all DNA-based components used to prepare the first two layers without affecting cell viability. The fact that particles tend to recapture Signal strands after ATP consumption proves the successful functioning of the network and the survival of all DNA strands even after 24 h.

Since the rate of DNA uptake by the cells cannot be controlled (without taking any extensive measures), the rate of DNA release from the upstream network is instead programmed to match the uptake kinetics. The strategy can therefore be used to deliver DNA to other cell lines. Furthermore, due to modularity of our design, therapeutic oligos such as siRNA, miRNA and antisense oligos can be delivered into cells to enable advanced applications in gene therapy and gene silencing.

We observed that 40 µM ATP is sufficient to transfer 1.24×10^{11} Signal strands per cell. We anticipate that installation of these delivery systems in the TME, where eATP concentrations of 50-200 µM have been detected, may provide a versatile and selective approach to deliver DNA/RNA to the diseased tissues.[28,29] Critically, such an ATP-driven system actively consumes the ATP and offers routes for self-regulating delivery that adapts to the levels of ATP in the TME.

6.4 Experimental

6.4.1 Materials

All chemicals and reagents were purchased from Sigma Aldrich or Merck and used without further purification unless otherwise stated:

2,2,2-trifluoroethyl methacrylate (ABCR GMBH, 99 %), N-isopropylacrylamide (97 %), 2,2'-azobis(2-methylpropionamidine) dihydrochloride (ABCR GMBH, 96 %), N,N'-methylenebis(acrylamide) (99%), divinylbenzene (DVB, 80 %), acryloxyethyl thiocarbamoyl Rhodamine B (POLYSCIENCES, INC.), Al_2O_3 90 neutral (CARL ROTH GMBH), 1-Ethyl-3-(3-dimethylaminopropyl)carbodiimide (ABCR GMBH, 98 %), potassium persulfate (≥99 %), acrylic acid (Acros Organics, 99.5 %), disodium ethylenediaminetetraacetate dehydrate (biology grade), tris(hydroxymethyl)aminomethane hydrochloride (Trizma buffer substance pH=8), 2-(N-morpholino) ethanesulfonic acid, sodium chloride (99 %), magnesium chloride (99 %), phosphate buffered saline (PBS, pH = 7.4), Hoechst 34580 (Thermo Fisher, 98%), CellMask™ green plasma membrane dye (Thermo Fisher, 98%).

T4 DNA Ligase Storage Buffer (Promega): 10 mM Tris-HCl (pH 7.4 at 25 °C), 50 mM KCl, 1 mM dithiothreitol (DTT), 0.1 mM EDTA, 50 % glycerol.

BsaI-HF® v2 storage buffer (NEB): 10 mM Tris-HCl, 200 mM NaCl, 1 mM DTT, 0.1 mM EDTA, 200 µg/mL BSA, 50% glycerol.

1X NEB CutSmart® Buffer: 50 mM potassium acetate, 20 mM Tris-acetate, 10 mM magnesium acetate, 100 µg mL-1 BSA. Annealing Buffer: 10 mM Tris-HCl (pH 8.0), 50 mM NaCl, 10 mM $MgCl_2$.

Cell Culture media: HeLa cell line (provided by ATCC) were cultured and maintained in Dulbecco's MEM Eagle (containing Earle's Balanced Salt Solution, with stable glutamine, 2.2 g/L $NaHCO_3$, PAN Biotech) supplemented with 10 % fetal bovine serum and 1% penicillin/streptomycin. Incubation of cell line was done at 37 °C in 5% CO_2 atmosphere with 95% humidity. Serum free media supplemented by 10% Insulin-Transferrin-Selenium (***Cell buffer***) was used as we suspect that nucleases in the fetal bovine serum can negatively affect our reaction.

Only before the experiment, ***Cell Culture media*** was exchanged with ***Cell buffer***. Cells were thereafter incubated overnight at 37 °C in 5% CO_2 atmosphere with 95% humidity before using them for further experiments.

Cell buffer: 10% Insulin-Transferrin-Selenium (ITS-G, 100X, Gibco™), 1% MEM NEAA (Non Essential Amino Acid Solution, 100X, without L-Glutamine, PAN Biotech), 1% ROTI®Cell HEPES solution (1 M, Carl Roth), 1% Penicillin-Streptomycin (5000 U/mL, Gibco™) in MEM Eagle containing: EBSS (Earle's Balanced Salt Solution), stable glutamine, 2.2 g/L $NaHCO_3$ (PAN Bitoech).

DNA-Cell buffer: 1X *NEB* CutSmart® Buffer in Cell buffer.

MilliQ water was used throughout all experiments unless otherwise stated.

All oligonucleotides (except amine-modified oligonucleotides) were purchased from Integrated DNA Technologies Inc. (IDT) and Biomers GmbH (as listed below in Table S1). The oligonucleotides as received were dissolved in 1X TE buffer, pH = 8.0 (Thermo Fischer). Amine-modified oligonucleotides were synthesized following a well-defined procedure (as described in **Experimental section 6.4.2.4**).

General Characterization Methods and Instruments

DLS measurements were performed on the LS Instruments NanoLab 3D at 25 °C operating with a red laser (λ = 685 nm) and a scattering angle of Θ = 90 ° using standard disposable PS cuvettes (BRAND GmbH & Co. KG). The distributions of the hydrodynamic radii were obtained by a CONTIN mode analysis.

Zeta-Potential (ζ-potential) of microgels was measured using a Zetasizer Nano ZS (Malvern Panalytical) at 25 °C. All samples were measured in triplicate in disposable folded capillary cells.

Fluorescence and Brightfield Microscopy was performed on EVOS™ M7000 Imaging System equipped with DAPI, GFP, RFP and Cy5 filter cubes using 4×, 20×, and 40× objectives.

Confocal laser scanning microscopy (CLSM) was performed on Leica Stellaris 5 microscope (LasX v4.3.0.24308) with four laser lines and three HyD S detectors using plan-apochromat objectives (63×, 1.40 numerical aperture, oil immersion).

DNA concentrations were determined using a DeNovix-S-06873 (DeNovix OS 0.8.1 v4.1.5) spectrophotometer with a standard value of 33 µg/OD_{260}.

The temperature-controlled fluorescence measurements were performed on a TECAN (SPARK control v3.1) microplate plate reader using Corning® 384-Well black polystyrene plate with non-binding surface. Excitation and emission wavelengths for Atto 488 are 485 nm and 535 nm and for Atto 647N are 620 nm and 679 nm respectively.

***p* values** were calculated by performing a t-Test (Two-Sample Assuming Equal Variances) in Microsoft excel using a built-in Data analysis tool pack.

The amine-modified oligonucleotides were synthesized on a H-8 custom LNA, DNA/RNA automatic synthesizer from K&A Laborgeräte. The synthesized oligonucleotides were purified by **High Performance Liquid Chromatography (HPLC)** on a Dionex Ultimate 3000 (Thermo Fischer Scientific).

6.4.2 Methods

6.4.2.1 Synthesis of surfactant-free, poly(2,2,2-trifluoroethyl methacrylate)-Rhodamine labeled core particles.

The synthesis is analogous to a previous report.[25,30] Divinylbenzene (DVB) and 2,2,2-trifluoroethyl methacrylate (tFMA) were purified using column chromatography (Al_2O_3, neutral). The initiator potassium persulfate (KPS, 159.49 mg, 590 µmol) was dissolved in deionized water (45 mL), degassed by bubbling with nitrogen gas (25 min) and thermostated at 70 °C for 15 min. To a solution of DVB (46.2 mg, 354.9 µmol) and tFMA (1.98 g, 11.8 mmol), a solution of acryloxyethyl thiocarbamoyl Rhodamine B (1 mg) and N-isopropylacrylamide (NIPAM, 150 mg, 1.3 mmol) in water (4.5 mL) was added. The mixture was ultrasonicated for 2 minutes and degassed by bubbling with nitrogen gas (10 min). The resulting mixture was added dropwise (over a period of 5 min) to the initiator solution starting the polymerization. The reaction mixture was stirred at 70 °C for 6 h (stirring rate = 600 rpm). The resulting dispersion was filtered while hot and dialyzed against deionized water (MWCO 8000 Da; solid content = 35.6 mg/mL by freeze-drying).

6.4.2.2 Synthesis of the PNIPAM shell to yield PtFMA-Rhodamine labelled-core-PNIPAM-co-GMA-shell microgel (MGs) particles.

The reaction conditions was adapted from a previous report[31]: NIPAM (3.37 g, 29.8 mmol, 84.2 wt %) was dissolved in deionized water (100 mL) together with co-monomer acrylic acid (AA, 418 mg, 398 µL, 5.8 mmol, 10.4 wt%), and the cross-linker *N*,*N*'-methylenebis(acrylamide) (MBA, 41.8 mg, 271 µmol, 1 wt %). The core particles (4.2 mL, 77 mg/mL, 170 mg solid content, 4.25 wt %) were added and the mixture was degassed for 30 min and heated to 45 °C. The initiator KPS (76.2 mg, 0.28 mmol) was dissolved in water (30 mL) and degassed (15 min). The polymerization was initiated by dropwise addition of initiator solution to a heated

reaction mixture and stirred (stirring rate = 450 rpm). Immediately following initiation, a temperature ramp from 45 to 65 °C was applied to the solution at an approximate ramp rate of 20 °C/h. The stirring rate was increased to 600 rpm and reaction was allowed to run for 4 hours. The resulting core/shell MG particles (amount of AA moieties assuming full conversion = 1450 µmol per g of MG) were filtered while hot and purified by dialysis (MWCO 8000 Da) against deionized water. The resulting core-shell MGs were further purified via centrifugation (5 × 25 min, 11000 rpm, 15 °C, replacement of the supernatant with Milli Q water per centrifugation step).

6.4.2.3 Functionalization of MG with amine-modified DNA.

The MG suspension was redispersed in 2-(N-morpholino)ethanesulfonic acid (MES) buffer (10 mM, pH = 4.5) via centrifugation (20 min, 9000 rpm, 15 °C, replacement of the supernatant with MES buffer). A two-step reaction achieves the functionalization of DNA on MGs. In the first step, activation of carboxyl acid groups in MG shell (120 µL, 1.943 mg/mL of MGs, 0.34 µmol of COOH groups) was carried out by stirring with EDC (1.1 mg, 7.2 µmol, 25 equiv. with respect to COOH groups) dissolved in 40 µL of MES buffer (10 mM MES, pH = 4.5) for 12 minutes at 25 °C. Finally, amine-modified DNA (0.08 µmol, 0.23 equiv.) dispersed in 350 µL PBS buffer (pH = 7.4) was added to activated MGs prepared in first step and the mixture was stirred for 4.5 h at 25 °C. The DNA functionalized MGs were purified via centrifugation (2 × 3 min, 8000 rpm, 25 °C, replacement of the supernatant with TE buffer (pH = 8.0), per centrifugation step).

6.4.2.4 Synthesis and purification of amine-modified oligonucleotide sequences.

The oligonucleotides were synthesized at 10 µmol scale employing the standard solid phase β-cyanoethyl-phosphoramidite chemistry in trityl-on mode. The DNA phosphoramidites (DMT (dimethoxytrityl)-dT, DMT-dA(bz), DMT-dG(dmf) and DMT-dC(ac)) were diluted to 50 mM with dry acetonitrile and synthesis occurred from the 3' towards the 5' end of the oligonucleotides on packed solid phase columns.

Cleavage of the oligonucleotides (DMT-on) from the solid support and base deprotection was achieved in one step to ensure optimal yields. The 34 µmol/g controlled pore glass (CPG) solid support was treated with 10 mL of ice-cold ammonia solution (30-32 % NH_3) overnight at room temperature to detach the DNA from the CPG support. The cleaved DNA (DMT-on) in ammonia was diluted with 10 mL of disodium phosphate buffer (75 mM containing 1 mM EDTA, pH = 8.3) and the crude product was obtained upon freeze drying. The obtained DNA was redispersed in MilliQ water and purified by preparative reverse phase-HPLC (RP-HPLC) followed by freeze drying to remove the solvent.

The DMT group was cleaved from the purified product by making a 2 wt % solution of the dry DNA in NaOAc/HOAc buffer (200 mM, pH 4.0, 200 mM NaCl) and heating the mixture to 50 °C for one hour. After neutralizing the reaction mixture with disodium phosphate buffer (750 mM, 10 mM EDTA), the synthesized DNA was precipitated into a 5-fold excess of isopropanol to remove contaminants and to exchange the counterions to sodium. The precipitate was dissolved in MiliQ water and freeze dried. The synthesized and purified strands were stored at -20 °C until further use.

The purity of the obtained oligonucleotides was confirmed with analytical HPLC.

6.4.2.5 DNA annealing.

All DNA strands were used as received. All the sequences are provided in Supplementary Table S1 and Table S2. The DNA strands received from IDT and Biomers were dissolved in TE buffer (10 mM Tris-HCl, pH = 8.0) to prepare a stock solution of 1 mM and stored at -20 °C for further use. The complementary DNA strands intended for double stranded complexes, i.e., Complex 1 and Substrate 1 were dissolved in annealing buffer (10 mM Tris-HCl, 50 mM NaCl, 10 mM $MgCl_2$, pH = 8.0) with the same stoichiometry at -20 °C overnight to prepare a stock solution of 0.125 mM.

6.4.2.6 CLSM image treatment and analysis.

All CLSM images were processed using ImageJ (Fiji). All images except in **Figure 6-2** were acquired as a *z*-stack. Atto 488, Atto 647N and Rhodamine B channels were merged together to form a composite image and then compiled as a *z*-projection for representation purposes. The size of the co-assemblies was determined by thresholding the compiled images. The masks obtained upon thresholding were analyzed in terms of size and total amount.[32]

6.4.2.7 Lifetime calculation.

The lifetime of the transient state is defined as the time that a transient profile (either obtained from time-dependent fluorescence measurements or assembly size analysis) takes to decrease to half of the initial and maximum value.

6.4.3 Supplementary Notes

6.4.3.1 Definition of activity units of both enzymes.

Definition of the Weiss Unit to describe the activity of T4 DNA ligase: 0.01 Weiss Unit [WU] of T4 DNA Ligase is the amount of enzyme required to catalyze the ligation of greater than 95 % of 1 µg of λ/HindIII fragments at 16 °C in 20 minutes.

Unit definition to describe the activity of BsaI: One Unit [U] is defined as the amount of enzyme required to completely digest 1 µg of pXba DNA in one hour at 37 °C in 50 µl assay buffer containing acetylated BSA added to a final concentration of 0.1 g/L

6.4.4 Supplementary Tables

Table S1. DNA sequences for the oligonucleotides synthesized following a well-defined procedure (**Experimental section 6.4.2.4**) with their abbreviations and modifications.

Name	Sequence 5'→ 3'	Figure	Modification
NH_2-x* (T_{20}-x*)	TTTTTTTTTTTTTTTTTTTT GAACCCGTATATCTATCCTA	Fig. 6-3, 6-4	5' Amino Modifier C6 dT

Table S2. DNA sequences for the oligonucleotides with their abbreviations, sequence, and modifications. 5' Phosphorylated DNA strands were purchased from IDT. All other DNA sequences were purchased from Biomers.

Name	Sequence 5'→ 3'	Figure	Modification
Substrate	CGGATTGGTATTGTATTACC	Fig. 6-3, 6-4	None
	AATCTTTAATACAATACCAATCCGATT	Fig. 6-3, 6-4	5' Phos
Complex	CATGAGAATTCCATTCACGGTCTCT	Fig. 6-3, 6-4	None
	GATTAGAGACCGTGAATGGAATTCTCATG	Fig. 6-3, 6-4	5' Phos
Input 1	AATCAATCGGA	Fig. 6-3, 6-4	5' Phos
Input 2	GTATTAAA	Fig. 6-3, 6-4	None
xA1Q (Linker)	TCAGGTAATACAATACCAATCCG TAGGATAGATATACGGGTTC	Fig. 6-3b	5' BMNQ 620
xA1Atto 647N (Linker)	TCAGGTAATACAATACCAATCCG TAGGATAGATATACGGGTTC	Fig. 6-7	3' ATTO 647N

xA1 (Linker)	**TCA**GGTAATACAATACCAATCCG **TAGGATAGATATACGGGTTC**	Fig. 6-3a, 6-4	None
A1*Atto 647N (Signal)	GGTATTGTATTACC**TGA**	Fig. 6-3, 6-4	3’ ATTO 647N
A1*Atto 488 (Signal)	GGTATTGTATTACC**TGA**	Fig. 6-2	3' ATTO 488
A1*Cy5 (Signal)	GGTATTGTATTACC**TGA**	Fig. 6-2	3’ Cy5

6.4.5 Supplementary Figures

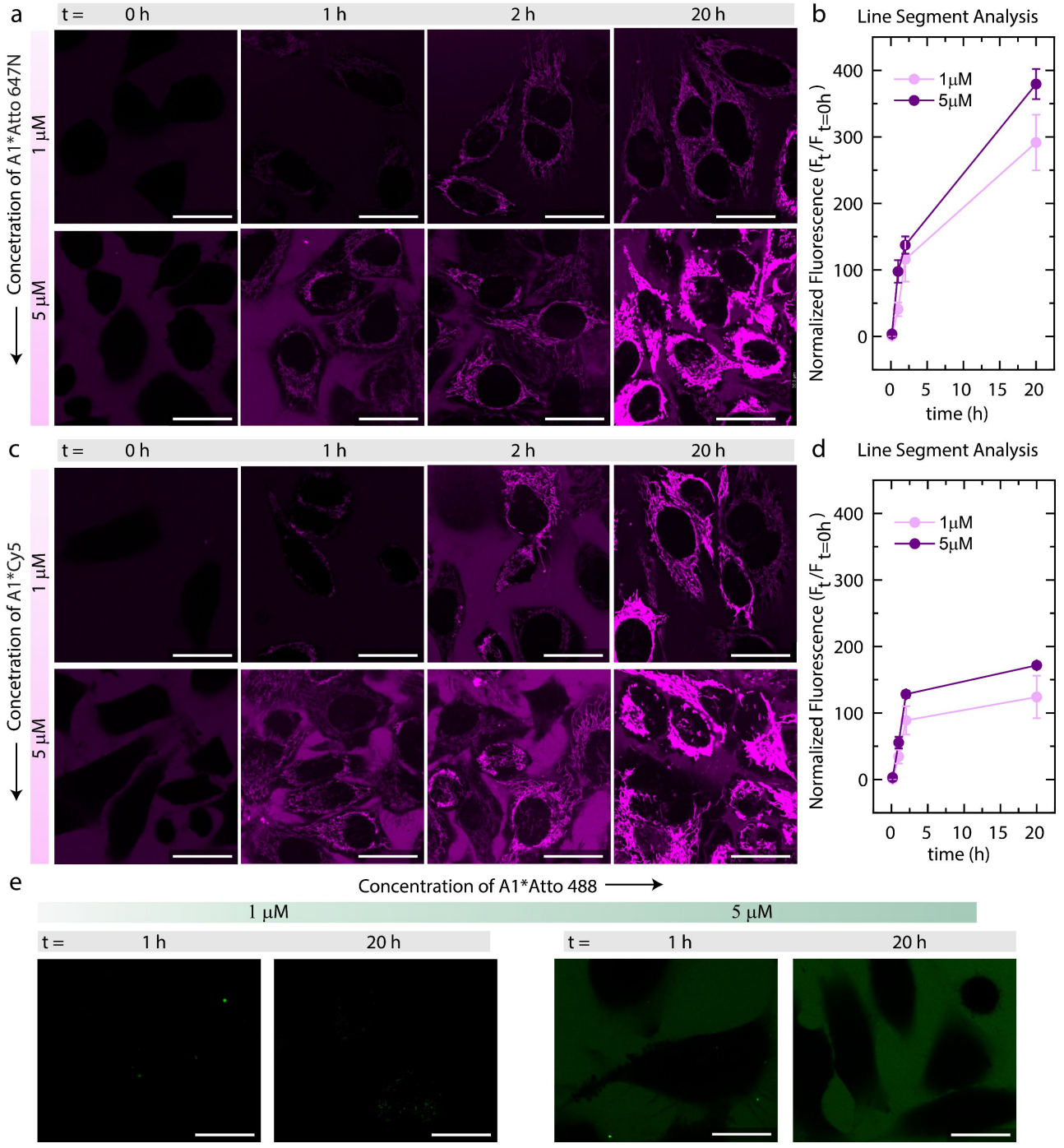

Figure 6-5. Screening of different dye labelled A1* (Signal) strand for internalization in living cells. (a), (c) in situ CLSM images of cells incubated with two different concentrations (1 and 5 µM) of A1*Atto 647N (a) and A1*Cy5 (c) at 0 h (right after Signal strand addition), 1 h, 2 h, and 20 h. (b), (d) Time-dependent line segment analysis of the FI changes within cells incubated with two different concentrations (1 and 5 µM) of A1*Atto 647N (a) and A1*Cy5. Each data point corresponds to an average contribution from five measurements, the error bars represent SD. The results are normalized with respect to t = 0 h data point. (e) in situ CLSM images of cells incubated with two different concentrations (1 and 5 µM) of A1*Atto 488 at 1 h and 20 h. Experimental conditions: HeLa cells at a concentration of 10^4 cells/mL were incubated in DNA-Cell buffer at 37 °C with respective dye labelled A1* (Signal) strand. Scale bars: (a), (b), and (c) 25 µm.

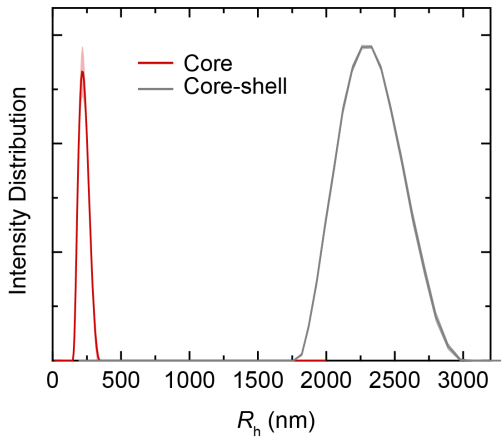

Figure 6-6. DLS CONTIN plots of: poly(2,2,2-trifluoroethyl methacrylate) (PtFMA) core-particles and pristine MG. The suspensions were prepared in MilliQ water with a final concentration of 0.06 mg/mL.

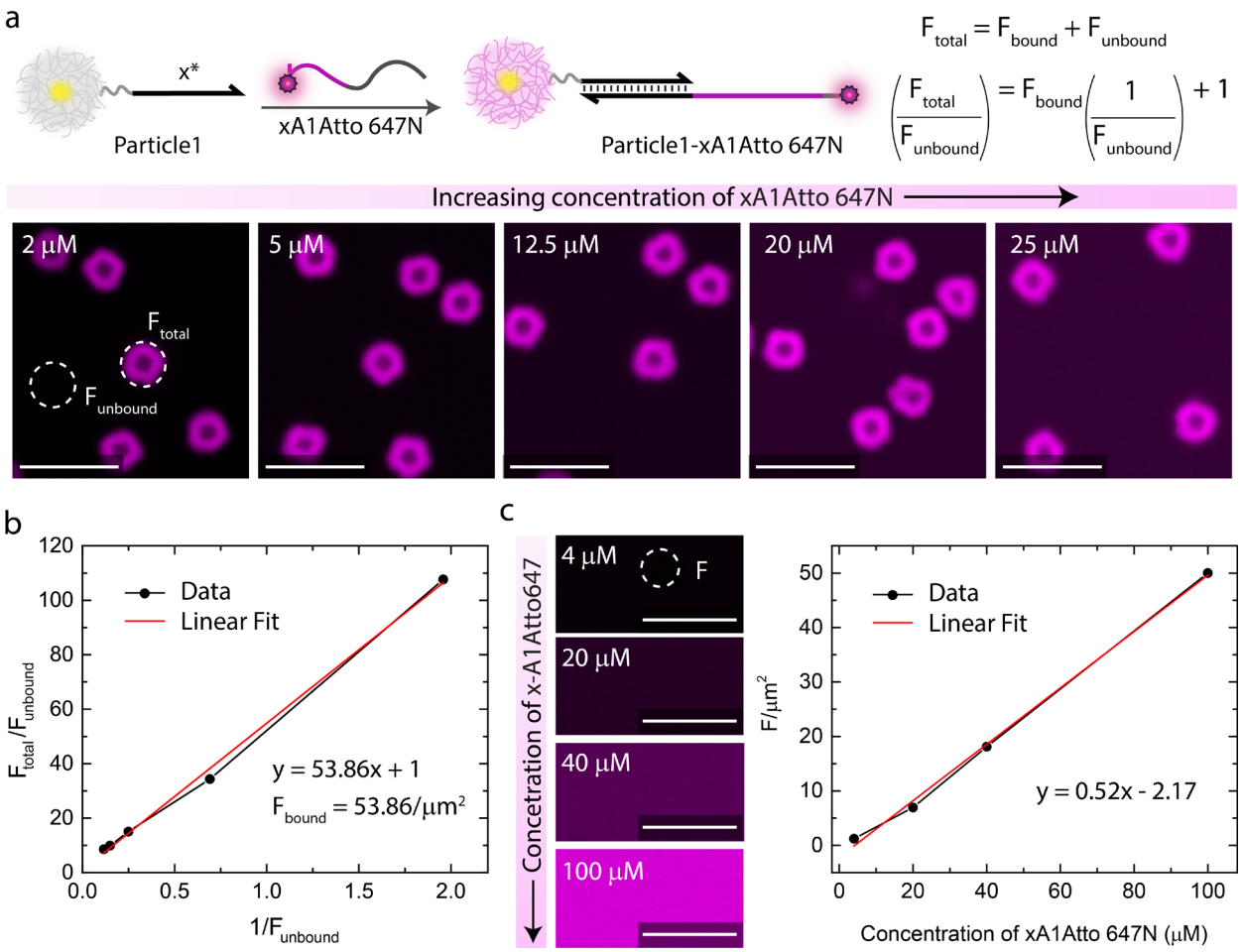

Figure 6-7. Measurement of DNA grafting density on Particle1. (a) The binding capacity of xA1-Atto 647N onto Particle1 via x/x* hybridization is measured as a proxy for the DNA grafting density. The mean fluorescence intensity per μm² over the particle (F_{total}, includes the contribution from both xA1-Atto 647N bound on Particle1 and free xA1-Atto 647N in the suspension) and in the background ($F_{unbound}$, includes only free xA1-Atto 647N in the suspension) is measured for increasing amounts of xA1-Atto 647N via CLSM. Experimental conditions: Particle1 is incubated with increasing concentrations of xA1-Atto 647N (2-25 μM) in TE buffer (pH = 8.0) at 15 °C at a final MG concentration of 0.05 wt %. F_{total} and $F_{unbound}$ represent average fluorescence intensity measured from 5 different regions. (b) The data is fitted with linear equation where the slope provides fluorescence contribution from xA1-Atto 647N on the particle (F_{bound}). (c) With the help of calibration curve between mean fluorescence intensity per μm² (F, measured via CLSM) and concentration of free xA1-Atto 647N, a corresponding DNA concentration for F_{bound} is calculated to be 53.86 ± 1.64 μM accounting for 3.3 × 10^6 strands/MG. Experimental conditions: Increasing concentrations of z-A2-Atto 647N (4-100 μM) dispersed in TE buffer. F represents an average fluorescence intensity from 5 different regions. Scale bars: (a), (c) 5 μm.

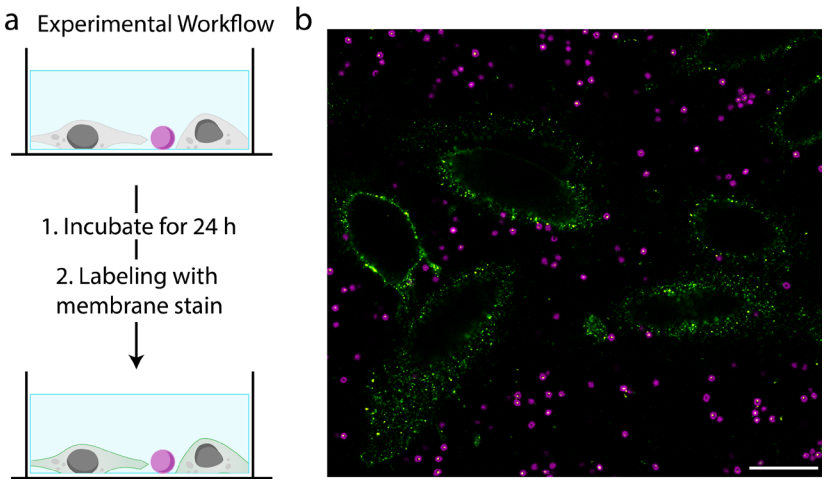

Figure 6-8. Checking the co-existence of Particle1-xA1-A1*Atto 647N with living HeLa cells. (a) Schematic representation of the experimental workflow where Particle1-xA1-A1*Atto 647N are incubated with cells for 24 h after which they are stained with green plasma membrane dye before acquiring the final CLSM in (b). Note that the plasma membrane dye gets partly internalized. Experimental conditions: Particle1-xA1-A1*Atto 647N at a final MG concentration of 0.05 wt% suspended in DNA-cell buffer containing HeLa cells at a concentration of 10^4 cells/mL. Green plasma membrane dye was added as per the guidelines of the supplier. Scale bar: (b) 20 µm.

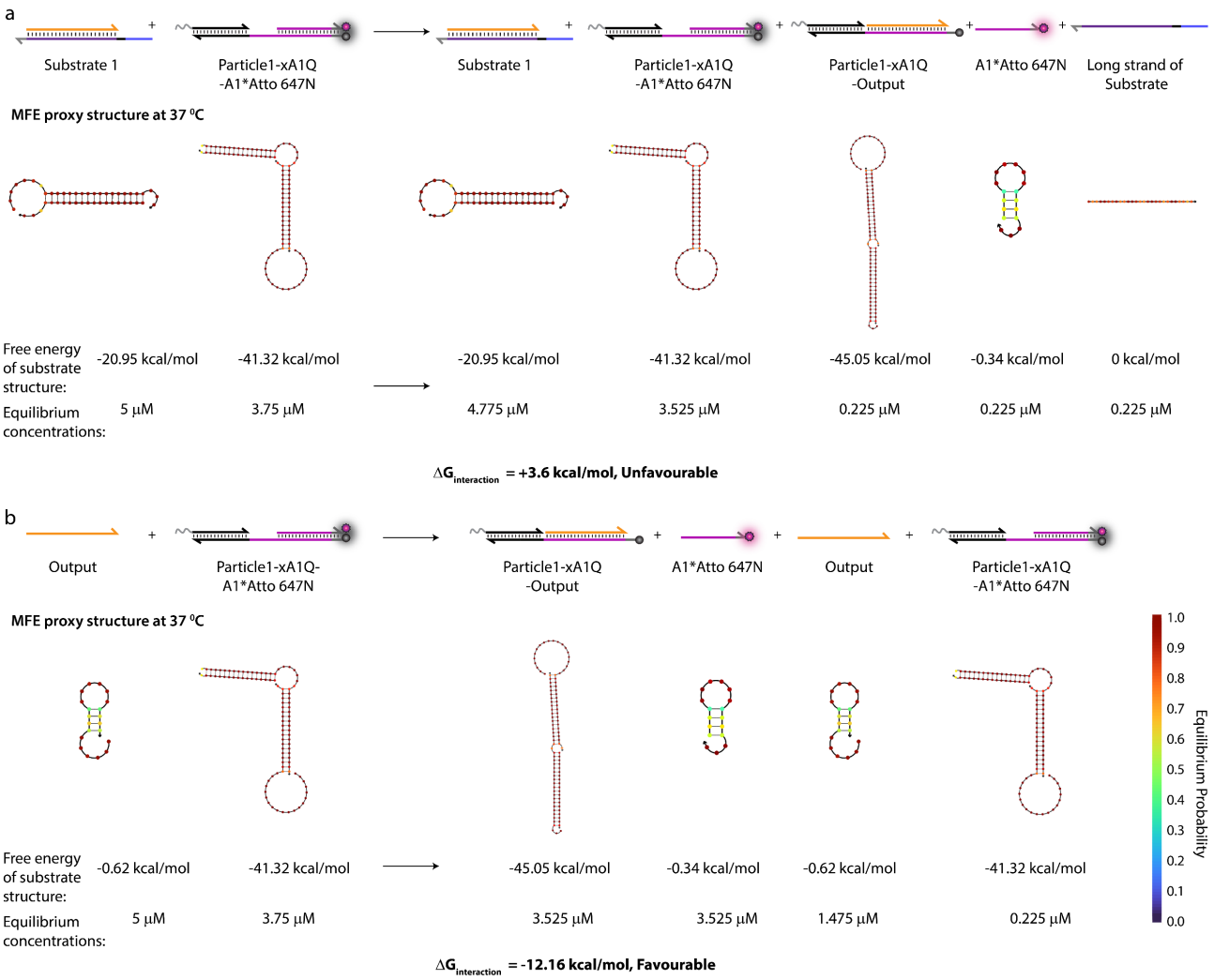

Figure 6-9. Free energy change for the interaction between (a) Substrate 1 and Particle1-xA1Q-A1*Atto 647N, (b) Output and Particle1-xA1Q-A1*Atto 647N calculated with NUPACK simulations setting the temperature at 37 °C and salt concentrations at 50 mM NaCl, 10 mM $MgCl_2$. Only free Output favorably releases the Signal strand from Particle1-xA1Q-A1*Atto 647N and the interaction between Substrate and Particle1-xA1Q-A1*Atto 647N is weakly unfavorable.

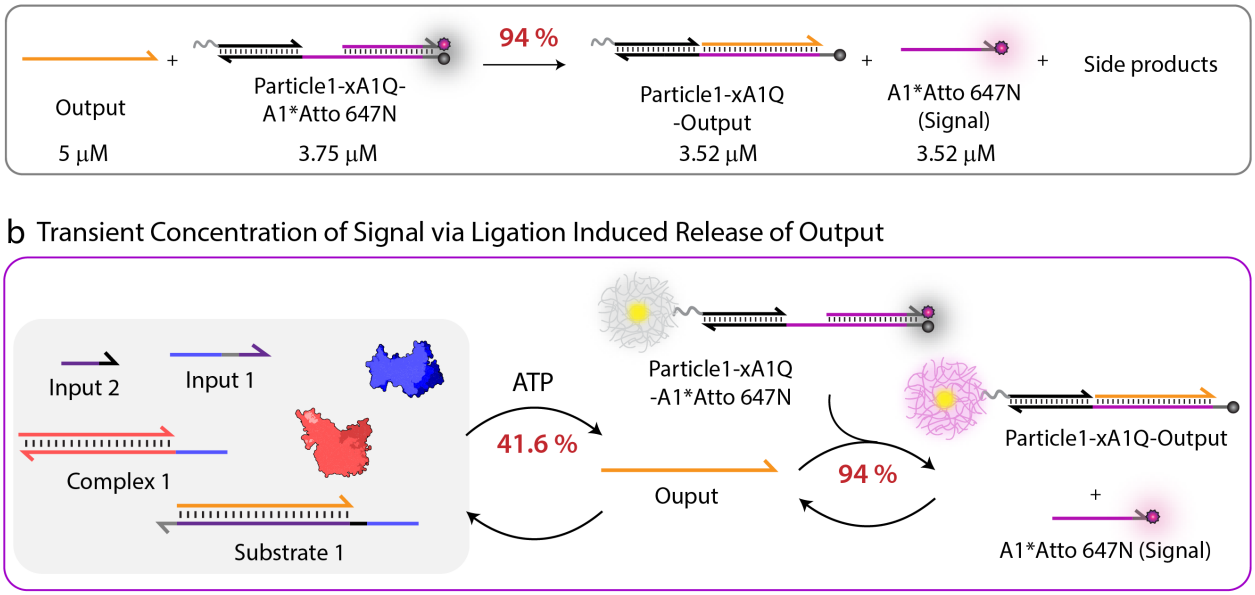

Figure 6-10. (a) Equilibrium concentrations of all components obtained from NUPACK simulations upon mixing 5 μM of Output and 3.75 μM of Particle1-xA1Q-A1*Atto 647N setting the temperature at 37 °C and salt concentrations at 50 mM NaCl, 10 mM $MgCl_2$. (b) Schematics for experimental verification of percentage yield of A1*Atto 647N (Signal) strand released in a transient system where Output is produced in situ via ligation. (c) Time-dependent fluorescence intensity changes demonstrating release of Signal strand when Output is added directly and when it is produced transiently via ligation. The percentage of fluorescence increase in case of direct Output addition provides a reference point which indicates the maximum fluorescence that can be observed in the transient system. In case of transient system, restriction can set in already at the hemi-ligated intermediate (e.g., Substrate 1, Complex 1 and only one of the Inputs) without completing to the fully ligated state which is the condition for expulsion of Output. Because of this, fluorescence intensity decreases by only 30% which indicates that Output is released with 41.6% efficiency with respect to Reference point. Since 94% of Output released can generate free A1*Atto 647N (Signal) (a), a final yield of 39% (1.47 μM) can be attributed to free A1*Atto 647N (Signal). Experimental conditions: For transient system (magenta curve), Particle1-xA1Q-A1*Atto 647N at concentration of 3.75 μM are dissolved in 1X NEB CutSmart buffer containing 20 μM Complex 1, 5 μM Substrate 1, 10 μM Input 1 and Input 2, 0.8 WU μL-1 of T4 DNA ligase and 0.8 U μL-1 of BsaI at 37 °C fueled by 40 μM ATP. For case with Direct Output addition (grey curve), Particle1-xA1Q-A1*Atto 647N at concentration of 3.75 μM is dissolved in 1X NEB CutSmart buffer at 37 °C followed by addition of 5 μM of Output.

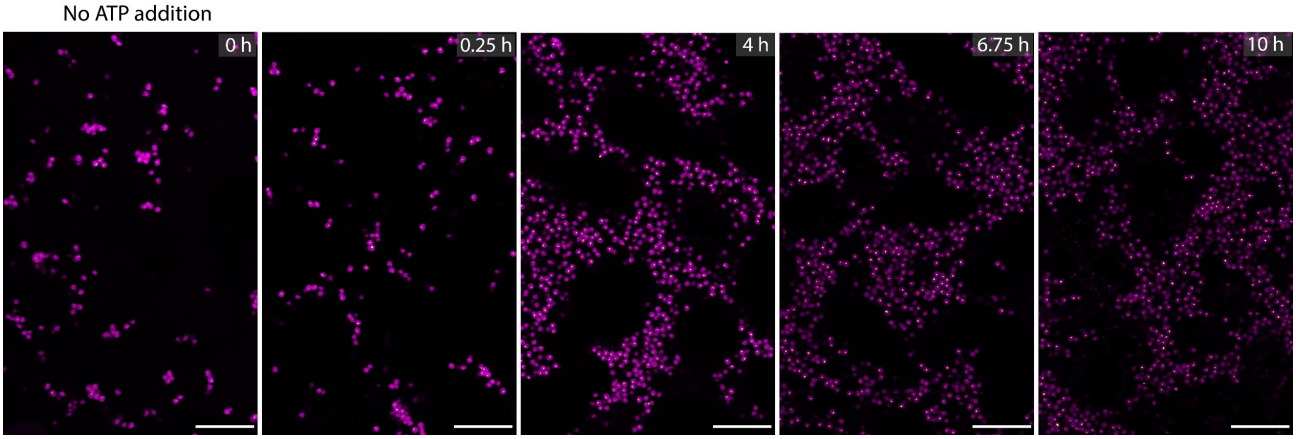

Figure 6-11. CLSM imaging of the control system combining all three layers together within extracellular medium without ATP addition. Please note that the gradual increase in particle density over time is due to the particles settling down to the bottom. Experimental conditions: Particle1-xA1-A1*Atto 647N suspended in DNA-Cell buffer at a final MG concentration of 0.05 wt% containing 20 µM Complex 1, 5 µM Substrate 1, 10 µM Input 1 and Input 2, 0.8 WU μL^{-1} of T4 DNA ligase and 0.8 U μL^{-1} of BsaI and HeLa cells at a concentration of 10^4 cells/mL incubated together at 37 °C and fueled by 40 µM ATP (b, d). Scale bars: 20 µm.

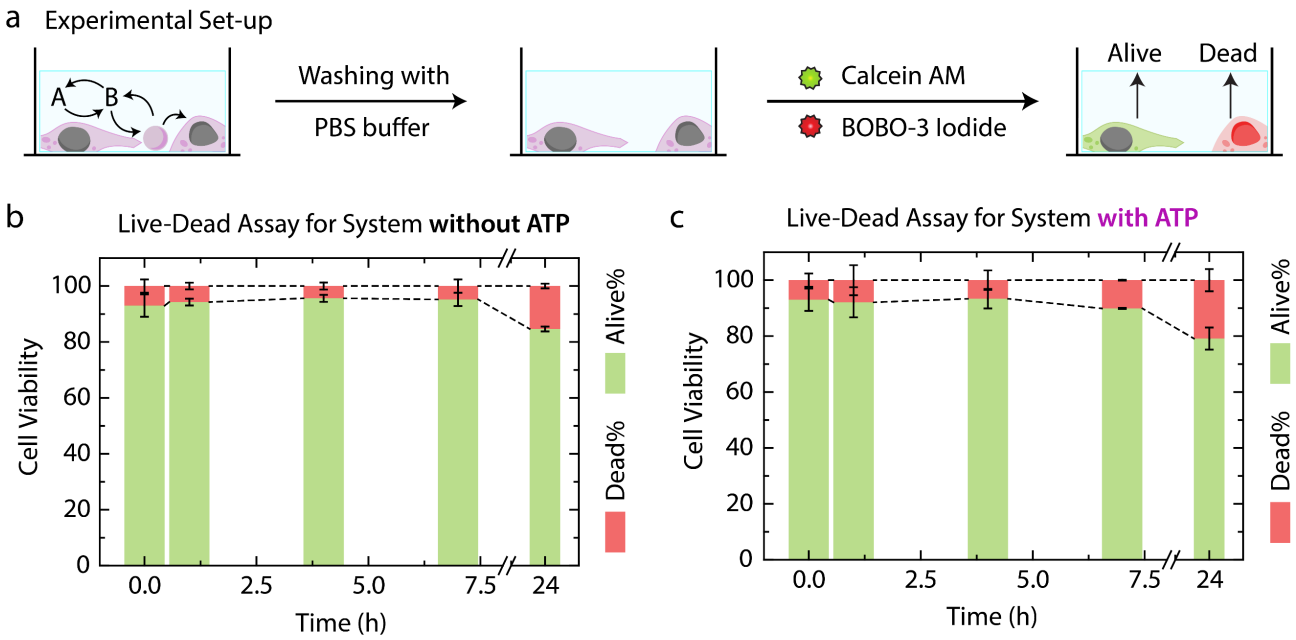

Figure 6-12. Cell viability test for the transient delivery of Signal strands for experiments performed in **Figure 6-4** and **Figure 6-11**. (a) Schematic representation of the experimental workflow where the extracellular medium containing Layer 1 and Layer 2 is exchanged with PBS buffer followed by introduction of two different labels, Calcein AM and BOBO-3 Iodide. Calcein AM only stains the live cells and is based on intracellular esterase activity, whereas BOBO-3 Iodide specifically penetrates the dead cells. (b), (c) Cell viability test on the samples containing all three Layers at different time points in the absence (b) and presence (c) of ATP. Five duplicate samples were prepared for five separate measurements., whenever needed, the extracellular medium was replaced with PBS buffer, equimolar concentrations of Calcein AM and BOBO-3 Iodide were added (as per the guidelines of the supplier), the sample was incubated for 15 min at 25 °C followed by acquiring microscopic images using FITC and TRITC filters for separate dyes. The images were manually analyzed to calculate the percentage of live and dead cells. The results represent an average contribution from two different images and error bars depict the SD.

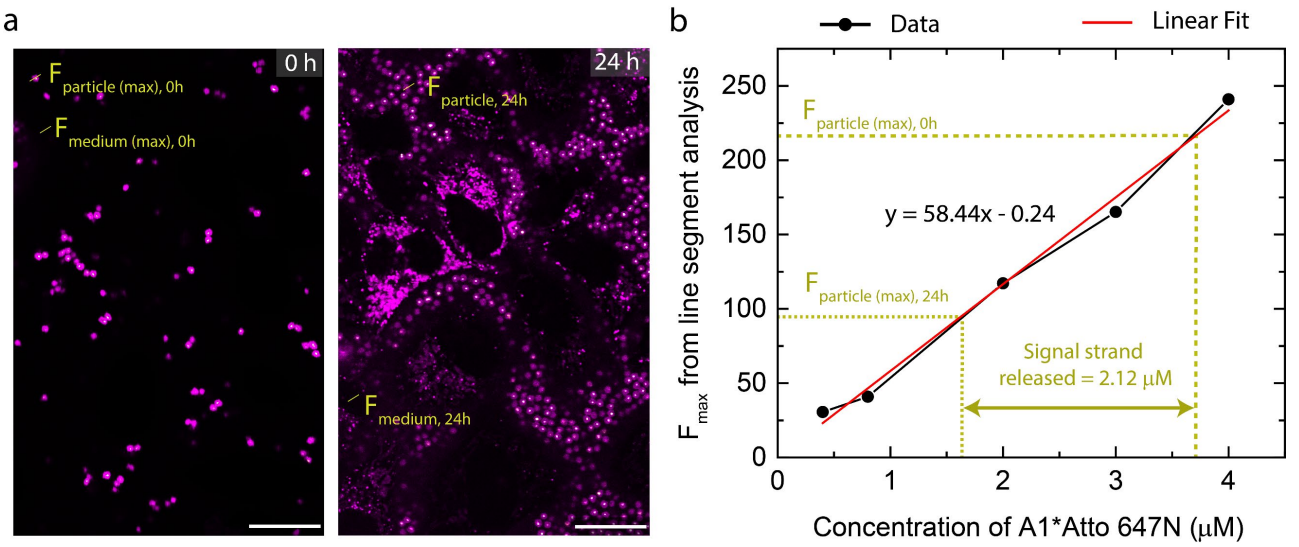

Figure 6-13. Calculation of the amount of A1*Atto 647N (Signal) strand released from Particle1-xA1Q-A1*Atto 647N into medium and delivered into cells after 24 h via controlled out-of-equilibrium delivery method presented in the paper (**Figure 6-4**). (a) The maximum fluorescence intensity obtained from the line segment analysis of particle at 0 h ($F_{particle(max),\ 0h}$) and 24 h ($F_{particle(max),\ 24h}$) is correlated with the calibration curve between fluorescence intensity and concentration of free A1*Atto 647N (b). The correlation indicates the concentration of Signal strand released from the particle to be 2.12 μM. Similarly, the maximum fluorescence intensity obtained from the line segment analysis of medium at 0 h ($F_{medium(max),\ 0h}$) and 24 h ($F_{medium(max),\ 24h}$) can be correlated with the calibration curve to acquire the concentration of Signal strand released into the cells to be 0.06 μM. Finally, the amount of Signal strand delivered into the cells comes out to be 2.06 μM or 1.24 x 10^{11} Signal strands per cell. Scale bars: (a) 20 μm.

6.5 References

1 Bazrafshan, A. *et al.* DNA Gold Nanoparticle Motors Demonstrate Processive Motion with Bursts of Speed Up to 50 nm Per Second. *ACS Nano* **15**, 8427-8438 (2021). https://doi.org:10.1021/acsnano.0c10658

2 Shirmanova, M. V. *et al.* Chemotherapy with cisplatin: insights into intracellular pH and metabolic landscape of cancer cells in vitro and in vivo. *Sci. Rep.* **7**, 8911 (2017). https://doi.org:10.1038/s41598-017-09426-4

3 Gilleron, J. *et al.* Image-based analysis of lipid nanoparticle–mediated siRNA delivery, intracellular trafficking and endosomal escape. *Nat. Biotechnol.* **31**, 638-646 (2013). https://doi.org:10.1038/nbt.2612

4 Sahay, G. *et al.* Efficiency of siRNA delivery by lipid nanoparticles is limited by endocytic recycling. *Nat. Biotechnol.* **31**, 653-658 (2013). https://doi.org:10.1038/nbt.2614

5 Hampton, T. Electric Pulses Help With Chemotherapy, May Open New Paths for Other Agents. *JAMA* **305**, 549-551 (2011). https://doi.org:10.1001/jama.2011.92

6 Munerati, M., Cortesi, R., Ferrari, D., Di Virgilio, F. & Nastruzzi, C. Macrophages loaded with doxorubicin by ATP-mediated permeabilization: Potential carriers for antitumor therapy. *Biochim. Biophys. Acta, Mol. Cell Res.* **1224**, 269-276 (1994). https://doi.org:https://doi.org/10.1016/0167-4889(94)90200-3

7 Peverini, L., Beudez, J., Dunning, K., Chataigneau, T. & Grutter, T. New Insights Into Permeation of Large Cations Through ATP-Gated P2X Receptors. *Front. Neurosci.* **11** (2018). https://doi.org:10.3389/fnmol.2018.00265

8 Burnstock, G. & Di Virgilio, F. Purinergic signalling and cancer. *Purinergic Signal* **9**, 491-540 (2013). https://doi.org:10.1007/s11302-013-9372-5

9 Ämmälä, C. *et al.* Targeted delivery of antisense oligonucleotides to pancreatic β-cells. *Sci. Adv.* **4**, eaat3386 (2018). https://doi.org:doi:10.1126/sciadv.aat3386

10 Ren, K. *et al.* A DNA dual lock-and-key strategy for cell-subtype-specific siRNA delivery. *Nat. Commun.* **7**, 13580 (2016). https://doi.org:10.1038/ncomms13580
11 Lee, S. W. L. *et al.* MicroRNA delivery through nanoparticles. *J. Control. Release.* **313**, 80-95 (2019). https://doi.org:https://doi.org/10.1016/j.jconrel.2019.10.007
12 Tarvirdipour, S., Skowicki, M., Schoenenberger, C. A. & Palivan, C. G. Peptide-Assisted Nucleic Acid Delivery Systems on the Rise. *Int. J. Mol. Sci.* **22** (2021). https://doi.org:10.3390/ijms22169092
13 Zadeh, J. N. *et al.* NUPACK: Analysis and design of nucleic acid systems. *J. Comput. Chem.* **32**, 170-173 (2011). https://doi.org:10.1002/jcc.21596
14 Deng, J. & Walther, A. Autonomous DNA nanostructures instructed by hierarchically concatenated chemical reaction networks. *Nat. Commun.* **12**, 5132 (2021). https://doi.org:10.1038/s41467-021-25450-5
15 Deng, J. & Walther, A. Fuel-Driven Transient DNA Strand Displacement Circuitry with Self-Resetting Function. *J. Am. Chem. Soc.* **142**, 21102-21109 (2020). https://doi.org:10.1021/jacs.0c09681
16 Walsh, A. S., Yin, H., Erben, C. M., Wood, M. J. A. & Turberfield, A. J. DNA Cage Delivery to Mammalian Cells. *ACS Nano* **5**, 5427-5432 (2011). https://doi.org:10.1021/nn2005574
17 Mikkilä, J. *et al.* Virus-Encapsulated DNA Origami Nanostructures for Cellular Delivery. *Nano Lett.* **14**, 2196-2200 (2014). https://doi.org:10.1021/nl500677j
18 Schüller, V. J. *et al.* Cellular Immunostimulation by CpG-Sequence-Coated DNA Origami Structures. *ACS Nano* **5**, 9696-9702 (2011). https://doi.org:10.1021/nn203161y
19 Lacroix, A., Vengut-Climent, E., de Rochambeau, D. & Sleiman, H. F. Uptake and Fate of Fluorescently Labeled DNA Nanostructures in Cellular Environments: A Cautionary Tale. *ACS Cent. Sci.* **5**, 882-891 (2019). https://doi.org:10.1021/acscentsci.9b00174
20 Fern, J. & Schulman, R. Design and Characterization of DNA Strand-Displacement Circuits in Serum-Supplemented Cell Medium. *ACS Synth. Biol.* **6**, 1774-1783 (2017). https://doi.org:10.1021/acssynbio.7b00105
21 Cilliers, C., Liao, J., Atangcho, L. & Thurber, G. M. Residualization Rates of Near-Infrared Dyes for the Rational Design of Molecular Imaging Agents. *Mol. Imaging Biol.* **17**, 757-762 (2015). https://doi.org:10.1007/s11307-015-0851-7
22 Andreas, N. *et al.* Determination of In Vitro Membrane Permeability by Analysis of Intracellular and Extracellular Fluorescein Signals in Renal Cells. *In Vivo* **33**, 1767 (2019). https://doi.org:10.21873/invivo.11667
23 Bondar, O. V., Saifullina, D. V., Shakhmaeva, II, Mavlyutova, II & Abdullin, T. I. Monitoring of the Zeta Potential of Human Cells upon Reduction in Their Viability and Interaction with Polymers. *Acta Naturae* **4**, 78-81 (2012).
24 Buschmann, V., Weston, K. D. & Sauer, M. Spectroscopic Study and Evaluation of Red-Absorbing Fluorescent Dyes. *Bioconjug. Chem.* **14**, 195-204 (2003). https://doi.org:10.1021/bc025600x
25 Han, K., Go, D., Hoenders, D., Kuehne, A. J. C. & Walther, A. Switchable Supracolloidal Coassembly of Microgels Mediated by Host/Guest Interactions. *ACS Macro Lett.* **6**, 310-314 (2017). https://doi.org:10.1021/acsmacrolett.7b00053
26 Han, K. *et al.* Social Self-Sorting of Colloidal Families in Co-Assembling Microgel Systems. *Angew. Chem. Int. Ed.* **56**, 2176-2182 (2017). https://doi.org:https://doi.org/10.1002/anie.201612196
27 Deng, J. & Walther, A. Pathway Complexity in Fuel-Driven DNA Nanostructures with Autonomous Reconfiguration of Multiple Dynamic Steady States. *J. Am. Chem. Soc.* **142**, 685-689 (2020).
28 Pellegatti, P. *et al.* Increased Level of Extracellular ATP at Tumor Sites: In Vivo Imaging with Plasma Membrane Luciferase. *PLoS ONE* **3**, e2599 (2008). https://doi.org:10.1371/journal.pone.0002599
29 Lecciso, M. *et al.* ATP Release from Chemotherapy-Treated Dying Leukemia Cells Elicits an Immune Suppressive Effect by Increasing Regulatory T Cells and Tolerogenic Dendritic Cells. *Front. Immunol.* **8** (2017). https://doi.org:10.3389/fimmu.2017.01918
30 Sharma, C., Samanta, A., Schmidt, R. S. & Walther, A. DNA-Based Signaling Networks for Transient Colloidal Co-Assemblies. *J. Am. Chem. Soc.* **145**, 17819-17830 (2023). https://doi.org:10.1021/jacs.3c04807

31 Meng, Z., Smith, M. H. & Lyon, L. A. Temperature-programmed synthesis of micron-sized multi-responsive microgels. *Colloid Polym. Sci.* **287**, 277-285 (2009). https://doi.org:10.1007/s00396-008-1986-8

32 Dehne, H., Reitenbach, A. & Bausch, A. R. Transient self-organisation of DNA coated colloids directed by enzymatic reactions. *Sci. Rep.* **9**, 7350 (2019). https://doi.org:10.1038/s41598-019-43720-7

7 Synopsis

In this final chapter, I summarize the thesis with a comprehensive overview of the results obtained during my research on chemical reaction networks (CRNs) for transient colloidal co-assemblies and delivery applications. Finally, I will close this thesis by providing an outlook for future research in this field.

7.1 Summary and Conclusion

Within the framework of this thesis, different transient co-assembling colloidal systems are established by coupling or integrating potential co-assembling microgel particles with out-of-equilibrium CRNs. The CRNs are designed by decoupling activation and deactivation reactions either temporally, chemically, using energy dissipation, or a combination of these strategies.

In **Chapter 2,** we established the conceptual foundation for **Chapter 3** by discussing different generations of pH-FS based on the coupling of acid and base producing steps in a CRN, principles of coupling such systems to self-assemblies with programmable lifetimes and highlighting emerging concepts for the design of autonomous materials. We used concepts of pH-FS to develop a transient colloidal system and introduced a rational design approach for chemo-structural feedback (**Chapter 3**). We achieved this by immobilizing enzymes of a deactivating acid-producing enzymatic cascade on pH-switchable microgels that can form co-assemblies at high pH. The co-assembled state thereby brings the two enzyme partners close enough for enhanced acid generation. The amplified deactivator production (acid) leads to an almost two-fold reduction in the lifetime of the transiently formed pH-state. The enzymatic formation of deactivator from dormant deactivator relies on activation pathway as high pH changes the initial reference point of the enzymes where slow acid production autocatalytically pushes them eventually into their optimum range to perform the deactivation. The fuel dependence of the transient system was exploited to maintain pH specifically between 7.5-8.0 for~3h. The duration of this high pH range is critical to attain transient co-assemblies. The fact that the Invertase-Glucose Oxidase cascade always tends to push the intermediate glucose above the Michaelis-Menten constant of Glucose Oxidase, assures complete consumption of fuel (sucrose). This is essential to reach a final low pH of 3.5 for the complete disassembly of the formed transient structures. Thereby, keeping all other conditions intact, the right concentration of fuel can essentially be used to match the dynamics of microgel particles with pH-FS to specifically achieve transient co-assemblies. Successive damping of the pH-response was observed upon reactivation of the transient system using the same refueling solution. The excess equivalents of gluconic acid produced over each cycle limit the highest pH achievable in the next cycle and consequently affect the yield of co-assemblies formed. Secondly, one of the side products from the enzymatic cascade (H_2O_2) acts as an inhibitor for Glucose Oxidase,[1] showing lower pH-feedback to the basic regime. However, H_2O_2 can be transformed back to O_2 by introducing sub-catalytic amounts of Catalase in the transient system.[2]

Since pH-FSs can accumulate significant quantities of salt and other aforementioned waste, the temporal transition between disassembled and assembled colloidal particles in subsequent cycles can be unfavorably influenced. To overcome such challenges, we shifted towards DNA-based reaction networks (**Chapter 4**). The programmability, predictability, and specificity of DNA were exploited to increase the robustness of transient colloidal systems. A toehold-mediated DNA strand displacement (TMDSD) reaction cascade directs two different microgels into transient co-assemblies. The microgels are functionalized with DNA and become an integral part of the network. The particles transduce two orthogonally different DNA trigger strands to introduce a linker, which brings two microgels together into co-assemblies. The activation pathway further forms an intermediate species, which initiates the deactivation reaction. The system thereby follows a complex trajectory, passing through a transient state and ultimately reaching thermodynamic equilibrium. Although dynamic, the system operates under non-dissipative conditions as it resides in a new state (lowest

energy state), and the original state cannot be acquired. The co-assemblies are only realized when inhibition is slower than activation (Strategy 3). The modularity of the design allows the installation of delay phases and accelerators by interconnecting modules to the upstream and downstream of the core network. In addition, *in silico* optimization of all DNA modules provides essential experimental guidance that helps reduce leakage and unnecessary interactions arising from any waste modules.

Moving away from the thermodynamically driven classic TMDSD reactions, we switched to ATP-fueled enzymatic TMDSD reaction cascade in **Chapter 5,** which operates under dissipative conditions. The ATP-powered ligation and restriction of DNA components transiently generate a linker strand at the molecular level, which temporally controls the downstream co-assembly of microgels. The linker strand is recovered as soon as ATP is consumed, disassembling the formed structures. The chemically and temporally decoupled, faster ligation and slower restriction assures transience in the system. The resettling ability of the network restores the original state of the system and allows the system to be reused for subsequent cycles.

Besides playing intricate role in energy transduction and intracellular signaling, ATP is also recognized as an extracellular messenger. It is one of the main biochemical components of the tumor microenvironment. As compared to healthy tissues where extracellular ATP is virtually absent (only 10-100 nM), the ATP levels in tumor microenvironment can be detected in the micromolar range (50-200 μM).[3,4] Such a drastic difference in the extracellular ATP levels of healthy and diseased tissues inspired us to explore our ATP-driven enzymatic reaction networks for selective drug delivery applications. We developed a model approach to deliver DNA strands in cancer cells (HeLa cells) when triggered by ATP. To achieve this, we installed the ATP-driven enzymatic reaction networks in the cell-culture media of HeLa cells for temporally controlled delivery of DNA (**Chapter 6**). The system operates at three different layers; the first layer controls the transient release of an Output strand from ATP-fueled enzymatic network. Output invades the second layer and displaces a Signal strand docked on a microgel particle. This immobilization prevents unnecessary internalization of Signal by cells. Only upon ATP introduction, Signal is available to be uptaken by cells, and the carefully chosen fluorophore labeling allows temporal tracking of DNA within cells. After ATP consumption, no Signal is available to be internalized as the system resettles to its original state. Such controlled delivery mechanisms can be proposed for specific organelle targeting for applications in gene silencing and gene therapy.

7.2 Future Perspective

The design principles presented in this thesis to develop transient functions for programming colloidal co-assemblies and time-controlled delivery of DNA within living cells lays a foundation for exploring other out-of-equilibrium operations such as bistability and oscillations. Many metabolic pathways in cells have the ability to exhibit bistability, i.e., to possess two different stable steady states and switching between them in response to chemical signaling.[5] It is a key phenomenon that explains cellular functions such as decision-making processes in cell cycle progression, cellular differentiation, and apoptosis. Oscillations, on the other hand, are associated with biological clocks, cell signaling, and cell division. The minimal model for synthetically producing bistability requires atleast one positive feedback loop and a zero-order inhibitor, which balances the positive feedback loop.[6] Such bistable switches, when coupled to slower negative feedback loops, produce oscillations. Combining these dynamic operations with design principles established for colloidal assemblies in this thesis can pave the way toward structure and materials enriched with dynamic and autonomous properties. Most synthetic oscillators require a continuous supply of fuel species and the removal of waste molecules to enable sustained dynamics on longer timescales. This is usually achieved by operating oscillations in a flow reactor[7,8] or a constant manual addition of fueling components[9].

Although all the transient systems presented in the thesis were achieved in a closed system, flow reactors or constant manual addition of fuel can offer an interesting approach to sustain the transient co-assemblies or

perform their reactivation. If we do not want to use manual or microfluidic addition of fuel and removal of waste, we can embed some minimal metabolic pathways that can produce or, ideally, regenerate fuel from the waste released in the system.

For example, for pH-FS systems, a sucrose regenerating pathway cannot be designed as sucrose itself is the primary carbon source, which is further transduced into ATP in cells. A semi-batch reactor can be instead used to intermittently introduce sucrose in tris buffer (fueling solution) during the course of cycles.[10] To solve the issue of increasing ionic strength over each reactivation cycle, an open-flow reactor with constant inflow of fueling components and removal of waste species might be useful to increase the robustness of the co-assembling system and sustain the dynamic behavior.

For toehold-mediated DNA strand displacement (TMDSD) reaction networks presented in the thesis, refueling cannot be achieved because the system resides in a thermodynamically different state at the end of the cycle. However, the successful operation of transient co-assemblies using DNA-based networks opens the possibility of developing and exploring catalytic reaction networks using toehold-exchange DNA strand displacement reactions. The exponential growth of functional nucleic acids such as DNAzymes and aptamers can also effectively provide an enzyme-free and catalytic approach to build resettable DNA-based reaction networks. Interfacing classical strand displacement reactions with redox chemistry is recently suggested to embed resetting ability in DSD-based systems.[11] This should be the next logical step to improve the applicability of DNA-based reaction networks. The focus can then be shifted towards increasing the self-regulating refueling capabilities of the system. This probably cannot be achieved with DNA alone and might require assistance from DNA processing enzymes.

The only waste produced in the ATP-fueled transient co-assembling system are the side products (AMP and PPi) from the ATP-induced ligation reaction. Because of the high relevance of ATP as the primary source of energy for cellular metabolism, we can take inspiration from cellular metabolic pathways that regenerate ATP from AMP and PPi. One of the versatile strategies involves step-wise catalysis of AMP and PPi to ADP by phosphotransferase.[12] ADP acting as an intermediate is further converted to ATP by adenylate kinase. Alternatively, photosynthetic conversion of ADP to ATP can provide a sustainable and orthogonal approach while operating multiple coupled reactions. Light-induced conversion of ADP into ATP requires a minimum of two membrane proteins, a photoconverter that establishes an electrochemical gradient across the membrane, generating the necessary force for the conversion of ADP to ATP by ATP synthase. Although, the requirement of membrane-based charge separation limits the application of this approach across a membrane. Recently, an electrobiological module for the production of ATP from electricity was proposed.[13] The growth of such orthogonal and biocompatible approaches for ATP regeneration can strongly complement the use of ATP as an energy source for driving out-of-equilibrium self-assembly functions with improved performance and durability.

Infact, the successful operation of ATP-fueled enzymatic reaction networks in the extracellular medium of living cells (HeLa cells) confirms the robustness of these systems. This opens up possibilities of potential integration of these systems with tumor microenvironment where the naturally increased extracellular ATP levels can be directly used to triger the downstream functions.

The results presented in this thesis established design principles for coupling or integrating micron-scale colloids on a relatively larger scale to CRNs of different origins. By careful modulation and matching of dynamics of interacting colloidal particles with the kinetics of CRNs, I was able to achieve transient colloidal co-assemblies without hitting any kinetic traps. This opens up the possibility of exploring other dynamic functionalities, such as oscillations and bistability. Moreover, the successful adoption of such dynamic structures for future applications in autonomous and smart materials relies on improving the robustness of such systems and their integration with necessary self-regulating fuel generation and waste removal modules.

7.3 References

1 Wong, C. M., Wong, K. H. & Chen, X. D. Glucose oxidase: natural occurrence, function, properties and industrial applications. *Appl. Microbiol. Biotechnol.* **78**, 927-938, doi:10.1007/s00253-008-1407-4 (2008).

2 Fan, X. & Walther, A. pH Feedback Lifecycles Programmed by Enzymatic Logic Gates Using Common Foods as Fuels. *Angew. Chem., Int. Ed.* **60**, 11398-11405, doi:https://doi.org/10.1002/anie.202017003 (2021).

3 Pellegatti, P. *et al.* Increased Level of Extracellular ATP at Tumor Sites: In Vivo Imaging with Plasma Membrane Luciferase. *PLoS One* **3**, e2599, doi:10.1371/journal.pone.0002599 (2008).

4 Lecciso, M. *et al.* ATP Release from Chemotherapy-Treated Dying Leukemia Cells Elicits an Immune Suppressive Effect by Increasing Regulatory T Cells and Tolerogenic Dendritic Cells. *Front. Immunol.* **8**, doi:10.3389/fimmu.2017.01918 (2017).

5 Craciun, G., Tang, Y. & Feinberg, M. Understanding bistability in complex enzyme-driven reaction networks. *Proc. Nat. Acad. Sci. U.S.A.* **103**, 8697-8702, doi:doi:10.1073/pnas.0602767103 (2006).

6 Wilhelm, T. Analysis of structures causing instabilities. *Phys. Rev. E* **76**, 011911, doi:10.1103/PhysRevE.76.011911 (2007).

7 ter Harmsel, M. *et al.* A catalytically active oscillator made from small organic molecules. *Nature* **621**, 87-93, doi:10.1038/s41586-023-06310-2 (2023).

8 Semenov, S. N. *et al.* Rational design of functional and tunable oscillating enzymatic networks. *Nat. Chem.* **7**, 160-165, doi:10.1038/nchem.2142 (2015).

9 Howlett, M. G., Engwerda, A. H. J., Scanes, R. J. H. & Fletcher, S. P. An autonomously oscillating supramolecular self-replicator. *Nat. Chem.* **14**, 805-810, doi:10.1038/s41557-022-00949-6 (2022).

10 Dúzs, B., Lagzi, I. & Szalai, I. Functional Rhythmic Chemical Systems Governed by pH-Driven Kinetic Feedback. *ChemSystemsChem* **5**, e202200032, doi:https://doi.org/10.1002/syst.202200032 (2023).

11 Gentile, S., Del Grosso, E., Prins, L. J. & Ricci, F. Autonomous and Programmable Reorganization of DNA-Based Polymers Using Redox Chemistry**. *Chem. Eur. J.* **29**, e202300394, doi:https://doi.org/10.1002/chem.202300394 (2023).

12 Resnick, S. M. & Zehnder, A. J. In vitro ATP regeneration from polyphosphate and AMP by polyphosphate:AMP phosphotransferase and adenylate kinase from Acinetobacter johnsonii 210A. *Appl. Environ. Microbiol.* **66**, 2045-2051, doi:10.1128/aem.66.5.2045-2051.2000 (2000).

13 Luo, S. *et al.* ATP production from electricity with a new-to-nature electrobiological module. *Joule* **7**, 1745-1758, doi:https://doi.org/10.1016/j.joule.2023.07.012 (2023).

Acknowledgments

First and foremost, I would like to express my gratitude to Prof. Andreas Walther for his unwavering belief in me and for affording me the opportunity to work on such a diverse and challenging subject. Your consistent support, exemplary guidance, and the freedom you granted me in my scientific pursuits have played a central role in shaping me into a more proficient and independent scientist. During my time in Walther Lab, I enjoyed working in an enriching environment surrounded by talented and skilled researchers, which was topped with well-equipped infrastructure and unlimited technical support.

Coming from a background in organic chemistry, pursuing PhD projects spread over DNA, chemical reaction networks, and colloids were made possible due to the invaluable assistance and encouragement I received from both past and present members of the Walther Lab.

I would like to extend my appreciation to:

Dr. Simon Ludwanowski, for generously sharing his expertise in microgels and assisting me with my first polymerization reaction.

Dr. Saskia Gröer and Cecilia Oluwadunsin Akintayo, for their invaluable guidance in acquainting me with the field of DNA Nanotechnology during the early stages of my PhD when I did not know anything about the subject.

Dr. Daniel Hönders for being the lab magician, knowing every technical detail of our instruments, and always ready to help.

Wei Liu, for her kindness and patience in meticulously demonstrating everything in the DNA lab during my initial days, effectively lowering the barrier to entry into the field.

Dr. Avik Samanta, for introducing me to Confocal Laser Scanning Microscopy, helping with Flow Cytometry and generously sharing his diverse expertise, indispensable tips, and tricks—whether related to laboratory work or scientific writing. Our countless stimulating scientific discussions will always be cherished.

Dr. Brigitta Dúzs, who has been a delightful neighbor and a source of warmth, maintains an enjoyable atmosphere in the office. I am deeply appreciative of her critical advice on manuscripts, figures, and presentations, which significantly contributed to the refinement of my PhD.

Ricarda Schmidt, the lab's DNA-synthesis expert, graciously facilitated the preparation of high-quality DNA, making the process significantly more manageable. In-house DNA synthesis undeniably provided me with greater optimization flexibility and led to some of our most remarkable results.

Dr. Aritra Sarkar for collaboration on the ATP project, sharing his knowledge of systems chemistry, and being my go-to problem solver.

Dr. Soumya Sethi introduced me to the intricacies of cell biology. I had an amazing time collaborating with her on the DNA delivery project. Thanks for inspiring me and providing deep insights into the field.

Romina Pilz and Lydia Braun for efficiently managing day-to-day laboratory operations. Christoph Dress (cell-lab manager), Melanie Miller (cell-lab technician), and Dr. Leonie Dreissen for setting up the cell-lab and for sharing their expertise in cell biology, ensuring its efficient functioning.

Renata Widera, for her unwavering administrative support throughout and her instrumental role in organizing work-related trips and conferences.

I would also like to acknowledge the hard work and collaborative efforts of Lydia Braun and Dr. Daniel Hönders, who greeted us in Mainz with fully set-up labs.

Special thanks to my office mates: Dr. Brigitta Dúzs, Claudius Lupfer, and Dr. Lorena Baranda, for fostering a welcoming and friendly environment in the workspace. I would also like to extend my appreciation to Giorgio Fusi, Oliver Skarsetz, Joshua Krehan, Johann Fritzen, Sjoerd Engels, and Ricarda Schmidt for making coffee and lunch breaks much more interesting and stimulating.

I am also thankful to Prof. Rafal Klajn, who hosted me during my two-month secondment at the Weizmann Institute of Science. This experience introduced me to the field of nanoparticles, cages, and fascinating

instrumentation techniques. I must also extend my gratitude to Dr. Julius Gemen of the Klajn lab for helping me settle down in the lab and exchanging his ideas on the secondment project.
My heartfelt thanks go to Lacey Chunilal for involving me in her secondment project, which exposed me to the field of Alzheimer's disease and TAU proteins.
I would also like to express my gratitude to my CREANET colleagues for the enriching scientific experiences and ideas shared during our scientific gatherings.
A very personal and heartfelt thanks go to those who have been close throughout this journey, aiding in both my personal and professional growth.
Lastly, I want to extend my gratitude to my parents, my sister, and my brother for their unwavering support, which has enabled me to achieve my aspirations.